



University
of Glasgow

Donadio, Oberdan (2012) *G-band waveguide to microstrip transition for MMIC integration*. PhD thesis.

<http://theses.gla.ac.uk/3354/>

Copyright and moral rights for this thesis are retained by the author

A copy can be downloaded for personal non-commercial research or study, without prior permission or charge

This thesis cannot be reproduced or quoted extensively from without first obtaining permission in writing from the Author

The content must not be changed in any way or sold commercially in any format or medium without the formal permission of the Author

When referring to this work, full bibliographic details including the author, title, awarding institution and date of the thesis must be given



G-band Waveguide to Microstrip Transition for MMIC Integration

by

Oberdan Donadio

Thesis submitted in fulfilment of the requirements for the
degree of Doctor of Philosophy

in the
School of Engineering
College of Science and Engineering

January 2012

Declaration of Authorship

I, Oberdan Donadio, declare that this thesis titled, ‘G-band Waveguide to Microstrip Transition for MMIC Integration’ and the work presented in it are my own. I confirm that:

- This work was done wholly or mainly while in candidature for a research degree at the University of Glasgow.
- Where any part of this thesis has previously been submitted for a degree or any other qualification at this University or any other institution, this has been clearly stated.
- Where I have consulted the published work of others, this is always clearly attributed.
- Where I have quoted from the work of others, the source is always given. With the exception of such quotations, this thesis is entirely my own work.
- I have acknowledged all main sources of help.
- Where the thesis is based on work done by myself jointly with others, I have made clear exactly what was done by others and what I have contributed myself.

Signed: Oberdan Donadio

Date: 02/09/2011

“A smooth sea never made a skillful mariner”

(English proverb)

Abstract

In recent years, Millimetre-Wave (MMW) frequencies (30-300 GHz) have been exploited for a variety of attractive applications such as astronomical observation, medical imaging, aircraft aided-control landing, security and concealed weapons detection. All this was also possible thanks to the advances in high frequency circuits where Monolithic Microwave Integrated Circuits (MMICs) represent a key factor. Systems working at MMW often use metal waveguides as interconnect elements and transitions are employed to transfer the signals from these elements to the Radio Frequency (RF) circuits.

The objective of this thesis is to design, fabricate and characterise electromagnetic transitions between rectangular waveguide (WR) and planar transmission lines at G-band frequencies (140-220 GHz). The first part of this work presents an overview of the electromagnetic properties of the atmosphere at MMW frequencies and their use for passive MMW imaging applications. Fundamental design concepts and prototypes of real-time imagers are also represented, based on the pioneering work carried out at QinetiQ Ltd. An extensive review of the scientific literature on waveguide transitions presents previous designs and architectures. The work proceeds through design, simulation, fabrication and measurements of G-band transitions highlighting advantages and disadvantages of different structures.

The *novel* design of Elevated E-plane probes, used as waveguide to microstrip transitions in this work, extends the fabrication technique of MMIC air-bridges to build suspended metal structures and provides an additional optimising parameter to improve the reflection performance of the transition by decomposing the substrate influence on the metal probe.

The innovative Elevated E-plane probe is fabricated on Semi-Insulated Gallium Arsenide (SI-GaAs) and it is MMIC-integrated, reducing system complexity and optimizing fabrication and assembly costs.

The core of the thesis details the fabrication processes and procedures and a separate section describes the manufacture of G-band rectangular waveguide blocks that host the transitions. The overall fabrication is carried out using in-house facilities at the University of Glasgow without the aid of external facilities.

Measured results are presented and discussed, validating design and simulations. This work has led to a successful design and fabrication of GaAs-integrated rectangular waveguide to microstrip line transition at G-band.

Acknowledgements

The investigation which is the subject of this Thesis was financially supported by EPSRC and QinetiQ Ltd. and was carried out as CASE award under the terms of QinetiQ Agreement No. 45358.

I would like to express my gratitude to my supervisor Dr. Khaled Elgaid for giving me the great opportunity of this Research project at the University of Glasgow and for his insightful guidance and advices throughout its course. I'm also particularly grateful to Dr. Roger Appleby, my industrial supervisor, who gave me the chance to collaborate with QinetiQ and for the fruitful discussions and meetings we had during the course of the project. Thanks to QinetiQ Ltd who contributed to support the research and allowed me to publish its results. Extra special thanks to Prof. Iain Thayne, my second supervisor, for his encouragements and useful feedbacks.

I would like to thank Susan Ferguson for introducing me to fabrication, for support and for being always an important source of information when needed. Special thanks to the Ultrafast group and to Helen Mclelland for helping during fabrication processes. Thanks to Wilson MacDougall, from the Mechanical Workshop, for his help in operating the CNC milling machine during the fabrication of my waveguides.

I particularly thank Alex Ross for helping me in the substrate thinning and for all the interesting conversations we had. Thank you Alex.

No acknowledgement would be complete without mentioning Dr. Gabor Mezosi, whom I thank for sharing his points of view and for his continuous encouragement. He has been a colleague and a precious friend.

Thanks to Dr. Michael Strain for his guidance and valuable comments.

I wish to thank the wonderful people from the JWNC, they are too many to list but I will remember you all. I also thank all nice friends I had around at the department, Lai Bun, Chi Jeon, Adel, Ian, Antonio, Giuseppe, Carla, Philippe, Giangiacomo, Marc, Corrie, Barry and please forgive me if I forgot someone.....

On a personal note, I want to thank my family for supporting me in my choices and for always being there when I needed. Finally, from the bottom of my heart I want to thanks Neus, who has always been by my side and helped me during my hardest moments. I could not have finished this work without her help!

Thank you all!

Publications and Events

Aspects of the work described in this Thesis has been published or presented in following papers and internal events:

- **O. Donadio**, K. Elgaid, and R. Appleby, "Waveguide-to-microstrip transition at G-band using Elevated E-plane Probe" *Electronics Letters*, 47(2), pp.115-116, January 2011.
- **O. Donadio**, K. Elgaid, "Fabrication of Broadband waveguide-to-microstrip transition at G-band", Postgraduate Student Colloquium, University of Glasgow, 2009.
- **O. Donadio**, K. Elgaid, "MMW Waveguide-to-planar Transmission line Design", Postgraduate Student Conference, 1st winner Posters Session, Heriot-Watt University Edinburgh, 2008.

Contents

Declaration of Authorship	i
Abstract	iii
Acknowledgements	iv
List of Figures	ix
List of Tables	xiii
Abbreviations	xiv
1 Introduction	1
1.1 Introduction	1
1.2 An Overview of Millimetre Waves	1
1.2.1 Atmospheric Absorption	2
1.3 Millimetre Wave Imaging	6
1.4 Passive Millimetre-Wave (PMMW) Imaging	8
1.4.1 Contrast Model and Materials Properties	9
1.4.2 System Performance	12
1.4.3 Different Systems	15
1.5 Trends towards Higher Frequencies	19
1.6 Conclusions	20
2 Rectangular Waveguide to Planar Transmission Line Transitions	21
2.1 Introduction	21
2.2 Aspects of Propagation in Rectangular Waveguide	22
2.2.1 Low Loss Transmission Line	22
2.2.2 Rectangular Waveguide Dimensions and Frequency Bands	22
2.3 Architecture of the Transitions	22
2.3.1 Ridge-Waveguide Transitions	24
2.3.2 Aperture-coupled Transitions	26
2.3.3 Transversal Transitions	31
2.3.4 In-Line Transitions	35
2.4 Some Considerations	40

2.5	Conclusions	41
3	Design and Methods	45
3.1	Introduction	45
3.2	Electromagnetic Design using EDA Software Packages	46
3.2.1	HFSS, FEM and Adaptive Meshing	46
3.2.2	Simulation setup	49
3.2.2.1	Materials assignment	49
3.2.2.2	Excitations	49
3.2.2.3	Boundaries	50
3.2.2.4	Analysis Setup	50
3.2.2.5	Custom Meshing Operations	51
3.3	Design Specifications	51
3.3.1	Considerations on Design options	52
3.4	WR5 Transition using In-Line Finlines	53
3.5	WR5 Transition Using Dipole Antennas	59
3.6	WR5-to-Microstrip transition using Transversal Launcher	62
3.6.1	Elevated E-plane Probe	74
3.7	Conclusions	77
4	Fabrication	81
4.1	Introduction	81
4.2	GaAs MMIC Processes	81
4.2.1	Photolithography	82
4.2.2	Metal Deposition	83
4.2.3	Electron Beam Lithography (EBL)	85
4.3	Fabrication of Transitions	88
4.4	First Level Fabrication	88
4.4.1	Substrate Preparation	89
4.4.2	E-beam Exposure, Development and Lift-off	90
4.5	Second Level Fabrication	91
4.5.1	Fabrication of Elevated Structures	91
4.5.2	Electroplating Process	92
4.5.3	Buffer Layers Removal	94
4.6	Bonding and Thinning	97
4.7	Scribe & Cleave for Die Dicing	99
4.8	Design and Fabrication for WR5 Transitions Housing	99
4.9	Considerations on Mechanical Manufacturing Tolerances	103
4.10	Assembly	104
4.11	Conclusions	107
5	Measurement Results	108
5.1	Introduction	108
5.2	Measurement Instruments	109
5.2.1	Instrumentation	109
5.2.2	Calibration	110
5.3	WR-05 Split-Block Lines Measurements	114

5.4	Channel Isolation	116
5.5	Performance of the WR5 Transitions	120
5.6	Measurements of Elevated E-plane Probe	122
5.6.1	Estimation of Loss Factor in Waveguide Bends and Transitions	127
5.7	Conclusions	130
6	Conclusions and Future Work	132
6.1	Conclusions	132
6.2	Future Developments	136
A	Rectangular Waveguide Theory	137
A.1	Modes and Propagation	137
A.1.1	From Maxwell's Equations to TE/TM/TEM	137
A.1.2	Modes in Rectangular Waveguides	140
B	Fundamental Parameters of Electromagnetic Transitions	147
B.1	Insertion/Return Loss, S-parameters and relative links	147
C	Mechanical CAD Tables	151
D	TRL Signal Flow Graphs Equations	158
	Bibliography	161

List of Figures

1.1	Electromagnetic waves spectrum	2
1.2	Atmospheric attenuation	3
1.3	Absorption modes	4
1.4	Polarization of a water vapor molecule	6
1.5	Block diagrams of systems for passive radiometry	8
1.6	MMW radiation from objects on the scene	10
1.7	Reflecting lens system	15
1.8	Lens system for 35GHz	16
1.9	Lens system for 35GHz using meander plate	16
1.10	Lens system for 94GHz	17
1.11	Reflection in receiver systems	18
2.1	Ridgewaveguide transition	24
2.2	EM field rotation in Ridge-waveguide	25
2.3	Aperture-coupled transitions	28
2.4	Cavity model for aperture coupled transitions	29
2.5	Aperture coupled transition using CPW slots	30
2.6	Shielding of aperture coupled transitions	31
2.7	Waveguides to coaxial probe transitions	32
2.8	Transversal transitions	32
2.9	Transversal transitions with vias	33
2.10	Transversal transition with offset	34
2.11	Antipodal finlines	35
2.12	Antipodal finlines assembly	36
2.13	EM field rotation in antipodal finlines	36
2.14	Resonances in antipodal finlines structures	37
2.15	Uniplanar Finlines	37
2.16	In-line tapered slotlines	38
2.17	Quasi-Yagi printed antennas transitions	39
2.18	Dipole antenna transition with vias	39
2.19	Transition with monopole antennas	40
3.1	Tetrahedron element	47
3.2	HFSS solution process	48
3.3	HFSS adaptive meshing refinement	48
3.4	Design of antipodal finlines transition	54
3.5	Microstrip line input impedance in waveguide	54
3.6	Propagation constant of microstrip mode	55

3.7	E-field distribution using antipodal finlines as transition	55
3.8	S_{11} parameter for antipodal finlines with resonances	56
3.9	S_{21} parameter for antipodal finlines with resonances	56
3.10	E-field at resonance for antipodal finlines	57
3.11	Design of back-to-back antipodal finlines	57
3.12	S_{21} parameter for antipodal finlines with resonances	58
3.13	E-field plot at resonance for antipodal finlines back-to-back configuration	58
3.14	Results of the meshing technique applied to Finline transition	59
3.15	Transition using printed dipole antenna	60
3.16	Design parameters of printed dipole antenna	61
3.17	S-parameters for printed dipole antenna	62
3.18	E-field plot for transition using printed dipole antenna	62
3.19	S-parameters for printed dipole at G-band	63
3.20	Waveguide to microstrip transversal transition	63
3.21	Design parameters of the transversal transition	64
3.22	Smith Chart representation of probe impedance by varying the length D	64
3.23	Smith Chart representation of probe impedance by varying the width W	65
3.24	Smith Chart representation of probe impedance by varying back-short distance L	66
3.25	Equivalent circuit for the transversal waveguide-to-microstrip probe	67
3.26	Design parameters for probe impedance matching network	68
3.27	Smith Chart representation of probe impedance broad band matching	68
3.28	S-parameters of broad band transversal transition	69
3.29	E-field at transversal transition junction	69
3.30	E-field plot on the probe and at microstrip cross-section	70
3.31	Propagating microstrip mode	71
3.32	Propagation constant of channelized microstrip line	71
3.33	S-parameters of microstrip line in metal channel	72
3.34	Design of broadband transversal transition in back-to-back configuration	72
3.35	Meshing technique for the transversal transition	73
3.36	Elevated E-plane probe structure	75
3.37	Design parameters for Elevated E-plane probe transition	76
3.38	S_{11} parameter for different probe elevations	76
3.39	S_{21} parameter for different probe elevations	77
3.40	Smith Chart representation of the Elevated E-plane probe impedance for different heights	77
3.41	Smith Chart representation of the Elevated E-plane probe impedance for different heights	78
3.42	S-parameters for single transversal transition using Elevated E-plane probe	78
3.43	Design of back-to-back transversal transition using Elevated E-plane probe	79
3.44	Meshing technique for the Elevated E-plane probe	80
3.45	S-parameters of back-to-back transition using Elevated E-plane probe	80
4.1	MA6 Mask Aligner	82
4.2	Metal evaporation systems Plassys I and PLassys II	84
4.3	Electron Beam Evaporation Chamber	84
4.4	E-beam lithography system VB6	85

4.5	Pattern definition through e-beam exposure	87
4.6	Unit cell design	89
4.7	EBL exposure process	90
4.8	Profile of developed e-beam resist	91
4.9	Photolithography technique for elevated structure	93
4.10	Electroplating system set up	94
4.11	Electroplating process and buffer layer removal	95
4.12	SEM micrograph of an array of Elevated E-plane probes	96
4.13	SEM micrograph of an Elevated E-plane probes	96
4.14	SEM micrograph of elevated microstrip and elevated CPW line	97
4.15	Wafer bonding technique	98
4.16	Thinned substrate sample	99
4.17	Thickness measurements of thinned substrate	100
4.18	Rectangular waveguide coordinate system	101
4.19	Slotted waveguide array antenna	102
4.20	CNC Datron [®] CAT-3D M6 milling machine	102
4.21	Design of G-band split-block waveguide line	103
4.22	Fabricated split-block waveguide lines	103
4.23	Split-block waveguide housing for transitions testing	104
4.24	Profile of milled rectangular waveguides	105
4.25	Split-block T-junction for waveguide to microstrip transitions	105
4.26	Assembly of transversal broadband transitions in back-to-back configuration	106
4.27	Assembly of Elevated E-plane probes in back-to-back configuration	106
4.28	Optical micrograph of assembled Elevated E-plane Probe	107
5.1	PNA setup for G-band measurements	109
5.2	Signal flow graph	110
5.3	Components of the OML V05-AL-22 calibration kit	111
5.4	Block scheme for S-parameters measurements	112
5.5	Blocks and signal flow diagrams for TRL calibration	113
5.6	S-parameters for the calibration kit 1 inch WR-05 waveguide line	114
5.7	Measurements of G-band split-block waveguides	115
5.8	Measured S-parameters for 1cm waveguide line	115
5.9	Measured S-parameters for 2cm waveguide line	116
5.10	Measured S-parameters for 3cm waveguide line	116
5.11	Comparison of S_{21} of waveguides with different length	117
5.12	Fabricated half split-block for waveguide to microstrip transitions	117
5.13	Three test cases for waveguides isolation	118
5.14	Measured S_{11} parameters for waveguides isolation	118
5.15	Measured S_{21} parameters for waveguides isolation	119
5.16	Simulated S_{21} parameters for waveguides isolation	120
5.17	Simulated S-parameters S_{11} and S_{21} of broadband back-to-back waveguide- to-microstrip transition	121
5.18	S-parameters S_{11} and S_{21} of broadband back-to-back waveguide-to-microstrip transition	121
5.19	Model for flange misalignments	122
5.20	S-parameter S_{11} for flanges misalignment along width	123

5.21	S-parameter S_{11} for flanges misalignment along height	123
5.22	Design of Elevated microstrip line	124
5.23	Measured S_{21} parameters for elevated microstrip lines	125
5.24	Measured S_{21} and S_{12} for waveguide transition using Elevated E-plane probe	126
5.25	Measured S_{11} for waveguide transition using Elevated E-plane probe	126
5.26	S-parameters	127
5.27	CAD perspective view of split-block G-band waveguide S-bend	128
5.28	Measured and simulated S_{11} parameters for the split-block S-bend	128
5.29	Measured and simulated S_{21} parameters for the split-block S-bend	129
5.30	Loss Factor for the split-block S-bend	129
5.31	Loss Factor for broadband and elevated E-plane probe transitions	130
5.32	Loss Factor for single broadband and elevated E-plane probe transitions	131
6.1	IEEE P1785 standard	136
B.1	S-parameters block for two-ports network	148
C.1	Mechanical Cad table for the fabrication of 1cm waveguide	152
C.2	Mechanical Cad table for the fabrication of 2cm waveguide	153
C.3	Mechanical Cad table for the fabrication of 3cm waveguide	154
C.4	Mechanical Cad table for the fabrication of G-band housing of transitions	155
C.5	Mechanical Cad table for the fabrication of G-band housing of transitions	156
C.6	Mechanical Cad table for the fabrication of G-band waveguide bend	157

List of Tables

1.1	Optical properties for materials at 100 and 500 GHz.	11
2.1	Rectangular Waveguide sizes and frequency bands.	23
2.2	List of the waveguide to planar transmission line in scientific literature (1/2)	42
2.3	List of the waveguide to planar transmission line in scientific literature (2/2)	43
2.4	Waveguide to planar transmission line transitions grouped in categories with their advantages and disadvantages. Electrical characteristics such as losses, bandwidth and level of complexity complete the table.	44
4.1	Nominal and measured values of thickness for different spin speeds with AZ4562 positive photoresist.	92
5.1	Mean value of S_{21} for three lengths of fabricated WR-05	115
A.1	Propagation modes and relative longitudinal field conditions	139

Abbreviations

ABC	Absorbing Boundary Condition
ADS	Advanced Design System
BSS	Beam Step Size
CAD	Computer Aided Design
CB-CPW	Conductor Backed Coplanar Waveguide
CNC	Computer Numerical Control
CPS	Coplanar stripline
CPW	Coplanar Waveguide
CW	Continuous Wave
DUT	Device Under Test
EBE	Electron Beam Evaporation
EBG	Electronic Band Gap
EBL	Electron Beam Lithography
EBPG	Electron Beam Pattern Generator
EDA	Electroni Design Automation
EM	Electromagnetic
EPSRC	Engineering and Physical Sciences Research Council
FEM	Finite Elements Method
FOV	Field of View
GaAs	Gallium Arsenide
GDSII	Graphical Data System II
Ge	Germanium
GSG	Ground-Signal-Ground
HF	Hydrofluoric Acid
HFSS	High Frequency Structure Simulator

IED	Improvised Explosive Device
IEEE	Institute of Electrical and Electronics Engineers
IF	Intermediate Frequency
InP	Indium Phosphide
IPA	Isopropyl Alcohol
IR	Infrared
ISM	Industrial, Scientific and Medical
JWNC	James Watt Nanofabrication Centre
LNA	Low Noise Amplifier
LRRM	Line-Reflect-Reflect-Match
MCM	Multi Chip Module
mHEMT	Metamorphic High Electron Mobility Transistor
MIBK	Methyl Isobutyl Ketone
MMIC	Monolithic Microwave Integrated Circuit
MMW	Millimetre Wave
PEC	Perfect Electric Conductor
PML	Perfect Matching Layer
PMMA	Polymethyl Methacrylate
PMMW	Passive Millimetre Wave
PMMWI	Passive Millimetre Wave Imaging
PNA	Performance Network Analyzer
PTFE	Polytetrafluoroethylene
RF	Radio Frequency
RFOW	Radio Frequency over Wafer
RO	Reverse Osmosis
SAR	Synthetic Aperture Radar
SI-GaAs	Semi-insulated Gallium Arsenide
SOLT	Short-Open-Load-Thru
SWR	Standing Wave Ratio
TE	Transverse Electric
TEM	Transverse Electromagnetic
TFE	Thermal Field Emitter
TM	Transverse Magnetic

TRL	Thru-Reflect-Line
UHR-EWF	Ultra High Resolution Electron Wide Field
UV	Ultraviolet
VNA	Vector Network Analyzer
WR	Rectangular Waveguide

To my beloved family

Chapter 1

Introduction

1.1 Introduction

The first chapter of this thesis gives an insight into the millimetre wave frequencies and the phenomenology that marks them for attractive applications such as *imaging*. An overview of the receiver architectures is discussed focusing on the direct detection technique as the preferred method for *passive imaging*. Sky temperature and material properties are crucial aspects at these frequencies and a contrast model is needed to interpret correctly the information carried by incoming signals.

Section 1.4.2 describes the fundamental parameters used to estimate the performance of the receivers, highlighting the unavoidable trade-offs involved in the design of a *real-time* system.

Early scanning receivers using reflecting lenses are introduced and some prototypes with their relative operating mechanisms are illustrated. The chapter ends by discussing the losses involved in the transitions between receiving antenna and RF circuits as a crucial part of the front-end design to achieve a good signal detection.

1.2 An Overview of Millimetre Waves

The Radio Frequency (RF) band 30-300 GHz has a wavelength from ten to one millimetre giving it the name Millimetre Wave (MMW) band. This range of frequencies, as shown in Figure 1.1, is located above the microwave band and below the low infrared (IR) region where the electromagnetic radiation is commonly called terahertz radiation.

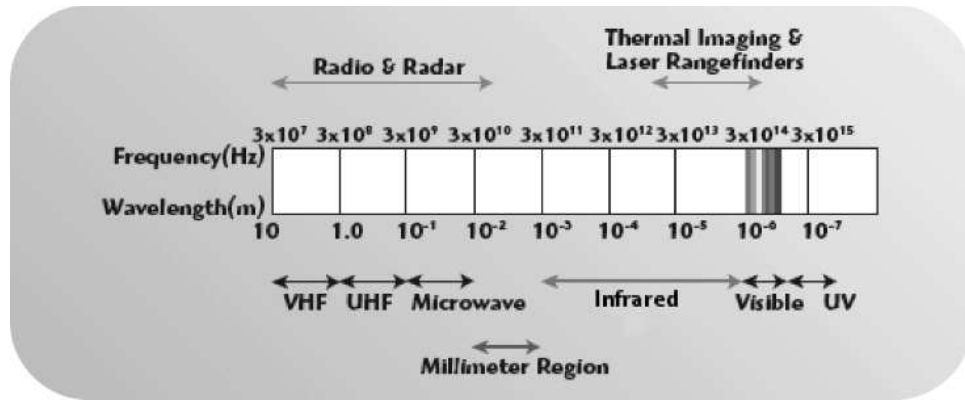


FIGURE 1.1: MMW band location in RF spectrum.

The advantages, associated with increasing the operating frequency of well developed microwaves applications to include the MMW range, could result in potential wider transmission bandwidth for the RF circuits and an improved resolution and directivity for a given antenna aperture.

However, these applications should take into account two major aspects:

- atmospheric transmission properties
- maturity of technology

The atmosphere presents some peculiar characteristics at MMW frequencies that are not generally encountered at microwave frequencies, focussing interest towards new applications and uses. However, the major problem is to have a mature and developed technology which allows proper detection and post processing of signals at these frequencies.

This chapter presents a qualitative overview of the aspects related to the MMW systems design, focusing on the particular application of the *Passive MMW (PMMW) imaging*. Examples refer to investigations and to pioneering work done at QinetiQ under the supervision of Dr. Roger Appleby.

Phenomenology and general design aspects will be discussed pointing out the limitations and advantages of taking such systems up to the G-band (140-220 GHz). The chapter ends with a discussion on the crucial role the electromagnetic (EM) interconnection segments have on the total system performance and pointing out their requirements.

1.2.1 Atmospheric Absorption

The reason for which MMW frequencies aroused the interest of the scientific community relies on the unique features of objects and the atmosphere at this range of wavelengths.

In fact, the EM transmission properties of the atmosphere depend on many factors such as: temperature, humidity, elevation, pressure and its gas percentage composition. The electromagnetic radiation at different wavelengths can be scattered and/or absorbed by atmospheric particles.

Scattering and *absorption* can be considered two different processes. Scattering happens when the EM radiation conserves the total amount of energy but the direction of propagation is altered. Absorption, instead, is a process that subtracts energy from the EM radiation and converts it to another form.

Attenuation (or extinction) is the sum of scattering and absorption and takes into account the total effect between the medium and propagating radiation. An example of a well known and often cited graph that represents the attenuation of the EM propagation is shown in Figure 1.2.

This figure shows the attenuation in decibels per kilometre (dB/Km) due respectively

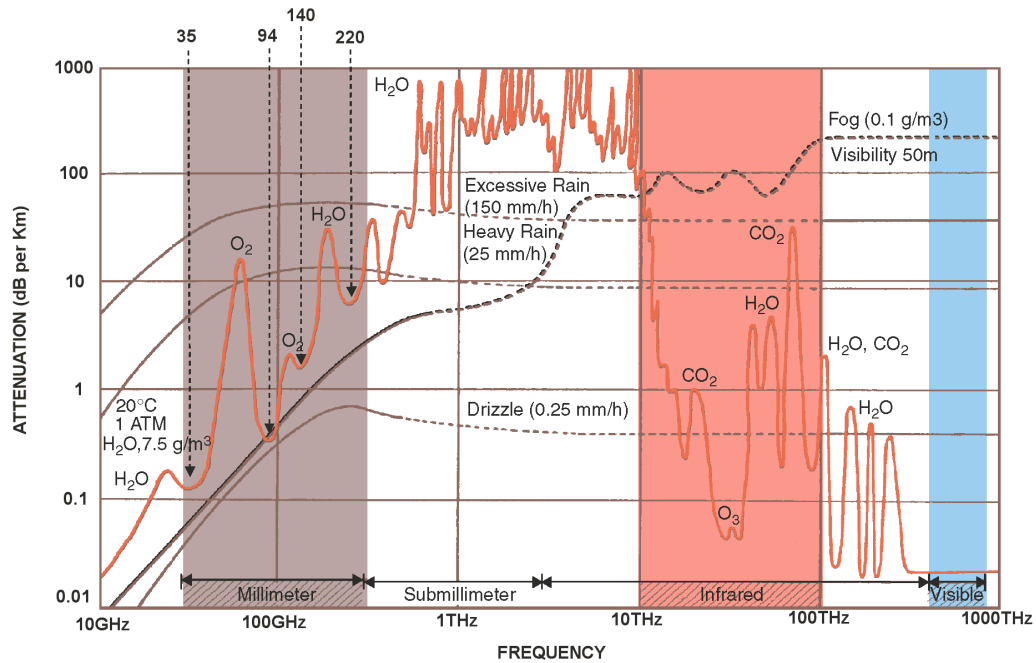


FIGURE 1.2: Attenuation of electromagnetic waves by atmospheric gases, rain and fog.

to atmospheric gases and particulates, typically rain and fog, in the range of 10GHz-1000THz. The gaseous attenuation, represented by the red plot, refers to a horizontal transmission path at sea level in clear air conditions. It can be noticed that the attenuation mainly due to scattering for different rainfall densities is also reported.

The gaseous attenuation is mainly due to absorption and it shows different peaks which refer to the absorption frequencies of the different gases constituting the atmosphere. Between two different absorption frequencies, there are the so called transmission "*windows*". These frequency bands have relatively low attenuation and are better candidates to transmit information compared to their adjacent frequencies. It can be noticed, from

Figure 1.2, that in the MMW band there are four transmission windows centred around the frequencies of 35, 94, 140 and 220 GHz. Three absorption peaks due to oxygen (O_2) and water vapour (H_2O) can be found in between these transmission windows.

The attenuation is further increased in poor weather conditions by drizzle and heavy rain which contribute to scattering effects. The relative plots in figure 1.2 show a knee behaviour at a few hundred GHz, after which they keep fairly constant up to 100 THz. A remarkable plot relative to fog condition shows that at MMW the attenuation is two orders of magnitude lower than in the visible spectrum.

A detailed analysis of the spectra of different atmospheric gases is beyond the scope of this introduction. However, a general and qualitative description of the causes of gases absorption and how they affect some applications could lead to a better comprehension of the exploited MMW phenomenology and the choices and trade-offs made in the MMW systems design.

The absorption of EM radiation relies on the interaction of radiation with matter. Whether the matter is in solid, liquid or gas state, the molecular absorption of the radiation can follow different processes depending on the wavelength and the amount of energy of the radiation itself.

Generally, the absorption is classified in *rotational*, *vibrational* and *transitional* modes; their frequency occurrence is presented schematically in Figure 1.3. At wavelengths up

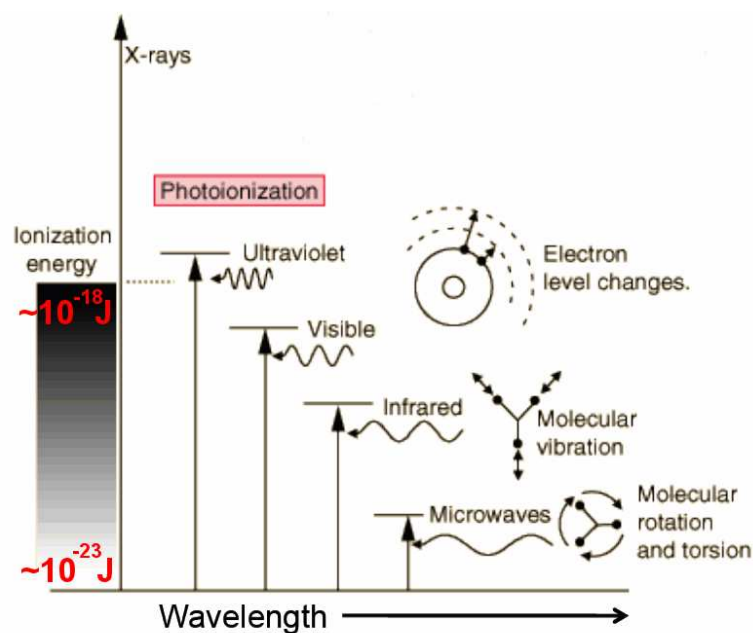


FIGURE 1.3: Absorption modes at different wavelengths.

to the visible spectrum, the majority of the energy is molecularly absorbed in form of

electron energy level changes. As we approach the infrared (IR) wavelengths the radiation is absorbed in the form of molecular vibrations, which can be considered as the superposition of vibrational modes whose cardinality and orientations depend totally on the molecules geometry and the nature of its chemical bonds. The EM radiation, at microwave and low IR frequencies, is mostly absorbed in gases as molecular rotations and torsions. Also, depending on the molecules geometry and charges distribution, it is possible to consider a molecular rotation as superposition of rotational modes referring to a fixed coordinate system.

At MMW frequencies the absorption spectra of most solids are flat, whereas gases have many absorption lines due to the rotational modes [1].

The composition of the atmosphere at sea level is:

- N_2 Nitrogen 78%
- O_2 Oxygen 21%
- H_2O Water vapour 0-2%
- Ar Argon 0.9%
- CO_2 Carbon dioxide 0.1% (varies with location)
- Neon, Helium, Krypton 0.0001%
- CH_4 , SO_2 , O_3 , NO , NO_2 in trace quantities

Each of these gas molecules interacts with the EM radiation and may or may not absorb energy in the form of rotations and torsions depending on their own molecular structure. Figure 1.2 shows that at MMW frequencies O_2 and H_2O are the only two atmospheric components showing strong and noticeable absorption lines.

The water vapour molecule has a zero net charge, but the nature of its chemical bonds is such that positive and negative charges do not completely overlap. Hence water vapour molecules are said to be *polar* because they show a *permanent electric dipole moment*. Absorption of microwave radiation happens when the electric field of a travelling EM wave exerts a torque on a molecular dipole as illustrated in Figure 1.4 for the case of water vapour.

Rotational motion of molecules can be quantized. Atmospheric absorption happens when quantum energy of microwave photons matches the ranges of energy separating quantum states of molecular rotations and torsions. Following this mechanism, water vapour presents absorption at 22GHz, 183GHz and 324GHz.

Molecules with mirror symmetry like Oxygen (O_2), Nitrogen (N_2) and Carbon dioxide

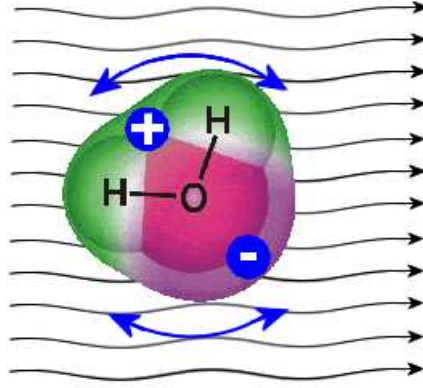


FIGURE 1.4: Rotation and torsion of a water vapour molecule due to electric field.

(CO_2) have no permanent electric dipole moments and so can not interact with an electric field. In fact, Oxygen presents two relevant absorption bands at around 60GHz and 118GHz. These are due to the particular chemical bonds of the O_2 molecules. The electron configuration of the oxygen has two unpaired electrons occupying two degenerate molecular orbitals. These orbitals are classified as *antibonding*. Unpaired electrons on antibonding orbitals can have the same spin, so that the molecule has a non-zero magnetic moment and it is said to be *paramagnetic*. The oxygen molecular configuration is also known as *triplet*.

The absorption frequencies of O_2 and H_2O are discrete, but as the gaseous molecules are constantly in collision with each other, the absorption frequencies broaden into bands whose extension is directly related to the temperature, an indicator of molecular kinetic energy.

Nitrogen (N_2), although it is very similar and presents a molecular composition close to Oxygen, does not have a magnetic moment and it does not present any major absorption frequency. In fact, its outer molecular orbital is fully complete and the two nitrogen atoms have a stable and strong bond.

As a consequence of gaseous absorption frequencies, developers design their RF, long distance, systems mainly centred on the transmission windows, where the attenuation is less dramatic. On the other hand, frequency bands, where the attenuation is substantial, were left unlicensed, allowing freedom of development of many short range applications for Industrial, Scientific and Medical (ISM) uses.

1.3 Millimetre Wave Imaging

In the last fifty years the interest in extending our vision of the environment culminated in developing systems for remarkable applications such as *radio astronomy* and *earth*

remote sensing.

Satellite and airborne remote sensing evolved mainly around two different techniques:

- *Passive Imaging*
- *Active Imaging*

Passive imaging relies on radiometric techniques used to measure the power of the EM radiation coming from a scene. For instance in earth remote sensing, the solar energy is absorbed by the earth's surface which, at energy balance, re-emits it mainly in the infrared spectrum [2]. In passive radiometric imagers, the receiver collects the energy naturally emitted or reflected and forms images containing information on the nature of objects in terms of intensities and transparency.

Active imaging, instead, is based on radar techniques where a pulse or a continuous wave (CW) with determined power is transmitted and then reflected by the objects of interest. From different delays and distortion of the reflected pulse, it is possible to define the profile of the observed scene. One of the most remarkable satellite based methods is called Synthetic Aperture Radar (SAR). This system combines the active imaging techniques with the continuous movement of the satellite along its orbit resulting in a system with a virtual larger receiving antenna that increases image resolution.

Conceptually, the two techniques are very different and as such they have advantages and disadvantages regarding their performance and type of information that they can collect. For example, while passive imaging relies on radiation intensity coming from a scene, the active imaging relies instead on transmitting and receiving pulses and provides a more accurate scene depth.

In both systems there is a noise floor that must be exceeded in order for the imagers to work effectively. The performance of an active imager is a function of receiver noise power, adopted scan technique, antenna performance and phenomenology involved. These effects can be separately optimised. Whereas a passive imager sensitivity, as further shown in Section 1.4.2, is limited by a combination of both receiver noise floor and noise associated with the thermal scene being imaged. Hence, passive imaging technology has to account the challenge of the thermal level of the scene.

If the environmental conditions present cloud layers or heavy rain the sky temperature increases significantly at MMW frequencies and its reflections become more difficult to be detected by a passive imager. Hence, there is the limitation of using passive imaging under controlled conditions. Active imaging systems have the ability to overcome these limitations, but they have always suffered from a lack of receiver components and suitable sources for the transmitters.

Active imaging involve a more complex electronics than passive imaging due to the required operations of transmitting signal with a determined power and detecting the information back-scattered by the scene, hence working as a radar system. Although MMW and sub-MMW sources become recently more available, mature technology has always been a barrier in the development of active systems due to high losses level in mixers and detectors.

On the other hand, passive imaging systems are typically simpler than active systems. However, passive imaging operations are not straight forward as they seem since the environment, being the source of illumination, have a strong impact on their performance. A list of various imaging system architectures is presented in [3] with their relative sensitivities in terms of minimum signal-to-noise ratio. These results also helped to state the program goals for the *DARPA Terahertz Electronics program*.

Passive imaging systems inherit their architecture directly from the IR radiometric receiving systems. The main topologies are illustrated as functional block diagrams in Figure 1.5. The tuned radio frequency receiver is used for the direct detection of the

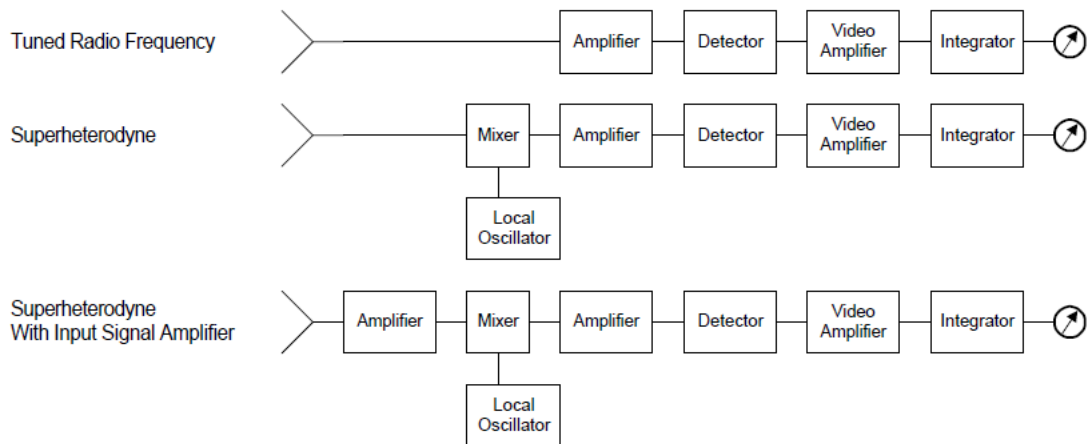


FIGURE 1.5: Functional blocks for different passive radiometry techniques.

signal and avoids local oscillators and pre-amplifiers which are used in super-heterodyne topologies. Local oscillators would add noticeable complexity to the design in case an array of receivers has to be employed. Direct detection has been the preferred approach for PMMW imagers and the following sections refer to it in the description of design characteristics.

1.4 Passive Millimetre-Wave (PMMW) Imaging

Similar to a visible camera or to an IR camera which detects radiation respectively in the visible and IR spectrum, a camera for PMMW imaging detects the naturally occurring

MMW radiation reflected or radiated by objects in a scene in order to form images. However, there are important differences between PMMW imaging and visible or IR imaging in terms of radiation intensity, spatial resolution and contrast model.

This section presents a qualitative analysis and discussion of the aspects that characterize PMMW imaging systems by considering contrast model and design parameters used to prototype outdoor imaging systems for 35GHz and 94GHz. The discussion points out the advantages and concerns in designing a possible PMMW imaging system at G-band.

1.4.1 Contrast Model and Materials Properties

In designing a PMMW imaging system it is important to understand the origin of the contrast in the scene. In the visible spectrum, the differences in reflectivities between objects and background is the main source of contrast. The objects reflect at different frequencies and so they appear with different colors. In MMW spectrum the contrast in outdoors scenes is produced in similar way but it is a function of the sky temperature [1] which is a source of incoherent illumination. At MMW frequencies the sky is relatively cold and it has a temperature of, typically, 100K on a clear day at the zenith rising to ambient temperatures at the horizon [4]. It is worth noticing that sun's illumination is not needed to generate MMW radiometric temperature based images. The radiation temperature is produced by the atmospheric emission. Objects in the scene reflect the radiation temperature of the sky forming images similar to visible pictures, depending on their material and optical bulk properties.

In fact, if the objects surface is smooth compared to the operating wavelength, they reflect specularly according to Fresnel's law. This implies that scattering effects can be neglected and light propagation obeys ray optics approximations. On the other hand, if the surface roughness become comparable with the observation wavelength then their reflections appear diffused.

Consider the situation illustrated in Figure 1.6. The radiation coming from a scene and detected by the imager has different components:

- Emissions from scene components
- Reflections of sky temperature by scene constituents
- Background emissions depending on environmental temperature

This means that the intensity of a MMW radiation at each point of the scene is determined by three contributions: self emission of components, reflection from the illumination source and background radiation.

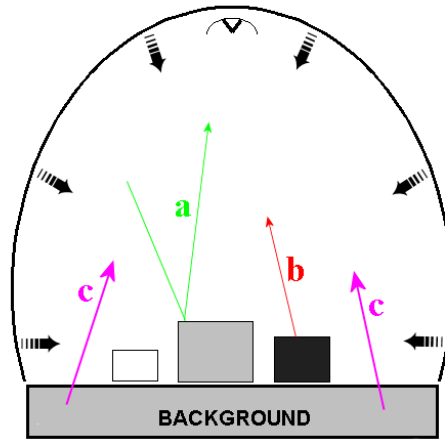


FIGURE 1.6: Scene objects radiation for a MMW imaging sensor: radiation reflected from objects (a), radiation emitted from objects (b), radiation transmitted from background (c).

As in the IR and visible spectrum, at MMW frequencies an object reflects and emits radiation depending on its emissivity (ϵ) and reflectivity (ρ). The object transmissivity (t) plays also a role revealing background information. All these parameters are related through the equation:

$$\rho + \epsilon + t = 1 \quad (1.1)$$

A perfect radiator has $\epsilon = 1$ and it is also known as *blackbody*, whereas a perfect reflector has $\epsilon = 0$. Emissivity and reflectivity of an object depends also on its dielectric properties (ϵ_r), surface roughness (ϱ) and angle of observation (θ):

$$\epsilon \equiv \epsilon(\epsilon_r, \varrho, \theta) \quad (1.2)$$

To better understand the image formation, consider the object surface brightness temperature T_s also called equivalent temperature as:

$$T_s = \epsilon T_0 \quad (1.3)$$

where T_0 is the object thermodynamic temperature.

Hence, objects with different emissivities have different radiated energy. An important factor in the generation of an image is the way the scene is illuminated. This information is captured by a scattered surface equivalent temperature T_{sc} :

$$T_{sc} = \rho T_{ill} \quad (1.4)$$

where T_{ill} is the temperature of the illuminating source and ρ is the reflectivity of the object.

TABLE 1.1: Optical properties for materials at 100 and 500 GHz.

Material	Emissivity		Reflectivity		Transmission	
	100GHz	500GHz	100GHz	500GHz	100GHz	500GHz
No object	0	0	0	0	1	1
Explosive on skin	0.74	0.95	0.26	0.05	0	0
Metal	0	0	1	1	0	0
Skin	0.65	0.91	0.35	0.09	0	0
Denim	0.09	0.49	0.01	0.01	0.9	0.5
T-shirt	0.04	0.2	0	0	0.96	0.8

By considering both factors the apparent temperature of the object T_e is:

$$T_e = T_s + T_{sc} = \epsilon T_0 + \rho T_{ill} \quad (1.5)$$

Moreover, some materials appear to be transparent allowing the radiation, coming from objects behind or in the background, to pass through and to be detected. This characteristic is accounted by the transmissivity t of the object.

Hence, the apparent temperature T_{rec} received by a PMMW sensor is equated as:

$$T_{rec}(\epsilon, \mu, \theta, \alpha) = \rho T_{ill} + \epsilon T_0 + t T_{back} \quad (1.6)$$

where T_{back} represents the temperature of the background. It is worth noting that the received temperature is a function of the dielectric materials in the scene (ϵ, μ) , the angle of observation θ and the angle of incidence α of the sky temperature on the scene objects.

By using eq. 1.6 it is possible to determine the **signature** of different materials in determined circumstances and operating frequency. Optical values for emissivity, reflectivity and transmission for some materials were found [5] and listed in Table 1.1.

The list of these few materials highlights the suitability of MMW in security applications where a possible *improvised explosive device* (IED) or metal weapon could be carried on a person and hidden under clothing. The values of reflectivity show that metal objects are highly reflective, whereas T-shirts (i.e. cotton) have a high value of transmission coefficient, hence resulting highly transparent at 100GHz. Values of ϵ , ρ and t for the same materials are also listed for 500GHz where they start to change substantially.

The ability to detect objects is related to the definition of **contrast**.

Contrast is the difference between the radiation reflected from the background when the object is present and that when the object is absent.

Eq.1.6 is of little use in identifying objects if the information regarding the temperature of the background is not provided. It could vary case by case.

However, if the imager can probe the scene with a sufficient resolution, it is possible

to detect variation of radiometric temperature that can flag the presence of a possible object or threat. This is, partly, the reason for which investigations are carried out to design imaging systems working at the upper bands of the MMW frequencies in order to reduce the spot size as explained in section 1.4.2.

Table 1.1 shows that contrasts of explosives on skin and metal on skin are dominated by differences in reflectivity. At 100GHz an outdoors scene is modelled with an environmental radiometric temperature of 100K. In this case the observed contrast of skin and explosives or skin and metal can be of 18K and 125K respectively. At 500GHz the environmental radiometric temperature is assumed to be 300K and the modelled contrasts have much lower values such as 2K and 4K respectively for explosives and metal again. Reflection of sky temperature is the primary aspect when metals and explosives have to be detected, consequently the direction along which the sky illuminates the scene is also important. If an imager is aimed at the zenith, it will detect the sky temperature and also a low level of downwelling radiation from the atmosphere itself. Moving towards the horizon the environmental temperature increases because the radiation has a longer path through the atmosphere.

Sky temperature is reflected back from objects to the imager, travelling across a portion of atmosphere once again where the contrast is further softened. Objects' contrast detected by an imaging system is reduced by atmospheric attenuation according the Koschmeider's equation [1]:

$$C(R) = C(0) \left(1 + \frac{b}{r(0)} [\exp(\alpha R) - 1] \right)^{-1} \quad (1.7)$$

where R is the range, α is the attenuation coefficient, b is the scattering parameter and r is the apparent averaged reflectivity of the object and background.

Particular attention has to be paid if a PMMW imaging system has to be designed at frequencies higher than 100GHz and operating over G-band (140-220GHz). The presence of two major absorption bands due to oxygen and water vapour have to be accounted when interpreting the results of reflections from the objects scene. In such cases, the sky temperature could vary from 200K to 280K [6] and a more sensitive receiver has to be employed.

1.4.2 System Performance

The performance of an imaging system can be defined by a set of equations describing *thermal sensitivity*, *spatial resolution* and *sampling* of the scene subtended by the system *field of view* (FOV).

The *thermal sensitivity*, ΔT_{min} , of an imager, also called *noise equivalent temperature*

difference, is the lowest temperature in the scene that is detectable by the receiver. It is defined as [7] :

$$\Delta T_{min} = \frac{T_a + T_R}{\sqrt{\beta\tau}} \quad (1.8)$$

where T_a is the antenna temperature, T_R is the noise temperature of the receiver, β is the frequency bandwidth and τ is the integration time of the receiver. For the smallest thermal sensitivity, β and τ need to have a value as high as possible.

The MMW radiation coming from the scene is, generally, focused on the receiver by an antenna system with an *aperture diameter* D. The half power beamwidth of an antenna, θ expressed in radians, with a circular aperture is given by:

$$\theta \approx \frac{1.22 \times \lambda}{D} \quad (1.9)$$

where λ is the wavelength of the radiation. From the Rayleigh law of diffraction it is then possible to define the *spot size*, s, at a distance range, R, from the center of the antenna as:

$$s = R \cdot \frac{1.22\lambda}{D} \quad (1.10)$$

The spot size is the footprint of the half power beamwidth of the antenna at a distance R and it also corresponds to the smallest resolvable object size at that distance. By increasing the aperture diameter D of the antenna or increasing the frequency of operation or both, it is possible to reduce the spot size achieving a better resolution for the imager.

For instance, let us consider the scanning and detection of an object of size around 300mm at a distance of 2m from the imaging system. One of the requirements is to use a spot size of 20mm which will give adequately 15 footprints across the object.

By using eq.1.10 the required aperture diameter of the antenna is D=1.05m for a working frequency f=35GHz and D=39cm for frequency f=94GHz. However, using the same aperture diameter of the antenna, at an increased distance R=20m the spot size will linearly increase to s=20cm. It is worth noting that by increasing the operating frequency it is possible to trade off size and resolution of the imager.

So far, the performance of an imaging system has been considered in terms of total antenna size, resolution and range. Consider now eq.1.8 where T_a represents the antenna temperature and contains the information coming from the scene, T_R is the receiver equivalent temperature and depends on the architecture and technology chosen for its realization. T_R is considered as additional internal noise.

Ideally a wide band system would provide a more sensitive detection, however the bandwidth, β , of the system has two limiting factors: technology and atmospheric attenuation. The last factor to consider is the single receiver integration time. If a *real-time* scanning operation is desired, the system integration time should be in the range of

10-25 ms in order to reproduce the observed scene with a good frame rate. This can be achieved by using a staring planar array of receivers or a scanning system. In the first case, the integration time of the system is equal to the integration time of the single receiver in the array. Because of the large number of receivers required, this solution is not cost effective, although preferred in some situations. In the second case, by assuming there are m picture points across the scene to be scanned with N receivers each having an integration time τ . Then, the whole system integration time is:

$$t = \frac{m \times \tau}{N} \quad (1.11)$$

From which:

$$\tau = \frac{t \times N}{m} \quad (1.12)$$

If the scanning system has a *field of view* (FOV) of h meters by v meters with the spot size at a distance R as defined in 1.10, then the number of picture points to scan, m , can be expressed as:

$$m = \left(\frac{2 \cdot h}{s} \times \frac{2 \cdot v}{s} \right) = 4 \times \left(\frac{h \cdot v}{s^2} \right) \quad (1.13)$$

where a factor of 4 takes into consideration the necessary bi-dimensional oversampling of each picture point to satisfy the *Nyquist-Shannon* condition in order to avoid *aliasing*. Hence, the 1.12 becomes [8] :

$$\tau = \frac{1}{4} \frac{s^2 t N}{(hv)} = \frac{1}{4} \frac{N s^2}{F(hv)} \quad (1.14)$$

which is the required integration time of a single receiver to achieve a system frame rate per second, $F = 1/t$, of the scene using a spot size s .

Moreover, by using 1.14 and 1.8 it is possible to express the thermal sensitivity of the receiver as:

$$\Delta T_{min} = 2 \times \frac{(T_a + T_R)}{s} \cdot \sqrt{\frac{F(hv)}{\beta N}} \quad (1.15)$$

Thermal sensitivity can be improved by reducing the frame rate, F , increasing the bandwidth β or the number of receivers N . By increasing the spot size s , it also improves the thermal sensitivity but this is achieved at the expense of the smallest resolvable feature size.

Vice-versa, the same eq. 1.15 can be rearranged to give:

$$N = 4 \times \left(\frac{T_a + T_R}{\Delta T_{min}} \right)^2 \cdot \frac{F(hv)}{\beta s^2} \quad (1.16)$$

which is the number of receivers N required for a frame rate F of the scene (hv) with a spot size s when it is necessary to reach a certain value for the sensitivity ΔT_{min} .

1.4.3 Different Systems

In the past many different methods to detect MMW radiation were developed. The traditional method, common in radioastronomy, used doped germanium (Ge) bolometers and it was analogous to the infrared detection. This approach needed a particular cooling system to reduce its inherent temperature noise. Alternatively, the technique of using tuned amplifiers before the actual detectors was crucial to the development of super-heterodyne receivers, Figure 1.5. These systems amplified the radiation in order to compensate the detector noise factor.

Recent availability of broad-band low-noise RF amplifiers at MMW frequencies, using InP and GaAs technology, allowed the development of a technique to detect MMW radiation from a scene by using a conical scanned array of receivers. This last solution proved to be the most cost effective, even when compared to planar antenna arrays coupled directly to amplifiers and detectors. In fact, these techniques do not have sufficiently low noise temperature to be used in very long distance PMMW imaging applications. The scanned receiver array technique represented the initial optimum solution for a *real time* imaging system [7]. The concept is based on a system of a reflecting lens as illustrated in Figure 1.7. The surfaces A and B represent two free standing wired grid polarizers

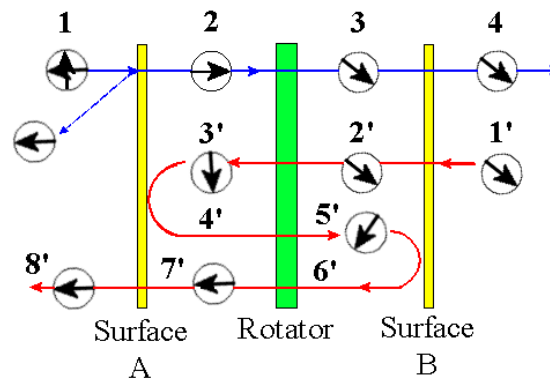


FIGURE 1.7: System of reflecting lens for wave polarization.

on either side of a *Faraday* rotator, having their polarization axes 45° apart.

A randomly polarized wave, 1, incident from left is linearly polarized by surface A, which allows one polarization to pass, 2, and reflects its orthogonal component. The resulting linear polarization is then rotated 45° by the Faraday rotator, 3, and eventually can pass through surface B, 4. If a wave with this last polarization is incident on the right side of the system, 1', it can pass through surface B, 2', and it is rotated 45° by the Faraday rotator, 3'. Surface A reflects back the radiation, 4', which passes a second time through the rotator where it further rotates of additional 45° , 5'. Surface B reflects

this incident wave because of its polarization, 6', and it passes a third time through the Faraday rotator, 7', which aligns its polarization conformally to exit surface A, 8'.

This system of reflecting lenses is the basis of the folded *Schmidt* camera, which if combined with a conical scanner, resulted in a real-time imaging prototype system operating at 35GHz [1]. The raytrace mechanism is illustrated in Figure 1.8. It consists of reflect-

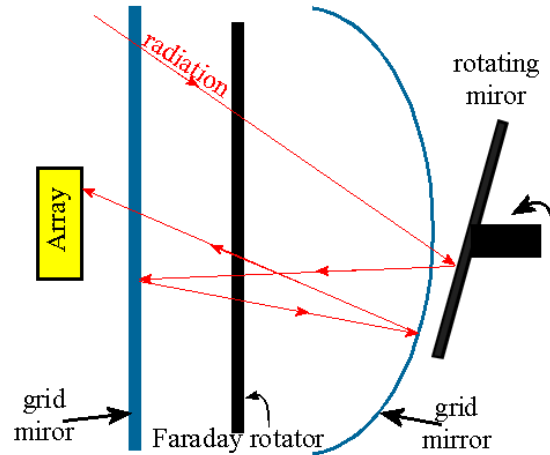


FIGURE 1.8: First prototype of lens system for an imager operating at 35 GHz.

ing lenses system as discussed and it differs by the use of a tilted rotating mirror that scans the incoming radiation from the scene. In this case, the curved polarising grid mirror, focuses the radiation on an array of 32 receivers.

This original concept was further modified to fabricate two additional prototypes, used for security scanning and for poor-weather navigation, working at 35GHz and 94GHz respectively. The raytrace of the two systems are illustrated in Figure 1.9 and 1.10. Figure 1.9 describes the imager prototype working at 35GHz and it is worth noticing

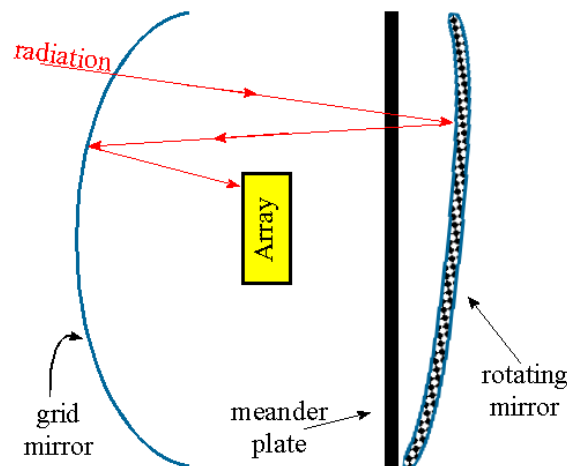


FIGURE 1.9: Raytrace for a 35 GHz imager prototype.

that the array of receivers is located between the grid mirrors. The rotating mirror and

the curved grid polarizer are replaced by a curved rotating mirror. In this case, a *meander quarter-wave plate* [7] is used as rotator. The polarizer is constructed from a grid of parallel metal lines whose spacing is small compared to the operating wavelength. The MMW radiation enters the system from the left and is polarized by the grid. Further, by passing through the meanderline, its polarization converts from linear to circular. The radiation is then reflected by the rotating mirror which changes the handedness of the circular polarization and it passes again through the meander line, where it converts its polarization from circular back to linear, but orthogonal to the original polarization. Finally, the radiation is reflected back by the polarizing grid and it is focused on an array of receivers.

The final system has an aperture of 1.6m and it has a field of view of $20^\circ \times 10^\circ$ able to cover an adult at 4m of distance.

The imager was used to collect images from people outdoors when carrying metal objects exploiting their high reflectivity to the sky temperature.

Figure 1.10 illustrates the raytrace for the imager prototype working at 94GHz and

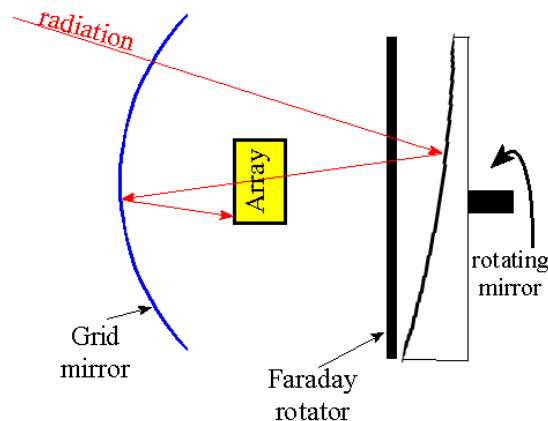


FIGURE 1.10: Raytrace for a 94 GHz imager prototype.

used in poor weather visibility. In this case the polarizer grid consists of parallel lines etched in copper on polytetrafluoroethylene (PTFE) substrate. The grid spacing is optimized for 94GHz.

For this design a Faraday rotator was initially adopted instead of the meanderline plate and an array of 150 receivers was employed. In its final realization, the Faraday rotator was substituted by a grooved quarter wave plate. The result of the design provides a system with an aperture of 50cm and a field of view of $60^\circ \times 30^\circ$. The array of receivers employed MMIC technology which enabled a compact form factor with reduced cost due to the reliability and repeatability of the MMIC process.

The architectures of Figures 1.9 and 1.10 allow linearly polarized radiation to be focussed on a block of receivers, likely in the form of small E-Horn antennas, oriented to receive

the same polarization.

In the design of real-time scanning imagers, it is necessary to consider the thermal sensitivity per receiver given in eq.1.15. Most of the time, it is possible to achieve the Nyquist-Shannon sampling condition by using two linear arrays of receivers instead of one, mounted above each other with an offset of half a receiver pitch. This arrangement relaxes the sensitivity requirements on the single receiver. The design needs to relate the receiver thermal sensitivity ΔT_{min} to the system thermal sensitivity ΔT_S by accounting for the atmospheric attenuation L_a , the loss, L_o , in the optics and the loss, L_t , in the EM transitions as follows:

$$\Delta T_S = \Delta T_{min} \cdot L_a \cdot L_o \cdot L_t \quad (1.17)$$

The atmospheric loss in clear air condition, from Figure 1.2, is 0.5 dB per Km at 100GHz, which gives an attenuation of 0.01 dB over a range of 20m. The optical loss is generally assumed to be ~ 3 dB. The loss in the transitions are the losses in the EM junctions between the receiver input and the first signal driver amplifier. This loss is mainly due to signal path attenuation and component impedance mismatch, which the designer is responsible for.

To stress the care that must be exercised in designing high frequency transitions for imaging applications, consider an impedance mismatch at a transition point between horn antenna and waveguide, with a reflection coefficient ρ . We have:

$$T_2 = T_1(1 - \rho) + T_\rho \quad (1.18)$$

where T_ρ is the equivalent temperature as seen from the point of reflection into the receiver, T_1 is the input temperature and T_2 is the temperature at the transition output as illustrated in Figure 1.11. Then the difference between output and input is:

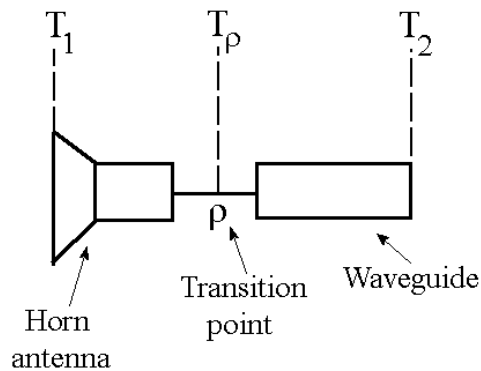


FIGURE 1.11: Schematic of reflection point due to impedance mismatch.

$$T_D = T_2 - T_1 = \rho(T_\rho - T_1) \quad (1.19)$$

By considering a typical temperature 300K for T_ρ and assuming $T_1=100$ K, with a reflection coefficient of -26dB we have an error $T_D=0.5$ K on the received temperature. If the imaging system aims to have a thermal sensitivity $\Delta T_{min}=1$ K, this type of reflection would dramatically influence the performance.

1.5 Trends towards Higher Frequencies

As mentioned in section 1.4.2, the trade-off between antenna aperture and operating frequency leads to imaging systems with much smaller dimensions than the prototypes illustrated in section 1.4.3, allowing the design of more portable devices which can be easily mounted on aircraft and helicopters for collision avoidance in poor weather conditions or for quick and temporary mountings in locations where stand-off security screening of personnel are required.

The limiting factors for the development of these type of imagers are related to the availability and reliability of RF circuits at frequencies beyond 100 GHz. Since PMMW imaging still prefers a direct detection technique of MMW radiation, the RF circuitry has to satisfy the main requirement of low noise characteristics which would otherwise compromise the single receiver sensitivity as highlighted in eq.1.8.

While initial investigations of RF circuit characteristics used in the prototypes of section 1.4.3 are described in [9], nowadays the industry provides commercially available receiver modules to the market [10] for frequencies up to W-band (75-110 GHz).

Meanwhile further investigations, carried out in the design of RF circuitry for imaging applications at G-band [11] and beyond [12], exploited the mHEMT MMIC technology and achieved promising results.

However, the single receiver structure still follows a hybrid architecture where amplifiers, detector and transition junctions are manufactured on different substrates. This solution is not cost effective since the different components have to be fabricated separately and delicate alignment and assembly procedures further extend production times. The integration of two or more components on a single substrate material would certainly be desirable in a manufacturing line.

Detector sensitivity still depends on the substrate material [13] and they do not lend themselves to easy integration. On the other hand a transition junction, as a passive device, could be integrated with the first stage amplifier of the receiver. Hence an overview of the possible transition geometries will help to select suitable solutions.

1.6 Conclusions

Atmospheric absorption bands characterize and dominate the EM spectrum at MMW frequencies and limit their use for communications. However, applications such as imaging for security screening exploit the concept of sky temperature as the illuminating source to reveal the properties that materials present at these frequencies. An overview of PMMW imaging systems and techniques has been presented and trade-offs for real time systems have been discussed. The key point for correct signal detection relies on delivering, with minimum losses, the signals from the receiving antenna to the RF circuits. Hence, care has to be taken in designing their interconnections.

The trend of designing smaller systems benefits from the recent advances in MMIC technology and a MMIC-integrated transition to a rectangular waveguide is a highly desirable feature when the receiving antenna is directly connected to a waveguide. The next chapter presents a literature review of the techniques used to realize this transition and it will help to consider the best solution to implement in MMIC.

Chapter 2

Rectangular Waveguide to Planar Transmission Line Transitions

2.1 Introduction

Generally a microwave transition is the mechanism by which an EM wave, travelling on one type of transmission line, is coupled into another type of line. Hence, there exist transitions between coaxial cable and microstrip lines, or coplanar waveguides to slot-lines etc...

This chapter presents rectangular waveguide as good candidates for low loss networks. The chapter then presents a literature review describing the different strategies that can be adopted to achieve an EM transition between rectangular waveguide and a generic planar transmission line, highlighting the use of scattering parameters as fundamental indicators of its performance. The architectures are subdivided into four categories depending on geometry and EM coupling mechanism. Each category is described citing previous works done and presenting its relative advantages and disadvantages.

The chapter ends with some considerations and two useful tables.

The first table is a summary of the different cited transitions, reporting their category, employed materials, operating bandwidth, measured S-parameters when available and their assembly characteristics. This table also includes the waveguide to microstrip transition developed in the present work.

The second table groups the transitions into four categories based on their architectures and lists pros and cons of each, considering aspects such as manufacture complexity, characteristics of materials, measurement suitability and robustness to fabrication tolerances.

2.2 Aspects of Propagation in Rectangular Waveguide

2.2.1 Low Loss Transmission Line

Rectangular waveguides are composed of a single metal conductor, whereas other microwave transmission lines such as coaxial cable, microstrip and CPW have more than one conductor functioning as signal line and reference ground. Signals propagate along the enclosed volume of the metal structure. Characteristic propagation is described in Appendix A where details are given on propagating modes.

Rectangular waveguides are the preferred transmission lines when low attenuation is desired, especially at high frequency where they represent the optimum choice as inter-stage connection between receiving antenna and first stage amplifier in a receiver front-end. The cross section of rectangular waveguides is often flared out to form a horn antenna which gives an enormous flexibility during the design and fabrication processes. All of these aspects justify the use of rectangular waveguides at MMW as the applications require a high level of sensitivity against the strong atmospheric attenuations at these frequencies. Although they are multi-mode lines, waveguides with appropriate dimensions can operate in single-mode propagation for better control of the propagating signal and its polarization. It is possible to associate waveguide dimensions to single-mode frequency bands.

2.2.2 Rectangular Waveguide Dimensions and Frequency Bands

Table 2.1 presents a list of the most common rectangular waveguide standards used in microwave and mm-wave bands. Each waveguide standard is associated with its operating frequency limits, which, partially or entirely, covers a frequency band. Interior waveguide dimensions are also listed in inches and millimetres. In most cases the waveguide cross-section has a 2:1 aspect ratio or very nearly so. However, it has to be highlighted that the waveguide has tolerances for its fabrication process that inevitably vary its dimensions from the nominal values with consequent variation of the frequency limits, especially for waveguides with very small cross-section.

The table is guidance for the different transition structures discussed in the present chapter.

2.3 Architecture of the Transitions

EM transitions can be interpreted as imperfections in electrical links and as such, they can be analyzed in terms of *insertion/return loss* or their equivalent network behaviour

TABLE 2.1: Rectangular Waveguide sizes and frequency bands.

Frequency Band	Waveguide Standard	Frequency Limits (GHz)	Inside Dimensions	
			(inches)	(mm)
C-band	WR-137	5.85 - 8.20	1.372x0.622	34.8488x15.7988
H-band	WR-112	7.05 - 10.00	1.122x0.497	28.4988x12.6238
X-band	WR-90	8.2 - 12.4	0.900x0.400	22.86x10.16
Ku-band	WR-62	12.4 - 18.0	0.622x0.311	15.7988x7.8994
K-band	WR-51	15.0 - 22.0	0.510x0.255	12.954x6.477
K-band	WR-42	18.0 - 26.5	0.420x0.170	10.668x4.318
Ka-band	WR-28	26.5 - 40.0	0.280x0.140	7.112x3.556
Q-band	WR-22	33 - 50	0.224x0.112	5.6896x2.8448
U-band	WR-19	40 - 60	0.188x0.094	4.7752x2.3876
V-band	WR-15	50 - 75	0.148x0.074	3.7592x1.8796
E-band	WR-12	60 - 90	0.122x0.061	3.0988x1.5494
W-band	WR-10	75 - 110	0.100x0.050	2.54x1.27
F-band	WR-8	90 - 140	0.080x0.040	2.032x1.016
D-band	WR-6	110 - 170	0.0650x0.0325	1.651x0.8255
G-band	WR-5	140 - 220	0.0510x0.0255	1.2954x0.6477
-	WR-4	170 - 260	0.0430x0.0215	1.0922x0.5461
-	WR-3	220 - 325	0.0340x0.0170	0.8636x0.4318
Y-band	WR-2	325 - 500	0.0200x0.0100	0.508x0.254
-	WR-1.5	500 - 750	0.0150x0.0075	0.381x0.1905
-	WR-1	750 - 1100	0.0100x0.0050	0.254x0.127

represented by the scattering parameters most commonly known as *S-parameters*. Their mathematical formulation and links are presented for completeness in Appendix B helping to understand the performance of the transitions treated in the present chapter.

An EM transition between rectangular waveguide and planar transmission line involves two major aspects:

- *Field matching*
- *Impedance matching*

Field matching is the operation that allows an EM field, propagating in a transmission line, to conform with the boundary conditions of a different line. An efficient field matching can be achieved by gradually changing the boundary conditions as the transmission line changes shape and conforms to the new structure. Field matching represents a prerequisite to a transition. *Impedance matching*, instead, provides maximum coupling between the two transmission lines while minimizing reflections.

The major obstacle in a transition with a rectangular waveguide is how to modify its three-dimensional boundary conditions in order to reshape the EM field to that of a

planar transmission line such as microstrip or coplanar waveguide (CPW). For this reason, a possible classification of transitions can be made on the basis of the architectural solution adopted. The transitions can be distinguished as follows:

- *Ridge-Waveguide transitions*
- *Transverse transitions*
- *In-line transitions*
- *Aperture-coupling transitions*

Following this classification, *Ridge-Waveguide* and *In-line* transitions focus mainly on re-shaping the EM field along its transition path, whereas both *Transverse* and *Aperture-coupling* transitions work as transducers focusing more on the impedance matching.

2.3.1 Ridge-Waveguide Transitions

The use of a Ridge-Waveguide in a transition between rectangular waveguide and a microwave planar line such as CPW is depicted in Figure 2.1.

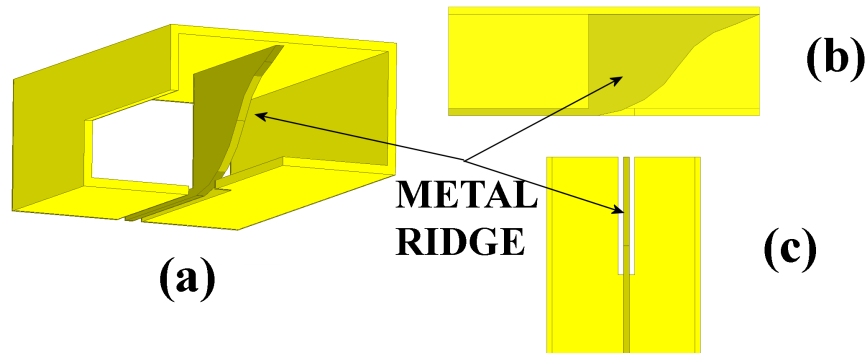


FIGURE 2.1: Perspective of a Ridge-waveguide transition to CPW (a), side view (b) and top view(c). Description of the Ridge waveguide at different cross-sections is also detailed in Figure 2.2

The mechanism of the EM field matching for this arrangement is described in [14], where a transition between rectangular waveguide and CPW at K-band is designed, fabricated and tested. The ridge structure is fabricated inside the rectangular waveguide and its tapered shape helps to split and rotate the propagating EM field distribution of the TE_{10} mode. Figure 2.2(1)-(4) shows how the TE_{10} electric field is modified by the presence of a gradually extending metal ridge until it matches the field distribution of the CPW, Figure 2.2(5)-(6). It is worth noting the non-radiating tapered slot which

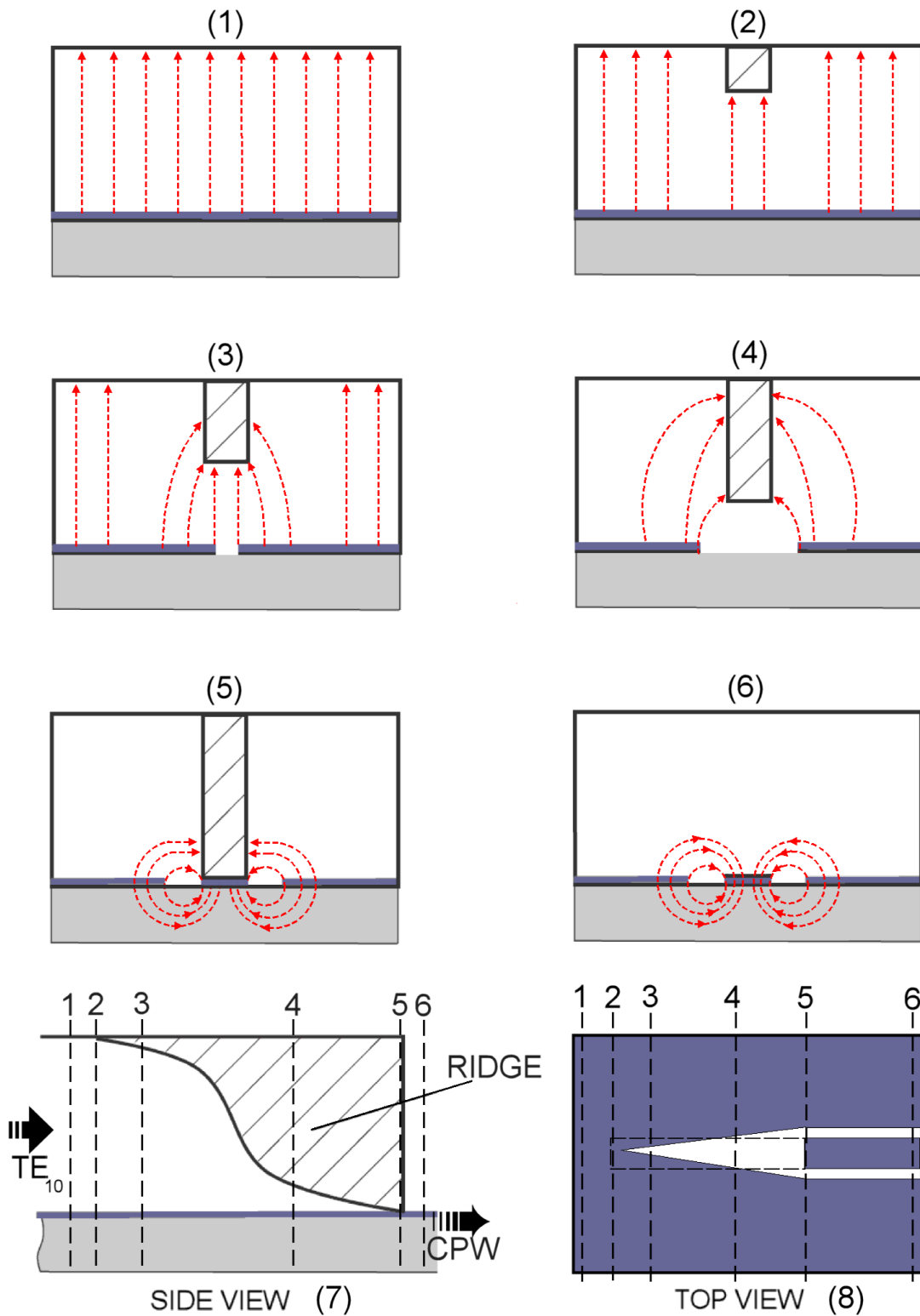


FIGURE 2.2: Cross-sections(1-6) relative to side view(7) and top view(8) of a Ridge-waveguide transition.

opens on the side opposite the ridge. The tapered slot helps the gradual excitation with equal magnitude and phase of the two slots of the CPW line. Two orthogonal perspectives of the transition are shown in Figure 2.2(7)-(8) for a side view and a top view of different cross-sections relative to the steps (1)-(6). The technique demonstrates a transition with a full band (18-26.5 GHz) response with reflection loss better than 11 dB and an average insertion loss of 1.75 dB. Although this architecture offers a full waveguide band performance, it has to be considered whether this arrangement is suitable at MMW frequencies where the dimensions in question are smaller. In fact, tolerances on the mechanical fabrication and alignment of the metal ridge could be prohibitive or, to some extent, not cost effective. However, the ridge-waveguide transition presents advantages when in-line axial alignment is desired between rectangular waveguide and CPW as commonly happens in probe devices used in Radio Frequency On Wafer (RFOW) measurements [15].

A ridge-waveguide structure at W-band (75-110 GHz) is demonstrated in [16]-[17] where a Lithium Niobate ($LiNbO_3$) anisotropic substrate with high dielectric constant ($\epsilon_x = \epsilon_y = 43$, $\epsilon_z = 28$) is employed. In this case, the metal ridge is made from $50\mu m$ thick copper shim stock and soldered into the rectangular waveguide. A cosine shape profile is employed for the ridge and a linear taper for the non-radiating slot was defined on the substrate. Parametric analysis is carried out on the length of the metal ridge and tapered slot respectively. As result, a threshold value for the ridge length is found after which the performance does not improve significantly, whereas an optimum value for the slot length was tuned. Experimental results reveal an $S_{11} < -15dB$ over the W-band and an $S_{21} = -3.5dB$ at 94GHz. However, it has to be noted that the transition is tested not in back-to-back configuration, hence appropriate losses have to be accounted when comparing this performance with other architectures measurements if not tested in similar manner.

The same structure is discussed in [17] where further sensitivity analysis is carried out on possible linear and angular offset of the ridge with respect to the centre line of the CPW. Simulated results shows the consistent response with linear offset and significant dependence of the return loss with angular misalignment.

The analysis reveals that care has to be taken towards mechanical tolerances that start to play an important role in the assembly process of ridge-waveguide transitions when exploited at the upper spectrum of the MMW frequencies.

2.3.2 Aperture-coupled Transitions

An interesting category of transitions was introduced in [18] where the use of a slot aperture was exploited to couple the EM energy into the rectangular waveguide.

The investigation of these early architectures, illustrated in Figure 2.3(a)-(b), proposes the energy coupling from a microstrip line via a slot in the its ground plane to a metal patch element placed on an additional substrate. This technique employs the proximity feeding mechanism of a microstrip patch antenna [19] which is the radiating element into the waveguide. A top view of the feed is also illustrated in Figure 2.3(d).

Experimental results show narrowband performance given its intrinsic relationship with the transmission bandwidth of the radiating patch.

The transition is designed and optimized for 11 GHz and measurements reveal a relative passband of 10%. Further versions of the same transition [20] are designed with a center frequency at 85 GHz and the authors investigate the option to widen the band by moving the patch element into the guide wall increasing its distance from the feeding structure 2.3(b). In some cases a proper step is defined on the rectangular waveguide profile to better position the radiating element, although increasing the complexity of fabrication and assembly, Figure 2.3(c).

The Aperture-coupled transitions present remarkable advantages when the location of the rectangular waveguide is desired only at the back of the planar circuit or when a waveguide backshort, generally used in the transitions presented in Section 2.3.3, has to be avoided due to space constraints. Moreover, this geometry avoids cutting the substrate into particular shapes, it does not compromise the rectangular waveguide line with any significant modification and it is suitable when no split blocks are needed.

The main disadvantage in using this technique is related to the presence of back-side radiation.

In fact, early experimental results in [18],[17] reveal the presence of EM radiation on top of the circuit which compromises the performance by reducing the energy transfer between microstrip and rectangular waveguide. The back-side radiation is related to the bidirectional nature of the radiation propagated from a slot aperture.

Additional versions of the transition are investigated in [21] where just a slot cut off in the ground plane of a microstrip line is used to couple the energy into the guide. A second substrate with appropriate thickness covers the aperture inside the rectangular waveguide and it works as $\lambda/4$ transformer to match the impedance of the microstrip with the impedance of the rectangular waveguide as illustrated in Figure 2.3(e).

Since the structure presents only a slot, back-side radiation is observed, but by keeping the length of the slot slightly longer than its resonating frequency it is shown that it is possible to couple energy into the guide and keep low levels of back-side radiation at the same time.

This approach is one of the first attempts to reduce the back-side radiation effect, but some other new precautions are also adopted in [22] where a single substrate is employed. Two radiating elements are excited by a CPW line instead of a microstrip. The use of

a CPW line allows the ground plane and signal line to be on the same side of the substrate. Additional vias connect the CPW ground planes to the metal of the rectangular waveguide in order to work as waveguide termination as in Figure 2.3(f). In this configuration, proper design of patch feeding reveals reduced levels of back-side radiation leakage which can be further reduced if a supplementary metal package is placed on top of the circuit trading-off performance against compactness. However if a metal cap is used, the total design has to take into account a possible frequency shift and reduction of the passband [22].

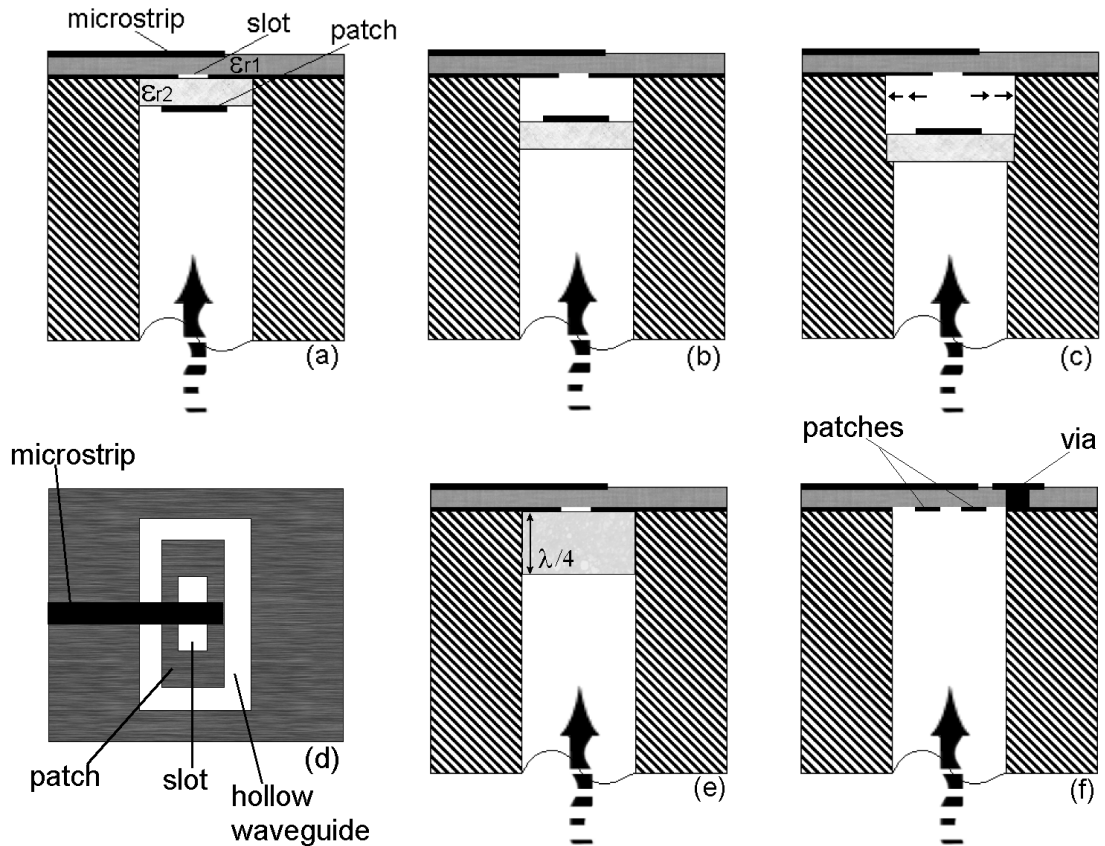


FIGURE 2.3: Aperture-coupling transitions using two different substrate materials(a-b) and a stepped waveguide(c). Top view of patch excitation(d). Transition using single substrate without resonating element(e) and with two radiating patches(f).

When designing rectangular waveguide transitions at higher frequency, mechanical tolerances become an issue.

In this scenario, the transition should preferably involve a single substrate and the minimum number of parts in order to be *robust* for fabrication and assembly tolerance. The work presented in [23] addresses some of these aspects by analysing the coupling mechanism between microstrip line and radiating element when defined on the same substrate material. The transition is illustrated in Figure 2.4(a)-(c) for three different views. Figure 2.4(d) summarises the coupling mechanism by exploiting the cavity model

for a patch antenna [24], here named *matching element*.

Low transmission loss is achieved by exchanging the fundamental TE_{10} mode of the rectangular waveguide and the *quasi-TEM* mode of the microstrip line through the fundamental resonant TM_{01} mode of the matching element, Figure 2.4(d).

The length of the matching element controls the frequency at which the TM_{01} mode resonates, hence the center of the passband. The transition was designed to work at 76.5 GHz. Figure 2.4(a)-(b) highlights the use of vias to prevent the transition from lateral radiation leakage and to minimize the back-side radiation.

The bandwidth of the transition is mainly limited to the bandwidth of the associated patch antenna. However, since the matching element is radiating in a waveguide and not in free space, the effect of the rectangular waveguide walls on the transmission bandwidth is investigated. A parametric analysis carried out on the dimensions of the rectangular waveguide cross-section with respect to the matching element dimensions reveals that there is a relationship between the length of the waveguide broad wall and the bandwidth of the transition. By increasing its length to a certain extent it is possible to trade off a relative passband of 6% with a reflection loss better than 10dB.

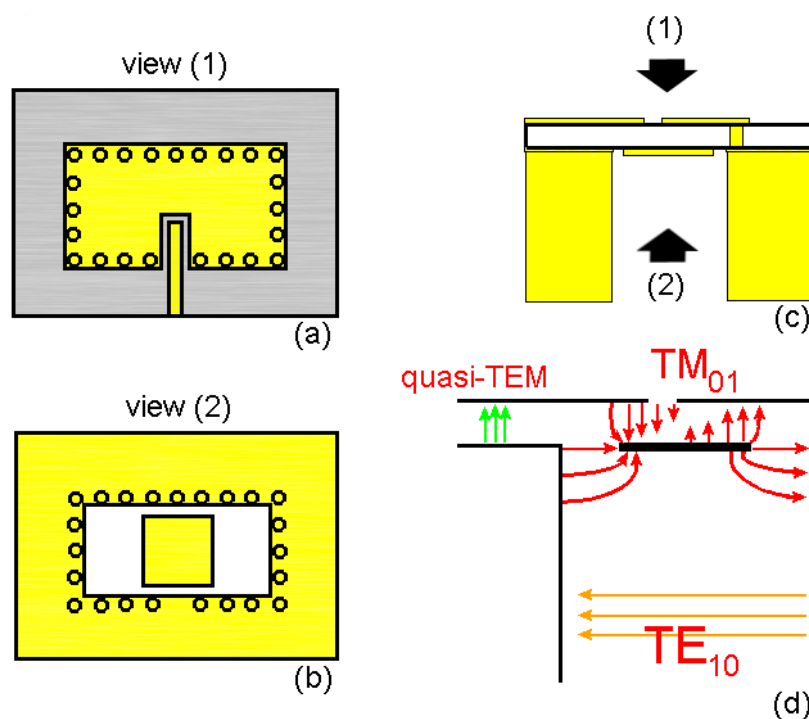


FIGURE 2.4: Top view(a) and inside view(b) of waveguide to microstrip transition(c) using cavity model(d).

Possible misalignment of the matching element with respect to the rectangular waveguide profile is also investigated to evaluate the maximum acceptable assembly tolerances. The design shows robustness for misalignments of $200\mu m$ in both directions parallel to the broad walls of the guide. However, the performance is very sensitive to misalignment

in directions parallel to the narrow walls that limits the maximum acceptable misalignment to $100\mu m$.

Further investigations are carried out on the same structure in [25] where the concept of the cavity model applied to the transition is extended. The proposed transition aims to work as a line divider between rectangular waveguide and two microstrip lines.

The position of the two lines with respect to the center of the matching element determines higher resonant modes in the cavity. The field distribution of these modes do not match the propagation mode in the rectangular waveguide. This effect is shown in the plot of the insertion loss which presents in-band dips at frequency where higher modes start to appear and consequently no energy transfer is supported by the structure.

A further analysis of the manufacturing tolerances reveals that the transition is sensitive to misalignment of the patch relative to the narrow walls as [23]. Roundness of the corners in the waveguide cross-section does not seem to compromise the insertion loss of the transition if it is limited to 0-0.7mm.

With the cavity model applied in [23] and [25] it can be deduced that higher order modes in the substrate present dips in the transmission characteristic at frequencies where no energy transfer can be associated to the structure. The same effect can be observed in transitions without resonating patch as in [26].

Figure 2.5(a)-(b) illustrates the transition from waveguide to CPW line accomplished using 90° bends of the two CPW slots. An early use of this excitation technique is recorded in [27] where the same CPW bends achieved a transition with a substrate integrated waveguide.

The radiating slots are defined on one side of the substrate, which covers the rectangular waveguide cross-section. A $\lambda/4$ transformer is employed as impedance matching element between slots and CPW line.

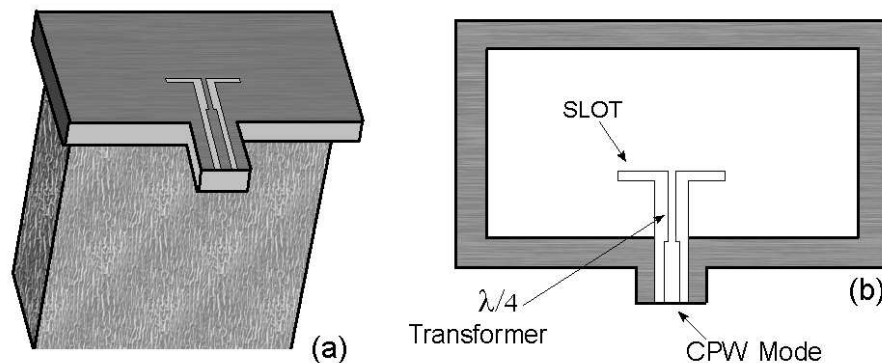


FIGURE 2.5: CPW to waveguide transition(a) using slot bends and $\lambda/4$ transformer(b).

The structure has the benefits of easy fabrication and hermeticity.

Also in this case back-to-back measurements show a resonating mode installed between

the ground planes of the CPW line and the contour of the waveguide aperture. The Alumina substrate used in the transition is partly responsible for this resonance which can be avoided by using a material with lower dielectric constant or by applying vias to connect the CPW grounds to the waveguide body.

The length of the two 90° bend slots is chosen to be $\lambda/4$, hence shorter than the resonating length which helps to reduce the back-side radiation as previously described.

Although the geometry and assembly of this transition is kept as simple as possible, a sensitivity analysis on manufacturing tolerances is presented in [28]. Results show that radiating slots and misalignment with the waveguide center line are responsible for the coupling efficiency of the transition, whereas errors on $\lambda/4$ transformer have an impact on the achievable matching level.

Similarly in [29], a $\lambda/2$ resonant slot aperture couples the energy between waveguide and microstrip as illustrated in 2.6(a)-(b) where a side view and a top view are illustrated. A periodically structured shield is used to suppress back side radiation from the slot avoiding unwanted coupling with the parallel plate mode supported by the cap packaging.

When this technique is employed, simulated and measured results show reduced reflection and an improved performance. However, the transition involves a secondary substrate where the periodic structure is defined, increasing manufacturing complexity.

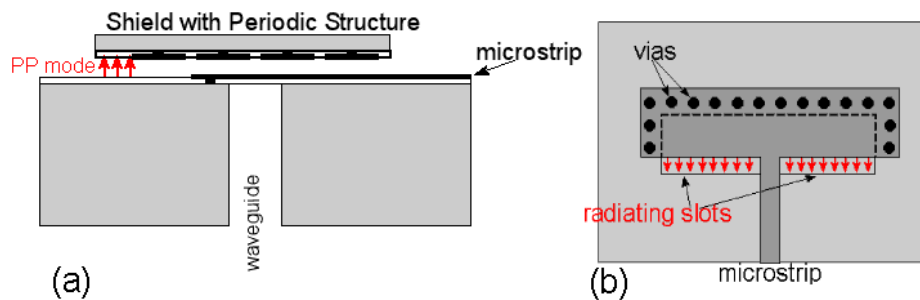


FIGURE 2.6: Waveguide to microstrip transition using slot aperture and shielding periodic structure(a). Top view of the radiating slots and vias structure.

2.3.3 Transversal Transitions

A planar transmission line and a rectangular waveguide can be combined together perpendicularly forming an EM junction. The structure derives from transitions between coaxial cables and waveguides frequently used at microwaves with a few examples illustrated in Figure 2.7. The MMW version of such a structure consists of a printed

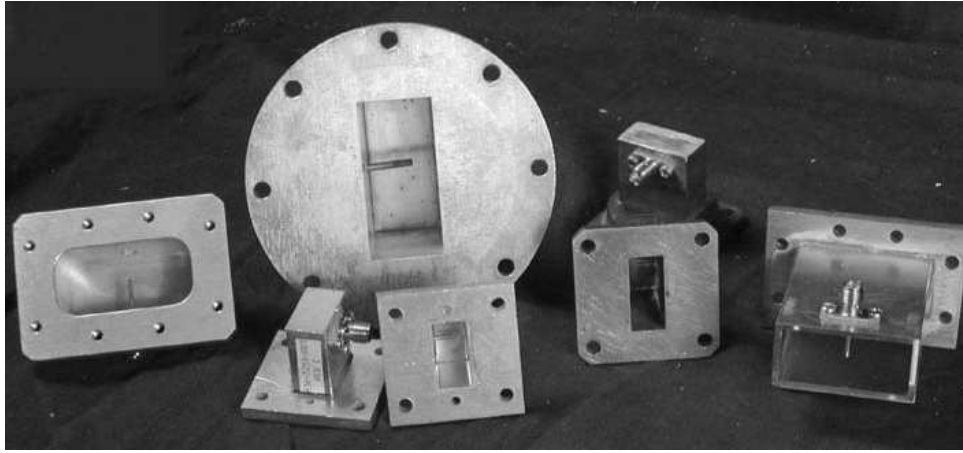


FIGURE 2.7: Examples of microwave waveguide transition using coaxial probes [30].

microstrip or CPW, a portion of which extends into the waveguide through an aperture, appropriately dimensioned, on the broad wall. The portion of the planar transmission

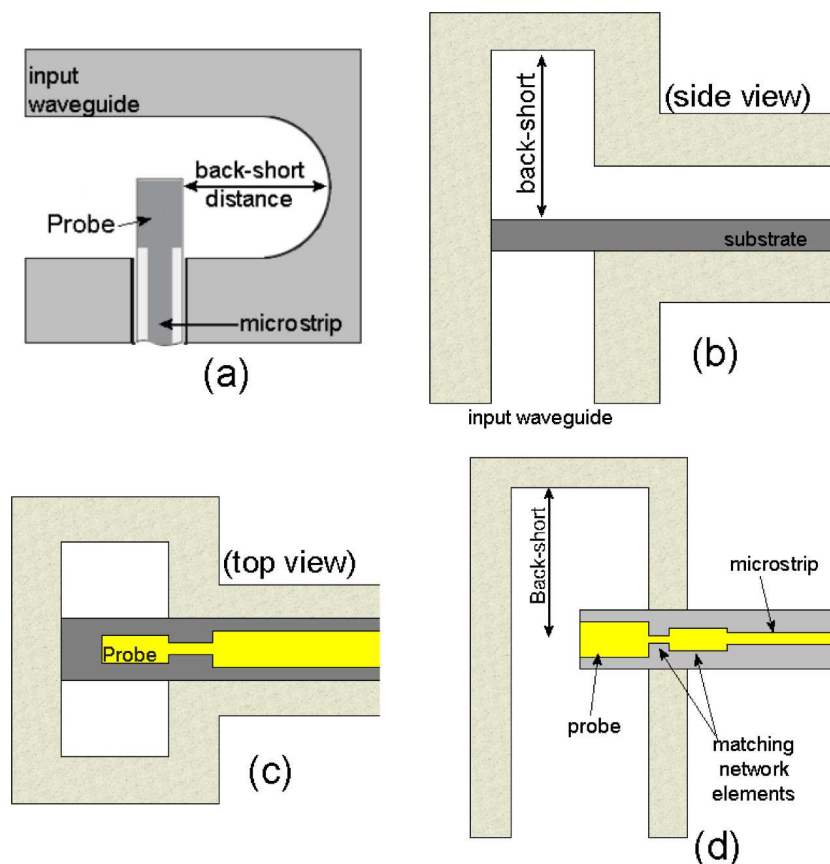


FIGURE 2.8: Transversal microstrip to waveguide transition using back-short(a). Substrate facing waveguide cross-section side view(b) and top view(c). Use of matching elements(d) to achieve broad band performance.

line, suspended inside the waveguide, works as a probe that couples energy between the two lines, Figure 2.8(a).

One of the first experiments is presented in [31], where the suitability of such structure in different MMW bands is demonstrated. The substrate is aligned with its surface facing the waveguide propagation direction, Figure 2.8(b)-(c). A waveguide termination,

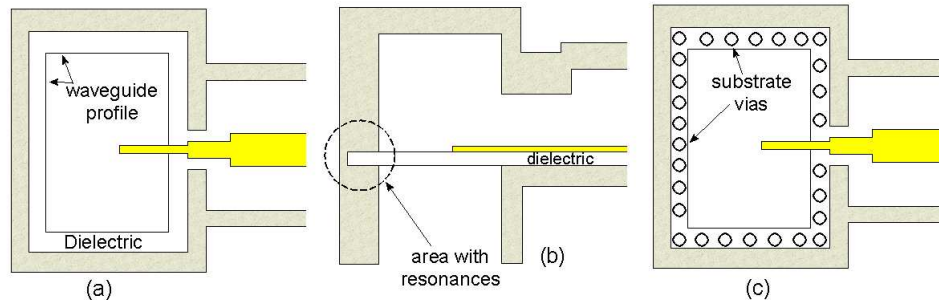


FIGURE 2.9: Transversal transition with substrate covering the full waveguide cross-section(a-b). Use of vias to prevent possible resonances in substrate material.

usually called a *back-short*, is frequently used and its distance from the probe has always been reported as $\lambda_g/4$ (where λ_g accounts for wavelength in waveguide). However, the position of the back-short should reflect properties of the material used to support the probe.

A remarkable work that investigates these aspects is presented in [32]. General guidelines are also mentioned in order to scale the transition to other frequency range when a specific ratio of the waveguide profile is kept. The configuration is depicted for one of the investigated alignments in Figure 2.8(d) where it is worth noting two extra printed matching elements which allows a full-band performance of the transition.

Transversal transitions are versatile when a rectangular waveguide is manufactured in split-block configuration. In such a case it is preferred to have the substrate aligned along the propagation direction of the waveguide. Description and fabrication of split-block device carrier are further discussed in Section 4.8.

In other situations the substrate faces the rectangular waveguide covering partially, or completely, its cross-section, [33][34]. This is employed when the dielectric material is used as a moisture barrier for the rest of the RF circuits, Figure 2.9(a)-(b). However, the structure could support resonances into the substrate due to the strong current discontinuity induced on the waveguide-wall [34]. Substrate vias could be used to mitigate the effects as in Figure 2.9(c), but in this case it is preferable to use less brittle dielectric materials such as Teflon.

Moreover, if the substrate material faces the rectangular waveguide, it is possible to exploit other features of the transition to control and to improve the transmission bandwidth, hence avoiding extra printed network elements and devolving the impedance matching function to the created EM junction as investigated in [35]. The structure illustrated in Figure 2.10(a)-(b) uses a simple microstrip line and two distinctive features such as an extended ground plane (p) and a misalignment (d) of the microstrip

relative to the centreline of the waveguide broad walls, Figure 2.10(c). A back-short is kept $\lambda_g/4$ away from the substrate. The extended ground plane works as a capacitive

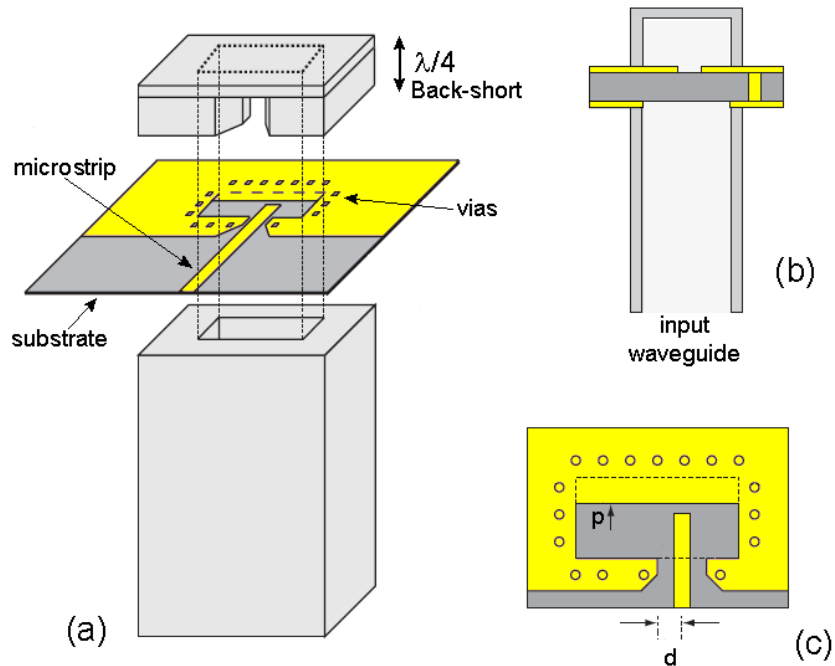


FIGURE 2.10: Perspective and side views(a-b) of transversal transition using extended ground p and center-line offset d for impedance matching(c).

obstacle which controls the reactance of the transition. The microstrip misalignment allows the selection of the waveguide local impedance, which is maximum at the centreline and it decreases when moving towards the narrow-walls. The overall effect is to control the frequency of two resonances allowing a design focused on either low reflection or broadband performance. The structure still uses vias which limit thickness and type of suitable dielectric materials.

Transversal transitions are suitable candidates for implementation at MMW frequencies. An example of their use at G-band is demonstrated in [36] where transition and RF circuits are combined together following a Multi-Chip Module (MCM) assembly. A good performance over the full waveguide band is achieved by employing Quartz as a substrate material for the transition and GaAs for the rest of the RF circuits. Despite the results, the overall structure still benefits from a hybrid architecture where two separate dielectric materials are employed respectively to collect the signal from the waveguide and to further amplify it, hence raising the question whether the same performance would be achievable by a full integrated structure.

Dielectric materials have a strong impact on the performance of a transition, as described

in sections 2.3.2 and 2.3.4, building unwanted resonances. In transversal transitions, the substrate material influences the impedance seen at the probe input. The reactive part of such impedance depends on the dimensions of the probe and the back-short position. The real part instead is strongly limited by the dielectric supporting the probe. Further network elements help to match the impedance of the probe with that of the planar transmission line.

Substrate dependency is discussed in [37] using a probe with radial shape aiming towards broadband performance. The effect of using different dielectric materials is also highlighted with the aim of Smith Chart representation and outlining design guidelines. Examples of radial probe used in transverse transitions are documented at low frequency [38] and very high frequency [39], where a remarkable application at sub-MMW frequencies (300-350 GHz) with relative amplifier chip integration is initially demonstrated .

2.3.4 In-Line Transitions

An interesting viable approach to interface a planar transmission line with a rectangular waveguide is based on the use of a tapered antipodal finline introduced for the first time in [40]. The transition essentially consists of three cascaded transmission lines: tapered antipodal finline, stripline and microstrip line. The geometry is depicted in Figure 2.11 and it follows the same principle used for the Ridge-Waveguide in Section 2.3.1. Two ridges at opposite sides of a substrate material are gradually tapered to concentrate and rotate the electric field by 90° , polarized as the microstrip mode. The substrate is

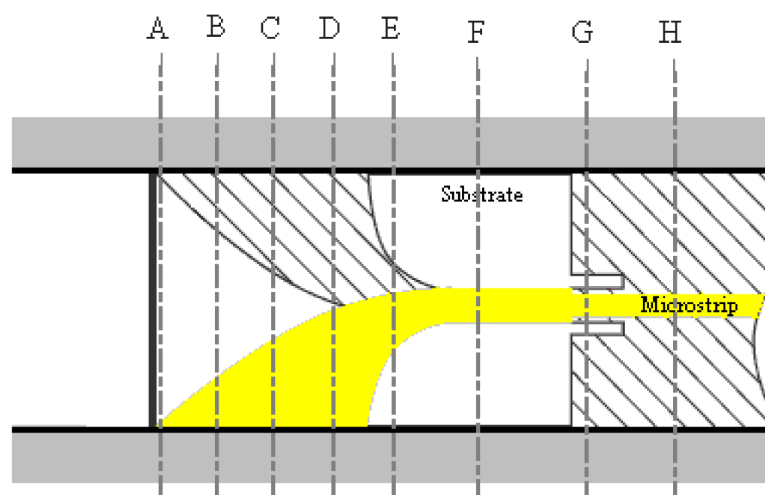


FIGURE 2.11: Tapered antipodal used for waveguide to microstrip transition.

positioned at the center and along the propagation direction of the rectangular waveguide fabricated in two halves clamped together as in Figure 2.12. This *In-line* transition is realized on quartz material and it is designed to work in the frequency range of 17.5-26

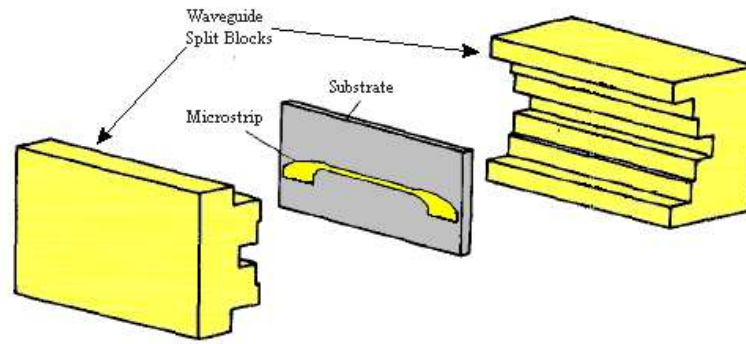


FIGURE 2.12: Waveguide split block structure holding the substrate material.

GHz. The performance shows robust results against small misalignment inside the guide and it also allows easy measurement procedures when back-to-back configuration is used. An overview of the E-field rotation is shown in Figure 2.13 relative to the cross-sections of Figure 2.11.

Parameters such as the shape and length (usually 1.5λ) of the tapers control the pass-

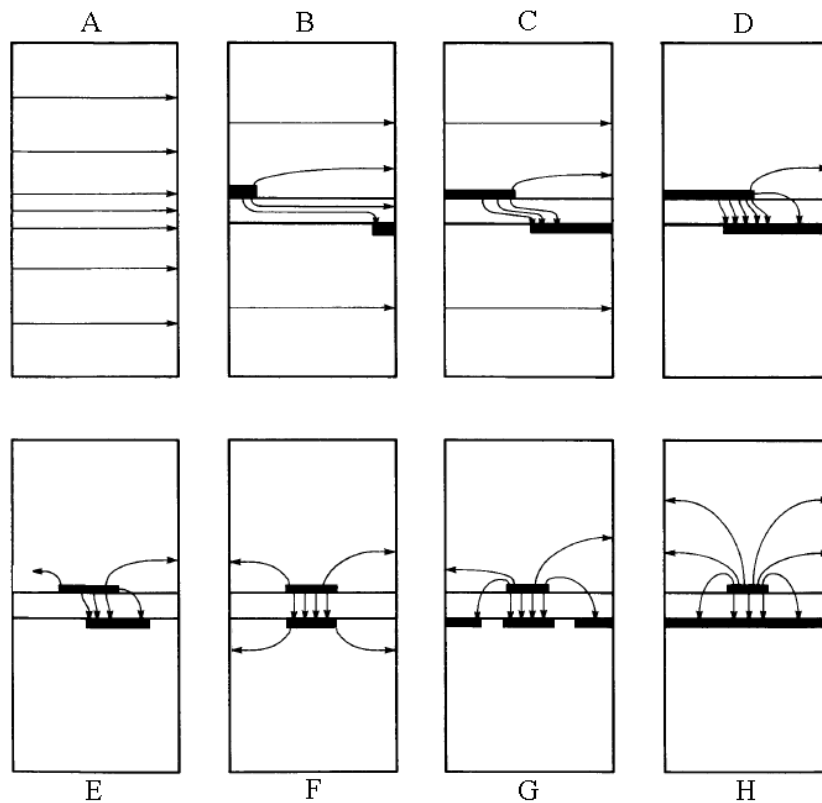


FIGURE 2.13: Rotation of the E-field along an antipodal finline. Cross-sections are relative to different points of the tapers of figure 2.11.

band of the component. The critical points in the assembly is the appropriate electrical contact points of the taper ends and microstrip ground with the two serrated chokes forming the rectangular waveguide.

This concept is further exploited at very high frequency such as G-band [41] and the tapers, optimized for 165 GHz, are defined on CuFlon substrate. Although the transition represent a good option when a wideband is desired, it is affected by some limitations. It is advisable to use very thin substrate with low dielectric constant such as teflon ($\epsilon_r = 2.1$) instead of brittle materials with high permittivity substrate such as Indium Phosphide (InP) or GaAs.

The transition is intrinsically affected by spurious resonances which build up between the tapers and the rectangular waveguide walls as illustrated in Figure 2.14. The resonances reduce the transmission band and appropriate design strategy has to be implemented to overcome the drawback [42].

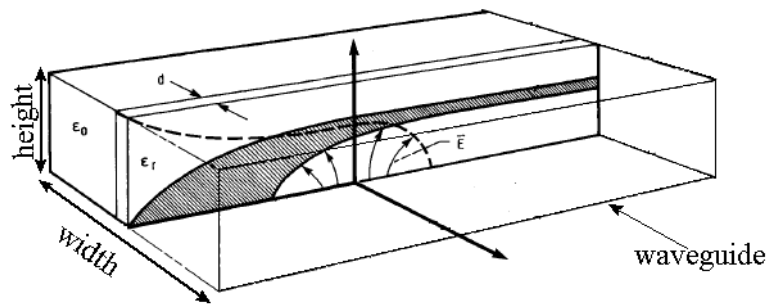


FIGURE 2.14: Possible spurious resonance between printed tapers and waveguide walls.

A solution to overcome the problem is to use unilateral fin-line in place of the antipodal fin-line as experimented in [43]-[44] respectively at frequencies 8.2-12.4 GHz and 27-31 GHz. In this case the EM field is not rotated 90° but it is gradually compressed along the plane of the substrate and then appropriately matched to a CPW line by using a broadband stub or a balun, Figure 2.15(a-b). However, low dielectric material is always preferred in order to increase the field matching between waveguide and tapered slot.

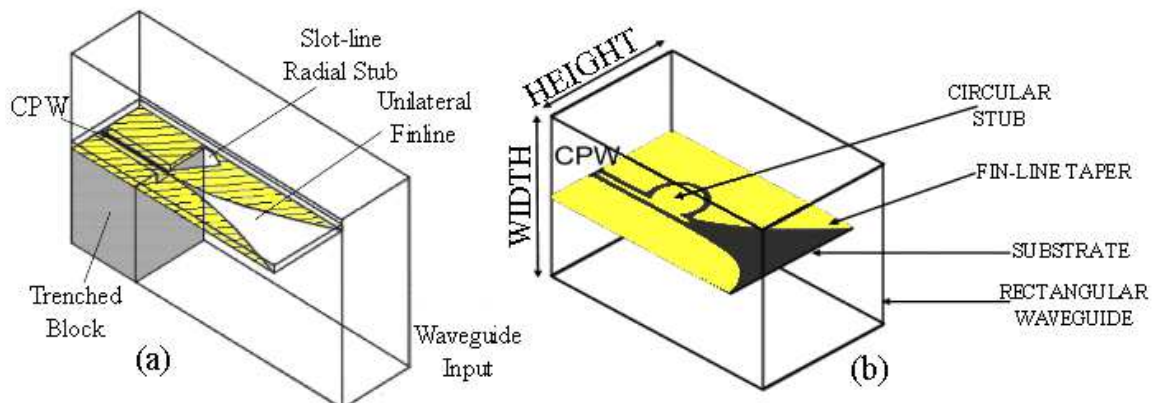


FIGURE 2.15: Uniplanar Finline used as waveguide transition to CPW line using radial stub(a) or circular stub(b).

Antipodal and unilateral fin-lines have relatively long structures and a solution to reduce their dimensions is to opt for *tapered slotline probe* as presented in [45, 46, 47], where a tapered slotline is inserted into the E-plane of a waveguide as an end-launcher. The

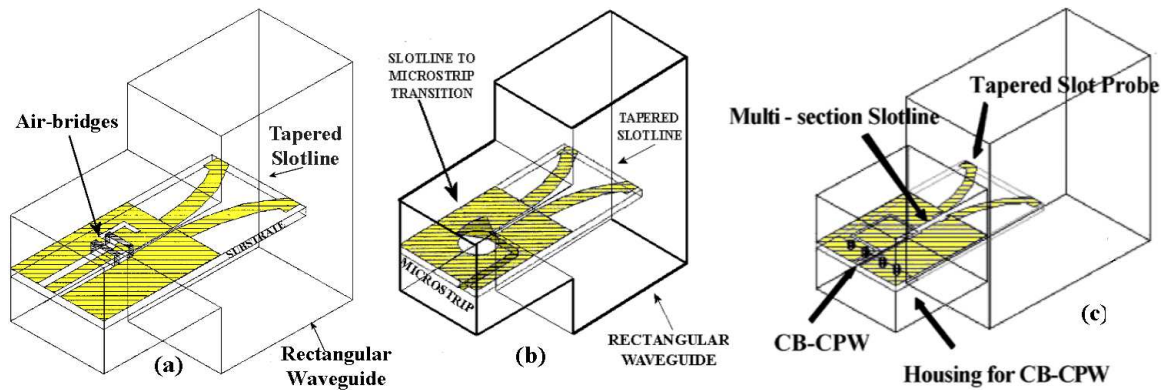


FIGURE 2.16: Tapered slotline used in waveguide transition to CPW using air-bridges(a) and vias(c) or waveguide to microstrip line using circular slot.

transition provides a shorter structure ($\lambda/4$ in free space) and is contactless with the waveguide broad walls easing assembly operations. Versions of the same transition differ in the use of CPW, microstrip or CB-CPW as planar transmission line. Broad band match between slot line and transmission line is accomplished by the use respectively of phase shifters, short stub and a multi-section slot transformer, Figure 2.16.

A tolerance analysis of this transition at V-band [47] shows the relative robustness of the design against possible vertical substrate misalignments.

If the transition is needed on high permittivity materials, planar antennas can also be used such as rectangular waveguide end-launchers. In fact fin-lines and the coplanar slot lines can be assumed to act as planar versions of horn antennas [48], hence it is possible to generalize and extend the concept to other antenna shapes achieving the same purpose and accounting for the resulting transmission bandwidth that depends on the radiating antenna chosen.

Examples are discussed in [49, 50] where a printed dipole is employed. The limitation on the bandwidth is partially removed by using parasitic director elements and the ground plane as reflector. The total antenna configuration recalls the end-fire quasi-Yagi structure as illustrated in Figure 2.17 a-b and its realization used both microstrip line and CPW.

These architectures confirm the possibility to exploit that a general antenna can work as transition between printed circuit and rectangular waveguide as long as the polarization of the antenna and the waveguide are the same. It is worth noticing that the dipole length is close to a free space $\lambda/4$, hence a high permittivity substrate is a prerogative for such solutions otherwise the antenna would not fit inside the waveguide.

Further prototypes considered the use of truncated bow-tie antenna as an alternative

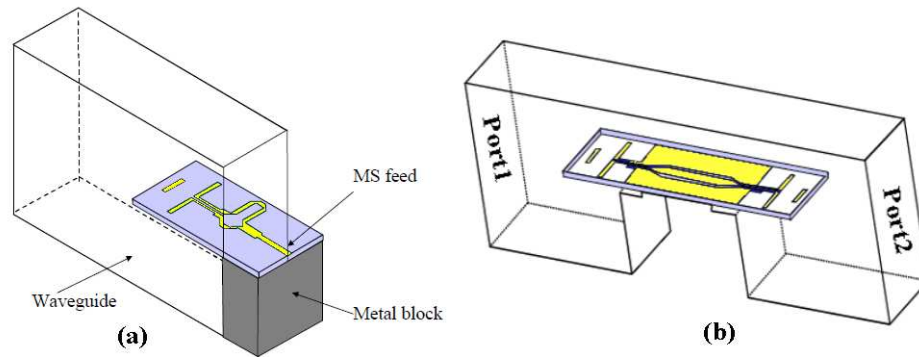


FIGURE 2.17: Quasi-Yagi antennas fed with microstrip(a) and CPW(b).

solution to achieve broad-band performance [51]. In cases where compactness and monolithic integration are desired and there is no particular broad-band requirement, a single dipole element can be an optimal solution [52]. The latest attempt to demonstrate the functionality of a dipole as an end waveguide launcher is discussed in [53] where a CB-CPW to waveguide transition for sub-MMW (340-380 GHz) is designed and fabricated, Figure 2.18. The structure is defined on InP using MMIC thin film technologies and it consists of a coplanar stripline (CPS) feeding, a $\lambda/4$ dipole and a mode converter from CPS to CB-CPW are very similar to the arrangement found in [50]. The substrate is placed on a machined pedestal so that it is aligned with the waveguide broad wall centerline. The design involves an adjoining waveguide stepped out in width to host a device wider than the rectangular waveguide cross-section. Reasonable performance is achieved with air-bridges and shorting vias, which are used to prevent possible unwanted slotline and parallel plate modes propagating along the CB-CPW.

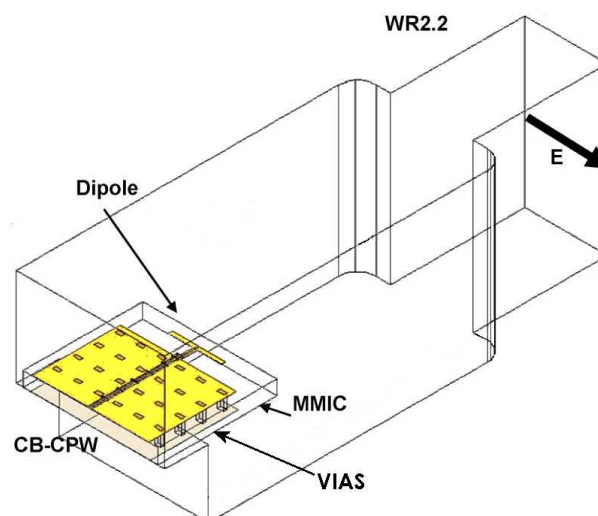


FIGURE 2.18: Waveguide to CB-CPW line using dipole antenna and vias to short possible propagating substrate modes.

Monopole antennas can be used as solution to limited space as in [54][55][56]. The main requirement is to provide a ground plane close to the antenna and this can be easily achieved by exploiting one of the broad walls of the rectangular waveguide, Figure 2.19(a-c).

A simple monopole antenna working as transition element requires impedance matching

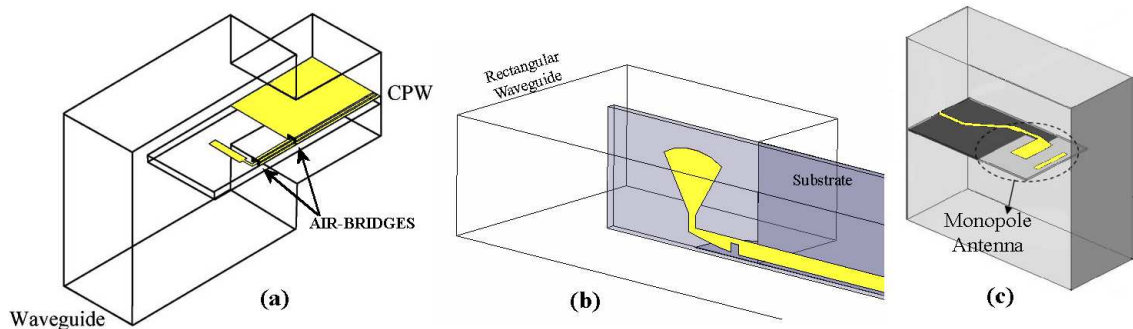


FIGURE 2.19: Monopole antennas used in waveguide transitions with the extended substrate(a) radial probe(b) or additional resonating elements(c).

which can be achieved by extending the substrate material inside the waveguide and using it as transformer Figure 2.19a.

However, the monopole structure presents asymmetries and use of air-bridges help to cut off slotline modes in case a CPW is used as transmission line.

Monopoles are nominally narrowband and supplementary features, as use of radial arm, Figure 2.19b, and parasitic elements, Figure 2.19c, can help to compensate this drawback and to increase the transmission bandwidth.

2.4 Some Considerations

A rectangular waveguide to planar transmission line transition can have different architectures.

However, the aim of designing an *integrated transition* at MMW frequencies sets some limitations on the suitable geometries and some crucial factors must be considered in order to produce an electromagnetically functional and mechanically realizable structure. Aspects such as:

- Substrate material and thickness
- Overall Device dimensions
- RF circuits location

- Available Technology
- Mechanical fabrication and tolerances
- Alignment, Bonding and Assembly strategy

They all play an important role during the decision making in the design process.

Table 2.2 and 2.3 summarize the transitions discussed so far. The last entry of the tables is the result of the present work and the following chapters detail the design procedure and fabrication process involved in its manufacturing and testing.

Table 2.4 groups the transitions in categories on the basis of their structure. The peculiarities of each group are listed in terms of advantages and disadvantages and a level of merit is assigned to their electrical characteristics such as transmission bandwidth and losses. A separate column completes the table assigning a level of complexity to each category.

2.5 Conclusions

An overview of the different strategies used in realizing transitions between rectangular waveguide and a generic planar transmission line is presented and discussed illustrating the EM coupling mechanism for each category.

Each architecture has got its own advantages and pitfalls relative to their use and the applications required.

The aim of a MMIC-integrated transition introduces important aspects to consider such as the substrate material used, whose dielectric constant plays a crucial role in the choice of the suitable geometry to adopt. A list of different transitions found in literature is finally presented highlighting their characteristics. The results of the present work are anticipated and included in the list for completeness. The last table presents the transitions in categories highlighting advantages and disadvantages with a reference to their electrical performance and level of complexity.

Year-Ref.	Alignment	Substrate Material	Planar Line	BW	Insertion Loss (S_{21})	Reflection Loss (S_{11})	Assembly/Characteristics
1992-[14]	RWG inline	R15880 Duroid	CPW	K-band	$S_{21} < -1.75$ dB	$S_{11} < -11$ dB Full Band	Taper length = $1.5\lambda_g$, $Z_{cpw} = 75\Omega$ Back-to-back configuration. Built on WR.
2008-[16, 17]	RWG inline	$LiNbO_3$ $\epsilon_r = 28 \sim 43$	CPW	W-band	$S_{21} > -3.5$ dB	$S_{11} < -15$ dB	Anisotropic substrate. Difficult assembly. No back-to-back testing.
1992-[18]	Aperture Coupled	$\epsilon_r = 2.33$	MS	X-band	$S_{21} < -1$ dB @1GHz	$S_{11} < -10$ dB	Three designs varying the location of the patch. Evaluation of the radiation leakage.
1994-[20]	Aperture Coupled	MS on Alumina, Patch on Quartz	MS	W-band	$S_{21} < -0.3$ dB single transition	$S_{11} < -15$ dB BW = 10%	Stepped waveguide and additional patch substrate.
1996-[21]	Aperture Coupled	MS on Alumina, Patch on Rogers 6100 ($\epsilon_r = 10.2$)	MS	C-band	N/A	$S_{11} < -15$ dB BW = 14.5 GHz @6GHz	Use of patch substrate as impedance transformer
1998-[22]	Aperture Coupled	LTCC ($\epsilon_r = 7.8$)	CPW-MS	K _a -band	$S_{21} < -4$ dB; -1 dB	$S_{11} < -15$ dB (BW = 5; 2 GHz)	Use of two patches and vias. Hermetic sealing and evaluation of radiation leakage
2003-[26]	Aperture Coupled	Alumina ($\epsilon_r = 9.9$)	CPW	W-band	$S_{21} < -2$ dB	N/A	Hermeticity. Bandwidth reduced by resonance. Use of CPW $\lambda/4$ transformer.
2003-[28]	Aperture Coupled	Alumina ($\epsilon_r = 9.9$)	CPW	W-band	$S_{21} < -2$ dB	N/A	Analysis of manufacturing tolerances. Evaluation of misplacement of slot relative to WR profile.
2002-[23]	Aperture Coupled	$\epsilon_r = 2.2$	MS	70.5-82.5 GHz	$S_{21} < -0.4$ dB (single transition)	$S_{11} < -14$ dB (BW = 5.22 GHz) @76.5 GHz	Single substrate. Cavity coupling mechanism. Sensitivity analysis on waveguide profile size and patch misalignment.
2007-[25]	Aperture Coupled	$\epsilon_r = 2.2$	MS(x2)	66.5-86.5 GHz	$S_{21} < -0.5$ dB @76.5GHz (single transition)	$S_{11} < -15$ dB (BW = 5.29 GHz) @76.5 GHz	Two microstrip/line divider. Resonance for TM_{20} mode.
2007-[29]	Aperture Coupled	Teflon	MS	E-band	$S_{21} > -15$ dB (single transition)	$S_{11} < -10$ dB (75-80 GHz)	Slot structure. Use of metal shield and EBG preventing radiation leakage to couple in package PP-mode.
1976-[40]	Antipodal Fin-line	Quartz ($\epsilon_r = 3.8$)	MS	17.5-26 GHz	$S_{21} < -0.2$ dB	N/A	Optimized experimentally. Design not critical to misalignment.
1986-[42]	Antipodal Fin-line	Duroid ($\epsilon_r = 2.22$)	MS	26-40 GHz	$S_{21} < -2.5$ dB back-to back	N/A	Analysis and modelling of resonances inside slots.
2002-[41]	Antipodal Fin-line	CuFlon	MS	G-band	$S_{21} > -1.3$ dB @165GHz	$S_{11} < -10$ dB BW = 140-180 GHz	First example of fin-line at G-band. Discussion on the use of InP and GaAs.
2005-[43]	Unilateral Fin-line	$\epsilon_r = 2.33$ -10.8	CPW	8.2-10.4 GHz	$S_{21}(\epsilon_r = 2.33) < -0.4$ dB; $S_{21}(\epsilon_r = 10.8) < -0.9$ dB	$S_{11}(\epsilon_r = 2.33) < -20$ dB; $S_{11}(\epsilon_r = 10.8) < -10$ dB	Use of substrate as impedance transformer.
2007-[44]	Unilateral Fin-line	TMM4 Rogers $\epsilon_r = 4.5$	CPW	27-31 GHz	$S_{21} > -1.5$ dB	$S_{11} < -10$ dB (on full band in back-to-back)	Use of smooth circular stub for finline to cpw transition.

TABLE 2.2: List of the waveguide to planar transmission line in scientific literature (1/2)

Year-Ref.	Alignment	Substrate Material	Planar Line	BW	Insertion Loss (S_{21})	Reflection Loss (S_{11})	Assembly/Characteristics
2001-[45]	Tapered CPS	Duroid $\epsilon_r=2.2$	CPW	8.2-12.4 GHz	$S_{21} > -0.75$ dB back-to-back	$S_{11} < -15$ dB (BW=40%)	Broad band CPS to CPW transition.
2002-[46]	Tapered CPS	Duroid $\epsilon_r=2.2$	MS	8.2-12.4 GHz	$S_{21} > -0.7$ dB	$S_{11} < -15$ dB (BW=40%)	Broad band CPS to MS transition.
2002-	Tapered CPS	Teflon ($\epsilon_r=2.2$)	MS	K_c -band	$S_{21} > -1.2$ dB	$S_{11} < -15$ dB (28-40 GHz)	Broad band CPS to MS transition.
2005-[47]	Tapered CPS	Alumina ($\epsilon_r=9.9$)	CB-CPW	V-band	$S_{21} < -2$ db back-to-back	$S_{11} < -10$ dB (55-65 GHz)	Use of multisection slotline transformer to increase the bandwidth.
1999-[49]	Inline Quasi Yagi antenna	Duroid $\epsilon_r=10.2$	MS	8-12.5 GHz	$S_{21} = -0.9$ db center band	$S_{11} < -12$ dB (BW=39%)	Use of CPS to MS balun.
2000-[50]	Inline Quasi Yagi antenna	Duroid $\epsilon_r=10.2$	CPW	8-12.5 GHz	$S_{21} > -1.0$ dB	$S_{11} < -10$ db (BW=33%)	Use of stub in CPS to CPW transition.
2006-[51]	Inline Bow-Tie antenna	RT $\epsilon_r=2.2$	Slot-line	X-band	$S_{21} < -15$ dB (simulated)	$S_{11} = -0.1$ dB (simulated)	Only simulated results are presented.
2007-[52]	Inline Dipole antenna	InP	MS	V-band	N/A	N/A	Narrow band transition.
2009-[53]	Inline Dipole antenna	InP	CB-CPW	340-380 GHz	$S_{21} < -1$ dB (deembedded single transition)	$S_{11} < -10$ dB (340-420 GHz)	Vias and air-bridges employed. Stepped out WR to fit chip.
2004-[54]	Inline Monopole antenna	RT5870 $\epsilon_r=2.33$	CPW	X-band	$S_{21} = -0.3$ db	$S_{11} < -17$ dB (full band)	Extended substrate used as impedance transformer.
2007-[55]	Inline Monopole antenna	RT5880 Rogers	MS	K_c -band	$S_{21} > -1.0$ dB	$S_{11} < -10$ dB (BW=28.2-39.3 GHz)	Use of broad band radial monopole.
2008-[56]	Inline Monopole antenna	RO4003 $\epsilon_r=3.38$	MS	X-band	$S_{21} < -0.3$ dB	$S_{11} < -13$ dB	Quasi Yagi monopole antenna.
1988-[31]	Transversal	RT $\epsilon_r=2.2$	MS	K_c, Q, V, W	$S_{21}(K_c, Q, V, W) > -0.1$;- 0.2;-0.35 dB (single transition)	$S_{11} < -10$ dB (full band)	WR split blocks mounting. Substrate facing waveguide input.
1999-[32]	Transversal	Teflon($\epsilon_r=2.2$), Die6($\epsilon_r=6.0$), Alumina($\epsilon_r=10.1$), GaAs($\epsilon_r=13$)	MS	W-band	$S_{21}(teflon) = -0.48$ dB, $S_{21}(alumina) = -0.86$ dB (per single transition)	$S_{11} < -20$ dB	Two substrate alignments. Use of printed matching network.
2000-[57]	Transversal	RT5880 $\epsilon_r=2.2$	MS	W-band	$S_{21} > -1.5$ dB(72-86 GHz), $S_{21} > -2.4$ dB(86-90 GHz)	$S_{11} < -11.5$ dB	Modelling dielectric edge in waveguide
2002-[33]	Transversal	CuClad $\epsilon_r=2.17$	MS	K_c -band	$S_{21} > -0.95$ dB (27-35 GHz)	$S_{11} < -18$ dB (27-35 GHz)	Substrate facing waveguide input.
2003-[34]	Transversal	RT5880 Duroid	MS	K_c -band	$S_{21} > -0.4$ dB	$S_{11} < -10$ dB	Resonance due to WR wall discontinuity.
2005-[35]	Transversal	Teflon $\epsilon_r=2.2$	MS	E-band	$S_{21} > -0.5$ dB	$S_{11} < -30$ dB(BW=16.8%);- 20db(BW=32.5%)	Use of extended ground as capacitive element. Use of waveguide local impedance.
2006-[36]	Transversal	Quartz	MS	G-band	$S_{21} \cong -1.5$ dB (single transition)	$S_{11} < -12$ dB	Use of different substrates for RF circuits and transition.
Present work	Transversal	GaAs ($\epsilon_r=12.9$)	MS	G-band	$S_{21} \cong -4$ dB @180GHz	$S_{11} \leq -10$ dB (150-200 GHz)	Use of Elevated E-plane probe. Integrated and MMIC compatible.

TABLE 2.3: List of the waveguide to planar transmission line in scientific literature (2/2)

Transition	Pros	Cons	Bandwidth	Losses	Complexity
Ridge Waveguide Transitions	<ul style="list-style-type: none"> -Split-Block structure -Possible back-to-back configuration -Full-Band performance -Robustness respect to Ridge offset from waveguide centerline 	<ul style="list-style-type: none"> -Complex procedure to mill the Ridge in waveguide -Critical electrical contacts between metal ridge and planar line -Substrate size limited to waveguide dimensions -Long tapered metal ridge -Suitable for <i>soft</i> substrate materials (i.e. FR4, Teflon), possible substrate breaking points caused by the ridge 	Full-Band	Low	High
Aperture Coupled Transitions	<ul style="list-style-type: none"> -No waveguide backshort required -No waveguide split-block work required -Suitable for arrays -RF circuits placement at the back of antennas -Compactness -Hermeticity for RF circuits -Robustness to misalignment along waveguide broadsides 	<ul style="list-style-type: none"> -Grounding vias required to reduce substrate leakage -Used with <i>soft</i> substrate materials -Complex back-to-back measurement operations -Back-side radiation leakage -Intrinsic narrow band performance -Losses due to multiple coupling mechanisms 	Narrow	High	High
Transversal Transition	<ul style="list-style-type: none"> -Suitable for soft and brittle substrate materials -Suitable for split-block structure -Easy alignment/assembly procedures -Suitable for back-to-back measurements -Microstrip/CPW compatible -Robust to waveguide centerline misalignment -Versatile for hybrid/integrated architectures -Suitable for integration with additional planar matching network elements 	<ul style="list-style-type: none"> -Extended waveguide back-short -Limited substrate channel size -Waveguide discontinuity due to protruding dielectric material -Critical grounding contact point at waveguide aperture 	Wide	Moderate	Low
Inline Transitions (Finline)	<ul style="list-style-type: none"> -Clamping split-block structure -Tapered impedance transformation -Wide band performance -No waveguide back-short required -Suitable for back-to-back measurements -Robust to misalignments from waveguide centerline 	<ul style="list-style-type: none"> -Long tapered fin-lines -Limited to <i>soft</i> substrate materials -Possible internal resonances -Required contact points with internal waveguide walls -Waveguide dielectrically loaded -Substrate size limited to waveguide dimensions 	Wide	Moderate	Moderate
Inline Transitions (Antennas)	<ul style="list-style-type: none"> -Compatible with microstrip, CPW, CPS -Use of waveguide walls as antenna ground/reflector 	<ul style="list-style-type: none"> -Pass-band depends on choice of printed antenna -Strong capacitive effect with internal waveguide walls 	Varies	Moderate	Moderate

TABLE 2.4: Waveguide to planar transmission line transitions grouped in categories with their advantages and disadvantages. Electrical characteristics such as losses, bandwidth and level of complexity complete the table.

Chapter 3

Design and Methods

3.1 Introduction

The present Chapter is dedicated to the design aspects and methods used to model and optimise waveguide transitions. The use of a computer based simulator called HFSS (High Frequency Structure Simulator) was found to be useful to understand the parameters design space of the different models and to plot the distribution of the EM field in the structures. This approach also gave an insight of the critical areas where undesired internal resonances could reside.

A general overview of the simulation settings such as boundary conditions and sources excitation is also presented with the HFSS solution process, which is characterised by the *adaptive meshing technique*.

The design specifications are provided. Hence, HFSS is employed to model some of the structures described in Chapter 2 in order to investigate their pitfalls and advantages and finally to identify a waveguide transition suitable to our purpose.

With this approach, examples of In-line, antipodal Fin-line and Transversal transition are considered, modelled and analysed.

In-line waveguide transitions appear to be feasible at G-band frequencies, but present limitations in the performance due to the thickness and type of substrate material imposed by the specifications. Both Antipodal Fin-line transition and printed dipole transition models are investigated. Transversal waveguide transitions represent good compromise between performance and complexity. Design guidelines are given illustrating the influence of fundamental parameters characterizing this type of transition.

As a result of the analysis carried out on the transversal transitions, the novel structure of the Elevated E-plane probe is presented and modeled. The probe height is introduced as a new optimising parameter for the transversal transition and its effect is illustrated

on S-parameters plots and Smith Charts. The results are also shown with their relative E-field distribution to highlight aspects of the EM field conversions between two different transmission lines. The Elevated E-plane probe benefits of all the advantages of the transversal transitions and its new feature provides an extra degree of freedom to exploit during the design process.

The chapter ends with the S-parameters plot of the Elevated E-plane probe transition when mounted in a metal housing in order to compare measurements with simulation results. Conclusions highlight the transversal transitions as good candidates to put forward in the fabrication process, which is described in the following Chapter 4.

3.2 Electromagnetic Design using EDA Software Packages

Electronic Design Automation (EDA) is a category of commercial software for designing electronic systems going from the single component to the entire system.

EDA software tools, in most cases, present a design environment that allows one to draw structures and to simulate their EM behaviour over a frequency band. For the work described in this thesis, a 3D EM simulator called HFSS (High Frequency Structures Simulator) by Ansys[©] is employed. The tool enables the design and simulation of high-frequency passive structures such as antennas, RF/microwave components and junctions. The following sections explain the main characteristics of HFSS giving an overview of its operating principles and design flow.

3.2.1 HFSS, FEM and Adaptive Meshing

HFSS is a software based on a frequency domain solver. It is frequently used to build three-dimensional structures by drawing them directly into the 3D modeler window where it is also possible to assign dielectric and metal materials and to set ports through which the energy flows into the structure. With HFSS it is possible to plot nearly any of the EM properties estimating how the design responds to the assigned excitations [[Ansoft](#)].

In contrast to other simulation tools HFSS uses the Finite Elements Method (FEM) to decompose a bigger EM problem into smaller parts and analyze them.

FEM method is based on the frequency decomposition of geometric structures into basis elements called tetrahedra [58]. Electric fields are calculated on these elements based on the type of stimulus applied to the entire structure and the resulting values are arranged in a matrix form on which mathematical operations are then applied to extrapolate the desired functions. An example of a single tetrahedron is illustrated in Figure 3.1 highlighting where E-field values are explicitly solved and where they are interpolated.

Once the structure is built, HFSS follows a predetermined procedure to analyze and

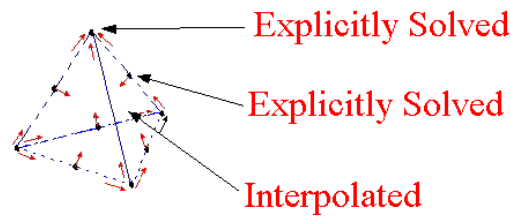


FIGURE 3.1: Tetrahedron, basic element of the FEM decomposition method. E-field values are calculated at its vertices and edge. E-field values are instead interpolated at the center of its faces.

solve the EM design. The solver starts to identify the different materials included in the design. At this stage excitations and boundary conditions are also defined as HFSS considers them in the overall design as power input/output and absorbing materials respectively.

Once all the materials and boundary conditions are identified, HFSS starts to sub-divide the structure with an initial mesh based on information introduced by the user such as *solution frequency* and *initial meshing operations*. Solution frequency represents the wavelength used by the solver to determine the initial tetrahedra dimension. Initial meshing operations are additional sub-divisions applied to areas where a finer mesh is desired in the initial structure decomposition.

Once the two settings are employed, HFSS starts the adaptive meshing loop, an iterative and automatic mesh refinement procedure during which E-field values are calculated and compared with the solution found in the previous iteration. If the difference between the two solution matrices is smaller than an assigned threshold value, the process is considered *converged* and it exits the iterative loop delivering the results. If the solution is not converged, the process proceeds for an additional *adaptive pass* where the structure is further meshed and the values of the solved matrix undergo a further comparison. The HFSS solver process is illustrated in Figure 3.2. The adaptive meshing process aims to concentrate and refine the tetrahedra dimensions in areas where the gradient of E-field is large, hence sub-dividing these areas with an automatic process. An example of initial mesh applied to an EM design and the result of the adaptive meshing process on the same structure is illustrated in Figure 3.3.

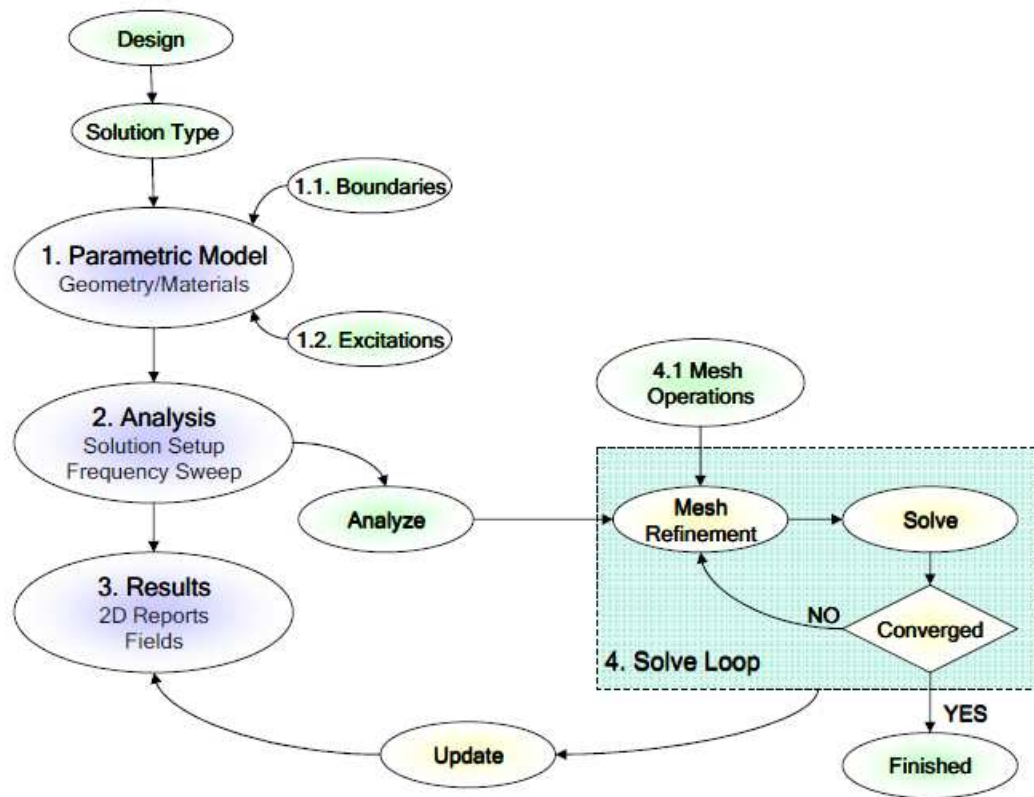


FIGURE 3.2: HFSS solution process. Crucial steps are the assignment of excitations and boundary conditions in the model. Solution frequency and frequency sweep are information introduced by the user during the analysis setup. The adaptive process consists of a solve loop during which the structure undergoes consecutive mesh refinements and E-field comparisons until the exit condition is reached. Results are then extracted from the solved EM field of the model.

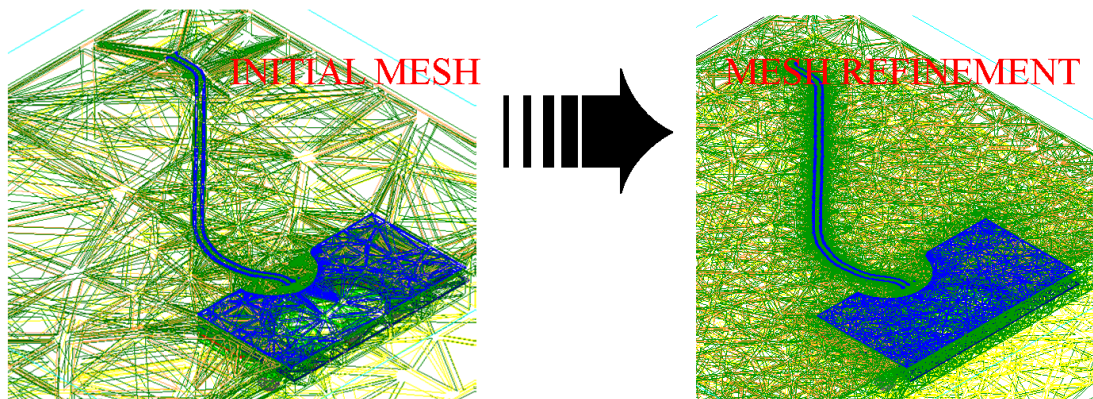


FIGURE 3.3: HFSS generates an initial mesh on the structure based on solution frequency value, material assignment and geometric shapes. Adaptive solving process refine the mesh based on the information collected in the previous solved pass. The mesh refinement accounts for the gradient of the E-field into the model.

3.2.2 Simulation setup

It is important to highlight some aspects of the simulation setup in order to appropriately assign the EM model and to generate correct results. The simulation setup has some key steps such as: materials assignment, excitations, boundaries assignment and analysis setup.

3.2.2.1 Materials assignment

HFSS handles materials depending on their characteristics. An extensive library is provided by default but it is also possible to define custom materials by assigning parameters as permittivity, conductivity, dielectric and magnetic loss tangent. If dielectric materials are assigned in the model, HFSS breaks down the dielectric region into tetrahedra based on the information of the guided wavelength λ_g :

$$\lambda_g = \frac{\lambda_0}{\sqrt{\epsilon_r}} \quad (3.1)$$

where λ_0 is the wavelength in free space, λ_g is the wavelength in the dielectric material and ϵ_r is the dielectric constant of the region considered.

3.2.2.2 Excitations

Excitations are assigned as stimuli of the EM structure. HFSS provides different type of ports such as: *waveports*, *lumped* ports and *terminal* ports. Lumped ports emulate an excitation localized internally to the structure usually between two conductor terminals. Lumped ports require a port impedance as reference for which the value is assigned by the user. With these settings no modes can be assigned and no de-embedding operation can be applied. However, the feature of punctual excitation enables the simulation of results as experimentally measured with EM probes.

Terminal ports are very similar to lumped ports but they can be applied in situations where more than two conductors touch the port. Modes can be plotted but the port impedance has to be assigned by the user. Terminal ports can be used only on the external volume of the entire model.

Waveports are the most sophisticated excitation provided by HFSS and for this reason they add extra computational complexity to the adaptive meshing process. Waveports can be applied internally and externally to a structure, they feature modes plotting and the port impedance is calculated by the solver. When a waveport is applied as excitation, an extra solver known as *port solver* is invoked before the adaptive meshing

process. The port solver applies a preliminary meshing process to the port surface on which port impedance and propagating modes are identified. This type of excitation is more complete, compared to lumped and terminal port and it involves intensive RAM usage. However, waveports are useful when it is necessary to identify propagating or decaying modes of the structure and to plot their relative propagation constant. For the work presented in this thesis, waveports are employed since modal coupling is part of the analysis.

3.2.2.3 Boundaries

HFSS provides a variety of boundary conditions that can be applied to an EM model. Generally, Absorbing Boundary Conditions (ABC) and Perfect Matching Layer (PML) are applied in situations with free space radiating structures such as antennas and reflectors. These boundary conditions emulate fictitious absorbing materials to reduce reflections from an incoming radiation and create free space conditions. In fact, HFSS considers the entire universe volume filled with perfect electric conductor (PEC) and these absorbing materials have to shield the airbox volume containing the designed structure.

However, closed systems such as waveguides do not need to consider free space radiation and the design of such structures can exploit the default external PEC condition as the external boundary assignment. Materials with characteristics such as reduced conductivity can always be applied by using this type of settings in order to simulate metals whose characteristics depart from the ideal PEC assumptions. This is the boundary condition assignment used in the present work.

3.2.2.4 Analysis Setup

HFSS uses information such as *solution frequency* and *frequency sweep* during simulation process. This information is set by the user in the *Analysis setup*. HFSS, then, generates the mesh over the structure based on the solution frequency information.

Frequency sweep represents the range of frequency over which the behaviour of the EM model is simulated. Hence, it is necessary to coordinate the two sets of information together by assigning the solution frequency as the highest frequency of the frequency sweep. This ensures the finest initial meshing size also conforming to the desired frequency band.

3.2.2.5 Custom Meshing Operations

The accuracy of the results generated with HFSS is strictly related to the *finite elements decomposition* of the model in all its parts. The unit element of this decomposition is the tetrahedron and the operation of sub-dividing the structure under test is called *meshing*. As previously mentioned, it is possible to manually reduce the tetrahedra dimensions in areas of the model where the electric field is believed to vary significantly and presents a high gradient. This is generally needed in order to highlight strong capacitive effects between metals or to identify a possible internal resonance. A custom meshing operation can be achieved using different strategies such as:

-*Lambda Resolution*

-*Dummy Objects*

-*Maximum Length Based*

The *lambda resolution* operates on the whole model. In HFSS, by default it is set to be equal to one third of the wavelength relative to the solution frequency assigned during the analysis setup. It is possible to override this value generating a more aggressive initial mesh of the model. The *Dummy objects* technique operates in sensitive areas and it is a more localised meshing method. It consists in manually creating fictitious objects with the same material properties of the volume where they are defined. It is purely a manual meshing strategy. The *maximum length based* technique can be applied to objects already present in the model. It consists to reduce the maximum tetrahedra dimensions to a specific size, which is set by the user.

It is worth noting that, by reducing the tetrahedra dimensions, the complexity of the simulation generally increases since HFSS deals with a bigger problem to solve represented by a bigger matrix values to handle. This entails longer simulation time and a more intensive use of the computational resources. It is good practice to do limited use of the meshing operations by reducing them to a minimum and aiming to a good trade-off between accuracy and complexity.

The following sections illustrate simulation results and the meshing strategy where adopted.

3.3 Design Specifications

The objective of our design process is to define a transition from rectangular waveguide to planar transmission line at G-band (140-220 GHz).

The operating frequency range, as discussed in Chapter 1, extends over the water vapour absorption band centered at 183 GHz. This factor has to be considered when designing the performance profile of the transition in order to account for attenuation of a signal's spectral components at these frequencies. The rectangular waveguide cross-section used in the design conforms to the standard waveguide dimensions $1.2954 \times 0.6477\text{mm}$ as listed in Table 2.1 for the G-band and named WR-05. The design process aims to model an integrated transition also providing the following features:

- GaAs integration
- Compatibility with MMICs processes
- Small size and simple structure
- Possible back-to-back architecture
- Robustness to fabrication tolerances
- Easy assembly

The First two features allow the integration of the transition structure directly on GaAs material together with MMICs with consequent reduction of manufacturing time. By having a small and simple structure, the transition can better overcome problems such as space limitations and expensive substrate material usage.

A back-to-back configuration enables the fabrication of symmetrical structures, ideal for experimental measurements as described in Chapter 2.

At MMW frequencies, robustness and easy assembly are desired requirements to counter balance the adverse effects of misalignments and assembly errors as highlighted in Chapter 5.

In order to better control the performance and to limit inter-modal coupling, the design of the transition accounts solely for the propagating TE_{10} mode in rectangular waveguide and the fundamental *quasi-TEM* mode [19] for planar transmission line which needs to be free from higher order propagating modes along its structure.

3.3.1 Considerations on Design options

The literature review in Chapter 2 showed waveguide transitions in several geometries, but not all can conform to the desired features described in the previous section.

Ridge waveguide transitions require expensive and delicate mechanical fabrication of the rectangular waveguide that is incompatible with the substrate material integration.

Moreover, they involve very long tapers and their fabrication in back-to-back configuration represents a limitation. The use of ridge waveguide transitions in realizing probes for RFOW measurements is justified by the de-embedding option that modern vector network analyzers feature to compensate small imperfections of the mechanical fabrication as further discussed in Section 5.2.2.

The assembly process of the aperture-coupled transitions with rectangular waveguide involves, in most cases, the use of *vias* to ground the reference plane of the planar transmission line to the waveguide body in order to reduce unwanted substrate waves and to shield the transition from back-side radiation leakage. The overall structure becomes very fragile when brittle material such as GaAs is employed. Moreover, back-to-back configuration of the aperture-coupled transition presents some difficulties when measurements have to be performed.

In-line and *transversal* transitions appear to be the most versatile structures for MMW use. The following sections investigate and extend their design to the G-band highlighting possible limitations and outlining reasonable solutions.

3.4 WR5 Transition using In-Line Finline

Some designs discussed in Section 2.3.4 exploited the use of *antipodal Fin-lines* to achieve EM fields rotation and impedance matching between rectangular waveguide and microstrip line, as illustrated in Figure 2.13.

By using antipodal Fin-lines, a wide range of impedance values can be realized overlapping the fins at opposite sides of the substrate material. The impedance match can be accomplished by tuning the Fin-line dimensions and by tapering the two fins to form microstrip signal line and ground plane respectively.

The tapered fins gradually allow a change from the rectangular waveguide impedance to the microstrip impedance. Hence, the length and shape of the taper determine reflection and operating bandwidth. Previous results, [40]-[44], show how to achieve broad band performance with a taper length L :

$$L \geq \lambda_g \quad (3.2)$$

where λ_g is guided wavelength in the substrate material relative to the desired center band frequency.

A G-band design of the antipodal Fin-line transition, similar to [41], is modelled in HFSS as shown in Figure 3.4. The structure consists of curvilinear tapers with length $L = 1.2mm$ followed by a balanced stripline with length $S = 0.45mm$ and cascaded with a microstrip line with signal width 0.17mm. Initially, Teflon material $50\mu m$ thick is employed as a substrate for the transition. Figure 3.4(b) illustrates the location of the

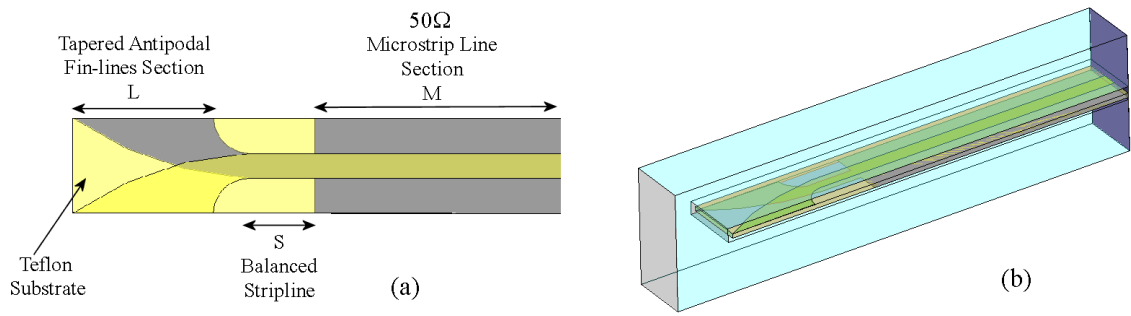


FIGURE 3.4: Antipodal Fin-line transition(a) consists of three sections:fin-line tapers L, balanced microstrip S and microstrip line M. The Antipodal Fin-line transition is located at the center line of the waveguide broad walls (b).

substrate, clamped at the centerline of the broad walls in the rectangular waveguide.

The microstrip line port is simulated with HFSS and relative results, Figure 3.5, show

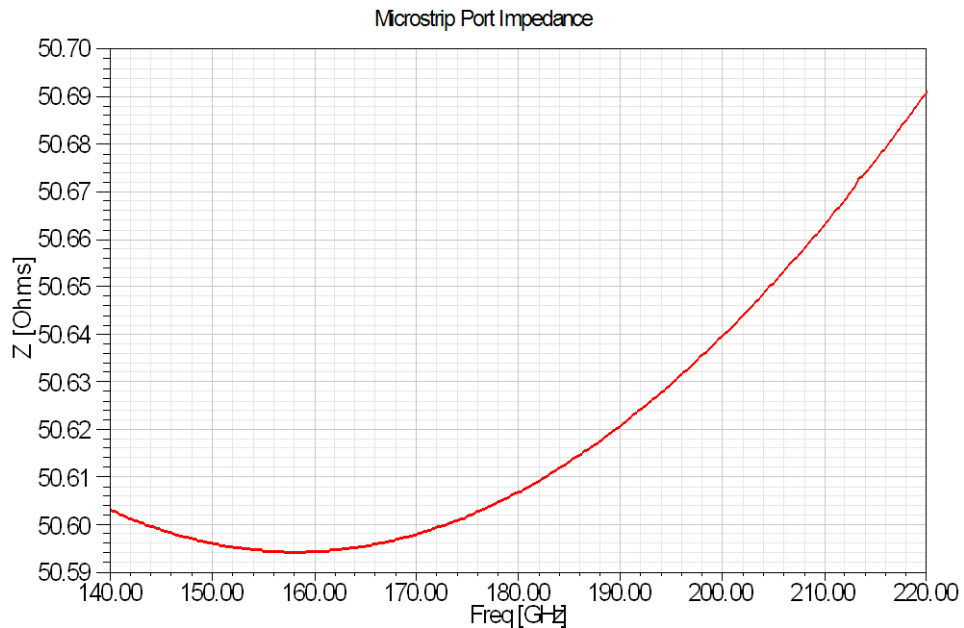


FIGURE 3.5: Input impedance of the microstrip line in waveguide. The microstrip is designed with an impedance $Z=50\Omega$. The waveguide walls increases the impedance of the microstrip adding a capacitive effect.

that the port impedance has a value of $\sim 50\Omega$ over the G-band. The propagation constant of the microstrip quasi-TEM mode is also plotted in Figure 3.6 showing its linear behaviour. At the upper end of the G-band a higher order waveguide mode starts to propagate due to the Teflon slab that dielectrically loads the rectangular waveguide and decreases the cut-off frequency of the first higher order mode.

However, this effect affects only the very upper end of the G-band. A 3D plot of the E-field relative to the transition mechanism of antipodal Fin-line at 180 GHz is illustrated in Figure 3.7 highlighting the E-field intensity pattern in the three cascaded sections.

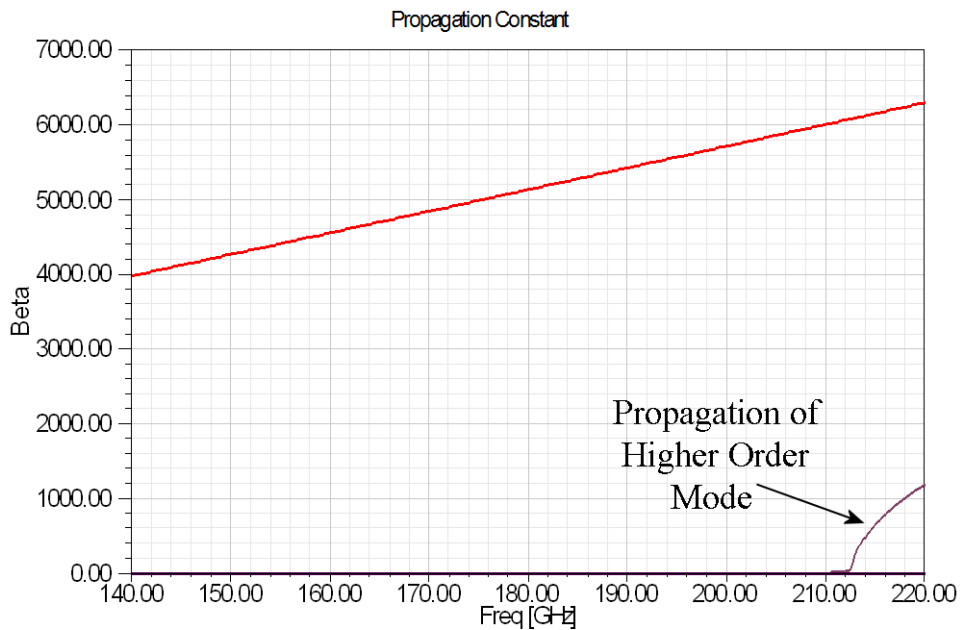


FIGURE 3.6: Linear propagation constant of the microstrip quasi-TEM mode (red). The first waveguide higher order mode starts to propagate at 212GHz.

The waveguide TE_{10} mode, coupled to the structure as its input, splits at the Fin-line taper point and finally converts into the microstrip line mode. By looking at the S-

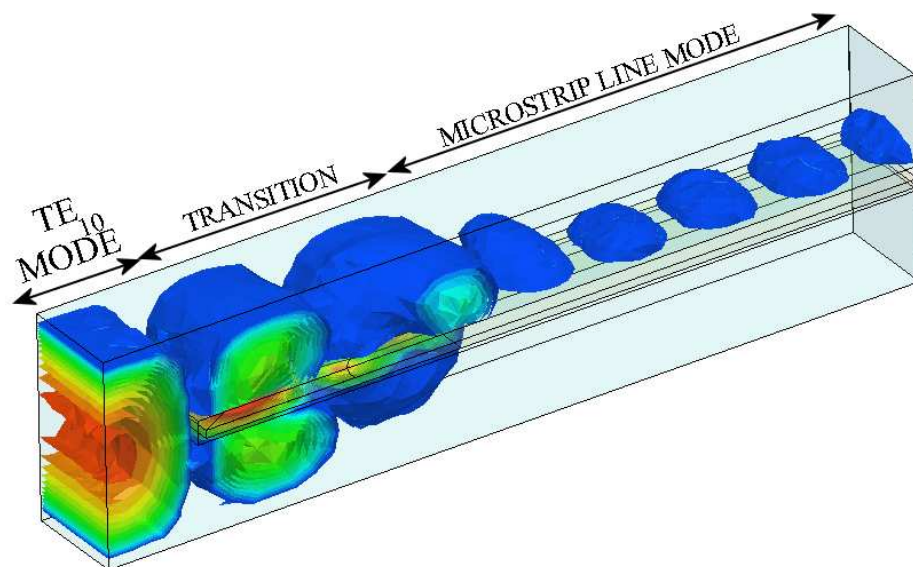


FIGURE 3.7: E-field distribution at 180GHz. The TE_{10} mode entering the transition from left is split, rotated and finally matched to the microstrip quasi-TEM mode.

parameters of the single transition, the effects of internal resonances is noticeable. As mentioned and modelled in [42], the antipodal Fin-line transitions are adversely influenced by resonances that build into the slots formed between tapers and waveguide walls. Figure 3.8 and Figure 3.9 show S_{11} and S_{21} of the transition. Two major resonances

arise respectively at 165GHz and 186GHz. The resonances appear in the band of interest and performance is compromised. A E-field distribution at 186GHz is also illustrated

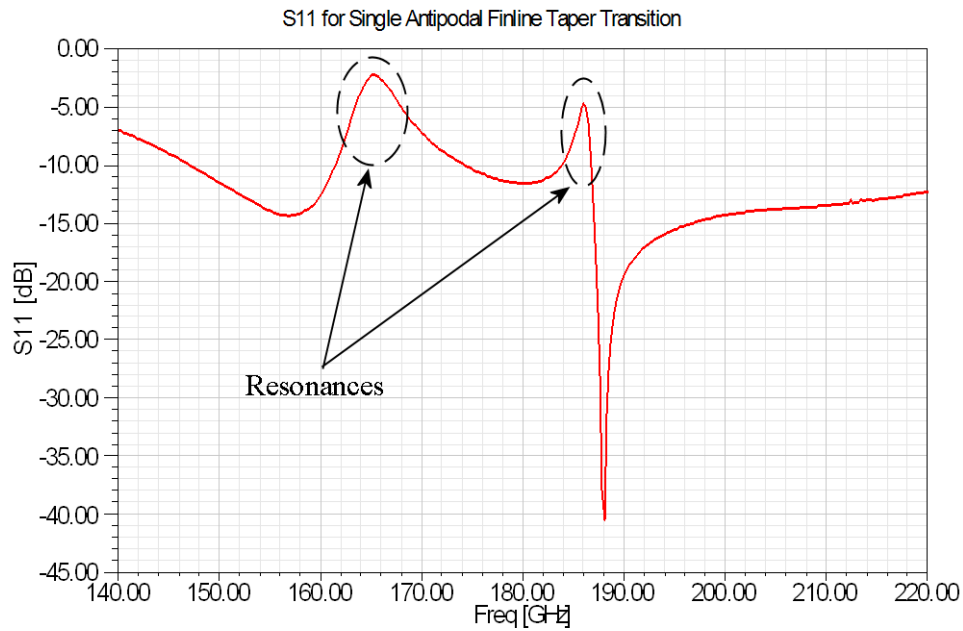


FIGURE 3.8: S_{11} of the single antipodal fin-line transition. Two resonances appear in G-band increasing the level of reflection and reducing the operating bandwidth.

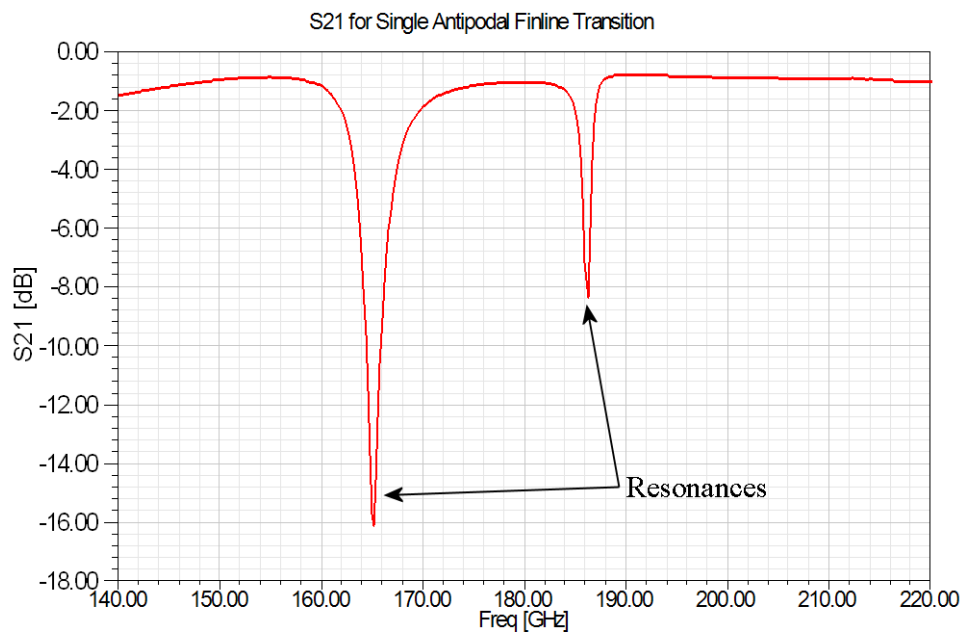


FIGURE 3.9: S_{21} of the single antipodal fin-line. The transmission at the resonant frequencies is adversely compromised.

in Figure 3.10 showing where the resonance builds and how the output microstrip mode is highly attenuated when compared with Figure 3.7. The antipodal Fin-line transition is also modelled in *back-to-back* configuration, Figure 3.11, where input and output are represented by WR-05 waveguides. The resulting S_{21} plot over G-band is presented in

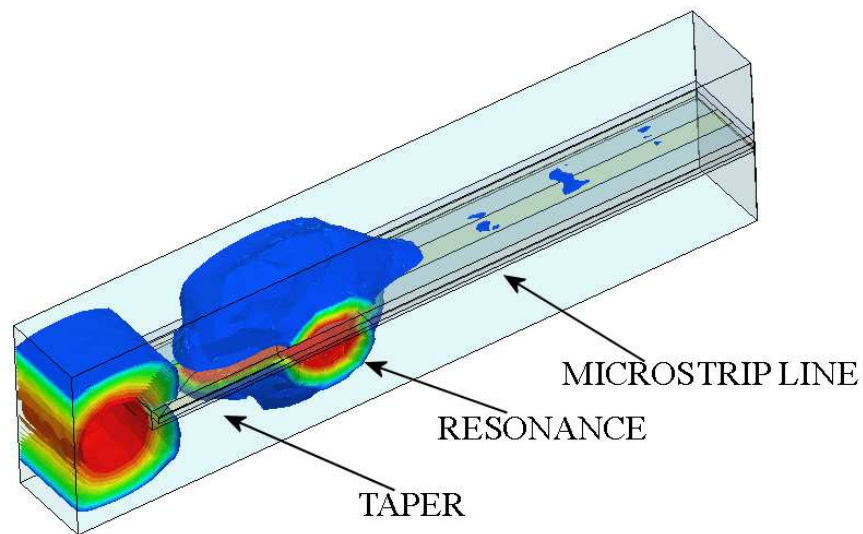


FIGURE 3.10: E-field distribution over the antipodal fin-line transition at 186GHz. The resonance builds between the tapered fins and the waveguide walls stopping the energy to flow along the microstrip line.

Figure 3.12. The resonances at the same frequencies persist to reduce dramatically the bandwidth of the transition. The E-field plot at 186GHz, for the back-to-back transi-

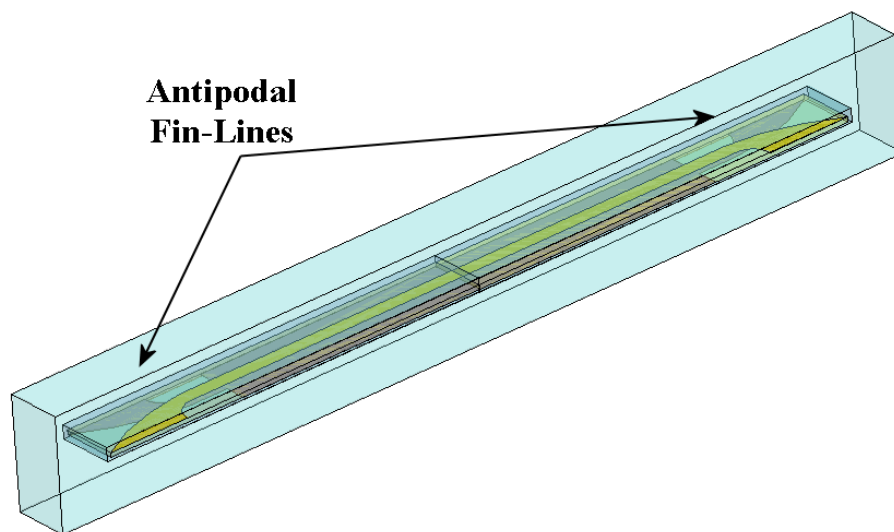


FIGURE 3.11: Design of the antipodal fin-line transition in back-to-back structure.

tion, is represented in Figure 3.13 highlighting again the sections where the resonances build. The model, just discussed, used Teflon as substrate material. The resonances are strictly related to the electrical dimensions and shape of the slot formed between the antipodal Fin-line taper and the rectangular waveguide walls. In case a substrate

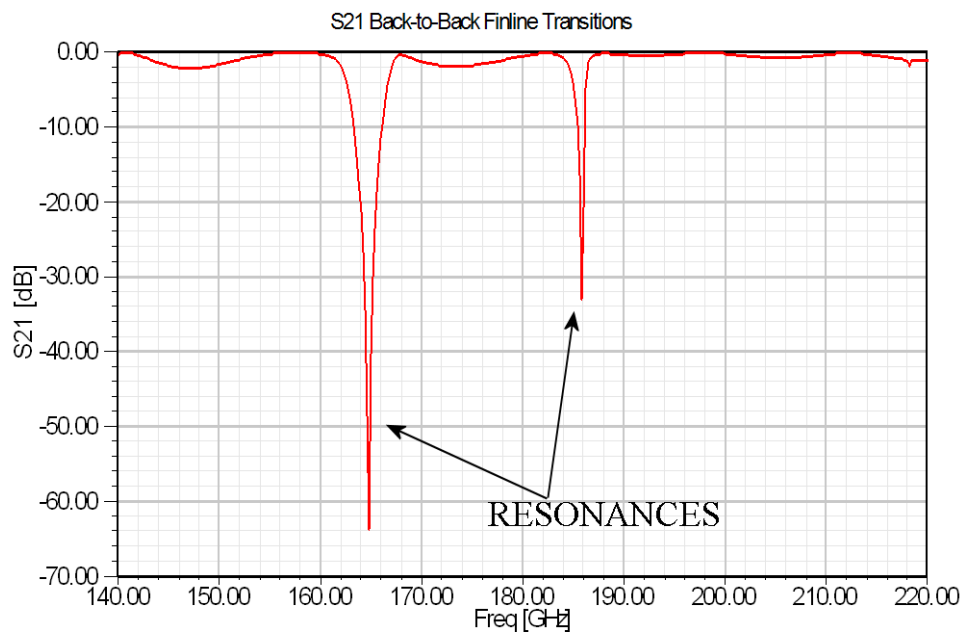


FIGURE 3.12: S_{21} parameter of the back-to-back antipodal fin-line transition. The resonances arise at the same frequencies of the single antipodal fin-line.

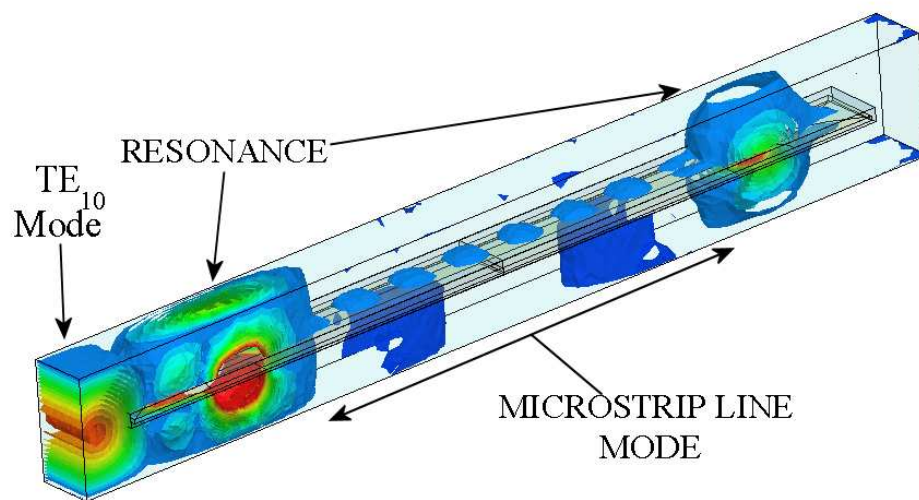


FIGURE 3.13: E-field distribution for back-to-back antipodal transition at 186GHz. The resonances build at the tapered fins regions.

material with higher dielectric constant as GaAs ($\epsilon_r = 12.9$) is implemented, the electrical dimension of the slot becomes even larger decreasing the resonant frequency values and also allowing their higher harmonic frequencies to resonate. The overall effect is a further reduction of the operating bandwidth.

The simulation of the antipodal fin-line transition highlights how important it to finely mesh the substrate material between the finlines where electric field coupling and rotation happen. For this type of simulation the *maximum length based* meshing operation is applied to the substrate whose thickness is chosen as maximum dimension for the tetrahedra. Figure 3.14 shows the meshed model with and without meshing operation, where it is possible to notice the finer mesh result in the latter case.

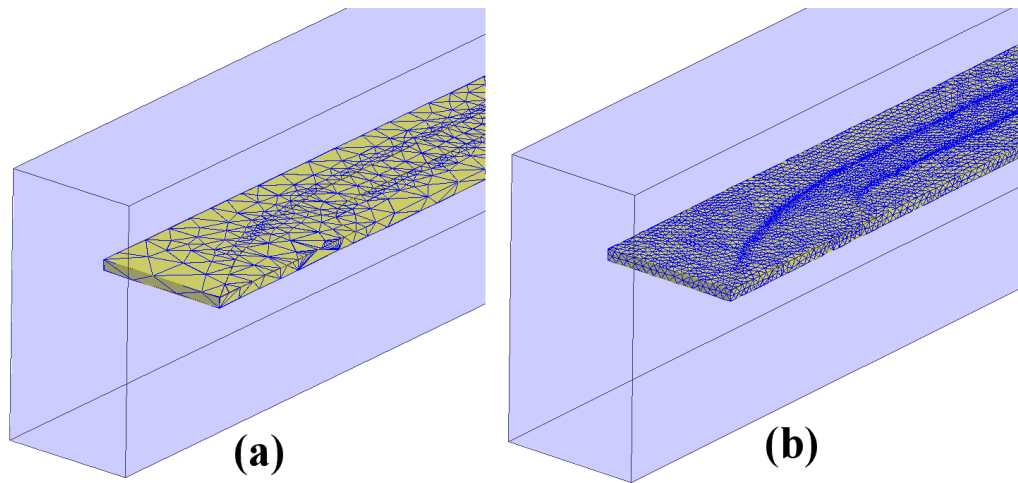


FIGURE 3.14: Meshed model without (a) and with (b) maximum length based operation.

The antipodal Fin-line transition develops from the *ridge waveguide transition* structure, Section 2.3.1, where no substrate is employed, hence its use is limited to substrates with very low permittivity values. Moreover, the tolerances involved in the assembly and relative clamping of the substrate material into the waveguide makes it very difficult to predict the resonant frequencies.

3.5 WR5 Transition Using Dipole Antennas

An interesting option to design waveguide transition using printed antennas, is discussed in Section 2.3.4. A simple dipole can be used to collect the propagating waveguide mode and convert it into a microstrip mode. An example [52] is modelled in HFSS as shown in Figure 3.15 where the substrate material is InP with $100\mu\text{m}$ thickness. The substrate is supported by a metal pedestal at the center line of the waveguide broad walls. The two arms of the dipole are printed on the opposite sides of the substrate and a $\lambda/4$

transformer is used for impedance matching between antenna and microstrip line. The design involves the metal pedestal which works as ground plane for the microstrip line and as reflector for the antenna at the same time.

The design starts by defining the dimensions of the dipole arms [59] based on the

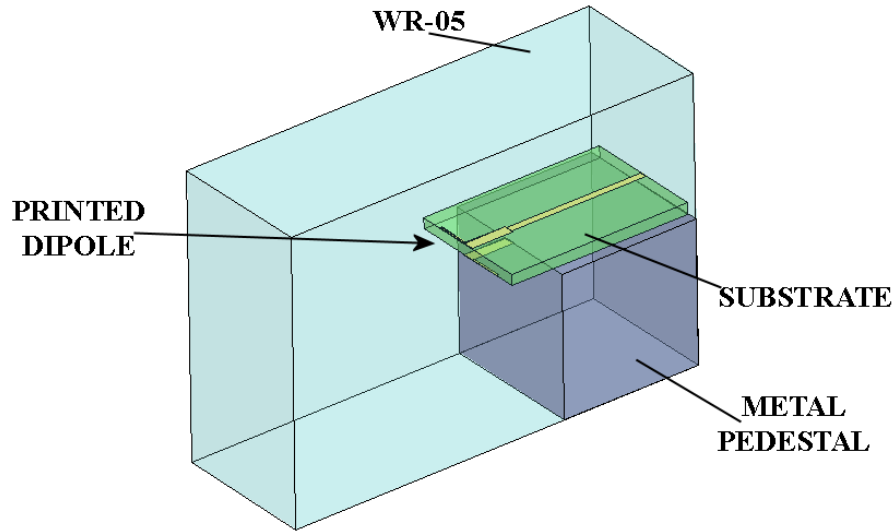


FIGURE 3.15: Dipole antenna is printed on both sides of the substrate. A metal pedestal support the transition at the center line of the waveguide broad walls.

information of the substrate material and operating frequency. The length of the dipole λ_d is given by:

$$\lambda_d = 0.47 \cdot \lambda = 0.47 \cdot \frac{v}{f} \quad (3.3)$$

with:

$$v = \frac{c}{\sqrt{\varepsilon_{eff}}} \quad (3.4)$$

$$\varepsilon_{eff} = \frac{\varepsilon_r + 1}{2} + \frac{\varepsilon_r - 1}{2} \left[\left(1 + \frac{12 \cdot h}{w} \right)^{-\frac{1}{2}} + 0.04 \cdot \left(1 - \frac{w}{h} \right)^2 \right] \quad (3.5)$$

Where λ is the free space operating wavelength, f is the frequency, c is the speed of light, v is the speed of light in the substrate material, ε_{eff} and h are respectively the effective dielectric constant and height of the substrate and w is the width of the printed line.

The substrate thickness depends on the technology process employed. Then, the effective dielectric constant, ε_{eff} is determined by the substrate thickness and the width of the metal strips used as antenna arms.

The example using InP with $100\ \mu\text{m}$ thickness is modeled in HFSS for a V-band (50-75GHz) design with parameters illustrated in Figure 3.16.

The dimensions used are $S=40\ \mu\text{m}$, $L=540\ \mu\text{m}$, $T=130\ \mu\text{m}$, $M=500\ \mu\text{m}$ and $W=77\ \mu\text{m}$

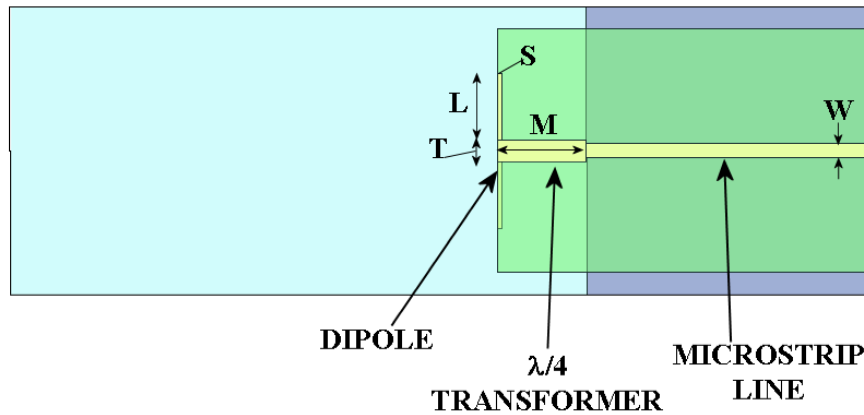


FIGURE 3.16: The arms of the dipole antenna with length L and width S are connected to a microstrip with width W through a $\lambda/4$ transformer with length M and width T .

for a design optimized at 60GHz.

During design, the structure followed different parametric iterations since the initial values for the length of the antenna resulted from (3.3) relate to a dipole printed on infinite substrate. When the antenna is used inside the rectangular waveguide the dimensions of the antenna change to take into account the waveguide walls, closely located, and the metal pedestal that alter the input impedance of the antenna in the waveguide. Moreover, the substrate is not infinite but terminates at the antenna input port. The simulated S-parameters S_{11} and S_{21} of Figure 3.17 show the narrowband performance of the transition as it follows from the intrinsic characteristics of the single dipole. The same transition structure is modeled in HFSS to operate at G-band by properly scaling the design parameters as $S=10\ \mu\text{m}$, $L=150\ \mu\text{m}$, $T=50\ \mu\text{m}$, $M=200\ \mu\text{m}$ and $W=32\ \mu\text{m}$ for a design at $f=180\text{GHz}$.

However, the substrate thickness is limited by fabrication to a minimum of $50\ \mu\text{m}$ showing that this restricts performance at V-band. Simulated S-parameters of the design at G-band frequencies are shown in Figure 3.19 where S_{11} is limited to a minimum of -15dB. The performance of the transition could be improved if the fabrication process allowed the thinning of the substrate material down to $\sim 30\ \mu\text{m}$.

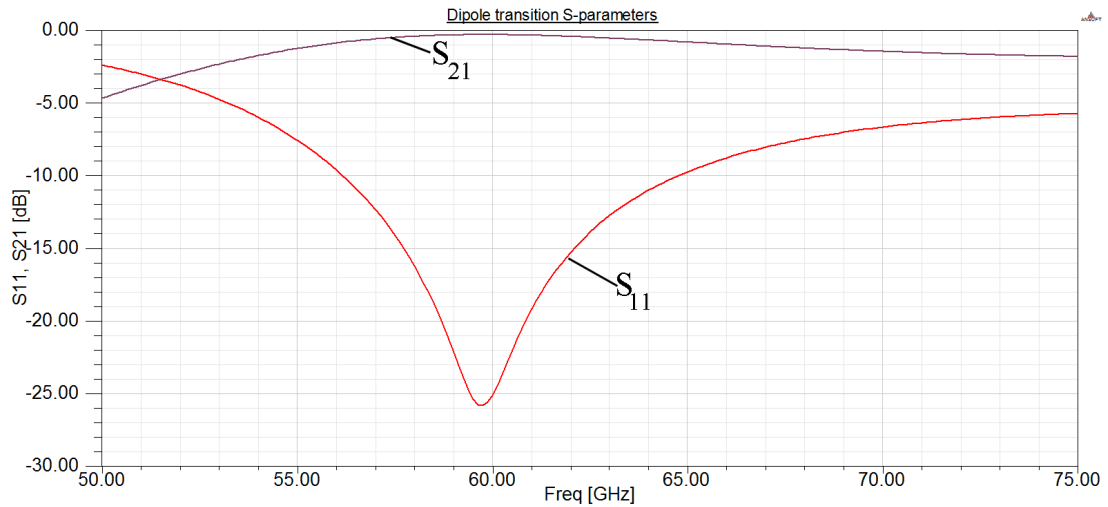


FIGURE 3.17: S-parameters of the dipole transition at V-band and optimized for 60GHz.

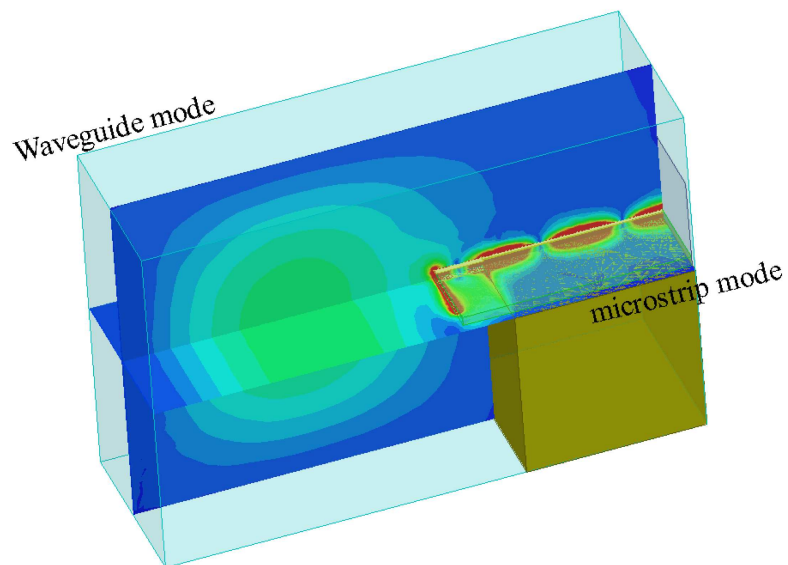


FIGURE 3.18: E-field distribution of the dipole transition showing how the waveguide TE_{10} mode is collected by the dipole and converted into microstrip mode.

3.6 WR5-to-Microstrip transition using Transversal Launcher

As described in Section 2.3.3, a transversal transition consists of a T-junction between rectangular waveguide and planar transmission line. The EM field is coupled from one structure to the other by using an extension of the planar line which works as probe into the waveguide section. Figure 3.20 illustrates a model of the transversal transition designed with HFSS 12.

In this case, the microstrip signal line protrudes into the waveguide forming the probe. In [60] an analysis of similar structure involving a coaxial line whose signal pin projects

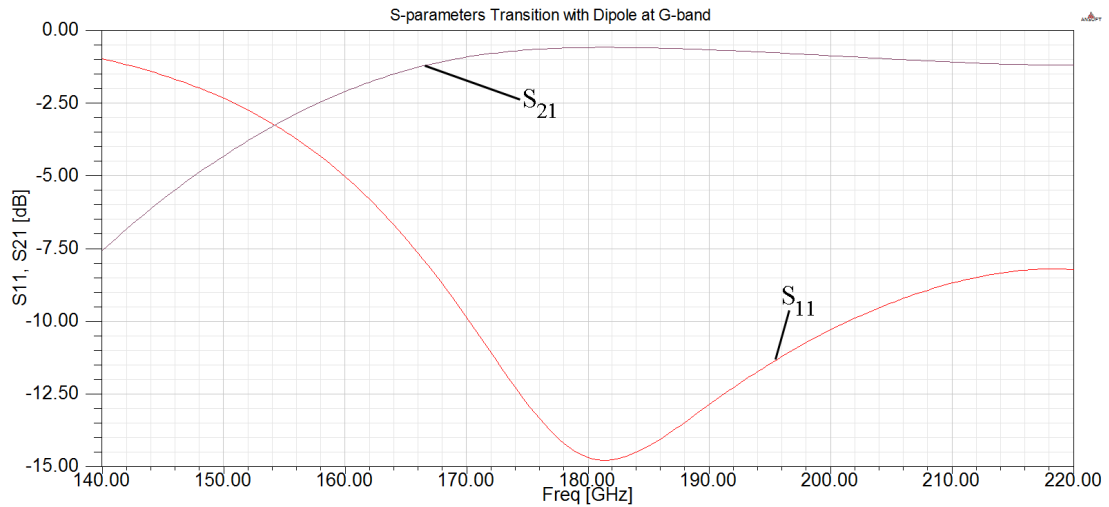


FIGURE 3.19: S-parameters plot of waveguide to microstrip transition using printed dipole in the G-band. Since the substrate thickness is limited by fabrication processes to $50\mu\text{m}$, the performance at G-band frequencies results in poorer operation than the same structure designed for the V-band.

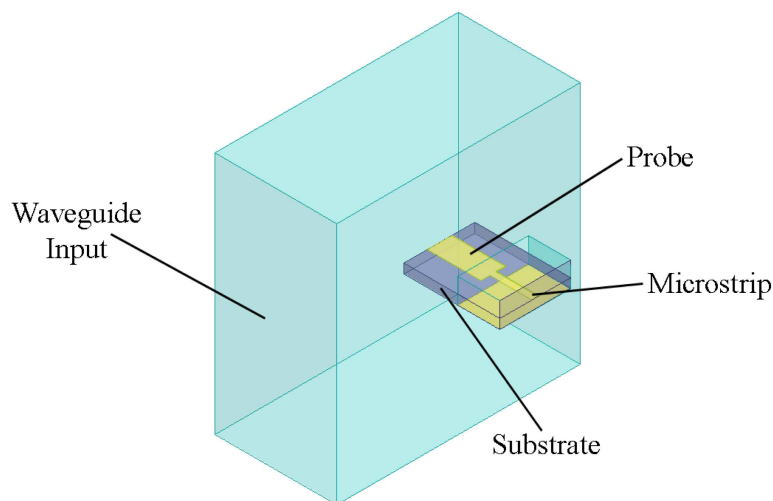


FIGURE 3.20: Waveguide to microstrip transversal transition. The microstrip line extends into the waveguide and works as probe supported by the substrate material.

into the waveguide shows that fundamental design parameters are the distance of the probe from a back-side short, the width of the probe and also its length. By using a microstrip line, the equivalent parameters are shown in Figure 3.21 where W is the width of the probe, D is the length and L is the distance of the back-side short from the centerline of the probe. By changing these parameters, the input impedance of the probe changes and impedance matching with rectangular waveguide can be achieved. The effect of each of the fundamental parameters can be illustrated on a Smith Chart revealing guidelines for the matching procedure.

By varying the length of the probe D and keeping the other two parameters fixed, the input impedance change in both its real and imaginary parts. A short probe presents

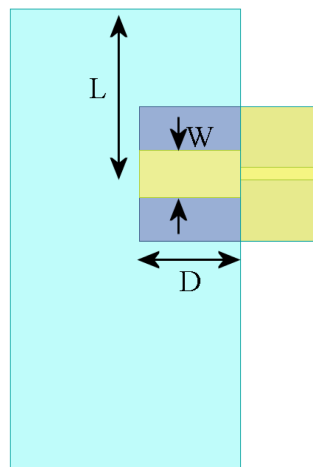


FIGURE 3.21: Design parameters of the transversal transition are represented by the distance L of the waveguide back-short and length D and width W of the probe.

a very high input impedance as it happens with short monopole antennas. By increasing the probe length the input resistance decreases. Figure 3.22 shows how the input impedance of the probe moves over the Smith chart by changing the length of the probe from $D=100\mu m$ (1) to $D=300\mu m$ (5) with $50\mu m$ step when the other two parameters are kept fixed to $W=130\mu m$ and $L=460\mu m$. The input impedance of the probe moves from the edge of the Smith Chart where it assumes high values towards the center of the chart. The width W of the probe controls the capacitive effect between the probe and

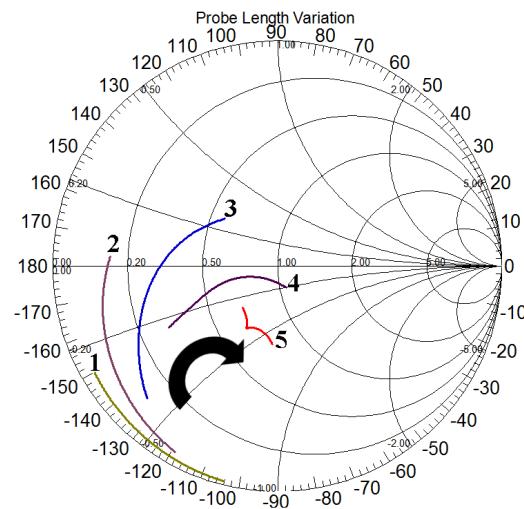


FIGURE 3.22: By increasing the length D from $D=100\mu m$ (1) to $D=300\mu m$ (5) in steps of $50\mu m$, the probe input impedance shifts from the edge of the Smith Chart toward its center, normalized to 50Ω , highlighting the effect of the probe length in reducing the input impedance of the probe.

the opposite waveguide wall. Figure 3.23 shows how the input impedance of the probe shifts towards the capacitive lower half of the Smith Chart by increasing the width of

the probe from $W=35\mu\text{m}$ (1) to $W=175\mu\text{m}$ (5) with $35\mu\text{m}$ step. Probe length and back-side short are kept fixed to $D=300\mu\text{m}$ and $L=460\mu\text{m}$ respectively. The back-side short

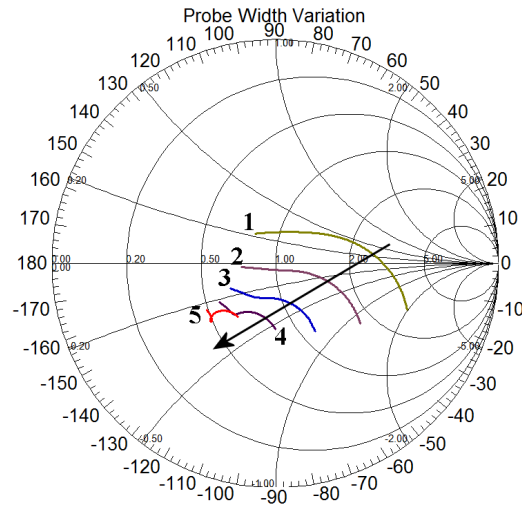


FIGURE 3.23: By increasing the width of the probe from $W=35\mu\text{m}$ (1) to $W=175\mu\text{m}$ in $35\mu\text{m}$ steps, it increases the capacitive effect between the probe and the opposite waveguide wall. As result the input impedance of the probe shifts toward the lower half of the Smith Chart.

L acts as stub and by varying its distance from the probe it compensates the capacitive effect between probe and opposite waveguide wall. Figure 3.24(a) shows the probe input impedance varying when the back-side short distance changes from $L=300\mu\text{m}$ to $L=450\mu\text{m}$ with $50\mu\text{m}$ steps, whereas Figure 3.24(b) illustrate its variation with L changing from $L=450\mu\text{m}$ to $L=600\mu\text{m}$. Width W and length D of the probe are kept fixed to $W=130\mu\text{m}$ and $D=300\mu\text{m}$.

The overall change of the probe input impedance is shown in Figure 3.24(c) where it is possible to notice the back-short impedance matching function. The most important factor to consider in tuning the fundamental parameters of the transition is that there is a combination of the three parameters for which the probe input impedance varies very little over frequency and this result allows the design of a broadband transition.

Figure 3.22, 3.23 and 3.24 highlight the existence of this parameter combination and it represents the starting point for the impedance matching strategy with the microstrip line.

It is possible to summarise, with some limitations, the function of each parameter with an equivalent lumped elements circuit. The transition inherits the design parameters space from the waveguide to coaxial probe transition [61]-[62], from which it is developed. Figure 3.25(a)-(b) illustrates the waveguide-to-microstrip T-junction and its derived equivalent circuit. Z_{wg} represents the rectangular waveguide impedance, which is resistive and frequency dependent. L_{BS} accounts for the inductive effect of the waveguide back-short used to resonate out the existing capacitance C_p due to the

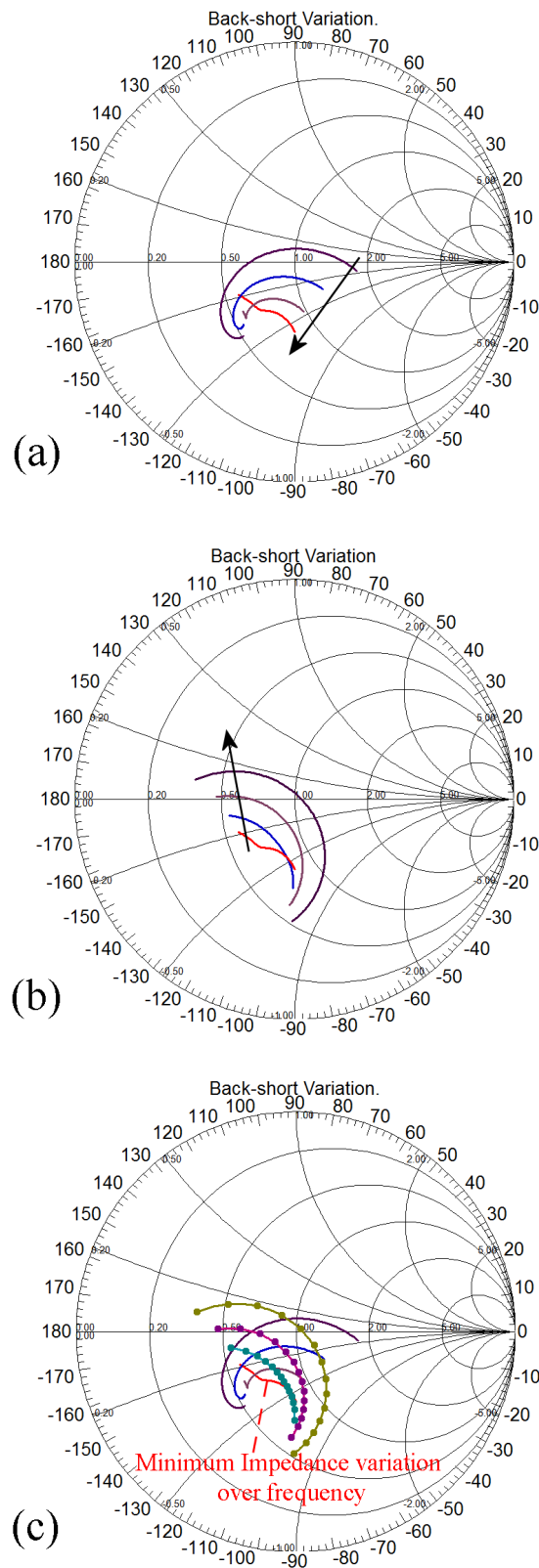


FIGURE 3.24: Probe input impedance variation when waveguide back-short distance is increased from $L=300\mu\text{m}$ to $L=450\mu\text{m}$ (a) and from $L=450\mu\text{m}$ to $L=600\mu\text{m}$ (b). Both variations are presented in (c) where they reveal the tuning effect of the back-short distance to obtain a small frequency variation of the probe input impedance over the G-band.

distance between the probe and the opposite waveguide wall. The probe has its own inductance, represented by L_p , which also depends on the supporting substrate material. The terminals TT' represent the reference plane T that separates the waveguide from the microstrip line, Figure 3.25(a).

The equivalent lumped element circuit is a simplification of the transition and it reduces to a L-C impedance network. However, as for the waveguide-to-coaxial line transition [63], there is no simple analytical expression for L_p , L_{BS} and C_p . Hence, HFSS is a crucial tool in the design process.

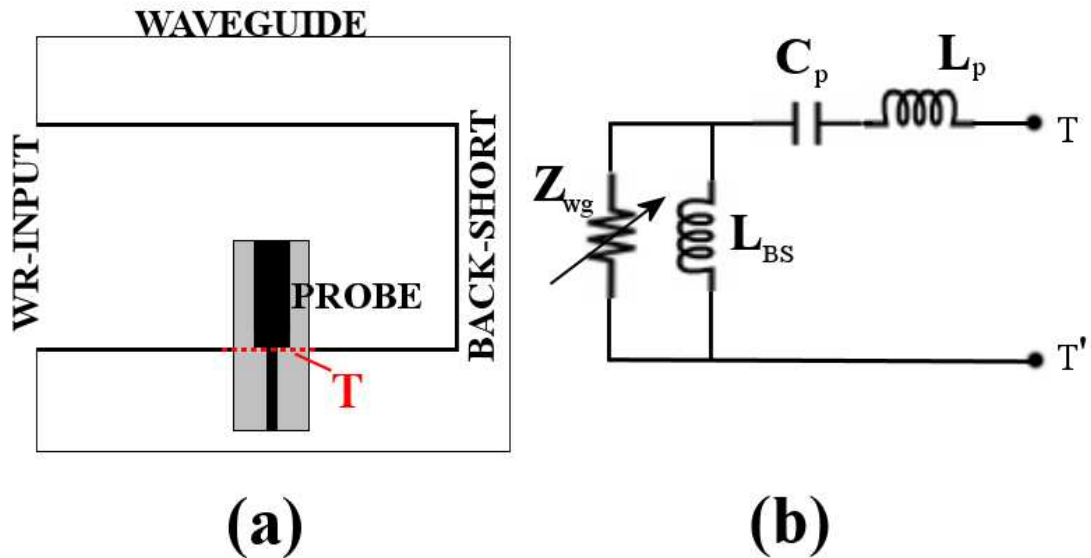


FIGURE 3.25: Waveguide-to-microstrip T-junction (a): the reference plane T separates the waveguide and the microstrip line and it corresponds to the terminals TT' in the equivalent circuit (b).

In [32] a method to achieve an impedance matching of the probe to a microstrip line using two matching network elements is reported. The network is illustrated in Figure 3.26 and consists of a microstrip high impedance element and $\lambda/4$ transformer in series. Fundamental parameters dimensions used for the simulation are: $D=300\mu m$, $L=460\mu m$ and $W=170\mu m$, the substrate material is GaAs $50\mu m$ thick. The overall desired function of the matching network is to bring the input impedance of the probe close to 50Ω being the impedance of the microstrip line. The optimized values of the parameters involved in the matching network are: $I_W = 20\mu m$, $I_L = 30\mu m$, $T_W = 66\mu m$, $T_L = 163\mu m$ and $M_W = 32\mu m$. Figure 3.27 shows the probe input impedance change on the Smith Chart. The high impedance microstrip element introduces an extra inductance which brings the probe impedance close to the centerline of the chart where all the real impedance values $loci$ are (1)-(2). Then the $\lambda/4$ transformer allows a 90° rotation to bring the impedance closer to 50Ω , center of the chart. Simulated S-parameters confirm the broad band characteristic of the transition as shown in Figure 3.28 for S_{11} and S_{21} . The distribution of the E-field around the probe at 220GHz is illustrated in

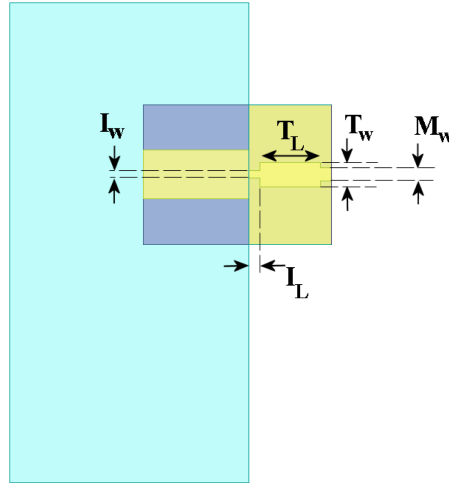


FIGURE 3.26: Transversal waveguide to microstrip transition using network matching elements [32]. The probe is connected to the microstrip through an high inductance element having length I_L and width I_W and a $\lambda/4$ transformer with length T_L and width T_L . The width of the microstrip is M_W .

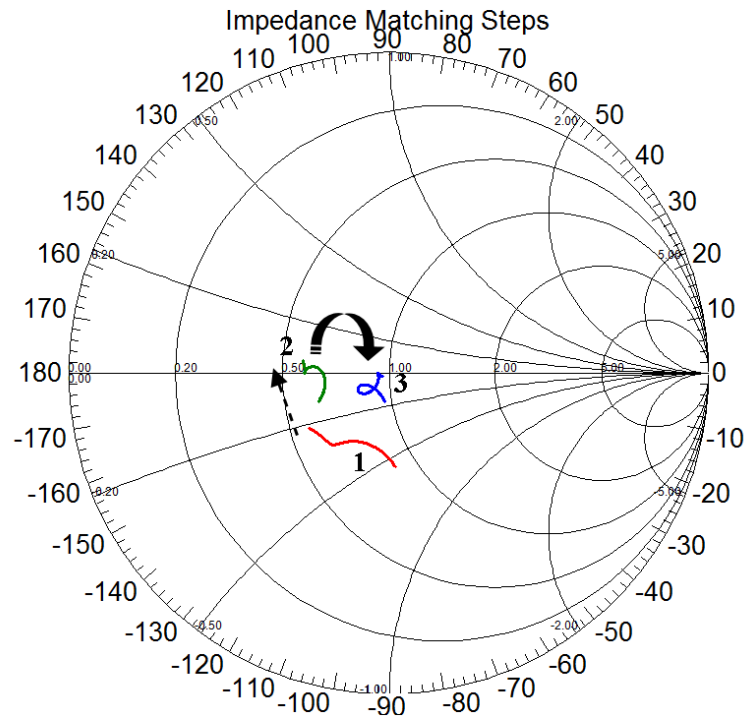


FIGURE 3.27: The high inductance element bring shifts the probe impedance toward the Smith Chart center line. The $\lambda/4$ transformer rotates the probe impedance *loci* of 90° to bring it closer to the center of the Chart, normalized to 50Ω .

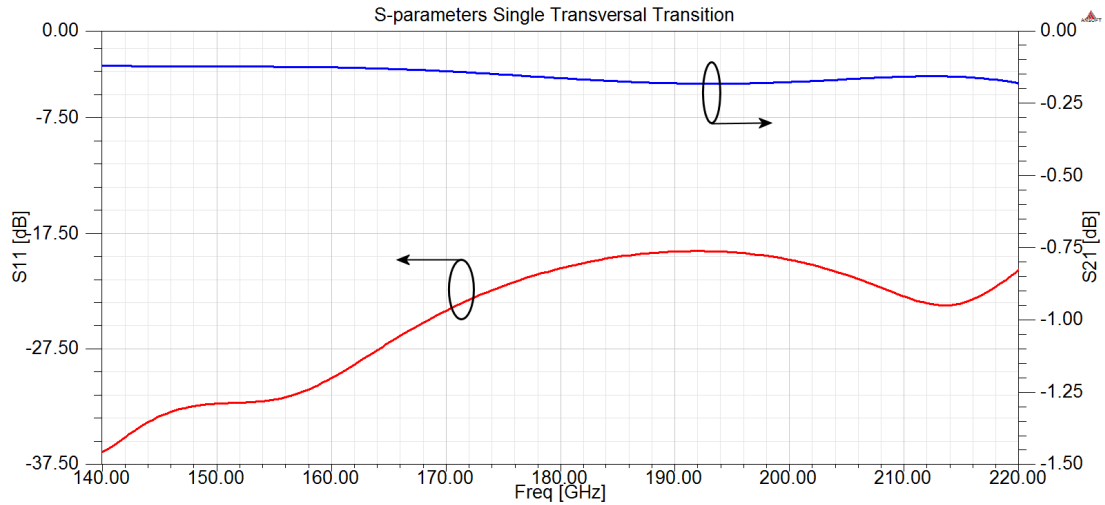


FIGURE 3.28: S-parameters plots for a single transversal waveguide to microstrip transition. S_{11} is relative to the waveguide input, whereas S_{21} identify the transmission on port 2 (microstrip) due to an excitation on port 1 (waveguide). The broad band performance of the transition is revealed by the S_{11} lower than -17.5dB over the entire G-band.

Figure 3.29(a)-(b) where the waveguide TE_{10} mode couples to the probe, which transduces it into microstrip mode. The plot of the E-field inside the GaAs substrate that

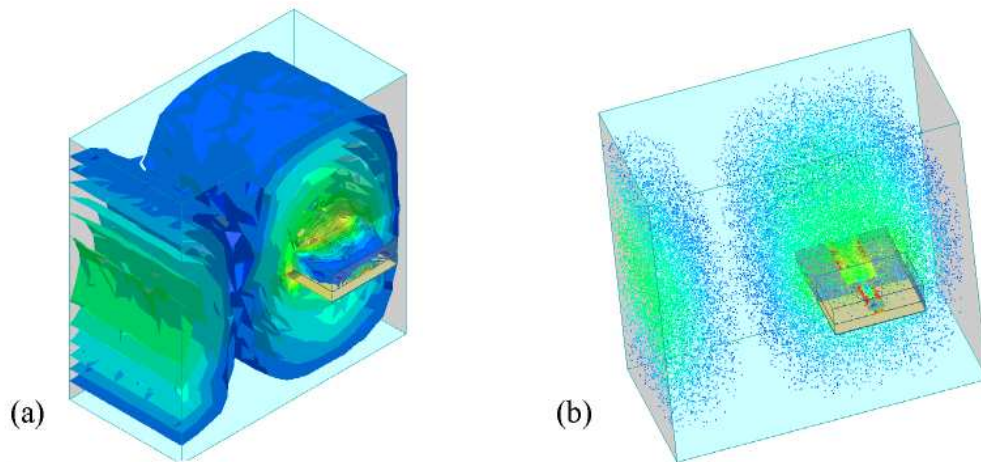


FIGURE 3.29: 3D perspectives (a)-(b) of the E-field at the junction between rectangular waveguide and microstrip at $f=220\text{GHz}$. The waveguide TE_{10} mode couples energy into the microstrip line using the probe as trasducer (b).

supports the probe, Figure 3.30(a)-(c), highlights how the microstrip mode is excited and Figure 3.30(d) confirms the quasi-TEM field distribution at the microstrip cross section. The design of a transversal transition also involves dimensional design of the microstrip channel to avoid possible unwanted higher order modes propagating. As in [64], the channelized microstrip structure can be considered as a cavity partially loaded with substrate material. The metal channel, housing the microstrip, can support propagating modes very much like the rectangular waveguide modes. As such, they also

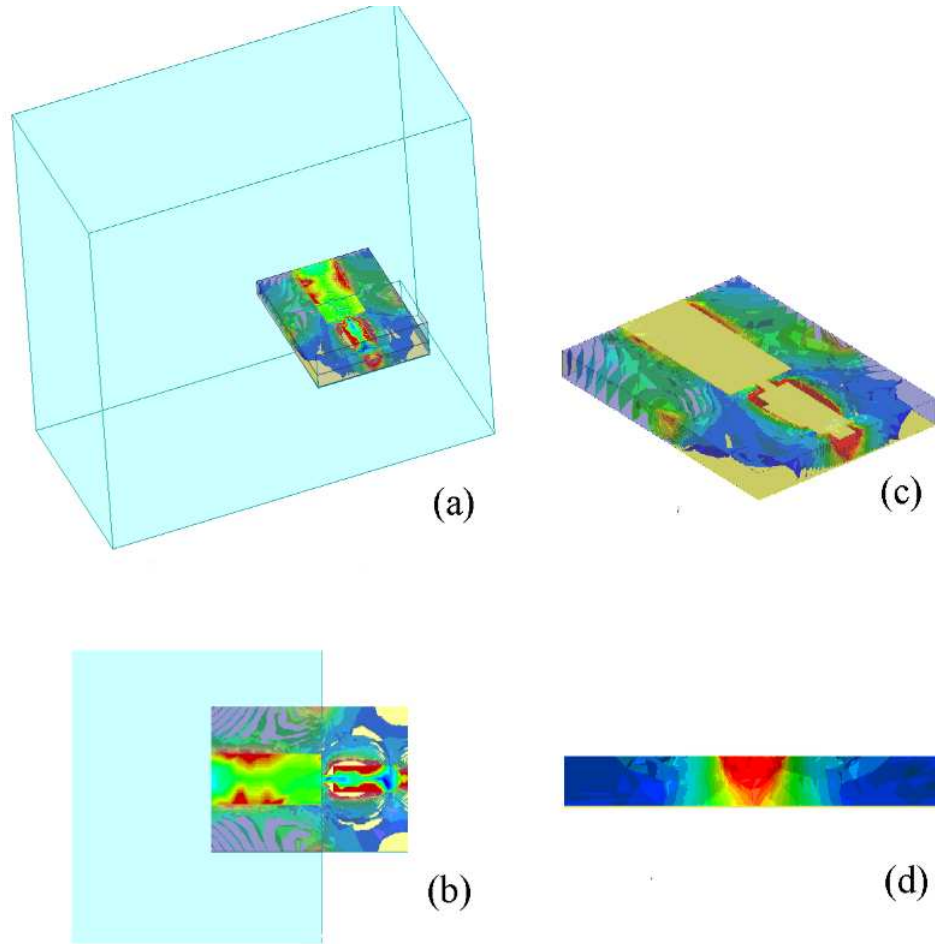


FIGURE 3.30: EM field is induced on the probe and in the substrate material supporting it (a)-(b). The probe collects the energy coming from the TE_{10} mode and rotates the EM field conforming it to the quasi-TEM mode of the microstrip line (c). Quasi-TEM mode at the microstrip cross-section (d).

have a cut-off frequency under which they only attenuate and do not propagate. The cut-off wavelength λ_0 of the lowest order waveguide mode supported by a channelized microstrip is given by [64]:

$$\lambda_0 = 2A \cdot \sqrt{\frac{1}{1 - \frac{h}{B} \left(1 - \frac{1}{\epsilon_r}\right)}} \quad (3.6)$$

where A and B are the dimensions of the channel width and height respectively. The parameters h and ϵ_r represent the thickness and the dielectric constant of the substrate inside the channel.

In our model the dimensions of the channel are chosen to be $A=500\mu m$ and $B=200\mu m$ in order to push the cut-off frequency out of the G-band when GaAs ($\epsilon_r = 12.9$) $50\mu m$ thick is used as substrate. The simulated E-field distribution in the substrate channel is shown in Figure 3.31 defining the microstrip mode profile along the channel. The prop-

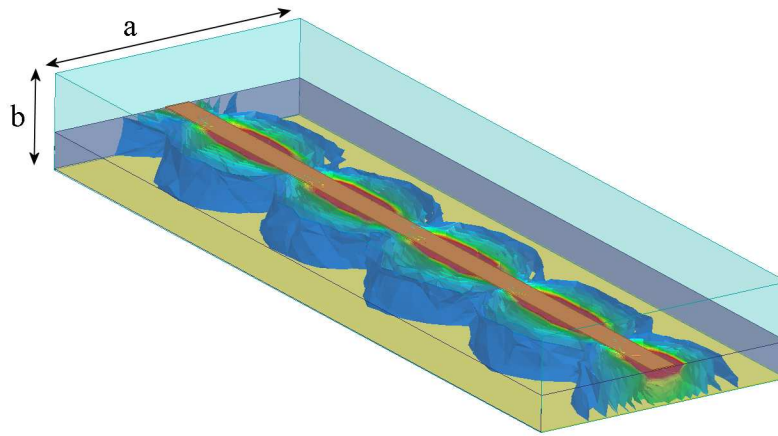


FIGURE 3.31: Propagation of the E-field along the microstrip line located into a metal housing having width a and height b .

agation constant is also illustrated in Figure 3.32 confirming that, with the dimensions chosen, the microstrip quasi-TEM is the only propagating mode along the structure. The simulated S-parameters of a channelized microstrip are also shown in Figure 3.33

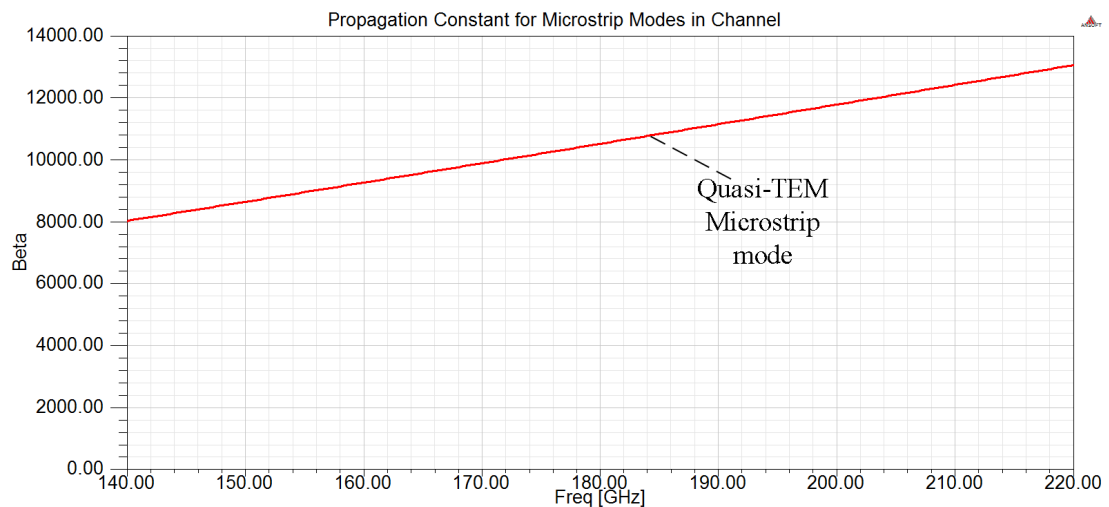


FIGURE 3.32: Propagation constant of the quasi-TEM mode of the channelized microstrip line. No higher order mode propagates unlike the case of the antipodal fin-line propagation constant of Figure 3.6.

confirming good propagation properties for the microstrip mode without unwanted cavity resonances which otherwise appear as sharp spikes in the S-parameters plot. Two transitions are cascaded in a back-to-back structure and separated by a microstrip line 3mm long and are modeled, Figure 3.34(a). The E-field distribution of the TE_{10} waveguide mode propagating from input to output waveguide is also illustrated in Figure 3.34(b).

However, some considerations have to be made as, at these frequencies, the integration of current multistage MMIC low noise amplifiers [65] requires wider dimensions than the designed microstrip channel, entailing a lower cut-off frequency. In this case, a strategy

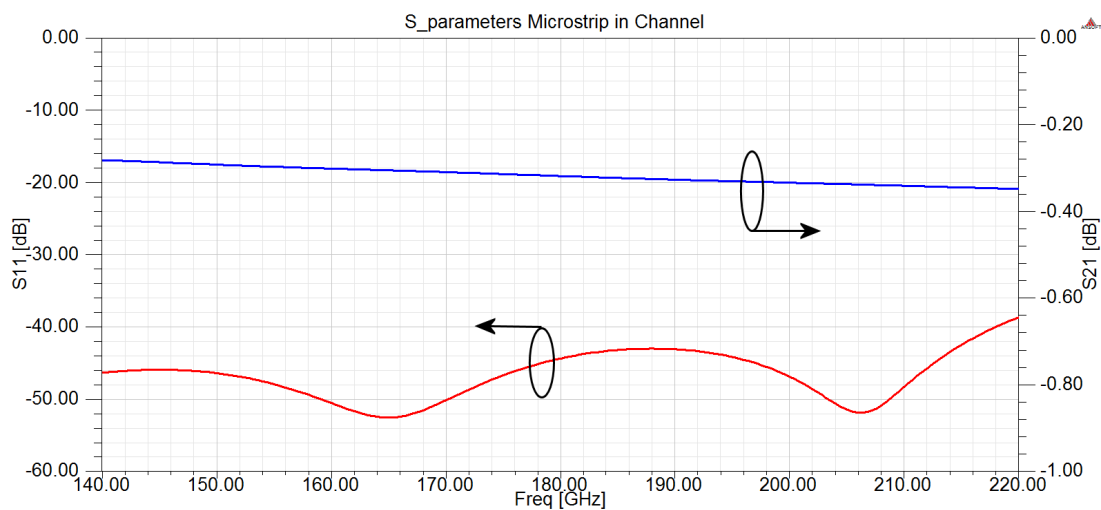


FIGURE 3.33: S-parameters plot for the channelized microstrip line. Reflection, lower than -40dB over the entire band indicates good power transmission. The S-parameters do not show sharp spikes as confirmation for no cavity resonances along the structure due to appropriate dimensioning of the channel cross section.

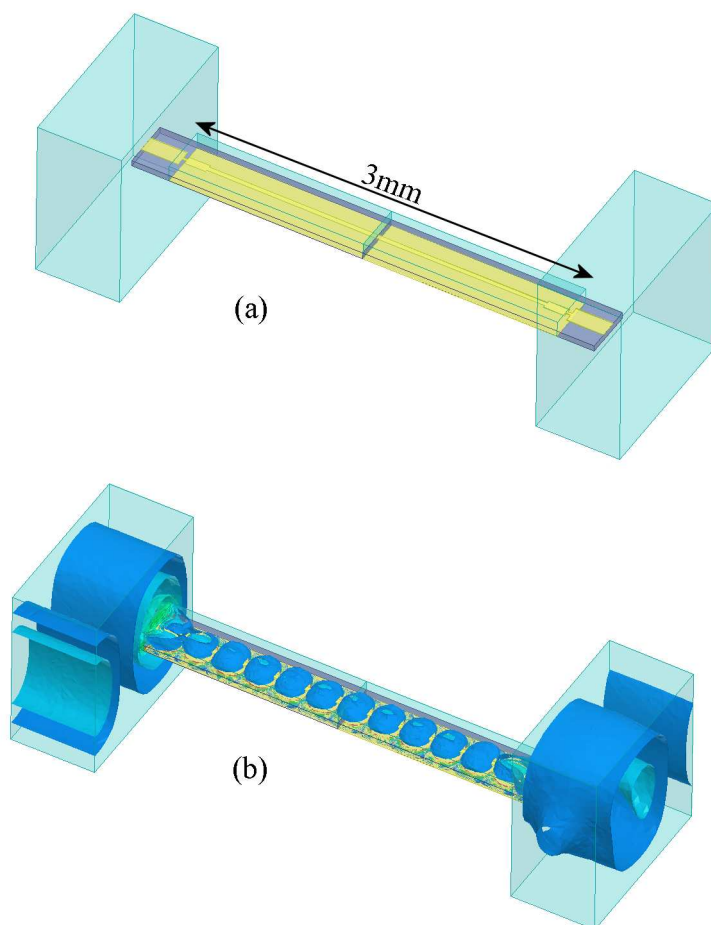


FIGURE 3.34: Two transversal transition connected in back-to-back configuration and separated by 3mm microstrip line (a). E-field plot of the transitions in back-to-back configuration (b). Waveguide mode is converted in microstrip mode and re-converted in waveguide mode at the output.

to control power leakage of unwanted modes is unavoidable and it has to be implemented to mitigate its effect. An approach to the problem is mentioned in [39] where the bottom part of the microstrip channel, hosting the MMIC, is wider than its top part. The proposed profile claims to reduce the leakage of the waveguide TE_{10} mode power in the microstrip channel.

Furthermore, the dimensions of high gain LNAs for passive imaging (i.e. 50-60dB) and the required access space for their DC bias injection can substantially widen the cavity housing the MMIC. In-band resonances could be excited causing oscillations by shorting the input and output of the amplifier in positive feedback. A possible solution to the problem is to employ Electronic Band Gap (EBG) structures [29] [66] in the MMIC cavity to suppress package resonances.

In terms of meshing strategy for the transversal transitions, the *dummy objects* technique is employed to achieve an accurate and converged solution of the simulation. The critical area of the model is represented by the volume around the probe and the matching network elements. An additional geometry, following their profiles, is added in order to increase the local mesh. An example of the structure and its dummy object is illustrated in Figure 3.35 where it is possible to see the printed probe and microstrip line enclosed in the dummy object.

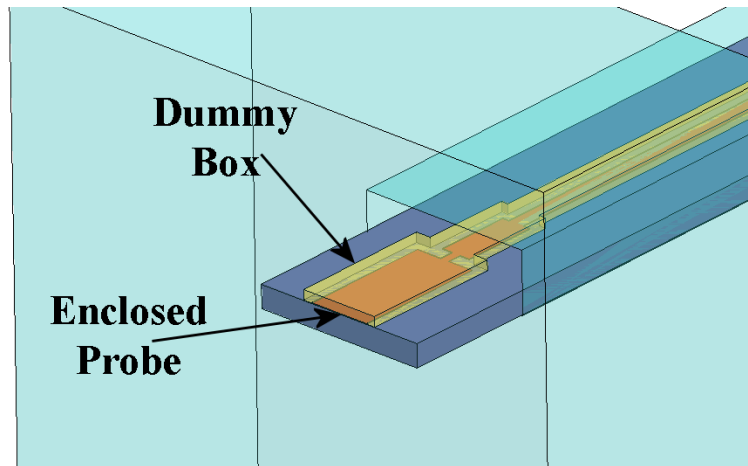


FIGURE 3.35: The printed microstrip line and the probe are enclosed in a fictitious geometry called "dummy object" aiming to increase the mesh refinement locally around the probe.

3.6.1 Elevated E-plane Probe

Fundamental aspects of transversal transitions are highlighted in the previous section. Width and length of the probe and its relative distance from the waveguide back-short are tuned to achieve a small variation of the probe input impedance over the G-band. There is a limitation in this approach which is the substrate material employed. The achievable range of values for the probe input impedance are dictated by the dielectric constant and thickness of the substrate employed.

The use of GaAs material is part of the design specifications for an integrated transition, whereas its thickness is limited by the cut-off frequency of possible propagating higher order modes along the microstrip as discussed in 3.6.

An investigation is carried out to identify options to change the probe input impedance without changing substrate type or thickness.

It is possible to modify the interaction between probe and GaAs material if the probe is detached and air-lifted over the substrate realizing an elevated structure. This geometry can still provide good EM coupling between waveguide and probe which still has the same length.

The result is that new capacitive values for the interaction between probe and opposite waveguide wall can be achieved. Furthermore, the elevated probe results electrically shorter as the composite material of air and GaAs presents a lower effective dielectric constant ϵ_{eff} resulting in a smaller impedance transformation.

The structure of the *Elevated E-plane Probe* is illustrated in Figure 3.36(a) where the probe projects into the waveguide. The elevated probe is supported by metal posts which land on the substrate, Figure 3.36(b), and the height H of the posts, Figure 3.36(c), represents a new tuning variable added to the design procedure.

Design parameters are optimized to $W=100\mu m$, $D=280\mu m$ and $L=500\mu m$, as in Figure 3.37(a). The probe supports have dimensions $P_L = 10\mu m$ and $P_W = 15\mu m$ and have a separation distance $S = 130\mu m$ from each other as indicated in Figure 3.37(b)-(c). The microstrip signal line has a width $M = 32\mu m$. The effect on the S-parameters due to the elevation height of the probe is shown in Figure 3.38 for S_{11} and in Figure 3.39 for S_{21} . By increasing the height of the probe, better impedance matching can be achieved confirming the influence of this parameter on the performance of the transition. The Smith Chart plot of the S_{11} at the waveguide input reveals how the impedance varies with increasing the probe height H . Figure 3.40 shows that for values $H = 2\mu m - 6\mu m$ the impedance approaches the center of the Smith Chart delivering better impedance matching. The Smith Chart is normalized to the waveguide impedance. To confirm the effective tuning value of the probe elevation, Figure 3.41 shows how, at the microstrip input, the S_{11} changes with the height of the elevated structure. In this case the Smith Chart is normalized to 50Ω . It is worth noting that the elevation of the probe increases

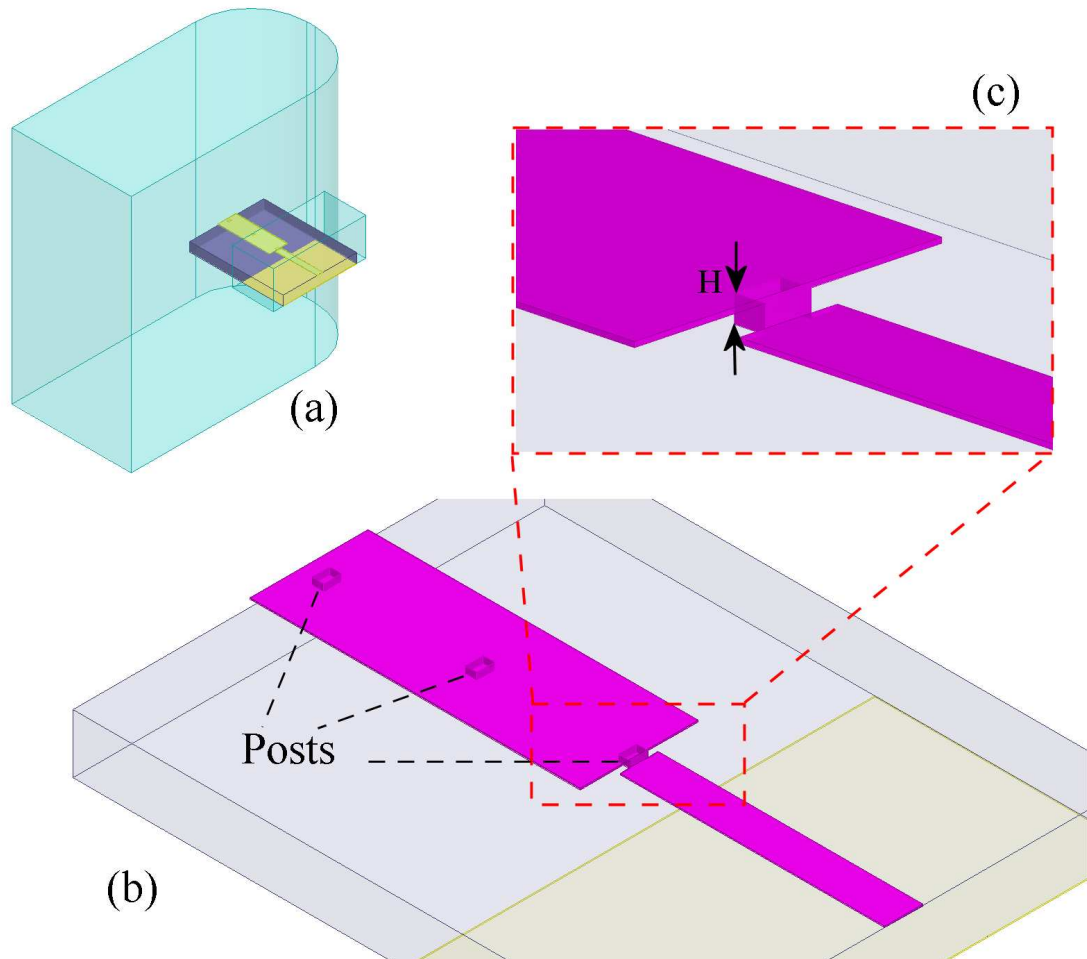


FIGURE 3.36: Elevated probe used in transversal transition (a). The probe is elevated from the substrate and supported by three metal posts (b). One of the post works as contact pin between the elevated probe and the microstrip (c). All the posts have the same height H .

the inductance of the transition by moving the S_{11} plot towards the upper half of the Smith Chart. For completeness the S-parameters plot is presented in Figure 3.42 for an elevation height $H = 6\mu m$. The design is optimized for low reflection at 183GHz, critical frequency as it is the center of the attenuation band of the water vapour in the G-band. The Elevated E-Plane probe transition is designed in back-to-back configuration for fabrication and further measurements. Figure 3.43(a)-(b) show the two cascaded transitions separated by 3mm of microstrip line and the E-field plot illustrates the coupling mechanism very similar to Figure 3.34.

A custom meshing strategy is also used in the design of the Elevated E-plane probe. The *dummy objects* technique was employed and an additional volumetric geometry is added around the elevated probe in order to increase the mesh refinement. Figure 3.44 shows the fictitious object at the location of the probe.

The transition is housed into a waveguide split-block which works as a device carrier for measurements. Hence, the back-to-back transitions structure is also simulated with the

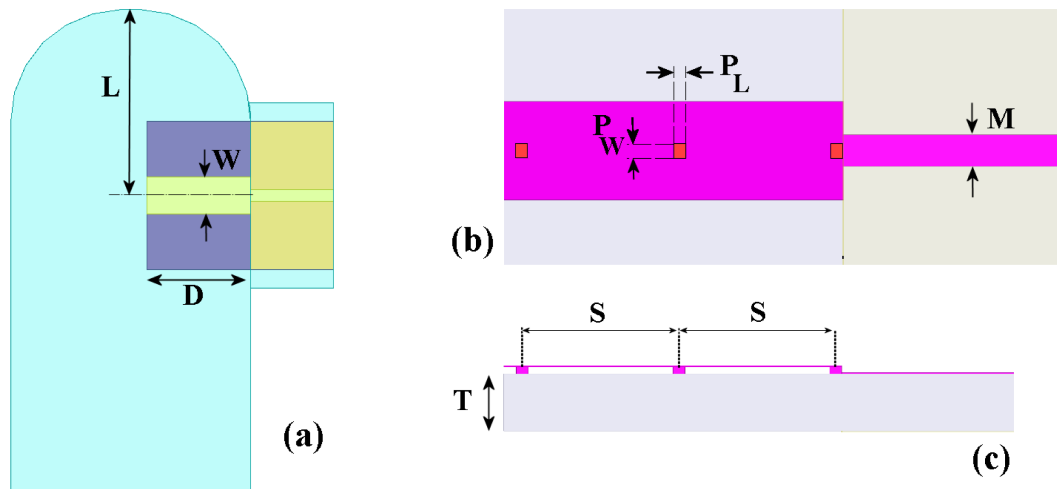


FIGURE 3.37: The transition has optimized parameters $L=500\mu\text{m}$ $W=100\mu\text{m}$ and $D=280\mu\text{m}$ (a). Supporting posts have dimensions $P_W=15\mu\text{m}$ and $P_L=10\mu\text{m}$ (b). The posts are spaced by $S=130\mu\text{m}$ (c). Thickness of the GaAs substrate is $T=50\mu\text{m}$.

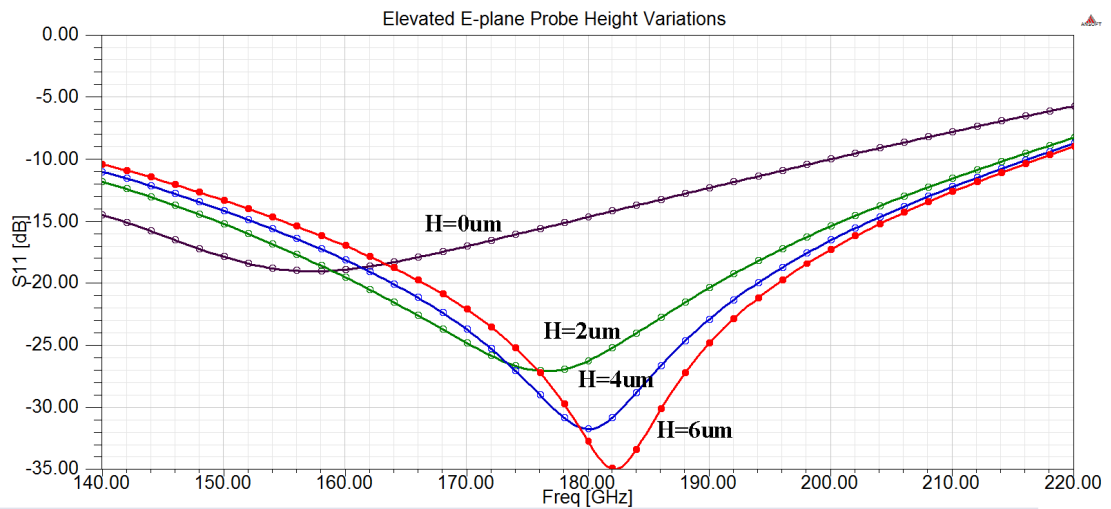


FIGURE 3.38: S_{11} parameter of the waveguide to microstrip transition using Elevated E-plane Probe. Probe height is increased from $H=0\mu\text{m}$ to $H=6\mu\text{m}$ improving the reflection level of the transition. The elevation H represents a new optimizing parameter for the transversal transition.

waveguide bends of the housing (see Section 4.8). The final model and E-field distribution at 183GHz is shown in Figure 3.43(c)-(d).

The simulated S-parameters of the back-to-back structure accounting the housing is illustrated in Figure 3.45 where the S_{11} presents the lowest reflection level at 183GHz.

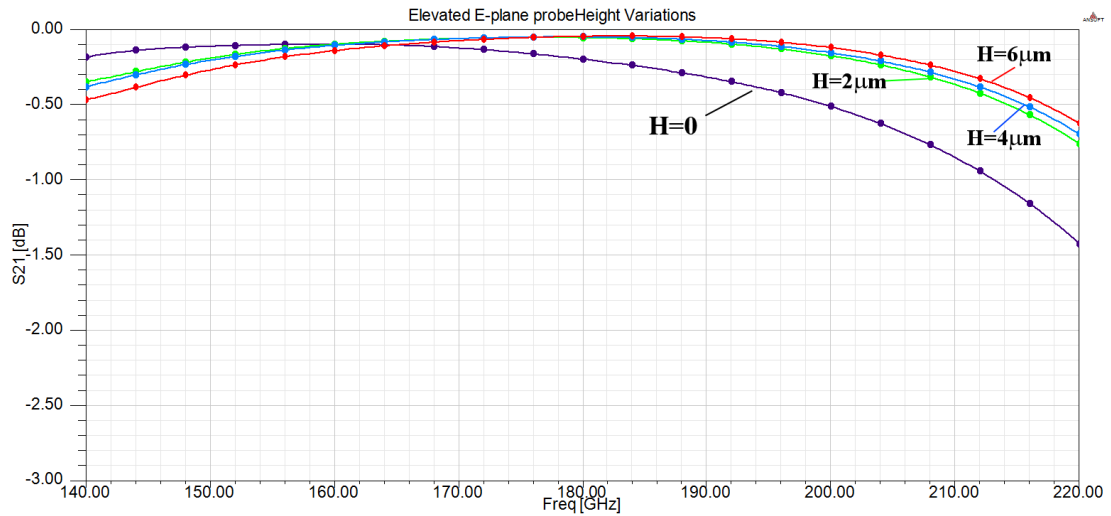


FIGURE 3.39: S_{21} parameter of the waveguide to microstrip transition using Elevated E-plane Probe. Probe height is increased from $H=0\mu\text{m}$ to $H=6\mu\text{m}$ improving the transmission of the transition. The elevation H represents a new optimizing parameter for the transversal transition.

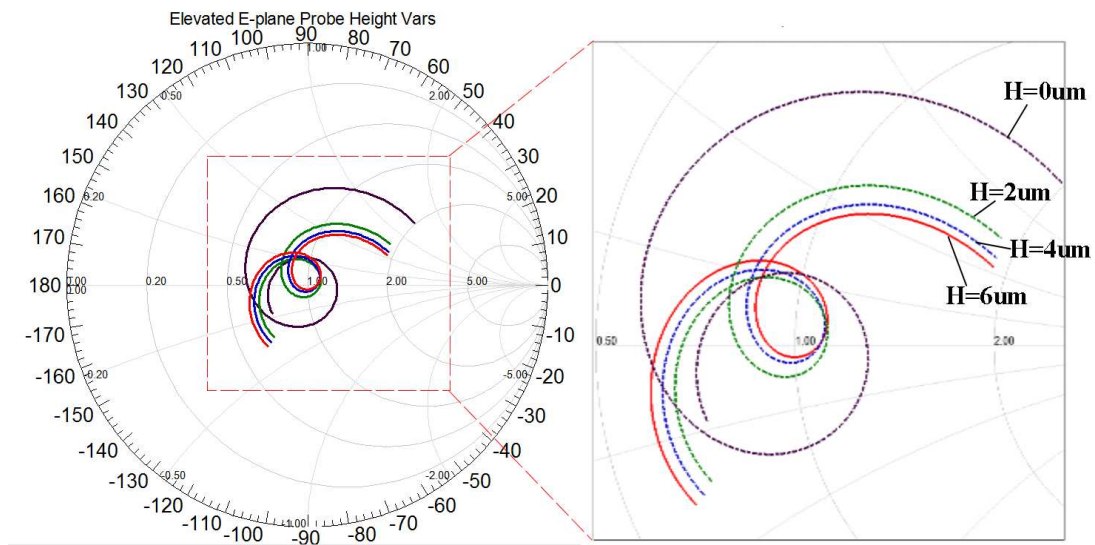


FIGURE 3.40: The effect of increasing the elevation height of the probe from $H=0\mu\text{m}$ to $H=6\mu\text{m}$ constrains the impedance of the transition toward the center of the Smith Chart resulting in improved impedance matching.

3.7 Conclusions

The use of HFSS as a simulation tool has been discussed focusing on the design of waveguide to microstrip transitions. Design specifications and considerations narrow down the variety of possible geometries to adopt at G-band frequencies based on restrictions from substrate material and fabrication processes available. Examples of transitions using antipodal fin-lines and printed dipole antennas are presented and the advantages and disadvantages discussed. Transversal transitions are the preferred option for use in

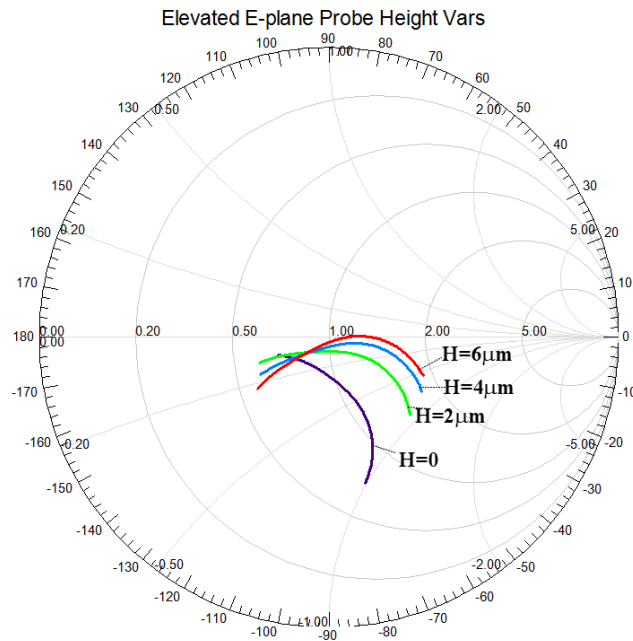


FIGURE 3.41: S_{11} at the microstrip port. The effect of increasing the elevation height of the probe from $H=0\mu\text{m}$ to $H=6\mu\text{m}$ brings the impedance loci closer to the center of the Smith Chart, which is normalized to 50Ω .

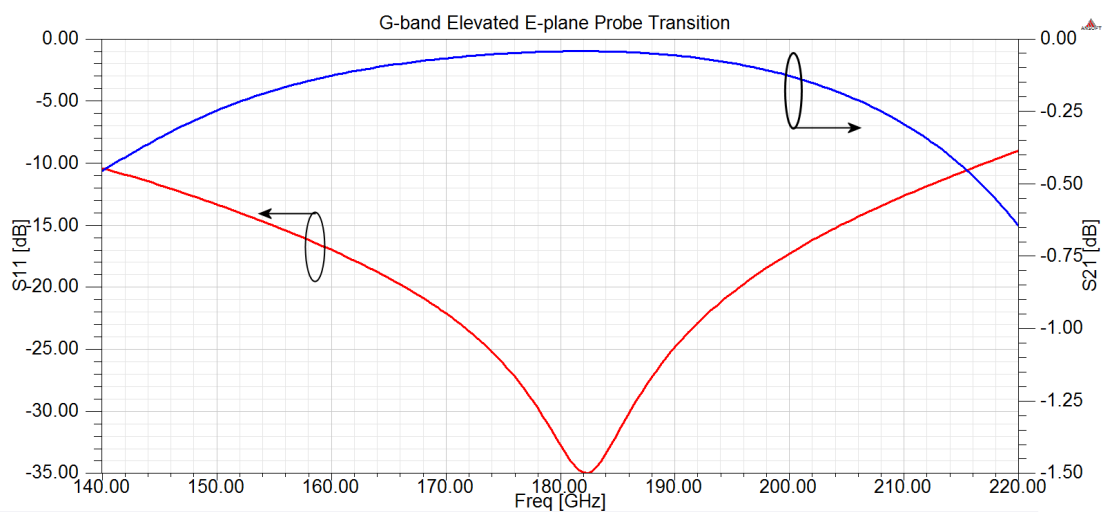


FIGURE 3.42: S-parameters of the single waveguide to microstrip transition using Elevated E-plane probe. The transition is optimized for $f=183\text{GHz}$ and the reflection level is below -10dB for nearly the entire G-band.

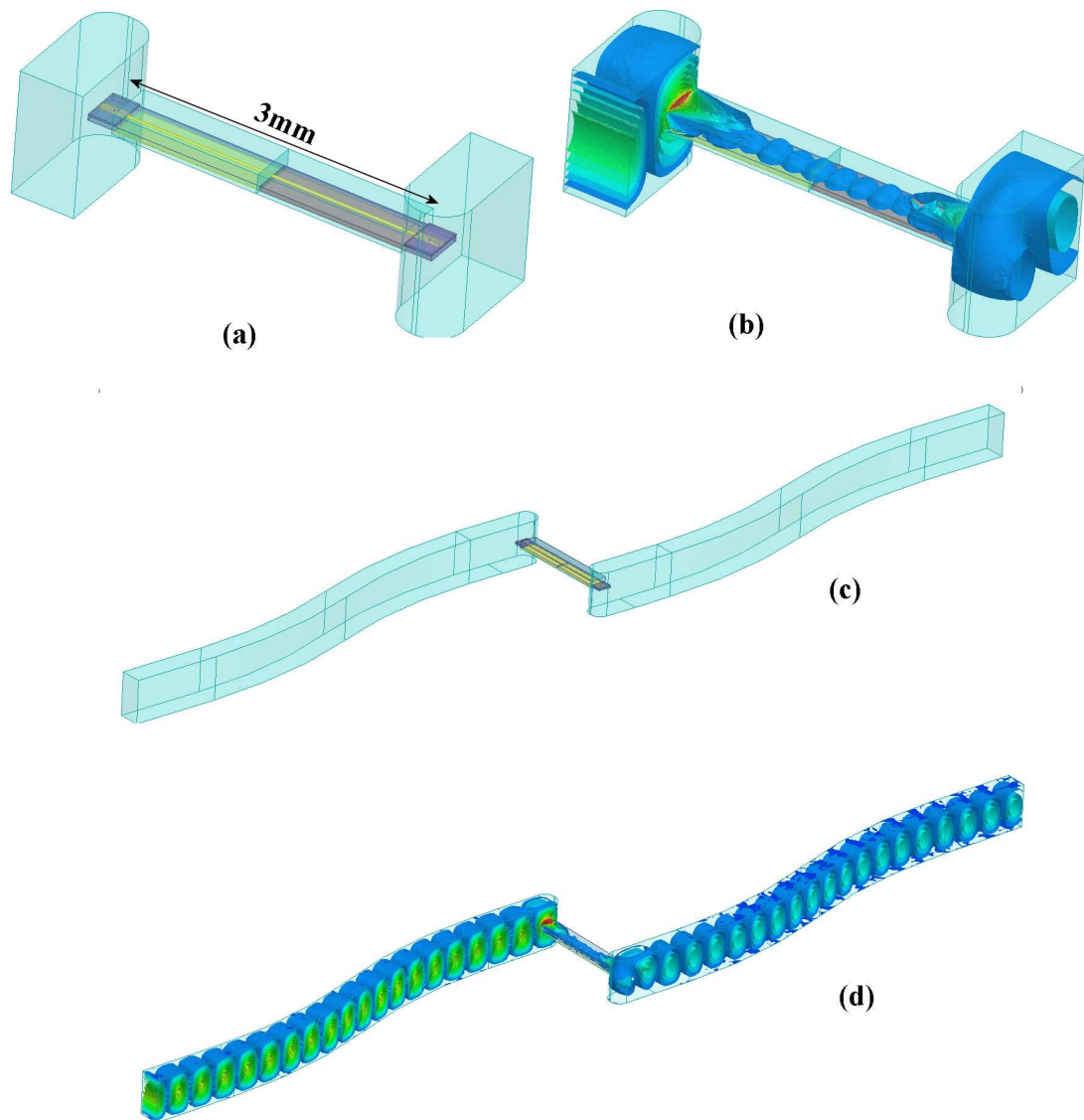


FIGURE 3.43: Two transitions using Elevated E-plane Probes are cascaded in back-to-back configuration and separated by a microstrip 3mm long (a). E-field distribution shows conversions between TE_{10} waveguide mode and microstrip mode (b). The back-to-back structure is modeled with two waveguide bends (c) as input and output of the transition in order to take into account the metal split-block used to house the transitions with relative E-field distribution along the structure (d).

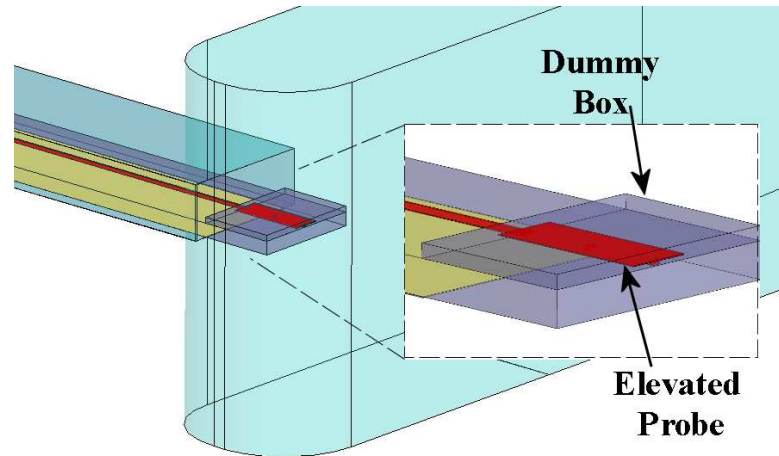


FIGURE 3.44: The additional geometry called "dummy object" aims to increase the mesh refinement around the Elevated E-plane probe.

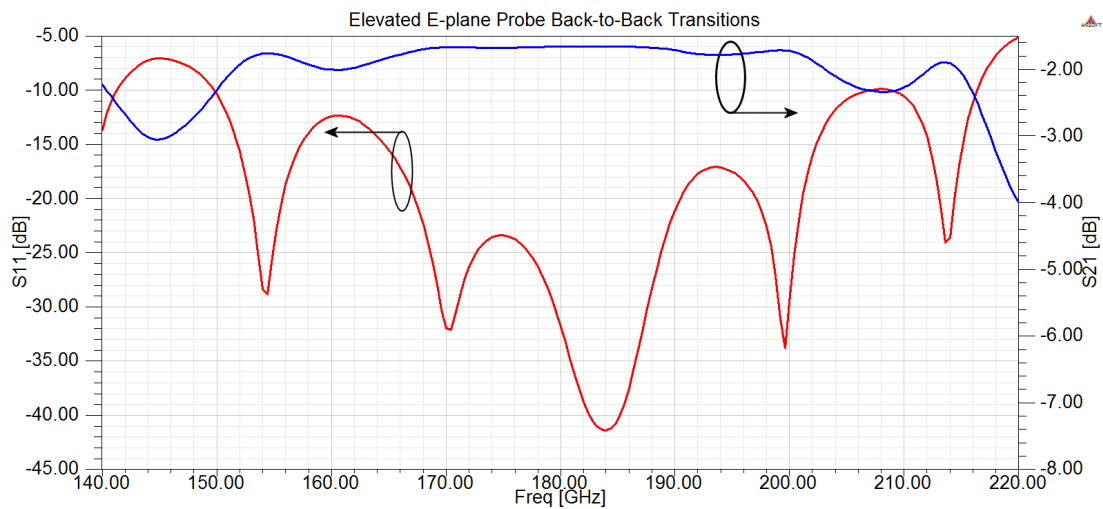


FIGURE 3.45: S-parameters of two waveguide to microstrip transitions using Elevated E-plane probe in back-to-back configuration accounting the reflections due to the input/output waveguide bends of the housing. The performance is optimized for $f=183\text{GHz}$.

the G-band and an example of a broad band transition is designed highlighting the key parameters to optimize for a satisfactory result.

The E-plane probe implemented in the transversal transition is presented as a *novel* structure together with the concept of probe elevation height as an additional parameter to optimize. Performances are illustrated in terms of S-parameters to compare with measurement results. The transversal broadband transition and E-plane probe transitions are both selected with reference to fabrication discussed in the next Chapter.

Chapter 4

Fabrication

4.1 Introduction

This Chapter is dedicated to the processes and procedures used to fabricate the transversal waveguide to microstrip transitions described in Chapter 3.

The first sections present an overview of the main tools used in the MMIC thin film processing at the University of Glasgow. Photolithography, E-beam lithography and metal evaporation systems are described. The main part of the chapter illustrates the procedures followed to define printed lines and elevated structures. The procedures used to fabricate the Elevated E-plane Probe and elevated lines are an extension of the III-V air-bridges for MMIC technology. Finally details are presented of substrate handling for material thinning and the processing tools used.

The mechanical manufacturing of G-band rectangular waveguides in split-block configuration is then detailed, exposing the fundamental reason for this choice. The design of the split-block housing used for testing the waveguide to microstrip transitions is also presented along with results of the fabrication.

The chapter ends with the procedures followed including alignment and bonding of the substrate supporting the probes and the split-block housing, detailing waveguide profiles and waveguide to microstrip junctions.

4.2 GaAs MMIC Processes

The Elevated E-plane probe transition described in Chapter 3 will be fabricated on SI-GaAs material. The fabrication exploits in-house Thin-film fabrication technology developed over the last 20 years at the University of Glasgow which is now housed in the James Watt Nanofabrication Centre (JWNC) including several hundreds of squares

meters of A-class Clean Room facilities.

Thin-film technology involves processes such as photolithography and E-Beam Lithography (EBL) to define patterns onto substrate materials covered with light-sensitive chemical compounds called *resist*. Vacuum metal film evaporation is used instead to deposit layers once the resist has been exposed and developed. The following sections give an overview of the lithographic and metal deposition processes and the machines used for the present project.

4.2.1 Photolithography

The photolithography process involves a preliminary preparation step in which a layer of *photo-resist* material is spread out onto the surface of a substrate by mechanical spinning. The photo-resist layer thickness depends on its viscosity and rotation speed used. The substrate is then baked in oven in order to harden and increase the adhesion of the resist to the substrate surface.

The pattern transfer onto the substrate is achieved using pre-defined quartz masks. Technical personnel at JWNC are in charge of this fabrication. A Chrome (Cr) covered quartz plate is E-beam patterned (see section 4.2.3) and developed. The Cr is then etched away and the quartz cleaned from the residual E-beam resist, leaving only the pattern to be used in the photolithographic alignment. This mask generally called a *master* is used to fabricate photolithographic copies on ferric oxide (Fe_2O_3) coated quartz, which is less expensive; their use prevents damage to the more expensive master.

The mask and coated substrate are mounted in the MA6 Mask Aligner, Figure 4.1 which is located in the JWNC.

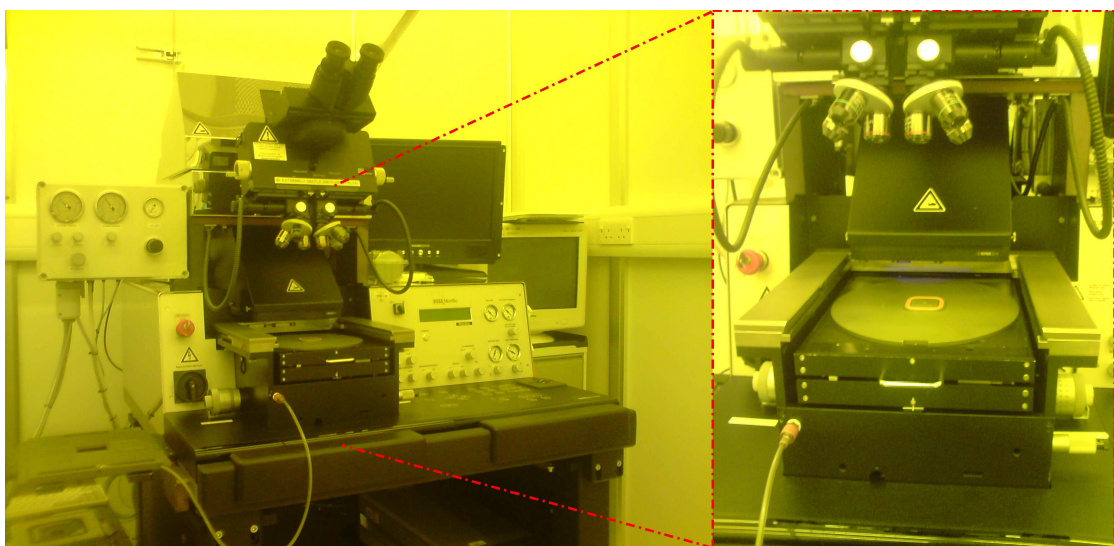


FIGURE 4.1: MA6 Mask Aligner (left) used for photolithography at the University of Glasgow in the JWNC. View of the sample holder vacuum system and optics for alignment (right).

A column vacuum system is used to bring mask and substrate in proximity or in contact to perform alignment procedures. UV light is then vertically focused onto the mask by a system of lenses.

The light-sensitive layer of resist is exposed to the UV light through the mask "windows" for a determined period of time depending on type and thickness of resist. The substrate is then removed from the MA6 and immersed in appropriate developer for a period of time depending on resist type.

It is possible to use positive or negative resist which has different chemical compounds. Exposing and developing a positive resist dissolve the areas exposed to the UV light, which breaks the chemical bonds of the resist material and leaves it vulnerable to the developer. Negative resist works in a complementary way. The UV light passes through the open windows on the mask and exposes the resist material, *cross-linking* it. In this case, the result is that the areas exposed to the UV light are resistant to developer, whereas the rest of the resist dissolves. The developed substrate is, then, ready for metal evaporation. For this project, two types of positive resist are used.

MA6 also allows one to perform a back-patterning of a substrate material, during which it is possible to align the features of the two opposite surfaces together. This procedure is called *back alignment* and it differs from the top alignment since it is performed by using a system of lenses connected to a PC, instead of microscope lenses as for top alignment.

4.2.2 Metal Deposition

Deposition of metals is carried out by using two evaporation systems called Plassys I and Plassys II, Figure 4.2; they are Electron Beam Evaporators (EBE) and consist of a vacuum chamber which is generally used with a pressure lower than $4 \times 10^{-6} Torr$. The metals to be evaporated are located in a number of crucibles forming a rotatory carousel. A high voltage Electron Beam, focused on one crucible, heats the metal locally to a temperature at which it evaporates, as illustrated in Figure 4.3. Above the crucible, there is a system of two shutters and a piezoelectric crystal resonator. These elements provide a constant and uniform rate of metal deposition on the substrate.

When the metal starts to evaporate, the lower shutter opens leaving the evaporated metal to hit the crystal resonator that measures the evaporation rate. Once a constant rate is achieved, the second shutter opens leaving the metal to be deposited on the target where the substrate is mounted with clamps. Both evaporators are remotely controlled by a personal computer where a list of recipes are stored and available to be used. Each recipe controls the whole deposition process and contains settings information as crucible number and content, melting current threshold, expected rate and information

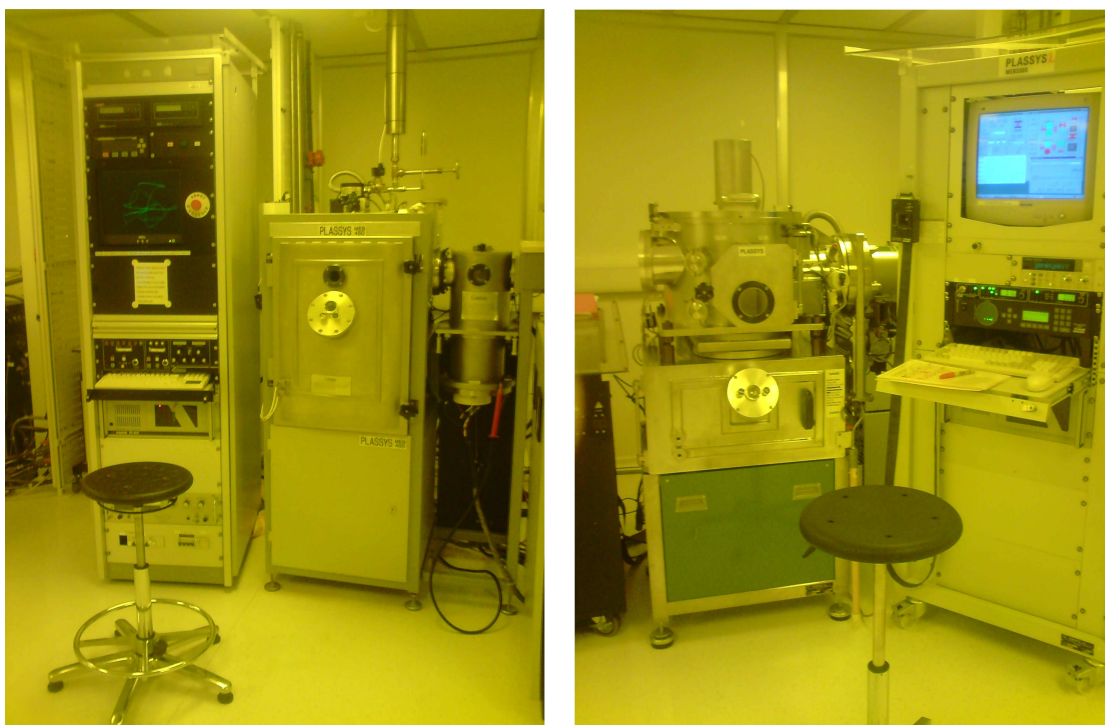


FIGURE 4.2: Plassys I (left) and Plassys II (right), used for the metals evaporation processes at the JWNC.

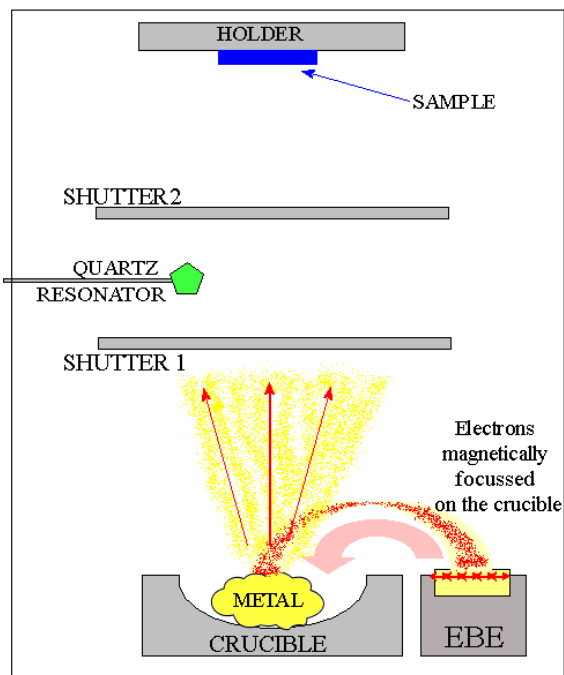


FIGURE 4.3: EBE system. The electron-beam is focused on the crucible and melts the metal. A system of two shutters allows the evaporated metals to hit the target holder where the substrate is located. A quartz resonator monitors the evaporation rate in real-time.

on rotation of the target. This type of system allows the deposition of more layers of metals in a single run without bringing the chamber to room pressure reducing possible contamination.

After the recipe is terminated the pressure inside the chamber increases to room pressure in order to unload the substrate material from the target for further processing.

4.2.3 Electron Beam Lithography (EBL)

The EBL is the method used to directly pattern resist on a substrate without using pre-patterned masks. The advantages of this method are better precision and aberration-free exposure.

A schematic of a typical EBL system is shown in Figure 4.4, where it is possible to distinguish the two main parts: the column and the chamber. At the top of the column, there is a zirconium oxide-coated tungsten cathode tip which is heated to provide energy to electrons to overcome their work function barrier and allowing thermal field emitter (TFE) process to take place.

The electrons are then accelerated, aligned and focused by a series of lens and magnets

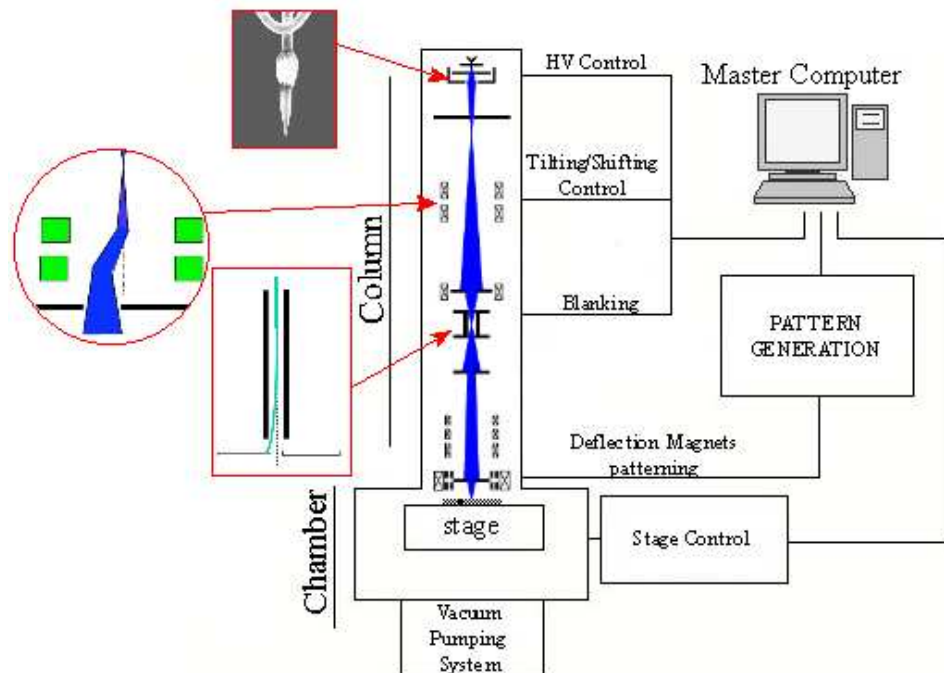


FIGURE 4.4: VB6 EBL column. The pattern definition is computer controlled. Stage movement and beam deflections are used during substrate exposure.

located along the column. The magnets are remotely controlled by a computer and they are used to tilt and shift the electrons beam if required. Some stages are dedicated to blank the electrons beam when not required or during stage movements. At the bottom

of the column there is an additional magnetic system, which is computer controlled and dedicated to the pattern definition [67]. For the work presented in this thesis a Leica Electron Beam Pattern Generator 5 (EBPG5) is used for the exposure of the photolithographic masks described in Section 4.2.1 and a Vistec VB6 UHR-EWF e-beam tool is used to pattern directly the substrate material.

As mentioned above, the EBL method benefits from better accuracy when compared to the traditional Photolithographic process which is limited to $1\text{-}3\mu\text{m}$ due to optical diffractions occurring at mask level. However, the EBL software needs several parameters to be set in order to properly define a pattern and this is done along with the pattern generation and upload process to the EBL system.

Pattern Definition

A few steps are required in order to convert a determined geometry into a readable format for the EBL system.

A designed pattern is exported as Graphic Data System II (GDSII) format from a layout software as L-Edit or ADS from Agilent. The file is then read and fractured by a Unix based software called CATS from Synopsys.

At this stage, each area of the pattern is divided into trapezioids which correspond to each region of exposure of the Electron beam. Information such as *resolution*, *pattern extension*, *layer* and *proximity correction* are set and stored in an intermediate file. Proximity correction accounts for scattered secondary electrons which affect the areas adjacent to the beam foot print. This correction is applied pre-loading an appropriate file before the fracture of the pattern. Proximity correction depends on substrate material and resist type and thickness. A set of proximity files is provided as library and they are ready to be used for different requirements.

The resulting fractured file containing all of this information is then read using an application called BELLE, created by Prof. Stephen Thoms at the University of Glasgow. With BELLE it is possible to instruct the EBL system with parameters such as *dose*, *current*, *spot size* and *beam step size (BSS)* of the electron beam. Dimensions and type of substrate material are also entered at this stage. An optional *alignment* set of parameters can be entered in case of exposing a second pattern on the substrate when desired. Once all the settings are entered the resulting file is then saved and transferred to the EBL system.

The relative sample material is loaded into the system and the electron-beam scans row by row the trapezia composing the pattern following a determined *beam step size* as result of previous settings. The pattern shape is then a discrete set of exposed pixels as illustrated in Figure 4.5. The general rule of thumb for properly setting the pattern writing are:

- $Beam\ spot\ size = \frac{1}{5} \cdot (minimum\ feature\ size)$
- $BSS = n \cdot (resolution)$, $n \in \mathbb{N}$
- $BSS \leq BeamSpotSize$

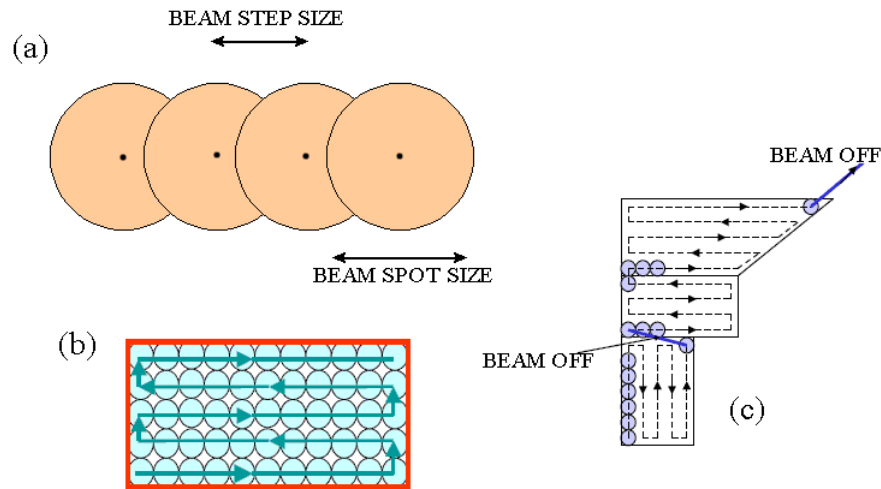


FIGURE 4.5: Beam Step Size (BSS) is generally smaller than the beam spot-size (a) for a continuous and uniform exposure of the resist. A fractured shape is continuously scanned by the e-beam (b). E-beam blanking happens when there is a jump from one fractured shape to the other (c).

Resist Development

Generally, E-beam resists are high molecular-weight polymers with long molecular chains. The resist material is spin-coated on the surface of the substrate material and then oven backed to harden and to allow the solvent to evaporate. During the exposure of the coated substrate, the electron beam breaks the long polymer chains reducing the average molecular weight. Consequently, the exposed areas become vulnerable to developer solvent which washes them away leaving the desired pattern in the e-beam resist coating. Resist thickness, type and concentration in conjunction with e-beam dose strongly affect the development process whose temperature and duration are critical parameters.

For a determined resist type and exposure dose, thicker coating involves longer developing time, whilst higher temperature reduces it enhancing the developer action. This could compromise adjacent areas resulting in uncontrolled pattern enlargement commonly called *overdeveloping*. Hence, for a correct pattern, developing time and temperature have to be calibrated relatively to selected parameters for the exposure process.

More resist layers can be spun consecutively and exposed at the same e-beam dose.

Frequently, these layers have different concentrations, hence their developments happen with different speeds. The effect can be exploited to create an *under-cut* profile of the resist easing further *lift-off* processing as highlighted in Section 4.4.2.

For this project, polymethyl methacrylate (PMMA) [68] with two different concentration is used for the substrate resist coating and methyl isobutyl ketone (MIBK) [69] is used as its developer solvent.

4.3 Fabrication of Transitions

In this section the clean-room thin film processing used to fabricate the MMIC-integrable rectangular waveguide to microstrip transition described in Chapter 3 is presented. The whole process can be divided into two main sub-processes. The first relates to the fabrication of the on-surface part of the devices, the second consists of manufacturing steps to realize the elevated or *air-lifted* parts.

The simulated structure, without the rectangular waveguides and housing, can be directly exported in GDSII format from HFSS12, assigning separate layers respectively to planar lines, supporting posts, elevated metal parts and back-side grounds. The single device consists of a back-to-back probes architecture. The resulting file can then be imported into a layout software application and for the present case it is used a package offered by ADS2009 from Agilent called Momentum. This is generally used for MMIC design and simulation purposes, but its drawing features and ease of use provide an excellent environment for the final layout.

The single device is then repeated horizontally forming an array then framed into a cell also comprising of alignment marks and scribing rails as illustrated in Figure 4.6. The cell size is chosen to be $10 \times 10 \text{mm}^2$. Markers, printed lines, metal posts, elevated parts and back-side grounds are all located on different layers in order to pass them to their relative processes separately. Markers and lines are defined with EBL and they are part of the first fabrication level, whilst metal posts, elevated parts and grounds are processed with photolithography. Posts and elevated parts represent the second fabrication level.

4.4 First Level Fabrication

This section describes the fabrication steps to define markers and the first level of our devices. The material used is a 4 inch wafer of semi-insulated Gallium Arsenide (SI-GaAs) with $630 \mu\text{m}$ initial thickness. A preliminary *scribe and cleave* operation is performed to divide the whole wafer in substrate samples of 1in^2 each. With these dimensions it

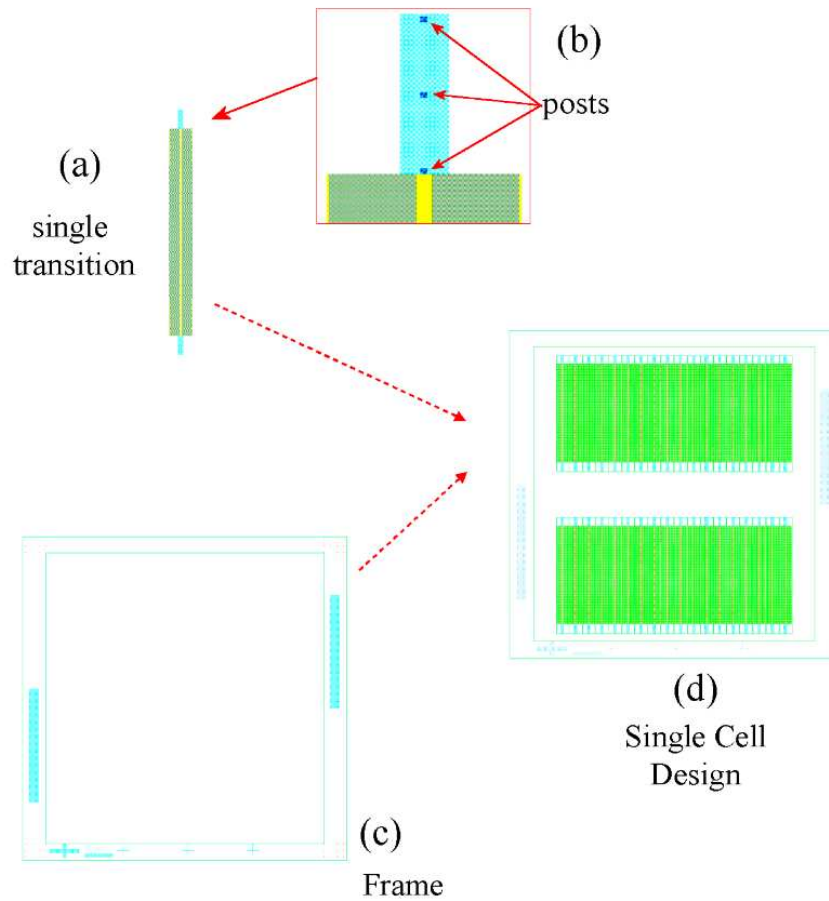


FIGURE 4.6: A single transitions device (a) including the metal posts layer (b) is repeated to form arrays then framed (d) into a cell defined by markers features (c).

is possible to allocate 4 cells of $10 \times 10 \text{mm}^2$ and to minimize possible damage during substrate handling in the last fabrication steps.

4.4.1 Substrate Preparation

Before any process the single cleaved substrate sample undergoes a cleaning process in ultrasonic bath with methanol, acetone and isopropyl alcohol (IPA) consecutively for the duration of 5 mins each followed by a Nitrogen (N_2) blow dry. This process removes possible stains and dust from the surface of the sample and reduces oxidation.

The sample is spin-coated with a layer of PMMA(2010) at 3000 rad/min followed by an oven-baking process of 1hr at 120°C . A second layer of PMMA(2041) is spun on top of the first layer at 5000 rad/min and a second oven-baking process of 2hrs at the same temperature takes place. The second PMMA layer has lower concentration and higher molecular weight resist solution. The sample is then ready to be loaded into the EBL

vacuum chamber and exposed to define the pattern previously generated by the software fracturing process described in Section 4.2.3.

4.4.2 E-beam Exposure, Development and Lift-off

After the EBL exposure, the sample is developed in a solution of IPA:MIBK (2:1) at a temperature of 23°C for 1min and 30s and then washed in *reverse osmosis* (RO) water. The two PMMA layers have different concentrations, hence they develop with different speeds. The top layer being less sensitive to the e-beam than the lower layer results in the development of a process known as an *under-cut* profile as illustrated in Figure 4.7.

The aim of this particular profile is to ease the *lift-off* procedure after the metals

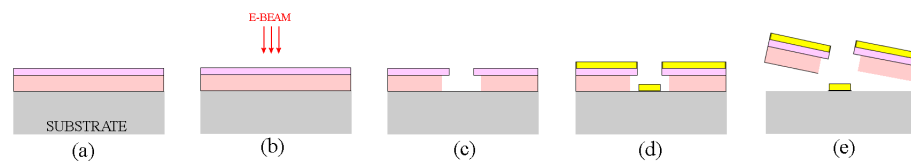


FIGURE 4.7: EBL exposure process. The substrate is covered with two layers of different e-beam resist (a). Exposure (b) allows the development out of an under-cut profile area in the resist (c). Metal evaporation (d) and lift-off leave the printed trace on the substrate (e).

evaporation.

The step between developed regions and residual resist is measured using a Dektak profilometer, results are shown in Figure 4.8. After development, a de-oxidizing process in a solution of Hydrochloric acid (HCl) and RO water (1:4) for 30s is the preliminary operation for the metals evaporation process described in Section 4.2.2.

For the first pattern, representing markers and scribing rail layers, a film of 50nm of *Nichrome* (*NiCr*) and a film of 50nm of *gold* (*Au*) are evaporated consecutively using EBE. Once the sample is unloaded from the EBE tool, it is left in acetone at a temperature of 50°C for at least 2hrs in order for the acetone to penetrate and dissolve the undeveloped layers of PMMA below the metals film. This is the *lift-off* procedure. The sample is then washed in IPA and dried with a N_2 gun, leaving the metal pattern on the GaAs surface. The process is illustrated in Figure 4.7.

The procedures from Section 4.4.1 to Section 4.4.2 are repeated again, after that the pattern of the planar lines and relative alignment data are uploaded to the EBL tool. The only difference in this repetition resides in the metal evaporation of a bi-layer of 50nm of NiCr and $1.2\mu\text{m}$ of Au.

The sample is then ready to undergo the process for the second level that constitutes supporting posts and elevated structures.

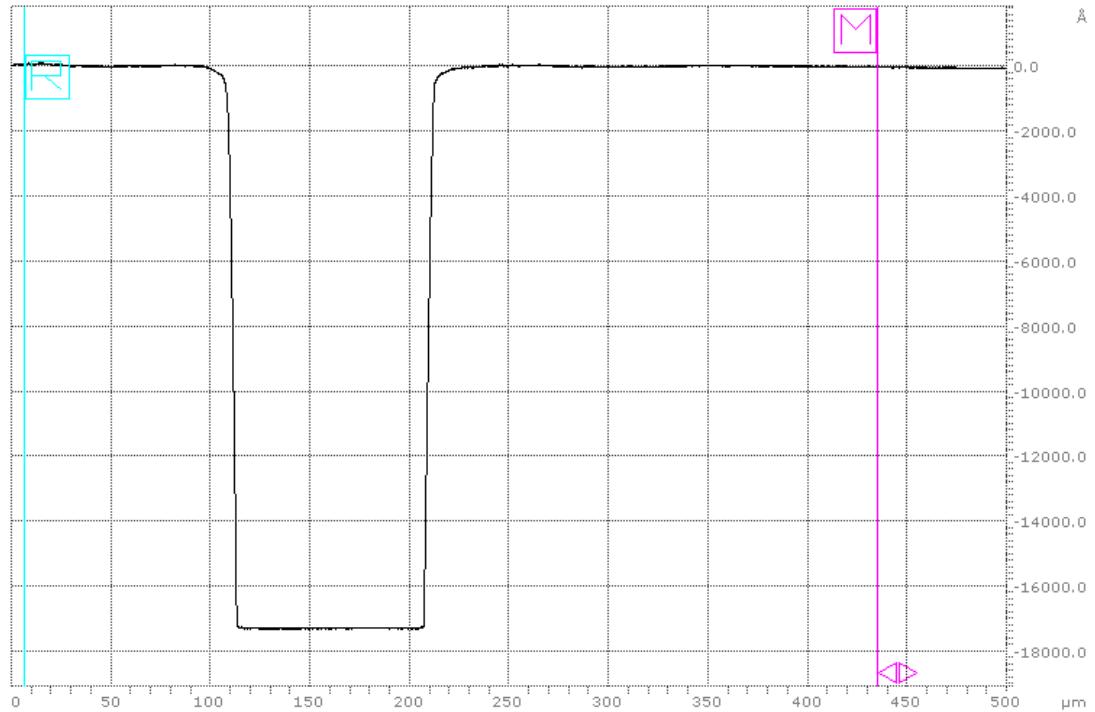


FIGURE 4.8: Depth of the developed area measured with Dektak profilometer. The thickness of the e-beam resist is $1.72\mu\text{m}$.

4.5 Second Level Fabrication

Supports and air-lifted structures are fabricated using an enhancement of the standard III-V *air-bridges* process based on photolithographic techniques.

Two photolithographic quartz ferrite-coated masks are prepared and used in the exposure of supports and metal tracks layers respectively.

4.5.1 Fabrication of Elevated Structures

The positive photoresist AZ4562 from Clariant[©] [70] is used to reach resist thickness of $5.5\mu\text{m}$ with a single spin-coating operation. This type of resist can be used for a wide range of thicknesses depending on spin speeds. Table 4.1 shows their nominal and measured values.

The fabrication of the elevated structures starts by spin-coating a layer of AZ4562 on the substrate at $4000\text{rad}/\text{min}$ for 30s and then oven baked at 90° for 30mins. The sample is then ready to undergo a first photolithographic exposure for the support elements followed by a development process using AZ400K [71] in a solution of 1:4 (AZ400K:H₂O) for 2mins. Being a critical fabrication steps, inspection with the optical microscope is necessary to validate the effective development of the areas for supports. The O₂ cleaning process using a dry etch machine can further remove an apparent invisible coating

TABLE 4.1: Nominal and measured values of thickness for different spin speeds with AZ4562 positive photoresist.

Nominal Thickness [70](μm)	Spin speed (rad/min)	Measured Thickness (μm)
8.77	2000	8.1
7.16	3000	6.2
6.20	4000	5.5
5.55	5000	N/A
5.06	6000	3.7

of undeveloped resist without compromising dramatically the profile shape of the resist-free regions.

At this stage a preliminary de-oxidization step, as described in Section 4.4.2 precedes the deposition of a *sacrificial* metal layer, commonly called "*seed layer*", by EBE vacuum evaporation. The layer is constituted of 50nm of *titanium* (*Ti*) and 50nm of Au.

The seed layer aims to protect the thick layer of unexposed AZ4562 and works as reference layer for a further photolithographic step. This layer also provides electrical contact for gold plating process.

The elevated metal tracks are defined by using a thin layer of positive photoresist S1818 from Microposit[©] [72]. This is spun onto the seed layer at 3000 rad/min for 30s and then the substrate sample is oven-baked at 90° for 15mins. Photolithographic exposure of the "*tracks*" areas using their relative quartz mask is followed by further development using a solution 1:1 of *Microposit* [73] and RO water for 1min and 30s that clears the areas interested by the electroplating process.

4.5.2 Electroplating Process

The final metal structure is grown onto the seed layer with a process of Au electroplating. The substrate sample is attached to a copper plate using hot wax and appropriate electric contacts between the seed layer and the copper plate are realized using silver epoxy. The set up for the electroplating process is illustrated in Figure 4.10, where sample and copper plate represent the *cathode* for the plating whilst a platinum cover metal grid works as *anode*. The process is carried out at the temperature of 50°C in a gold plating solution, previously prepared by JWNC personnel. During the process, the solution is stirred with a paddle at 100rad/min to provide uniform plating rate in time.

The solution allows an ion current density of 0.013A/mm² with which the cathode is gold plated for 20 mins depositing 2 μm of gold onto the seed layer in the resist-free areas [74].

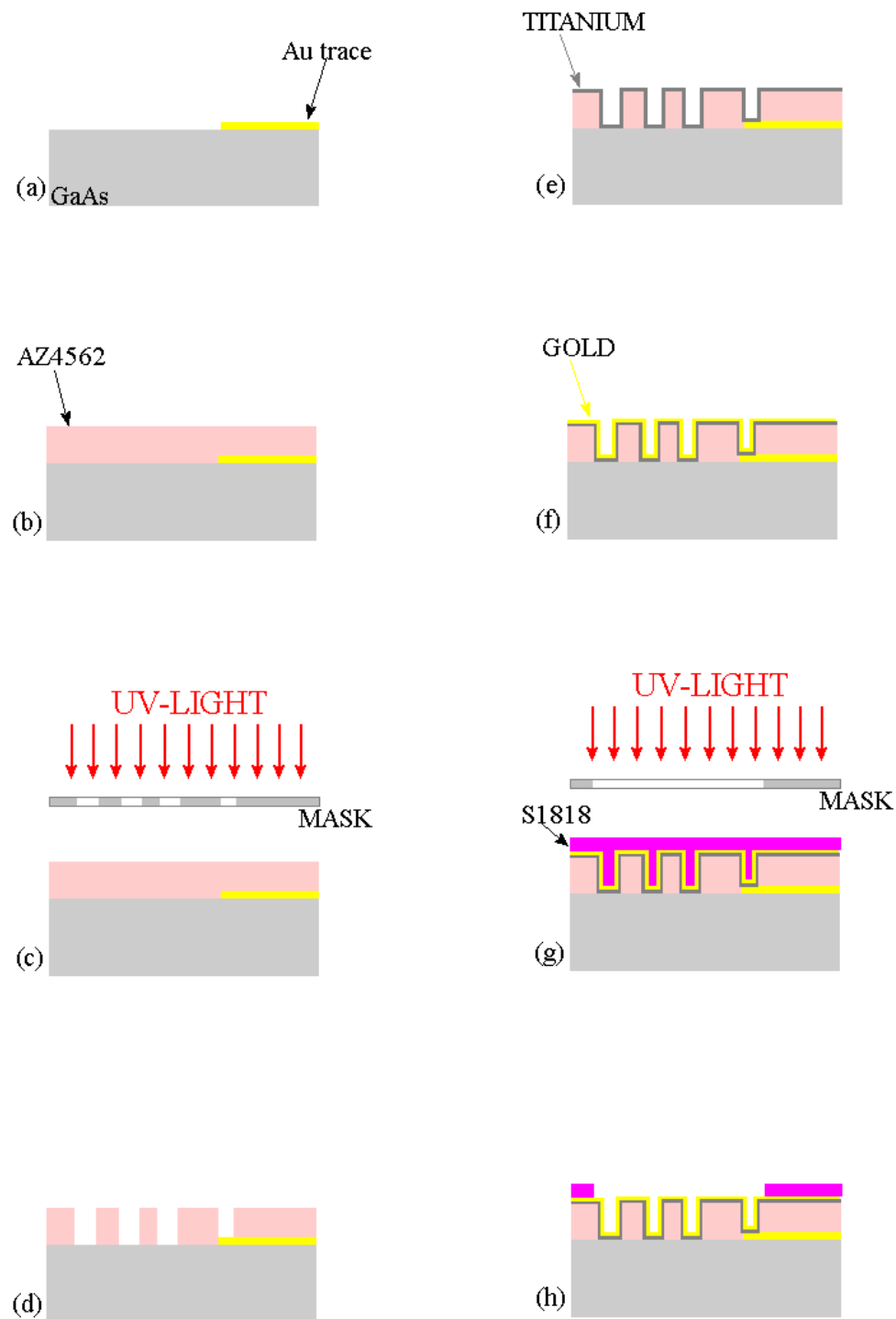


FIGURE 4.9: Substrate with printed lines (a) is covered with AZ4562 thick resist (b). A photolithographic exposure (c) and development define the resist-free areas (d). A bi-layer of Titanium (e) and gold (f) is evaporated forming the sacrificial layer. A second photolithographic exposure of the substrate covered with S1818 (g) followed by relative development leaves opened the areas interested by the electroplating process (h).

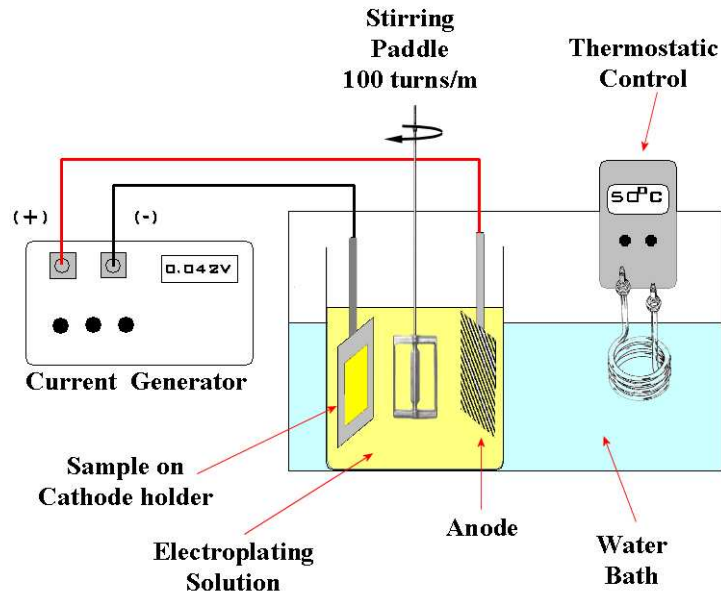


FIGURE 4.10: Electroplating set-up. The substrate to electroplate is attached to copper slide working as a cathode. The anode is represented by a platinum mesh. A paddle stirs the electroplating solution during all the process and the temperature is kept constant at 50°C by a thermostatic control. A generator provides the flowing current that allows the electroplating of the cathode. The process lasts 20mins for a total electroplated layer of $2\mu\text{m}$

4.5.3 Buffer Layers Removal

Electroplating represents the last step to form the elevated structures.

The next process aims to remove all the different layers of resists and metal which form the sacrificial buffer layer used.

The two layers of photoresist are flood exposed with MA6 and then developed. The seed layer is removed with two wet etch processes for gold and titanium films using respectively gold etching solution for 5 seconds and then 4:1 buffered Hydrofluoric acid (HF) for 30s. The cleaning process is shown in Figure 4.11. The sample is then gently washed with warm acetone and IPA consecutively, to finally remove any residual resist.

An SEM micrograph of an array of elevated probes, as result of the process, is shown in Figure 4.12 where it is possible to distinguish the rail guides for device separation. Figure 4.13 illustrates the single elevated probe emphasizing the supporting post working as pin contact with the microstrip line.

To validate the effectiveness and cleanliness of the process, some devices, at different locations on the substrate sample, were sacrificed. Their elevated probes were mechanically tilted and turned over with a plastic tip and a further optical microscope inspection

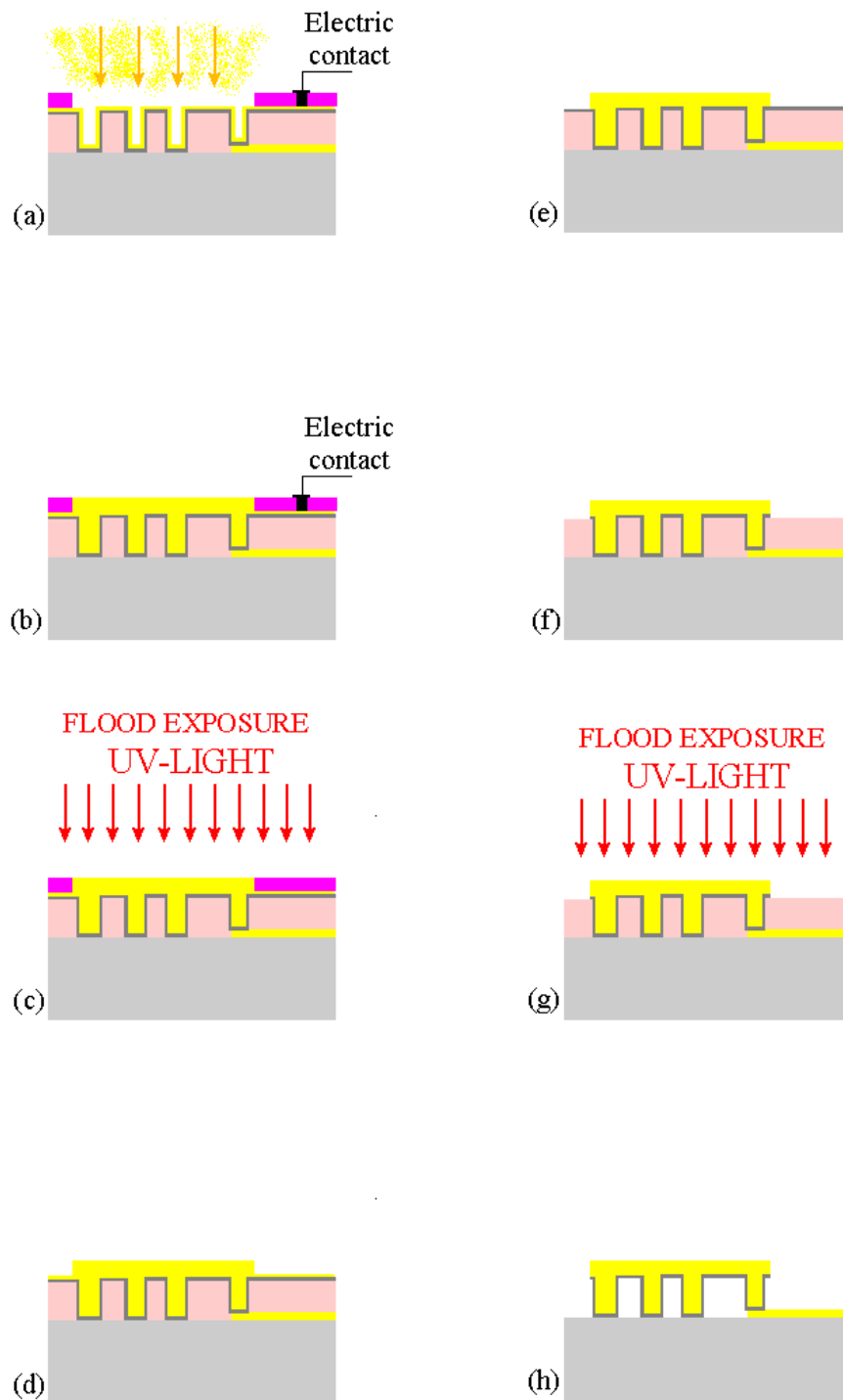


FIGURE 4.11: Electroplating and Buffer layer removal. An electrical contact is created to connect the seed layer (a) and electroplating takes place depositing gold in the seed areas exposed to the solution (b). Photolithographic flood exposure (c) and relative development clear the upper photoresist layer (d). Gold etch and titanium etch (f) allow a further flood exposure (g) to clean the devices from the AZ4562 thick layer (h).

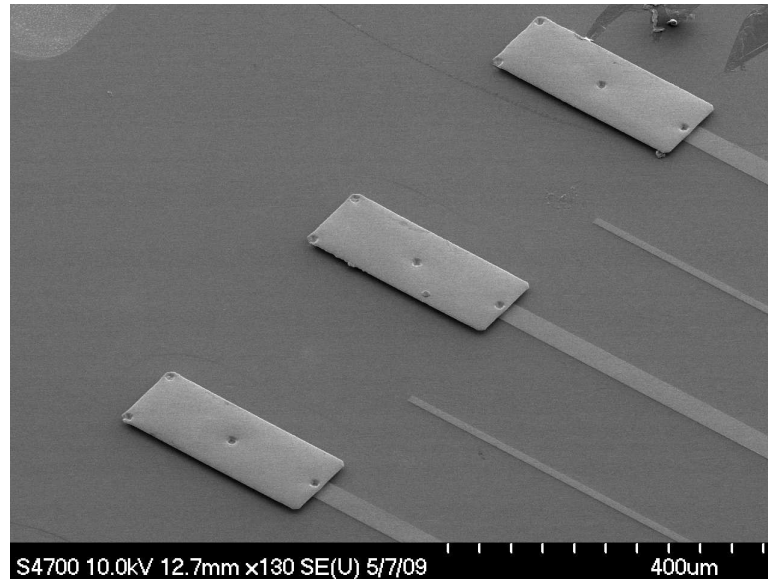


FIGURE 4.12: SEM micrograph of an array of Elevated E-plane probes fabricated on GaAs. The different devices are separated using a grid of lines as cleaving rails.

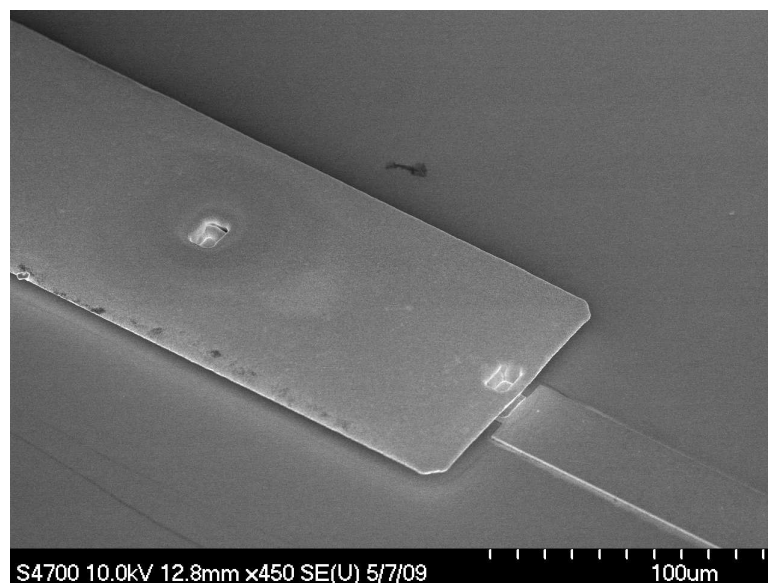


FIGURE 4.13: Enlargement of the area where the supporting post connects the probe to the printed microstrip line.

confirmed the removal of possible residual resist material underneath the elevated structures. However, an additional O_2 cleaning process in a Plasma Barrel Asher was carried out to remove any thin and invisible layer of residual resist.

A series of elevated microstrip and elevated CPW lines with different length, Figure 4.14, are also fabricated on the same substrate sample in order to estimate and validate the electrical connection of the elevated structures with on-wafer lines through RFOV probe measurements.

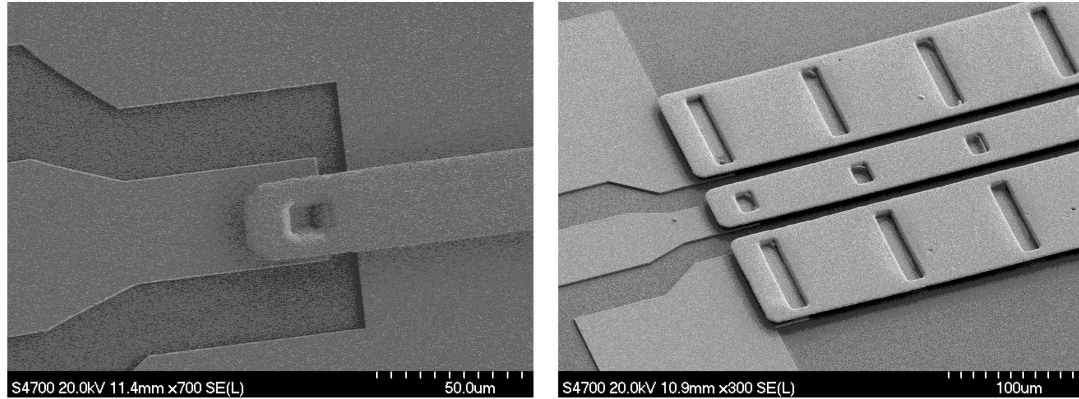


FIGURE 4.14: Elevated microstrip lines (left) and elevated CPW lines (right) are also fabricated using the same process on the same substrate sample. The elevated lines are measured in order to validate the electric contact of the elevated structures with the printed microstrip line.

4.6 Bonding and Thinning

In order to thin the substrate sample from an initial thickness of $630\mu m$ to $50\mu m$, it is bonded on a 4 inches sapphire disk which is used as carrier for the process. Before the bonding operations, the substrate is measured with a thickness Gauge in five different locations such as the four corners and center of the sample. Four layers of PMMA are then spin-coated at $2000\text{rad}/\text{min}$ on the sample to protect the elevated devices and baked at $180^\circ C$ on hot plate for 20 mins each. An extra layer of adhesive for wafer bonding from BrewerScience[©] is spun on top of the layers. The sample is then tilted upside down on the sapphire carrier and baked at the temperature of $180^\circ C$ on hot plate for 30mins, then left to cool down to room temperature.

At this stage the sample is measured again at the same locations to validate the effectiveness of the bonding and its thickness. The sapphire is then mounted in the Logitech[©] PM4 precision lapping machine that, with a axial rotatory movement in $9\mu m$ Alumina powder, thins the substrate down to $50\mu m$. Thickness measurements are taken several times during the process in order to monitor the thinning process that stops at about $10\mu m$ before reaching the desired final thickness. The lapped surface needs a necessary process of stress relief which will lend more mechanical resistance to the substrate avoiding an unwanted breakage.

In fact, the mechanical thinning process produces a deep surface roughness which contributes to increase material fragility. The roughness level can be reduced using an isotropic wet etching process [75] in a solution (1:4:40) of HCl, H₂O₂ and RO water. The etch rate was estimated to be $0.33\mu m/\text{min}$ at room temperature. The sample is then washed with clear RO water and IPA.

The etched back-side surface of the sample is, then, patterned to define the metal grounds

with a photolithographic process as described in Section 4.5.1 using a thin layer of photoresist S1818 after which a metal EBE of 50nm of NiCr and 500nm of Au is followed by lift-off.

The substrate is then immersed in a BrewerScience[®] solvent for wafer de-bonding in hot bath at 50°C for 48 hours. As the solvent has to fully penetrate in the gap between GaAs substrate and sapphire carrier. De-bonding is the most critical operation of the whole process where the substrate sample has to be handled gently to avoid any damage. The previous wet etch stress relief of the thinned surface is critical to the final mechanical stability of the 50 μ m GaAs membrane. The Bonding and thinning steps are illustrated in Figure 4.15. The result of the fabrication is shown in Figure C.4 where

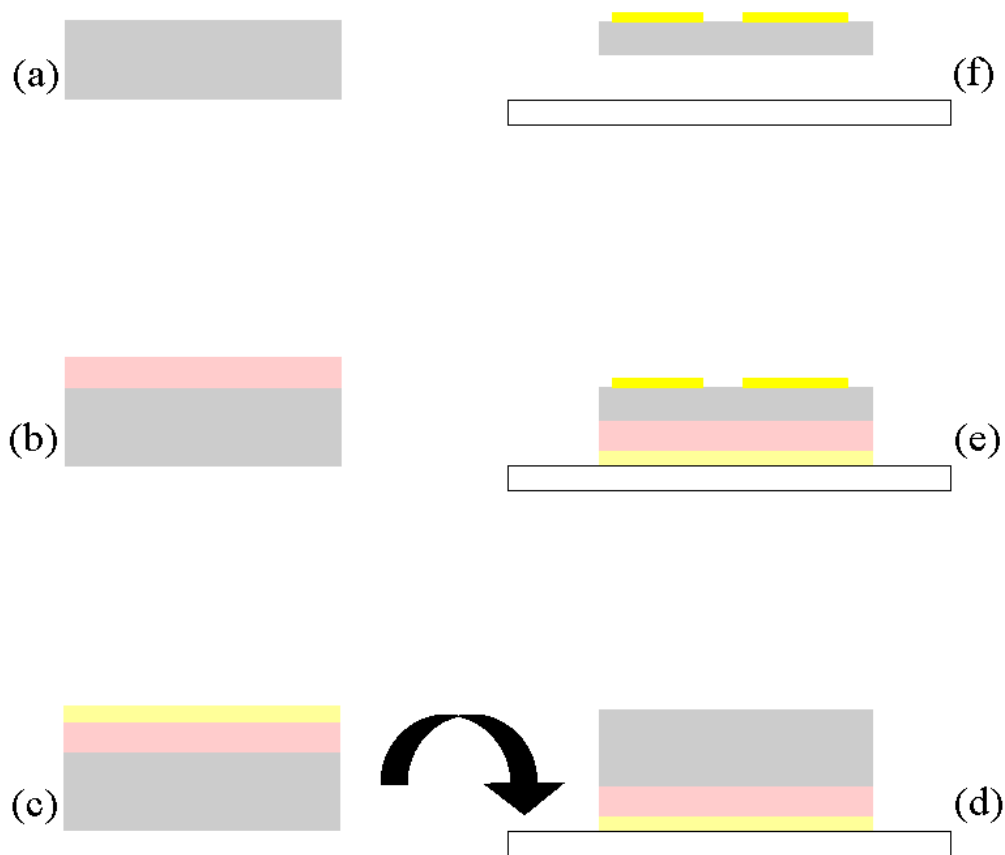


FIGURE 4.15: The substrate (a) is covered with a 4-layers of e-beam resist (b) and a layer of adhesive (c) with which it is bonded upside down on a sapphire carrier (d). Thinning process followed by photolithography and evaporation define the back-side grounds (e). Finally thinned and patterned substrate is detached from the carrier with solvent (f).

thinned substrate is supported by a 300 μ m thick quartz glass slide.

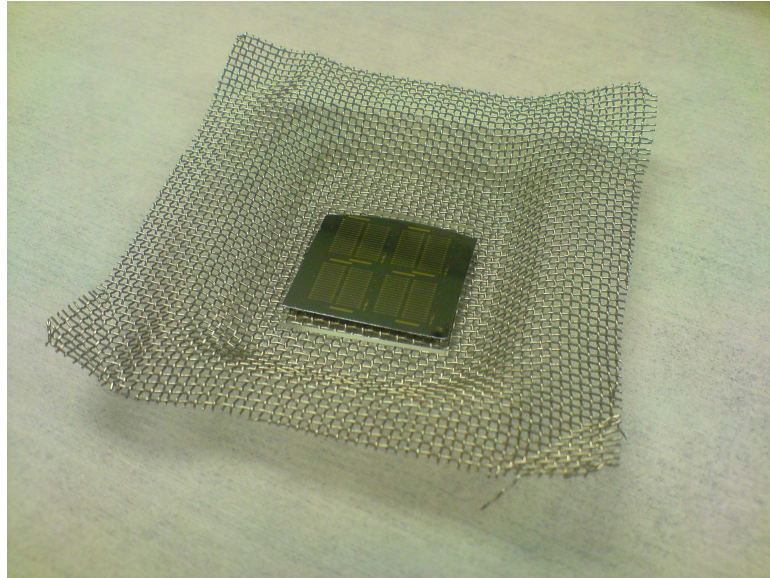


FIGURE 4.16: The result of the fabrication process before cleaving. The substrate lays on a $300\mu\text{m}$ thick glass slide in a metal mesh for sample handling.

4.7 Scribe & Cleave for Die Dicing

The GaAs membrane is transferred onto a piece of transparent adhesive on which scribing and cleaving operations are carried out.

First the substrate is divided in four cells, then following the same procedure the single devices are separated along the scribing rails defined during fabrication and finally are positioned into a vacuum GelPack[®] ready to be used singularly. As the aspect ratio of the single back-to-back transitions device is very high ($400 \times 3200\text{mm}^2$) the cleaving procedure can easily damage a full cell of devices if care is not taken. The thinned substrate can easily bend and it has to be located on a glass carrier during the entire cleaving operation to prevent it from damage. Yields of the fabrication can be noticeably increased if a *Cleave, Pick and Place* tool was employed. The thickness of a residual piece of cleaved substrate is measured to validate the results of thinning and etching processes. The achieved thickness is demonstrated in Figure 4.17 using a Mitutoyo[®] precision thickness Gauge.

4.8 Design and Fabrication for WR5 Transitions Housing

The transitions, fabricated in back-to-back configuration, need to be assembled in a rectangular waveguide test fixture which is then connected to the measurement instruments. The test structure is designed considering the total length of the transmission line used between the two transitions and a split-block architecture is chosen for its fabrication.

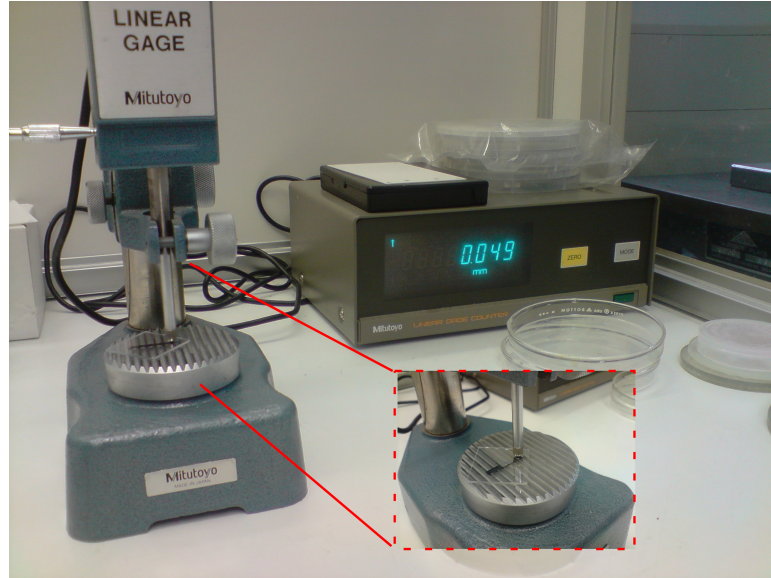


FIGURE 4.17: A small part of the thinned substrate is measured with a linear Gauge. Electronic measurement show the final thickness achieved and validate the process and its tolerance.

Rectangular waveguides can be milled in a single metal block divided in two halves, being a mirror images of one another. The two halves are then clamped together and kept in place using metal alignment pins and screws and the profile of the measurement instruments connection is finally defined around the rectangular waveguide input/output. The choice of this architecture relies on easy fabrication process and small relative deviation of the EM behavior of the result from the ideal case of rectangular waveguide. Let's consider the induced current density \underline{J} on the inner broadwalls of a rectangular waveguide due to the only propagating TE_{10} mode, as:

$$\underline{J} = \hat{n} \times \underline{H} \quad (4.1)$$

where \hat{n} is the unity vector orthogonal to the internal surface and \underline{H} is the magnetic field vector. Since the existing electric and magnetic fields relative to the TE_{10} mode can be written as:

$$E_y = E_0 \sin\left(\frac{\pi x}{a}\right) e^{-j\sqrt{k^2 - \left(\frac{\pi}{a}\right)^2} z} \quad (4.2)$$

$$H_x = \frac{-E_0}{2\pi f \mu} \sqrt{k^2 - \left(\frac{\pi}{a}\right)^2} \sin\left(\frac{\pi x}{a}\right) e^{-j\sqrt{k^2 - \left(\frac{\pi}{a}\right)^2} z} \quad (4.3)$$

$$H_z = \frac{jE_0}{2af\mu} \cos\left(\frac{\pi x}{a}\right) e^{-j\sqrt{k^2 - \left(\frac{\pi}{a}\right)^2} z} \quad (4.4)$$

where E_y, H_x, H_z are the fields components along $\hat{y}, \hat{x}, \hat{z}$, f is the frequency of interest, k is the wavenumber, E_0 is the maximum amplitude of the electric field, a and b are the

dimensions of the rectangular waveguide and x and z are the positions transversally and along the propagation direction as illustrated in Figure 4.18. From Eq.4.1, 4.3 and 4.4,

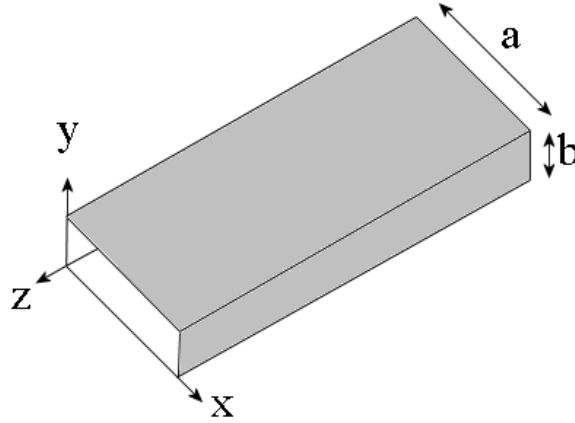


FIGURE 4.18: Coordinate system for the propagation of the TE_{10} mode in waveguide.

the density current $\underline{\mathbf{J}}$ can be written in its components as:

$$J_x = \frac{-jE_0}{2f\mu a} \cos\left(\frac{\pi x}{a}\right) e^{-j\sqrt{k^2 - \left(\frac{\pi}{a}\right)^2}z} \quad (4.5)$$

$$J_z = \frac{-E_0}{2\pi f\mu} \sqrt{k^2 - \left(\frac{\pi}{a}\right)^2} \sin\left(\frac{\pi x}{a}\right) e^{-j\sqrt{k^2 - \left(\frac{\pi}{a}\right)^2}z} \quad (4.6)$$

Eq.4.5 and 4.6 highlight that if a thin slot is opened along the propagating direction z , the J_z component is not perturbed. The J_x component can be perturbed apart from in the case where the slot is placed along the centerline where $J_x = 0$. These considerations are taken into account when designing *slotted waveguide array* antennas [24] in which slot apertures are located in between the centerline and the edges of the broad walls as illustrated in Figure 4.19. In this case, the current density flow is perturbed and a strong electric field is created across the slot which starts to radiate. Hence, by fabricating the rectangular waveguide in two halves, there is no current density perturbation and no substantial radiation happens from its broad walls.

The mechanical fabrication of the waveguide split-blocks is carried out at the University of Glasgow using the facilities of the Mechanical Workshop. Metal milling is employed to define waveguide profiles and connection flanges in two consecutive steps using a CNC Datron[©] CAT-3D M6 milling machine, illustrated in Figure 4.20. The standard MIL-F-3922-67B [76] is chosen for the waveguide flanges and used as connection interface with the measurements instruments.

In order to estimate the feasibility and tolerances of the milling process, a simple rectangular waveguide split-blocks for G-band frequencies is designed using Autocad[©] 2007

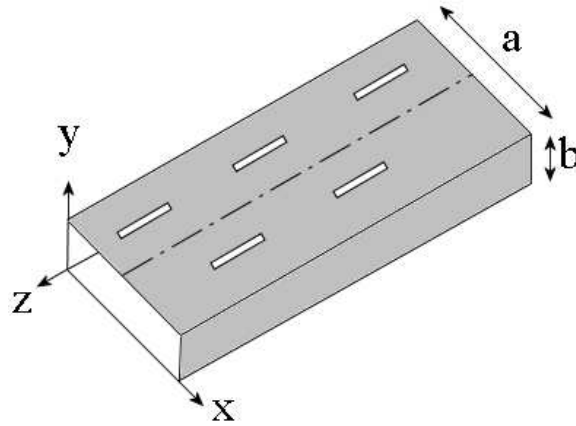


FIGURE 4.19: Slotted waveguide array antenna. The slots are located between waveguide centerline and its edges for maximum current perturbation.



FIGURE 4.20: CNC Datron[©] CAT-3D M6 milling machine at the University of Glasgow, Mechanical Workshop. The milling machine is computer controlled.

and relative mechanical CAD table is produced and supplied to the Mechanical Workshop for manufacturing. Illustration of the design is shown in Figure 4.21. Three copies of the same design with length of 1cm, 2cm and 3cm are fabricated using Brass blocks in order to estimate transmission loss per unit length. The outcome of the manufacturing is shown in Figure 4.22. The Design of the split-block housing for the transitions is carried out in similar manner. The substrate orientation is chosen to be perpendicular to the waveguides input/output direction and two S-shape bends are designed to realize the T-junction required between the waveguides and the transitions. The architecture allows a symmetrical milling process during the definition of the waveguide grooves. Dimensions of the waveguide bends are related to the length of the transmission line connecting the two transitions. A perspective of the design is shown in Figure 4.23. Full details of the mechanical CAD table with relative dimensions can be found in Appendix C.

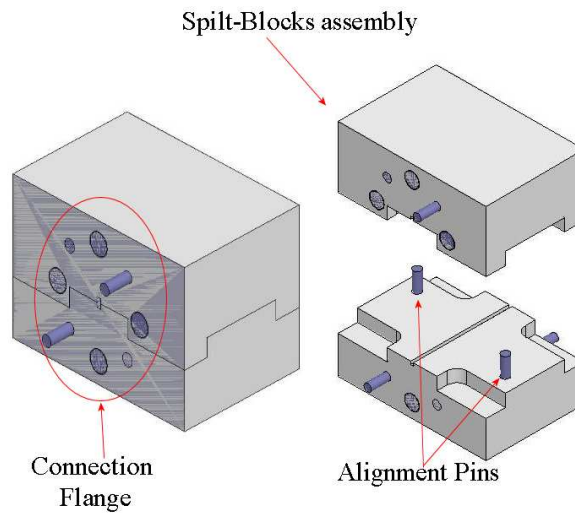


FIGURE 4.21: 3D view of the model for the G-band waveguide lines. Its split-block assembly needs internal alignment pins. The waveguide flange for connection uses the standard MIL-F-3922-67B [76].

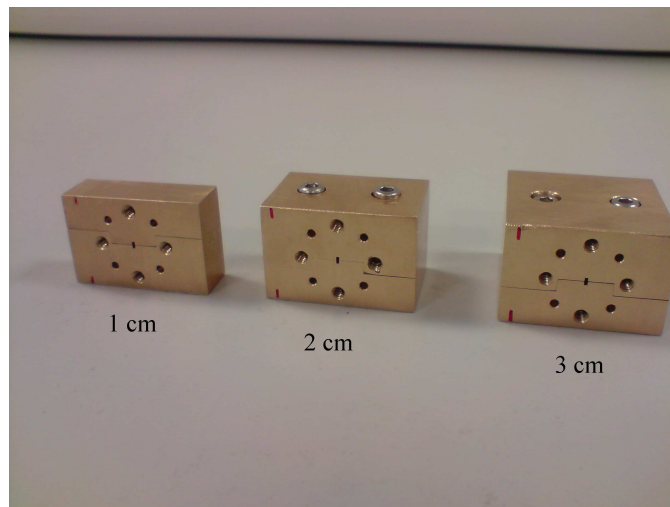


FIGURE 4.22: Three split-block G-band lines with length 1cm, 2c, and 3cm are fabricated.

4.9 Considerations on Mechanical Manufacturing Tolerances

Mechanical manufacturing has unavoidable larger tolerance when compared to the precision achieved with Clean-room fabrication. The CNC Datron[®] CAT-3D M6 milling machine shows a tolerance of $20\mu m/m$ just after calibration, but this value is related to a full linear movement of the end mill stage. The effective accuracy decreases when the stage movements involves curvilinear shapes such as the waveguide bends realized for the split-block housing of Figure 4.23. The milled waveguide groove can also present an

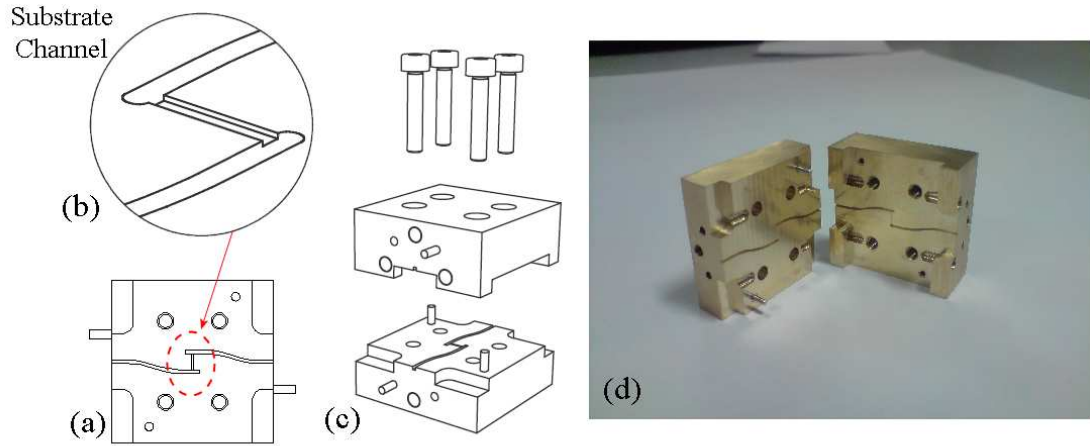


FIGURE 4.23: Top view of waveguide S-shape bends and substrate channel (a). Waveguide grooves realize a T-junction with the area designated for the substrate bonding (b). 3D perspective of the Housing assembly (c). Result of the mechanical fabrication for the split-block housing showing waveguide grooves and substrate channel (d).

undesired deformed profile if appropriate micro tools are not employed. Micro end-mills bend against the metal material during their rotation and the result is a waveguide groove with walls which are not parallel. To reduce this unwanted effect, the choice of the end mill cutter is crucial and its diameter has to be as close as possible to the dimensions of the features to cut out from the metal block.

For this work two micrograin solid carbide end mills with single flute from Datron[®] [77] are employed. A micro tool with 0.6mm of diameter is used to mill the waveguide grooves, whereas a diameter of 0.5mm is employed for the substrate channel. Optical micrography of the waveguide cross section when the half blocks are clamped together and the junction between the rectangular waveguide and substrate channel are illustrated in Figure 4.24 and 4.25 respectively.

4.10 Assembly

Before the measurement process, the fabricated back to back transition device has to be mounted into the split-block housing. The assembly operation is carried out using an optical microscope and positioning and alignment is performed by hand using tweezers with carbon fibre tips to reduce risk of possible breakage likely to happen with normal metal tips.

The split-block housing is first cleaned with acetone in an ultrasonic bath and then de-oxidised in a solution of 1:4 of HCl:ROwater for 1min. A conductive silver epoxy paste by Aremco-Bond[®] [Aremco] in its compounds 556-A and 556B is mixed and then spread into the substrate channel of the lower housing block using a thin plastic tip.

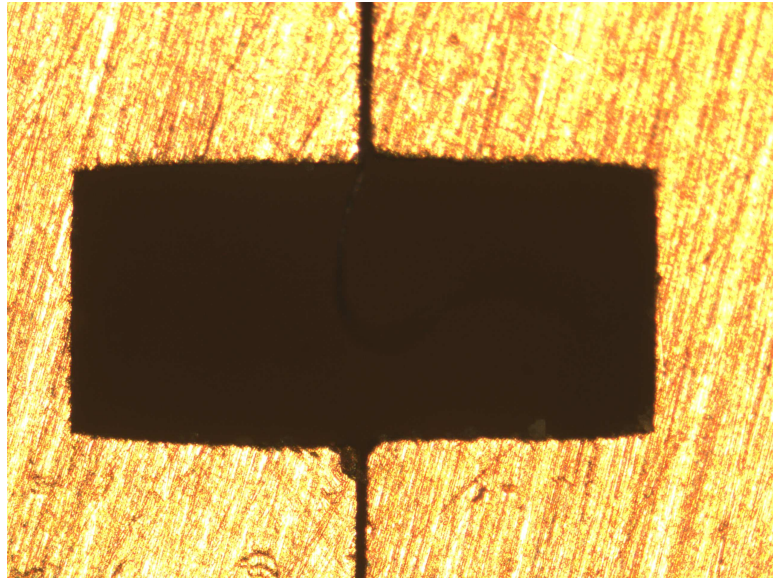


FIGURE 4.24: Profile of the rectangular waveguide formed by the two halves of the split-block.

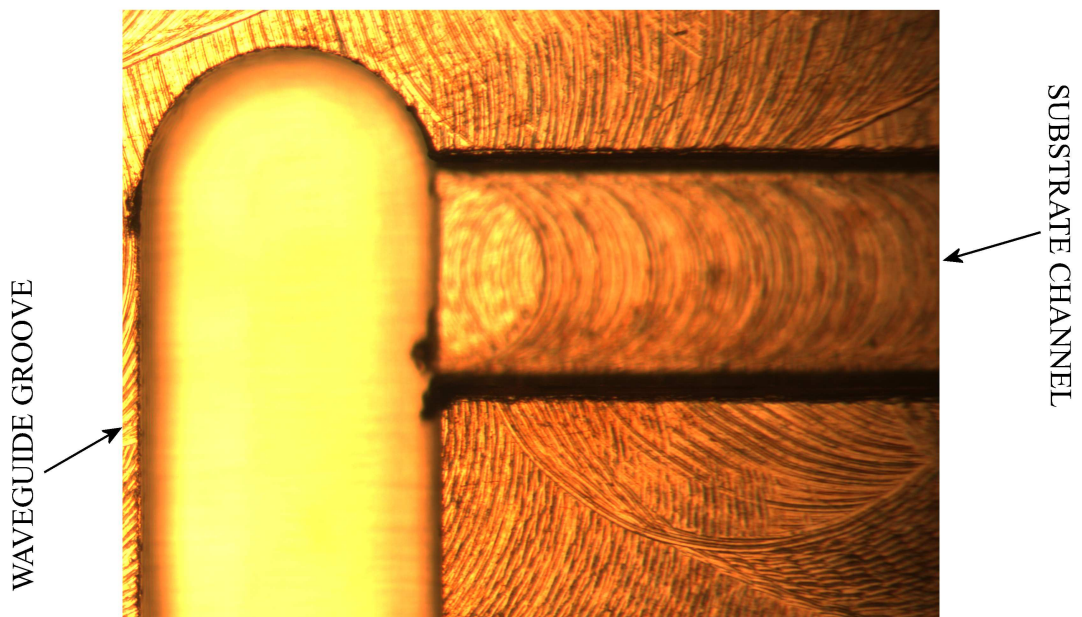


FIGURE 4.25: Optical microscope photograph of the T-junction between waveguide groove and substrate channel where the transitions have to be bonded.

The transitions are then collected from the GelPack using a thin sheet of cleanroom paper and located into the channel. After the alignment of the substrate the upper part of the split-block is mounted and the total device is placed on hot plate for 1hr at the temperature of 150C° to cure the silver epoxy paste. The device is then left to cool down and it is ready to undergo the measurement procedure.

Two transitions, a simple planar broadband transition [32] and the Elevated E-plane probe [32], are assembled using this process and the results are shown in Figure 4.26 and 4.27.



FIGURE 4.26: Two broadband waveguide to microstrip transition in back-to-back structure bonded into the substrate channel and having the probes protruding into the two waveguide grooves.

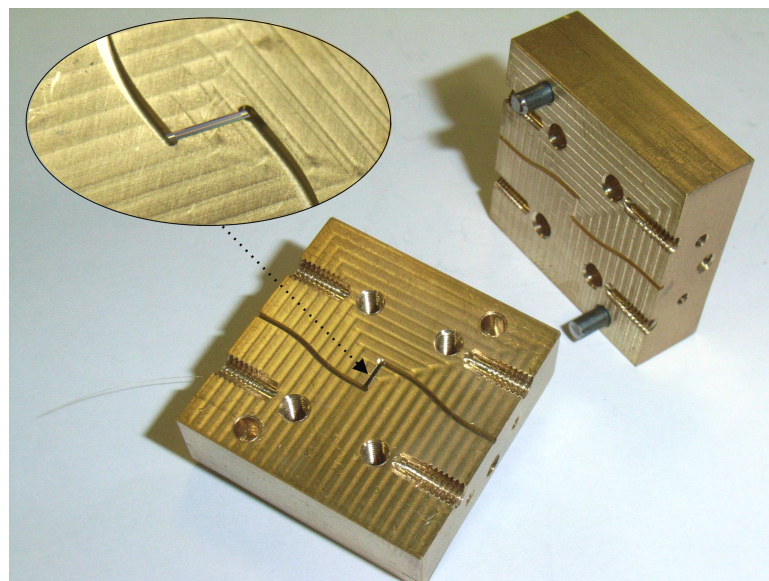


FIGURE 4.27: Elevated E-plane probes in back-to-back configurations are bonded into the substrate channel. Enlargement shows the result of the two T-junctions with the waveguide grooves.

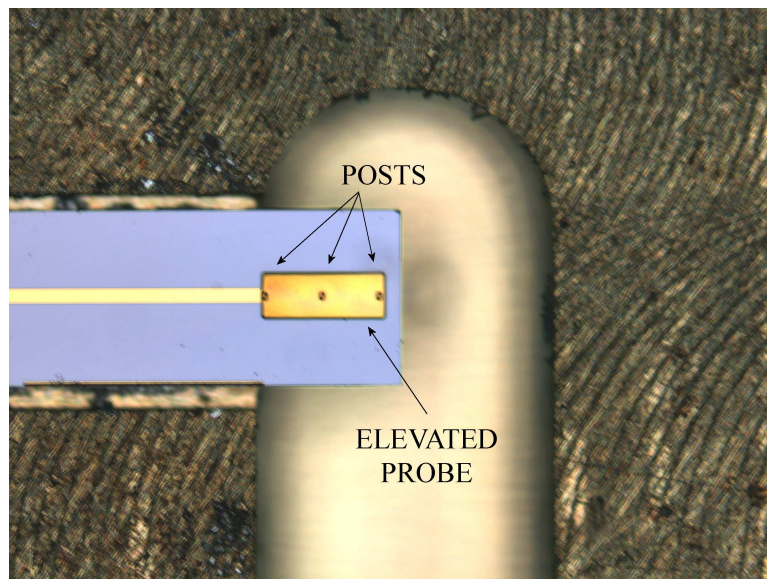


FIGURE 4.28: Optical micrograph of the Elevated E-plane Probe aligned and bonded in its channel. The three metal posts support the elevated probe from the substrate material leaving it suspended into the waveguide.

4.11 Conclusions

Fabrication techniques and processes for thin film MMIC technology used at the University of Glasgow are described. Procedures for the definition of printed line and elevated structures to form the Elevated E-plane Probe, and elevated microwave lines are detailed with emphasis on the fabrication of the elevated structures resulting from the extension of the air-bridges forming technique. The GaAs substrate used for their fabrication is thinned and preliminary bonding and etching techniques are also described.

Mechanical manufacture of a set of rectangular waveguide and split-blocks, housing the GaAs substrates, is illustrated mentioning fabrication tools, techniques and materials. Considerations on the results from the milling process are discussed and assembly operations, performed to bond the GaAs substrate into the split-block housing, are detailed. The next chapter is dedicated to the measurements procedures and the results when tested with a performance network analyzer (PNA).

Chapter 5

Measurement Results

5.1 Introduction

The Chapter presents methodology, tools and instrumentation used to perform waveguide measurements in the G-band. The calibration procedure is also detailed with signal flow graph formalism as part of the effectiveness of the measurements procedure.

The fabricated devices, described in Chapter 4, are tested and measurements are carried out to determine their electrical behavior and confirm simulations results. Split-block waveguides are measured to validate the mechanical fabrication process, estimating transmission and reflection properties. Loss factor per unit length is also calculated.

The metal split-block housing is tested under different measurements conditions in order to evaluate the influence of the substrate material and to validate the substrate channel isolation. This ensures that the effective transmission is accomplished by the waveguide-to-microstrip transition and very low power spills from the input waveguide to output waveguide through unwanted cavity modes.

Fabricated broadband waveguide-to-microstrip transitions relative to the design of Section 3.6 are tested and measured in the waveguide housing highlighting the influence of flange misalignments which are detrimental to the overall performance. Transitions using *Elevated E-plane probes* relative to the design of Section 3.6.1 are measured demonstrating the effectiveness and robustness of this *novel* structure. Simulated and measured results are compared validating the design procedure. The chapter ends with a discussion on the losses introduced by the split-block housing used as a test fixture for the back-to-back transitions and estimating the loss factor of the waveguide bends. Finally, the loss factor for the broadband transition and the elevated E-plane probe transition is derived from measurements and a comparison of the two is shown.

5.2 Measurement Instruments

5.2.1 Instrumentation

The S-parameters of the fabricated transitions are measured with a *performance network analyzer* PNA, consisting of a vector network analyzer extended with MMW modules. This measurement system is a two-channel MMW receiver designed to detect the magnitude and phase of the transmitted and reflected waves when the device under test (DUT) is connected. During operation, the RF source in the VNA is set to sweep over a specified bandwidth, the MMW modules work as mixers to center this bandwidth at MMW frequencies. An internal reflectometer samples the incident, reflected and transmitted RF waves and converts the signals to intermediate frequencies (IF). The signals are then detected and converted to digital. The data is processed with software and the magnitude and phase of the S-parameters and all the quantities that can be derived from the S-parameters with an algorithm such as impedance, standing wave ratio (SWR) and return loss are calculated. The PNA allows an increased accuracy in the measurement, achieved by using an error correcting software and a calibration procedure.

Figure 5.1 illustrates the two OML MMW vector network analyzer frequency extension modules for G-band used to perform the measurements in the present work. The system can be used for both on-wafer and waveguide measurements using respectively ground-signal-ground (GSG) probes or waveguide extensions to connect the DUT. The

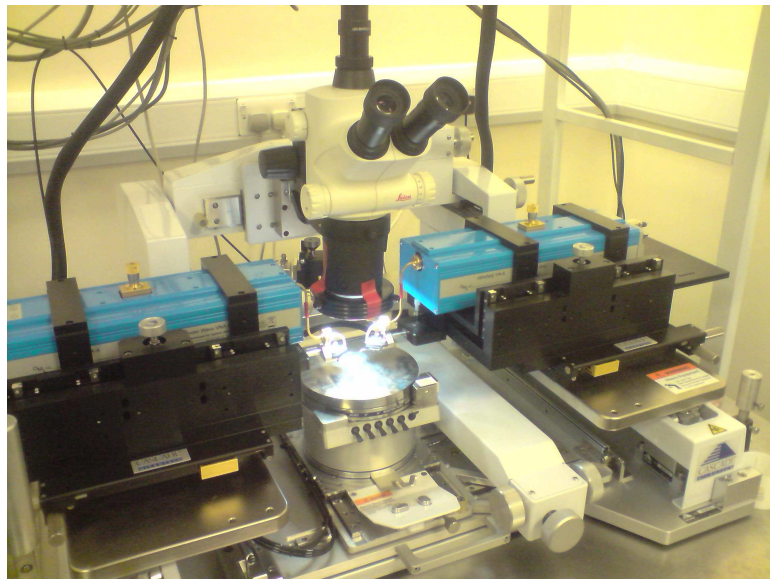


FIGURE 5.1: PNA setup for G-band measurements. The two OML G-bands modules, working as mixers, are connected to a VNA (not shown). The setup includes GSG probes for RFOV measurements. Probes can be removed and WR-05 waveguide extensions can be mounted to perform waveguide components measurements.

measurements system is assembled by CASCADE[©] and comprises features such as a

vacuum chuck holder and micrometer positioning systems for moving the stages for different measurement scenarios. In Section B.1 it was described how the transmitted and reflected waves can be represented by scattering parameters. An additional technique, useful in the analysis of microwave networks, is the *signal flow graph* representation [78]. A flow graph is constructed using *nodes* and *branches*. Each port of a microwave network has two nodes, identifying with a_i a wave entering the port and with b_i a wave reflected from the port. Branches are signal paths from one node to another and each branch has a scattering parameter associated.

Hence, for the two port networks illustrated in Figure B.1 the corresponding flow graph is shown in Figure 5.2. Generally the graph gives an intuitive illustration of the network

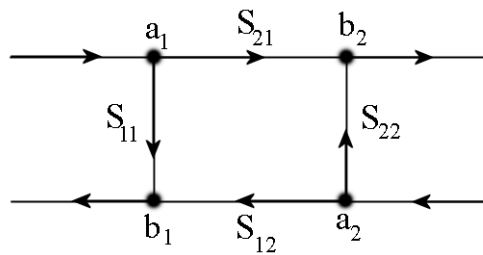


FIGURE 5.2: Example of signal flow graph for a 2-ports network element.

behaviour. In the example of Figure 5.2 a wave with amplitude a_1 enters at port 1 and it is split partly going through S_{11} out of port 1 and partly transmitted through S_{21} to node b_2 . At node b_2 , the wave exits port 2. If there is a load with a non-zero reflection coefficient on port 2 the wave is split again and partly is reflected entering back port 2 at node a_2 . When it re-enters port 2, the wave can be further partly reflected back out of port 2 through S_{22} and partly transmitted to port 1 through S_{12} . The signal graph can be extended for microwave networks in series and it can be used as a method to decompose the characteristics of a network in single blocks. Signal flow graph is a useful technique for understanding the calibration procedure.

5.2.2 Calibration

Every measurement instrument has imperfections and depending on the frequency of the observed signals the imperfections can be significant and they have to be accounted for to eliminate errors in the measurements.

Calibration is a method of determining these imperfections and it is performed using "known" standards. The number and type of standards depend on the type of calibration, hence the algorithm that is followed. Once the calibration is done, during the

measurements of the DUT, the information on the imperfections can be removed with a procedure called *de-embedding* and the results are then the true characteristics of the DUT.

Common two-port calibration types are: SOLT (short-open-load-thru), LRRM (line-reflect-reflect-match) and TRL (thru-reflect-line). In the measurements of the back-to-back transitions for this project, TRL calibration is chosen and it is performed using the calibration kit V05-AL-22 supplied by OML[©] and shown in Figure 5.3. The cali-

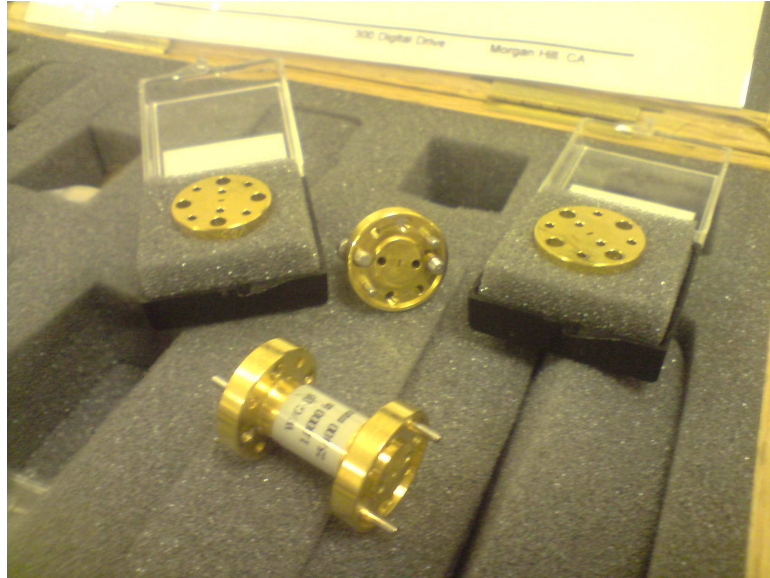


FIGURE 5.3: Components of the OML V05-AL-22 calibration kit. A Short is used as fixed load and two line are used for phase detection. A 1 inch waveguide line is also included to estimate calibration quality.

bration procedure is computer controlled by WinCal[©] a software package designed for calibration and measurements in which the information regarding a specific kit can be stored. WinCal also performs an automatic de-embedding algorithm at the end of the calibration procedure.

The TRL measurement is performed using a short element for the reflection and two line elements for the phase shift estimation. The Thru element is realized connecting directly the two waveguide extensions. A further waveguide element, 1 inch long, is also provided and it is used as a verification element to estimate the quality of the achieved calibration.

The TRL method is chosen as it relies on waveguide line components, whereas SOLT and LRRM involve the use of a load element which is not suitable for the measurement of our type of DUT. The use of TRL also gives an indication of how well the signals propagate through the fabricated waveguide lines when compared with the 1 inch line provided in the calibration kit.

One of the purposes of the calibration procedure is to bring the reference plane for our measurements right to the input/output point of the DUT. In the present case this is

represented by the terminal cross-section of the two waveguide flanges at the MMW OML modules, where the DUT is connected.

The TRL calibration procedure can also be considered in terms of signal flow graphs. A general use is to measure the S-parameters of a two-port device at the input/output reference planes. The situation is illustrated in Figure 5.4. Initially the measurement

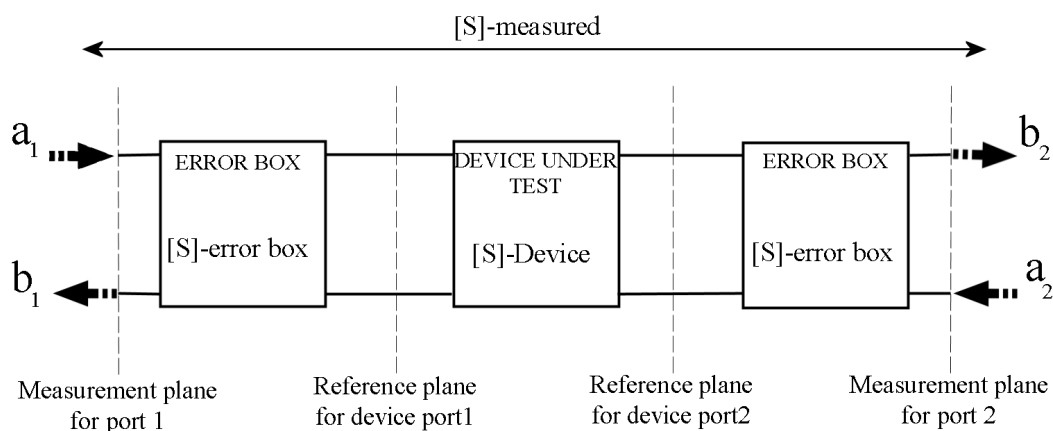


FIGURE 5.4: Block scheme for S-parameters measurements. The measured S-parameters of a network can be considered as composed of two blocks of S-parameters block-error and the S-parameters of the DUT. The S-parameters of the error-boxes are deembedded from the measurement planes to reference planes to estimate the DUT performance.

planes are at some point internal to the analyzer and the measurement results would include losses and phase delays caused by cables, connectors and possible transitions in probes and waveguide bushings. All these effects can be lumped into the error-box of Figure 5.4 placed between the desired reference plane and the DUT. A calibration technique aims to characterize the error-box and then to de-embed it during the measurement of the S-parameters of the DUT.

Signal flow graphs are used to derive the set of equations to estimate the S-parameters for the error boxes in the TRL procedure. The measurements of the Thru, Reflect and Line are shown in Figure 5.5 with their relative signal flow graphs. The measurement of each standard provides a S-parameters matrix. The assumptions for the calibration procedure are that the characteristic impedance at port 1 and port 2 is the same and the resulting error boxes are reciprocal and identical. The last statement means that $S_{21} = S_{12}$ for both error-boxes at port 1 and port 2. S-parameters of the DUT are measured at the measurement planes and corrected using the S-parameters of the error-boxes to finally give the S-parameters of the DUT at the desired reference planes. In fact, the measurement of the DUT corresponds to the measurement of a cascade of a three two-ports networks. Details and equations of the TRL signal flow graphs and how

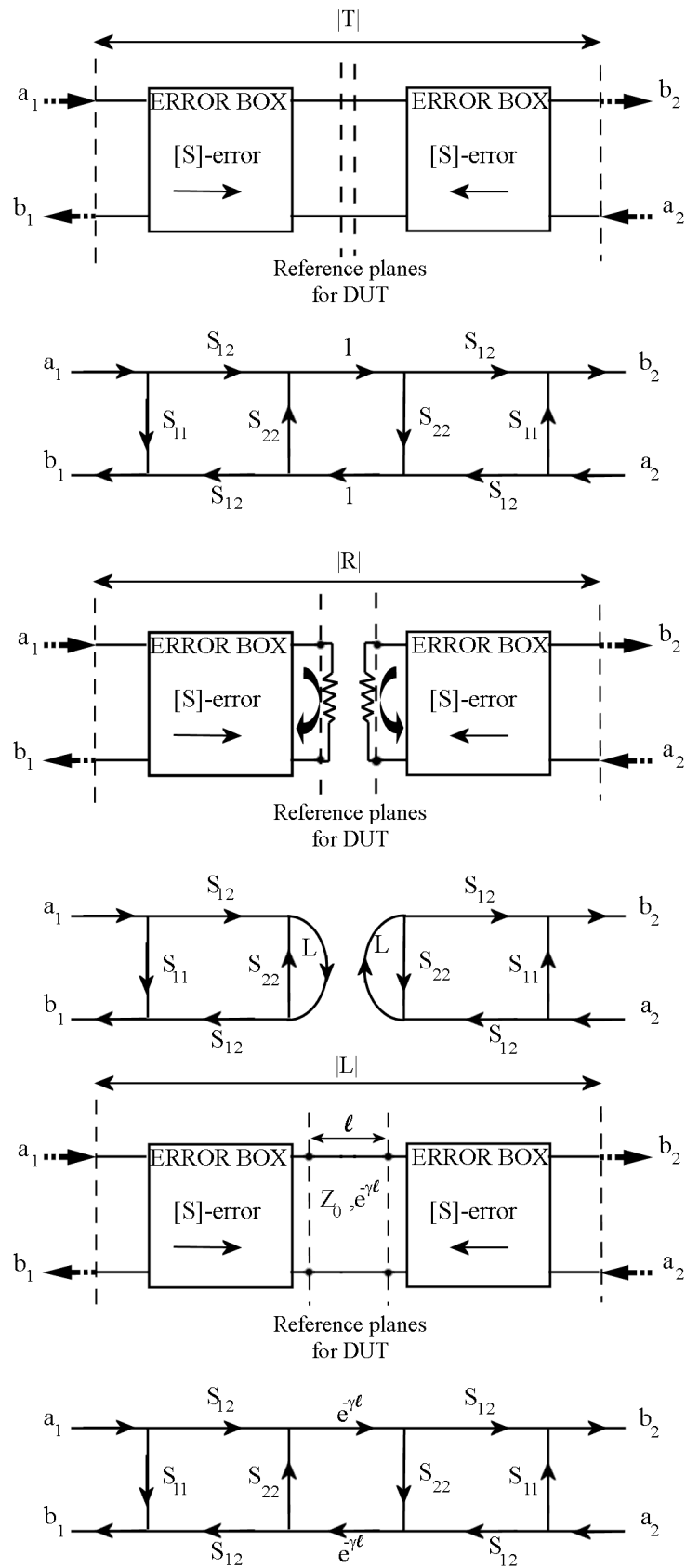


FIGURE 5.5: Blocks and signal flow diagrams for the three operations of a TRL calibration corresponding to Thru, Reflect and Line measurements.

to derive the error box S-parameters is detailed in Appendix D.

Once the TRL calibration is completed an estimation of its quality is performed by measuring a 1 inch WR-05 line. The measurements results are shown in Figure 5.6. The S_{11} has its highest value at about -30dB.

Since this line represents the perfect line for our measurement system, its S_{11} values are the lowest measurable values of reflection which all the fabricated waveguide lines can be compared to.



FIGURE 5.6: S-parameters S_{11} (red) and S_{21} (blue) of the calibration kit 1 inch WR-05 waveguide line. S_{11} shows good reflection loss of 30dB.

5.3 WR-05 Split-Block Lines Measurements

The three manufactured WR-05 lines of 1cm, 2cm and 3cm of Figure 4.22 were connected to the PNA and measured. An example of connected WR-05 line 2cm long is shown in Figure 5.7. The measurements results, illustrated in Figure 5.8-5.10, show maximum S_{11} levels around -20dB for all lines. The discrepancy with the results of Figure 5.6 arises from unavoidable misalignment between device flanges and measurement instrument waveguide connectors. Misalignment is due to the fabrication tolerances of the CNC milling process and it can increase the level of reflected power at the two ports [79].

Estimation of the insertion loss can be based on the S_{21} parameter measured using the three lines. This is shown in Figure 5.11. IF bandwidth is set to 50Hz in order to reduce the noise in the measurement results and the calculated *mean value* relative to each length over the entire G-band is listed in Table 5.1.

The results show loss is proportional to length and it is estimated as ~ 0.3 dB/cm, this is typical of what can be achieved with the mechanical fabrication process used.

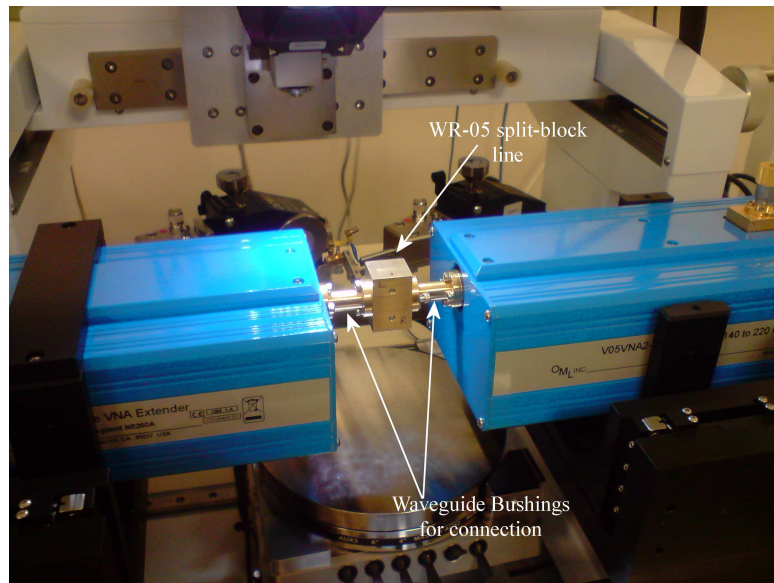


FIGURE 5.7: A WR-05 split block line can be connected to the OML modules of the PNA setup using two waveguide bushings. TRL is performed to bring the measurement reference planes up to the end of the waveguide bushing connected to the DUT.

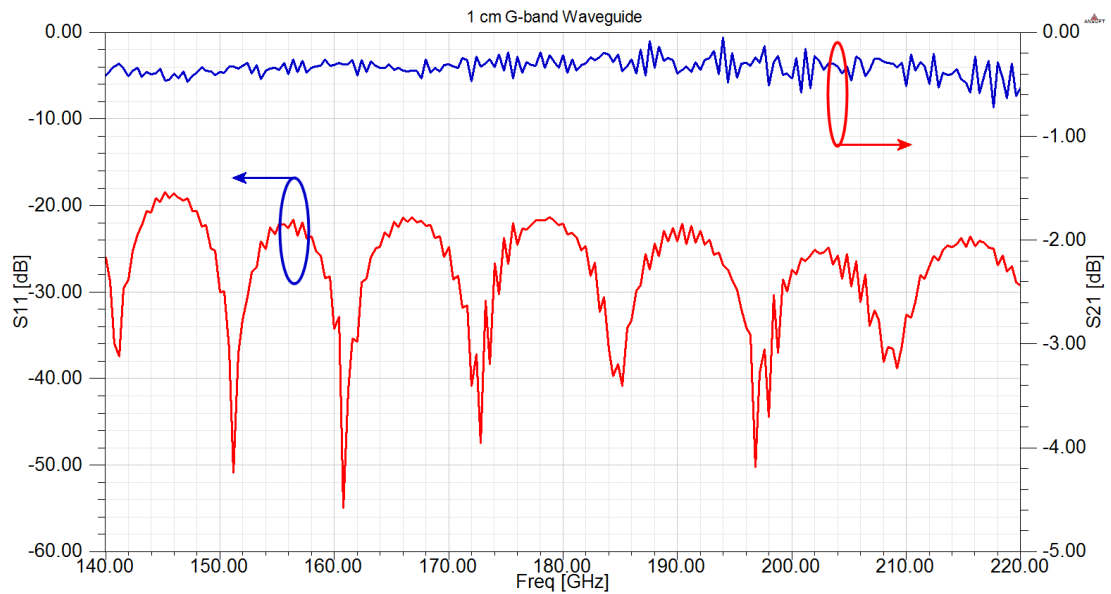
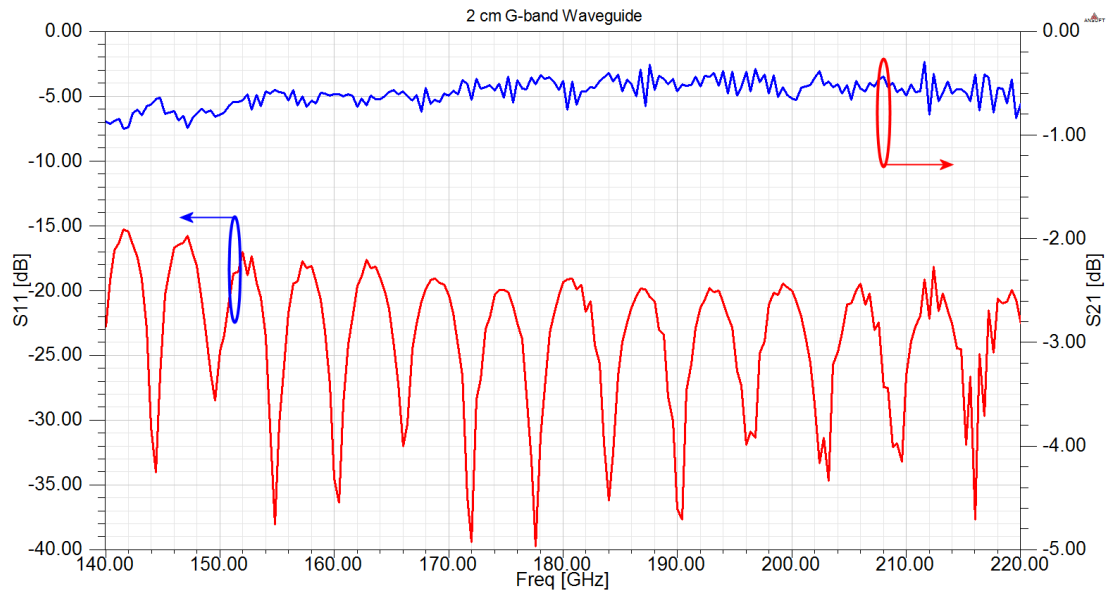


FIGURE 5.8: Measured S-parameters S_{11} and S_{21} for 1cm WR-05 split-block line.

Length	[S_{21}] Mean Value
1 cm	-0.34
2 cm	-0.6
3 cm	-0.83

TABLE 5.1: Mean value of S_{21} for three lengths of fabricated WR-05

FIGURE 5.9: Measured S-parameters S_{11} and S_{21} for 2cm WR-05 split-block line.FIGURE 5.10: Measured S-parameters S_{11} and S_{21} for 3cm WR-05 split-block line.

5.4 Channel Isolation

A preliminary test of the split-block housing was carried out in order to verify the isolation between the input/output waveguides before mounting the back-to-back transitions. The isolation test starts by inserting solely the empty split-block housing, as the DUT, in the PNA measurements setup. By measuring the level of S_{11} and S_{21} of the empty split-block it is possible to estimate how much power is transferred from input to output without the transitions. The aim of this measurement is to confirm that dimensions of the substrate channel are designed correctly and no EM waves effectively spill into the

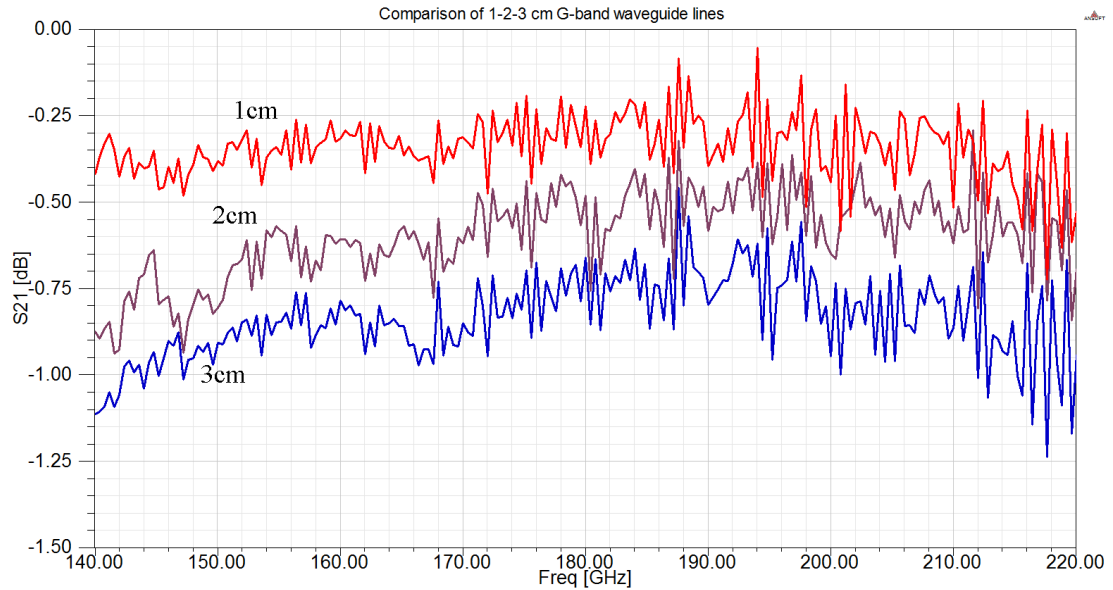


FIGURE 5.11: Comparison of measured S_{21} for three different length 1cm, 2cm and 3cm of fabricated split-block WR-05 lines.

substrate channel and propagate to the output waveguide. The situation is illustrated in Figure 5.12. Subsequently, the channel is loaded with a $50\mu\text{m}$ thick GaAs sample

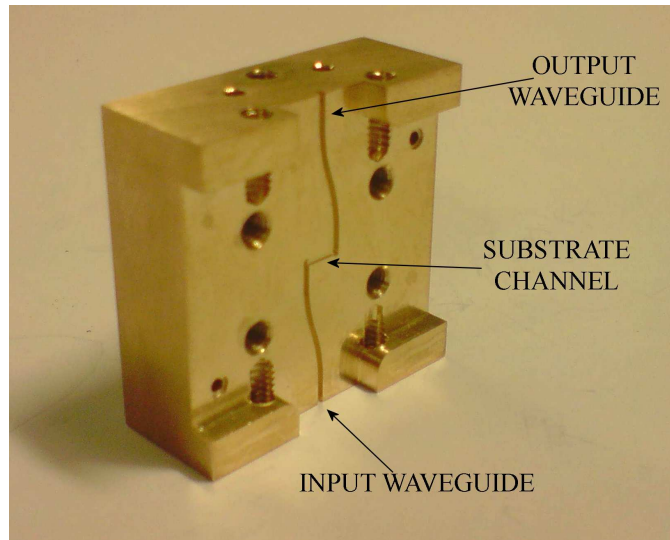


FIGURE 5.12: Half fabricated split-block for waveguide to microstrip transitions. Input and output waveguides are separated by the substrate channel whose dimensions have to put in cut-off possible waveguide modes propagation from one end to the other.

having the same extension of the channel. The measurements of such a setup provides information on how the substrate material modifies the profile of the channel that becomes electrically larger than its physical dimensions. The results of a well dimensioned design should show that there is no substantial change in the insertion and return loss with the previous case.

The last measurement test is carried out by using a substrate sample with the same

thickness as previously used that is extending into the waveguide volume in both sides. The extension length is chosen as to be the same of the substrate protrusion used for the fabricated back-to-back transitions.

This last measurement aims to show and verify what is the effect of the substrate edge with regard to the reflection loss and insertion loss. The extended substrate represents an abrupt discontinuity in waveguide and as such it should modify the level of S_{11} since the waveguide termination departs from the original *short* stub line behaviour. The level of S_{21} is also influenced by the substrate edge.

The extended substrate is bonded into the cavity and measurements are performed again. The three test cases are illustrated in Figure 5.13 and relative results are shown in Figure 5.14 for S_{11} and Figure 5.15 for S_{21} parameter.

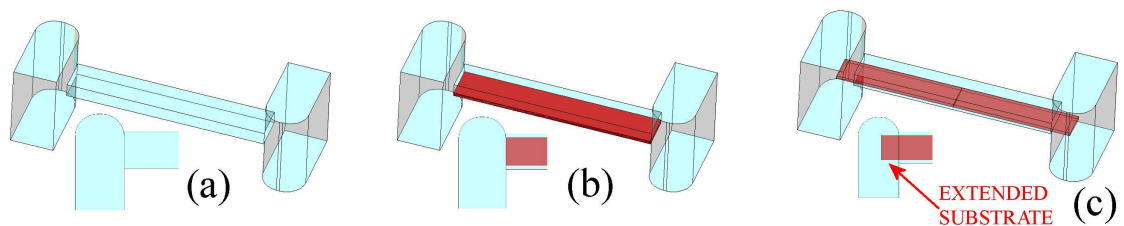


FIGURE 5.13: Three test cases for waveguides isolation. Empty substrate channel (a). Channel partly filled with $50\mu\text{m}$ GaAs substrate (b). Channel filled with GaAs substrate extending $300\mu\text{m}$ into the internal waveguides volume (c).

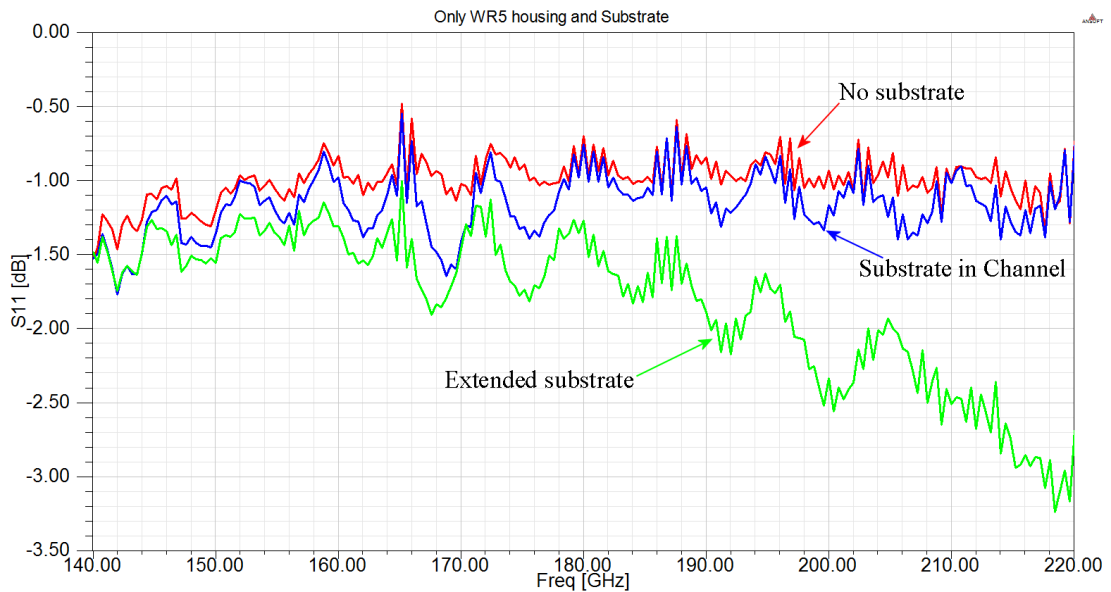


FIGURE 5.14: Measured S_{11} parameters for the three test cases of Figure 5.13. Substrate extension into the waveguide represents a strong discontinuity for the rectangular waveguide. The effect is more evident in the upper part of the G-band.

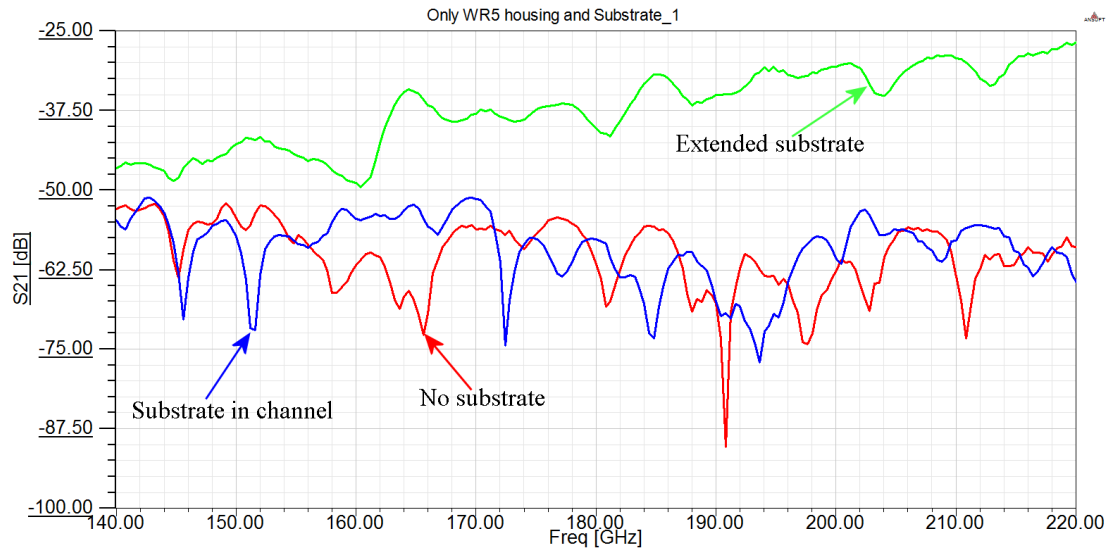


FIGURE 5.15: Measured S_{21} parameters for the three test cases. In the case of extended substrate into the waveguide, the EM energy starts to spill into the substrate channel. The effect is frequency dependent and more evident in the upper part of the G-band where it reaches an isolation level of -25dB due to the channel looking electrically larger as it is loaded with GaAs material.

Measurements show that there is no effective change in the levels of S_{11} and S_{21} in the cases of empty channel and when the channel is loaded with GaAs substrate. Moreover, the level of S_{21} is as low as -50dB and it can be considered as irrelevant.

When the substrate is protruding into the waveguide structures, insertion loss and return loss have a gradual change that varies with frequency becoming more marked at higher frequency. The effect shows that there is an increased transmission of power from one waveguide to the other through the substrate channel. This power is collected at the edge of the protruding substrate and travels along the channel as waveguide mode since it becomes electrically large due to the GaAs material.

However the level of transmitted power, although increasing with frequency, it is still very low being below -25dB at its highest point. Hence, all the preliminary measurements results carried out on the split-block housing validate correctness and effectiveness of the design for the isolation between input and output waveguides.

For completeness, simulated results of S_{21} relative to the measurements of Figure 5.15 are presented in Figure 5.16 for the three test cases of channel empty, partly filled and with substrate protruding into the waveguide. The simulated levels of transmission do not agree with the measurements as HFSS is not capable to simulate structures where the transmitted power between ports is below -40dB and then very low. This is a documented limitation of the adaptive meshing technique in the solver [Ansoft]. HFSS does not provide correct results in situations where the power flow is very low over the full frequency band as the mesh is not accurate and consequently fields values are

underestimated. However, it is still possible to notice that the level of transmitted power in the case of extended substrate is higher than the level of transmitted power in the other two cases, similarly to measurements results.

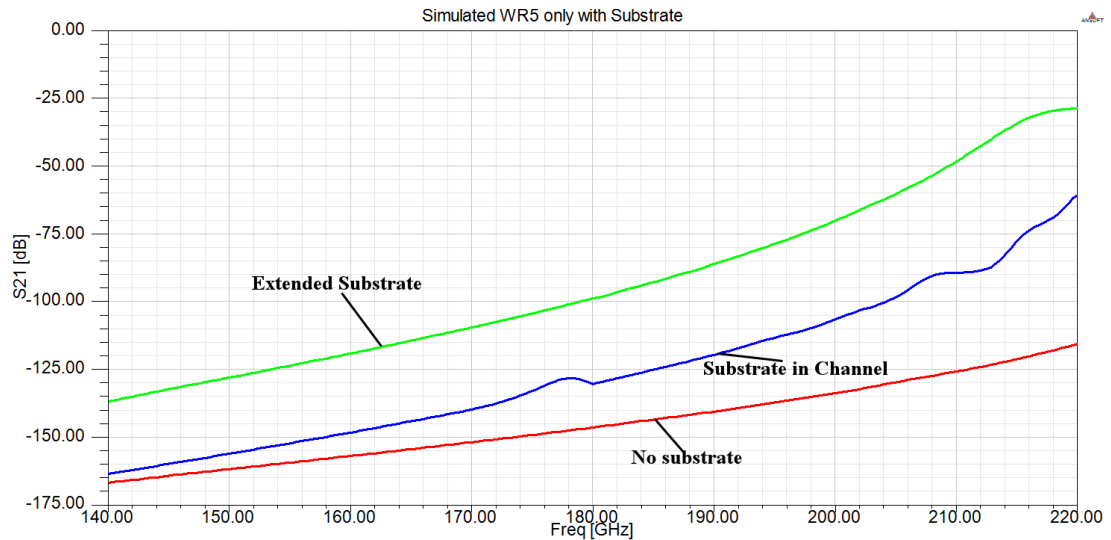


FIGURE 5.16: Simulated S_{21} parameters for the three test cases relative to the measurements results of Figure 5.15.

5.5 Performance of the WR5 Transitions

After performing the TRL calibration procedure, two designs of back-to-back WR-05 to microstrip transitions, mounted in the split-block housing, are measured.

The first design is very similar to the structure proposed in [32], the second design relates to the E-plane probes and it is discussed in Section 5.6.

The first design, as described in Section 3.6, aims to have a broadband characteristic over the entire G-band. Results from simulations show a level of S_{11} below -10dB for the case of an ideal connection to the PNA. However, the tolerance of the CNC milling fabrication plays a crucial role in the overall performance. Simulated and Measured S-parameters are shown in Figure 5.17 and Figure 5.18.

The results do not present a satisfactory performance for transmission and reflection represented by parameters S_{21} and S_{11} respectively. Although the back-to-back transitions show a broadband behavior, the level of reflection dramatically exceeds the threshold of -10dB which is considered the minimum reflection requirement for a further electronic signal amplification.

Flange misalignment between the split-block housing and the PNA connectors is preventing the correct operation.

The problem of large mechanical tolerances in the fabrication of waveguide components

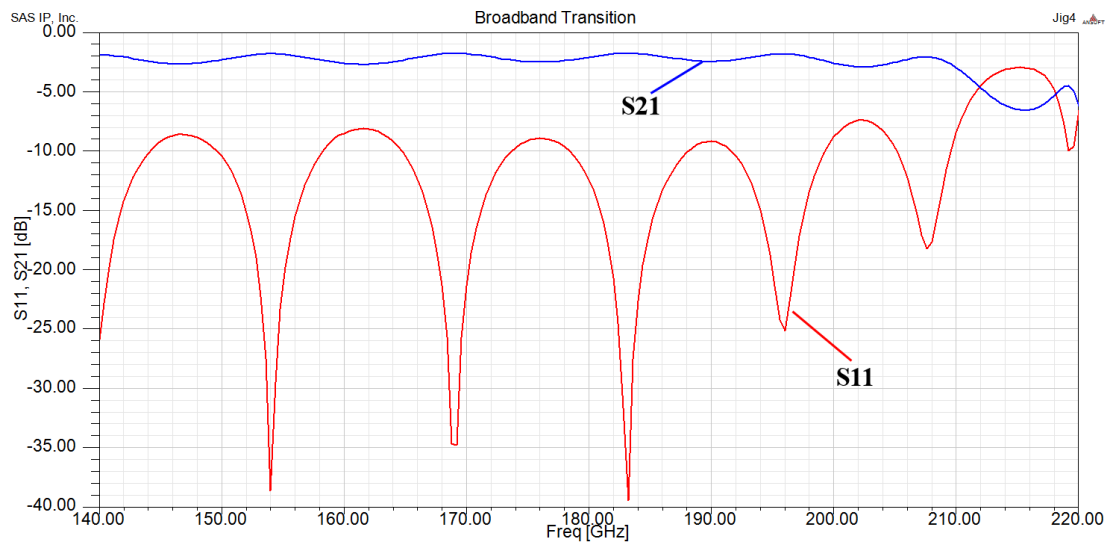


FIGURE 5.17: Simulated S-parameters S_{11} and S_{21} of broadband back-to-back waveguide-to-microstrip transition designed in Section 3.6.

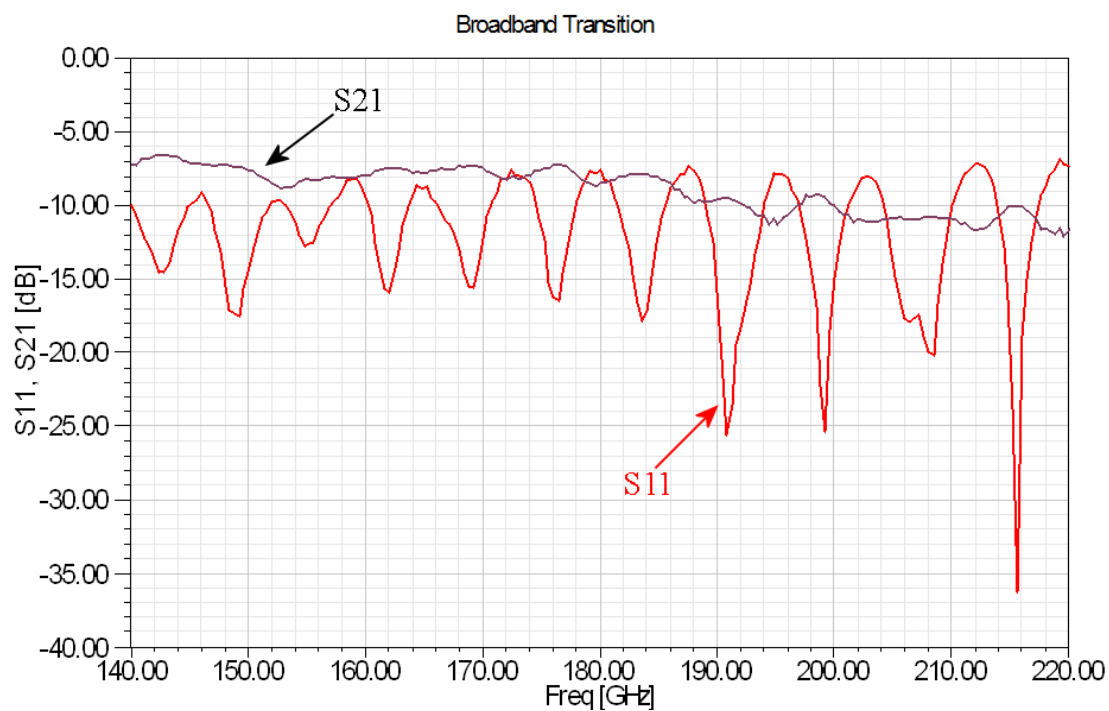


FIGURE 5.18: Measured S-parameters S_{11} and S_{21} of broadband back-to-back waveguide-to-microstrip transition designed in Section 3.6.

for frequency as high as the G-band has to be properly addressed during design. Even the calibration kit parts, manufactured with a very expensive processes, have to face the limitation of mechanical inaccuracy that can partly masks their correct working operation as confirmed by the results shown in Figure 5.6 for the case of the calibration kit waveguide line 1 inch long.

The effect of an offset between two identical waveguide flanges was investigated with HFSS12 simulating misalignments along the width and the height as illustrated in Figure 5.19. Simulation results for S_{11} of Figure 5.20 and 5.21, respectively for a vertical

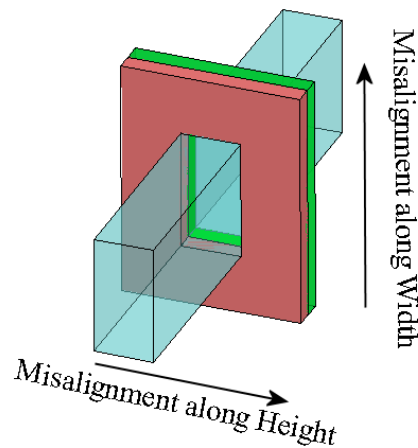


FIGURE 5.19: Two waveguide flanges can have relative offset along their width or along their height. The situation was modelled and simulated with HFSS12 with misalignment in the range of $0 - 100\mu m$.

and horizontal offset in the range of $0 - 100\mu m$ show that the level of return loss increases with misalignment in both directions. However, flange misalignments are the effect of the superposition of different causes [76] and they can not be taken into account as systematic error. Hence, the design of components, such as waveguide transitions, should aim for reflection levels well below -10dB in order to compensate the masking effect of unavoidable manufacturing limitations.

The Elevated E-plane probe addresses some of these aspects and it represents a more robust solution to the problem.

5.6 Measurements of Elevated E-plane Probe

A second design, corresponding to the Elevated E-plane Probe, is fabricated with the process described in Chapter 4 and is used as waveguide-to-microstrip transition.

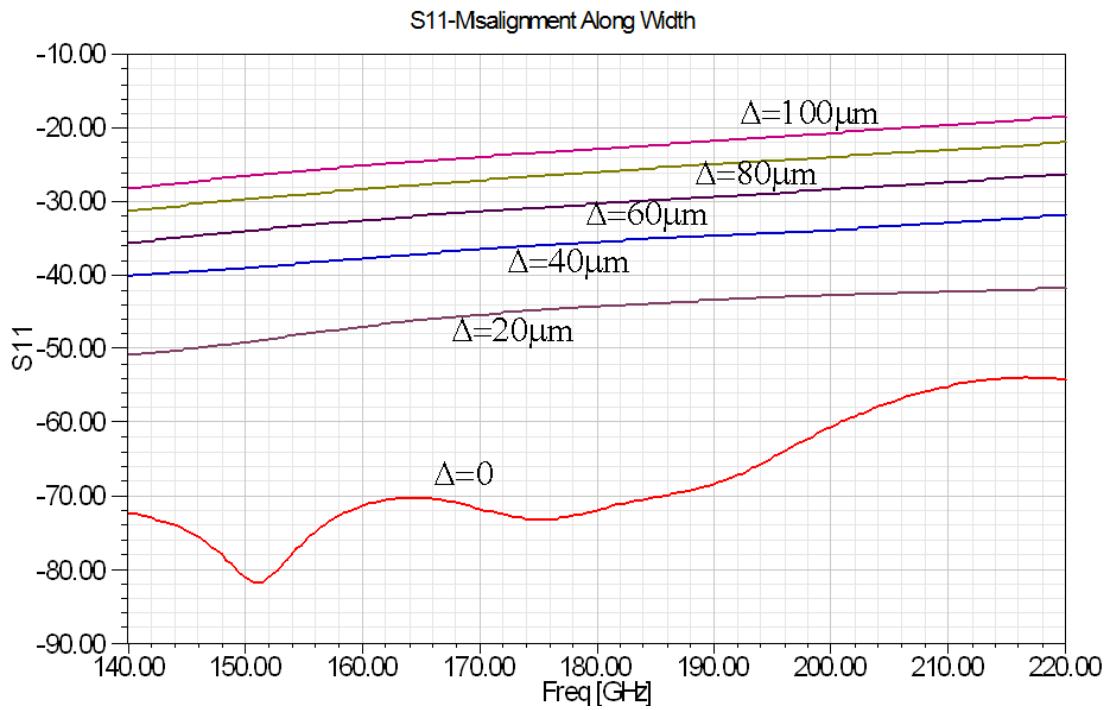


FIGURE 5.20: Simulated results of S_{11} for flanges misalignment $\Delta = 0 - 100 \mu\text{m}$ along their width.

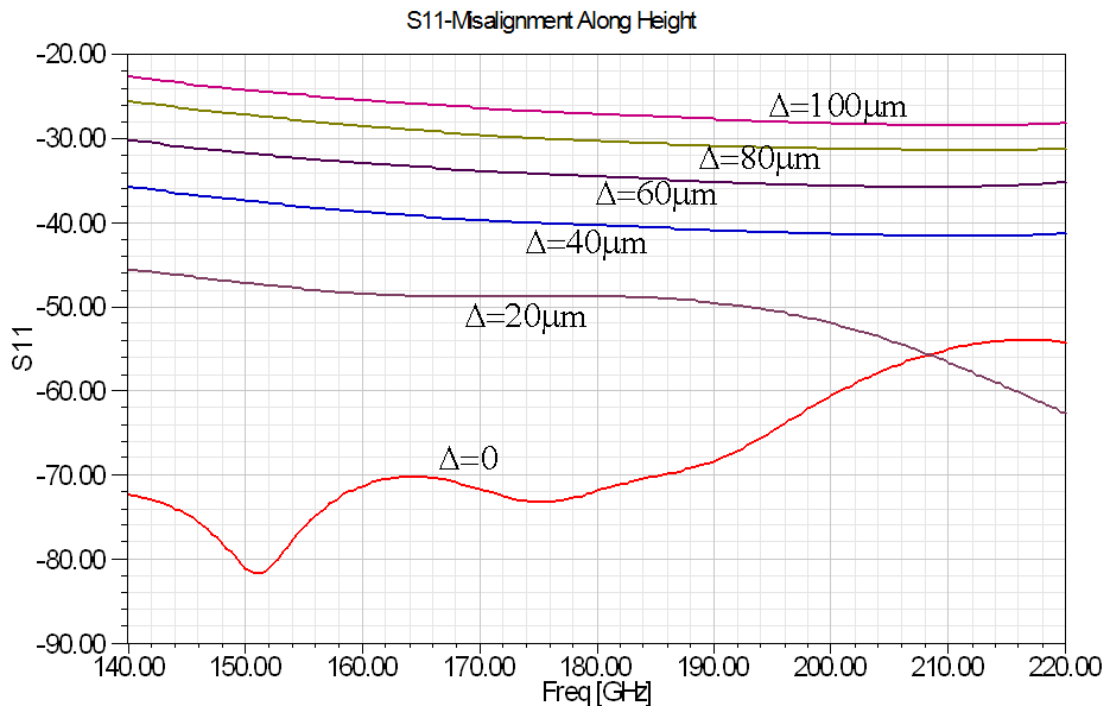


FIGURE 5.21: Simulated results of S_{11} for flanges misalignment from $\Delta = 0 - 100 \mu\text{m}$ along their height.

Before proceeding with the measurements of the transitions, there is a need to verify the correctness of the electrical contact between elevated structure, metal posts and on-substrate microstrip line. For this purpose, a series of elevated microstrip lines are designed and fabricated together with the *Elevated probes* on the same substrate sample. Figure 5.22 illustrates the design highlighting the transition from CPW to elevated microstrip. Mechanical stress can be induced on the metal posts when thinning the sub-

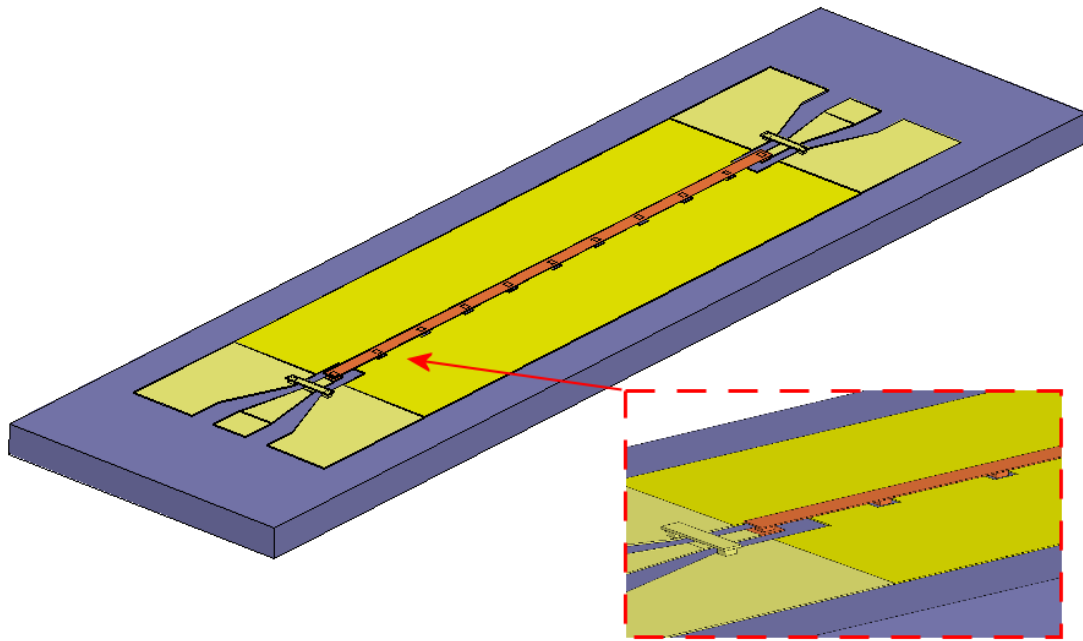


FIGURE 5.22: Design of Elevated microstrip line. The signal line is supported by a series of metal posts with $100\mu m$ spacing from each other. Posts land on GaAs material through a ground square cut-out. Airbridges are placed before the transition from CPW to elevated microstrip line.

strate down to $50\mu m$ with possible breakage of the electrical contact between elevated and on-substrate line. RFOV Measurements are used to confirm that S-parameters present similar behavior for both cases of $50\mu m$ and $630\mu m$ substrate thickness with the latter being mechanically more robust. The lines are measured using PNA, GSG coplanar probes from Cascade[©] with $100\mu m$ pitch.

Measured insertion loss, in terms of S_{21} , illustrated in Figure 5.23 for elevated microstrip lines $2.5mm$ long and relative to $630\mu m$ and $50\mu m$ GaAs thickness, demonstrates the effective signal propagation along the connecting posts. This result validates the robustness of the fabrication process with its extension to thin GaAs substrate and membrane. The measurements of Figure 5.23 also show the difference in insertion loss due to substrate thickness. Although the microstrip line is elevated from GaAs material and is shielded by the underneath ground, there is still signal power coupled into the substrate through the metal posts as they land on the bare substrate material through windows cut-out in the ground plane, Figure 5.22. The difference in insertion loss, being 1dB at

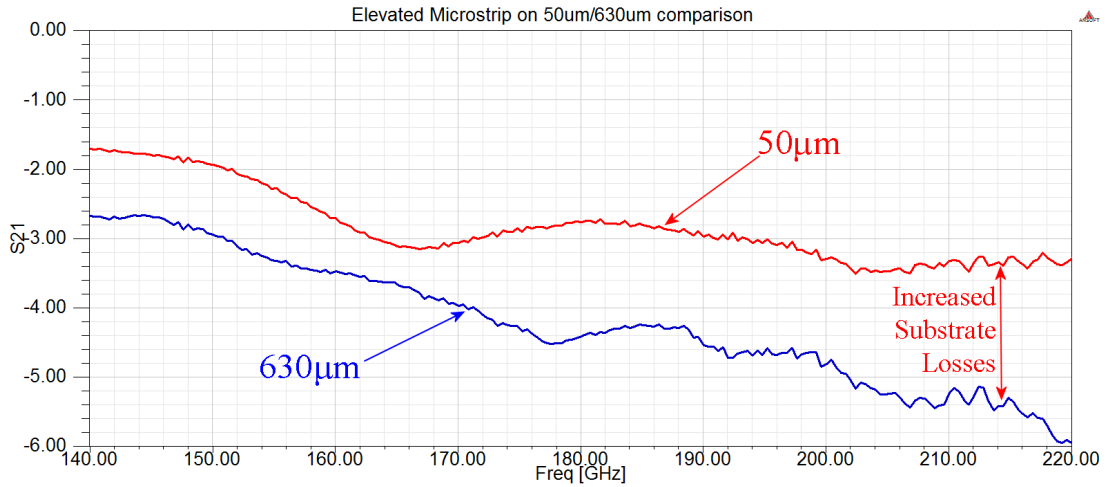


FIGURE 5.23: Measured S_{21} parameters for elevated microstrip lines on $630\mu m$ and $50\mu m$ of GaAs. The total length of the lines is $2.5mm$ which consists of $2mm$ of elevated line and two CPW transitions of $125\mu m$ each. The difference of the measurements is due to signal power spilled into the substrate. The effect is more and more evident with increasing frequency as more power can be coupled into substrate waves.

low frequency, increases in the upper part of the G-band due to the increased excitation of substrate waves.

Once the electrical contact of the posts was validated, the waveguide-to-microstrip transition assembled in Section 4.10, Figure 4.27, was connected to the PNA and measurements procedures were carried out.

Figure 5.24 shows the measured S-parameter S_{21} and S_{12} representing the insertion loss of two Elevated E-plane probes in back-to-back configuration and separated by $3mm$ of microstrip line. $S_{21} = -4dB$ is achieved at the center band $f = 180GHz$ which equates an insertion loss of $2dB$ per transition, including the losses of $1.5mm$ of microstrip line and a single waveguide S-bend. The result represents an improvement when compared to the insertion loss of the broadband transition as illustrated previously in Figure 5.18. Reflection loss is shown in Figure 5.25 where an $S_{11} \leq -10dB$ is achieved on a bandwidth $BW \simeq 150 - 200GHz$. Measured S-parameters and simulation results are compared in Figure 5.26 where they show good agreement.

Difference in level of S_{11} are due to flange misalignments between split-block housing and waveguide connections with the PNA. Difference in measured and simulated S_{21} also reflects the misalignment and it becomes more marked at the upper part of the G-band due to increased substrate losses.

In fact, GaAs material used in the simulations have nominal values for dielectric losses and dielectric constant ($\epsilon_r = 12.9$) which are generally used at a frequency of $f = 10GHz$. In reality the value is frequency dependent and no model is available so far in the simulator to accurately predict the variation of these nominal values.

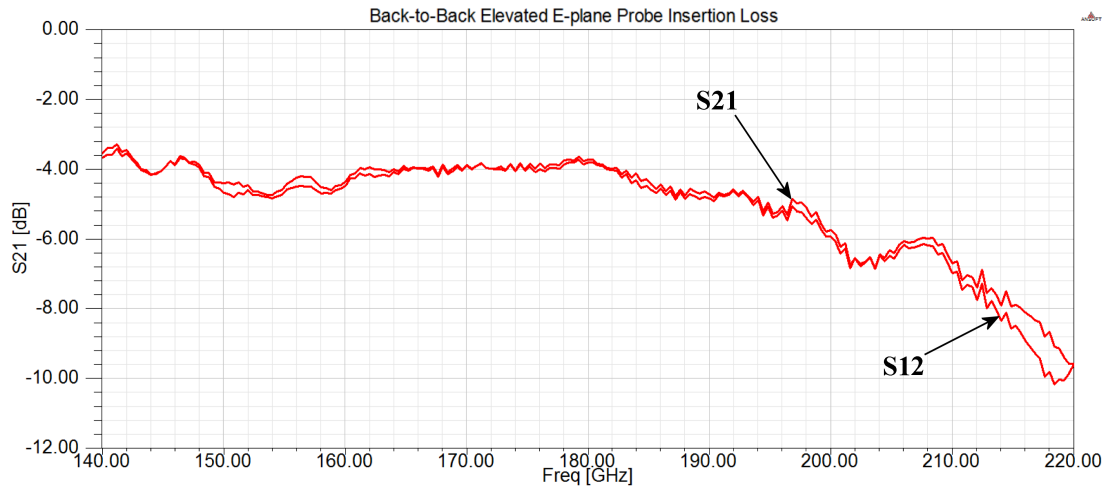


FIGURE 5.24: S_{21} and S_{12} measured results for the Elevated E-plane Probe operating as waveguide-to-microstrip transition in back-to-back configuration [80].

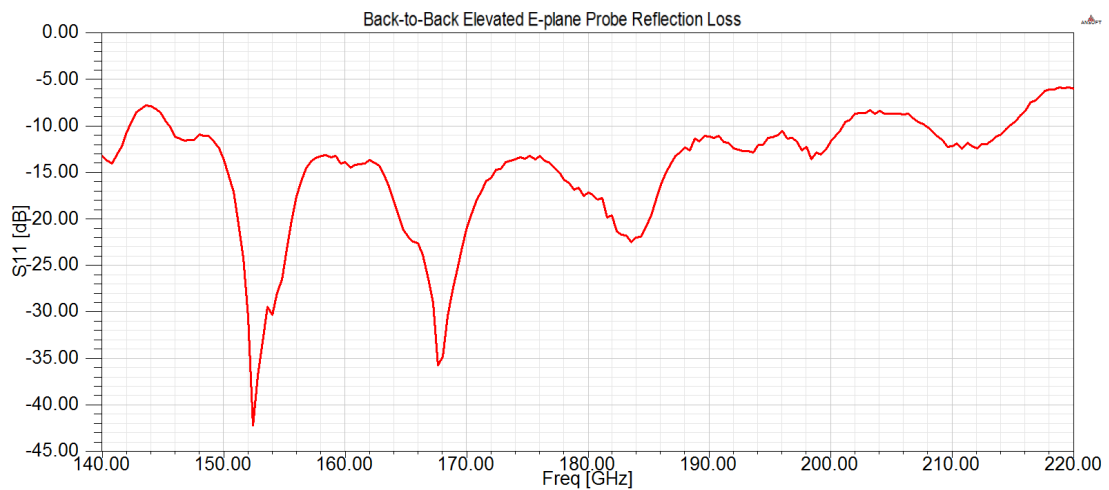


FIGURE 5.25: S_{11} measured results for the Elevated E-plane Probe operating as waveguide-to-microstrip transition in back-to-back configuration [80].

However, it would be possible to account for the material properties at MMW by measuring a GaAs printed transmission line and by using it as known standard to calibrate the values of dielectric losses and the permittivity of the substrate at these frequencies [81].

Some aspects of the fabrication have to be discussed to address the difference between measured and simulated results of S_{21} .

During the assembly process, silver epoxy is employed to attach the substrate material into the channel, whereas, in the simulation of the model, the gold microstrip ground is in perfect electric contact with the metal housing. Moreover, the quality of the bonding has an important role and becomes crucial [82] in avoiding unexpected losses between the microstrip ground and the metal housing. The bonding is carried out by hand and could present some irregularities and gaps compromising its conductivity, which is particularly required at the edge of the substrate channel aperture. If a bonding machine

was used the assembly process would be more accurate and controlled.

However, the measured results still follow the trend of the simulations and the overall waveguide-to-microstrip transitions show successful and acceptable performance using the Elevated E-plane probes.

The implementation of an Elevated probe, fabricated using MMICs processes, in a

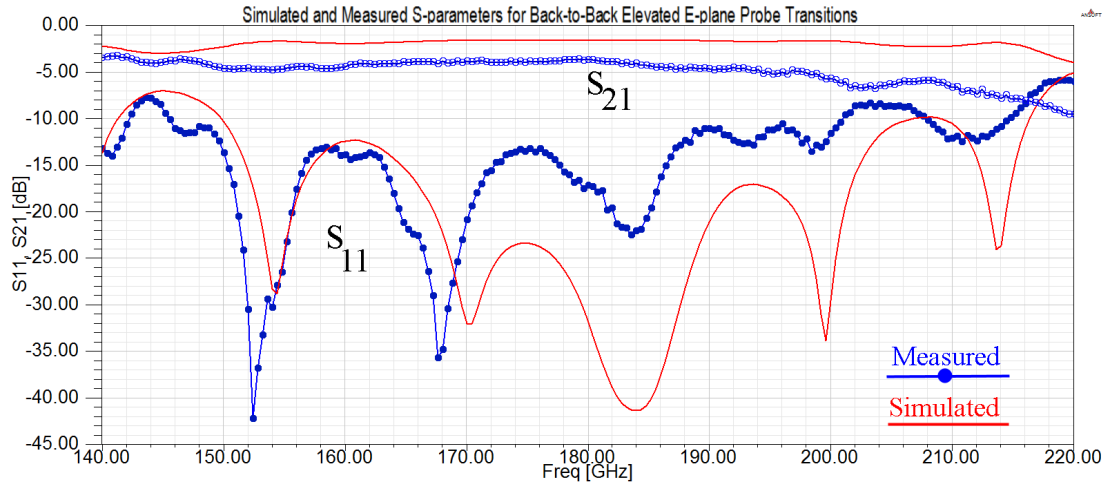


FIGURE 5.26: Measured and simulated results comparison for the Elevated E-plane Probe operating as waveguide-to-microstrip transition in back-to-back configuration [80].

waveguide-to-microstrip transition is demonstrated for the first time and it represents a *novel* structure [80]. The measurement results show S_{11} better than -10dB from 150GHz to 200GHz and $S_{21} \simeq -4dB$ at the centre of the G-band for two back-to-back waveguide-to-microstrip transition separated by 3mm of microstrip line. If a single waveguide-to-microstrip transition is used in a MMW receiver architecture, the Elevated E-plane probe allows a minimum reflection loss at $f = 183GHz$ as designed in Section 3.6.1 and 2dB of transmission loss including the microstrip path. The transition is a good candidate for the detection of signals in systems operating in the H_2O absorption band as highlighted in Section 1.2.1.

5.6.1 Estimation of Loss Factor in Waveguide Bends and Transitions

. The test fixture for the two Elevated E-plane probes, Figure 5.12, also comprises of two waveguide S-bends which are connected at the reference planes to the PNA. In order to evaluate the losses introduced by the bends in the overall performance of the back-to-back transitions, a single S-bend is designed and its CAD table is generated (Appendix C) for mechanical fabrication. A 3D perspective of the S-bend design and its manufacturing outcome is illustrated in Figure 5.27. Measurements are performed with PNA and S-parameters are extracted for the waveguide device. Simulated and measured

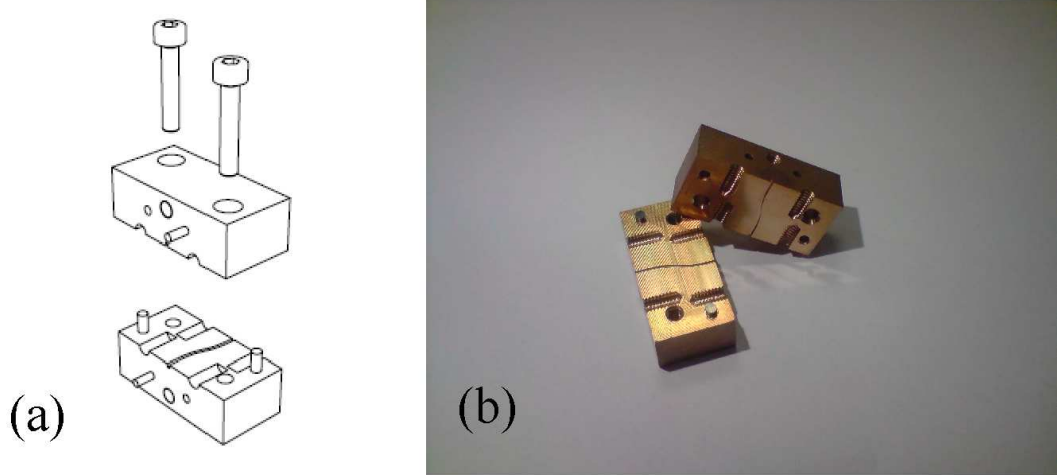


FIGURE 5.27: CAD perspective view of split-block G-band waveguide S-bend (a). Results of the CNC-milling fabrication of the S-bend(b).

results are compared and shown in Figure 5.28 and Figure 5.29 for parameters S_{11} and S_{21} respectively.

The simulated results account for flange misalignment between the device and the PNA waveguide extensions. Simulated S-parameters for an ideal situation of a device with no flange misalignment are also plotted and compared with the measured case. An estimation of an offset $\Delta x = 180\mu m$ along the waveguide width direction and an offset $\Delta y = 80\mu m$ along the height direction is accounted for in the simulation setup. The

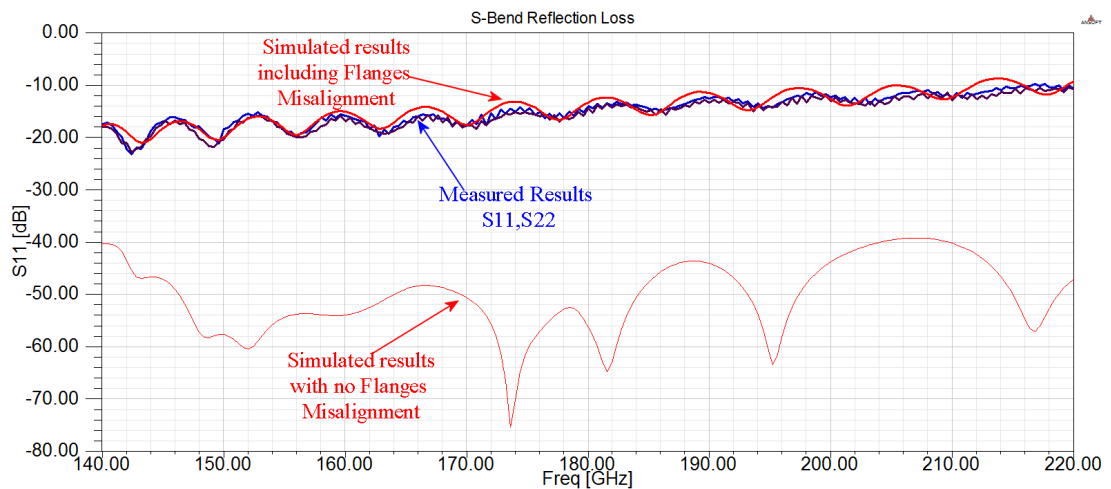


FIGURE 5.28: Measured and simulated S_{11} parameters for the split-block S-bend. The high level of reflection loss is due to flange misalignment. Simulated results for the case with no misalignment are also reported for comparison.

estimation of the losses due to the waveguide bends is calculated assuming no radiation losses for which the *Loss Factor*, α_L [83], can be equated as:

$$\alpha_L = 1 - |S_{11}|^2 - |S_{21}|^2 \quad (5.1)$$

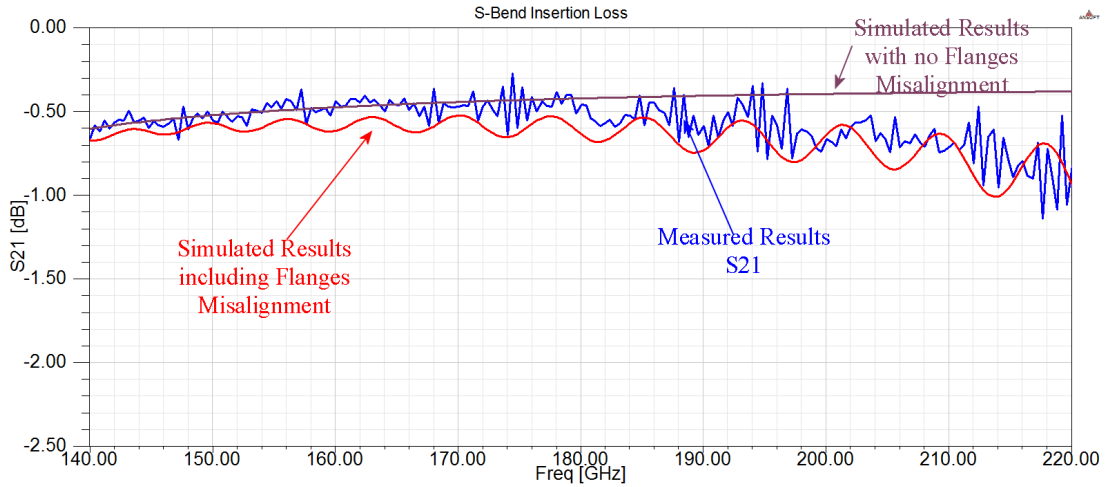


FIGURE 5.29: Measured and simulated S_{21} parameters for the split-block S-bend. Simulated results for the case with no misalignment are also reported for comparison.

Applying the equation to simulated and measured results, the Loss Factor can be plotted as in Figure 5.30. The loss factor is seen to equal the difference between a normalized in-

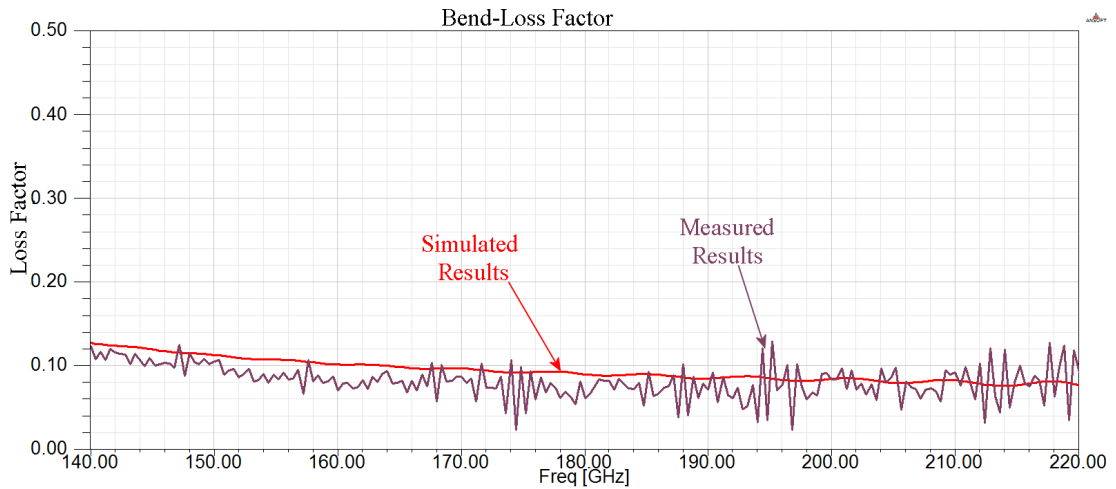


FIGURE 5.30: Loss Factor for the split-block S-bend relative to simulations and measurements results. Loss Factor de-embeds the reflection loss and insertion loss and reveals the effective losses due to finite conductivity and possible coupling with evanescent modes at the bend point.

put power and the power that is reflected and transmitted to the input and output ports, respectively. The mean value of the Loss Factor, $\overline{\alpha_L}$ across the G-band is calculated from the results and it measures:

$$\overline{\alpha_L} \simeq 0.1 \quad (5.2)$$

Representing the percentage of power loss in the waveguide bend.

Since the back-to-back transition is also a reciprocal structure, it is possible to isolate the flange misalignments and to calculate, by using (5.1), the loss factor from the measurements results of Figure 5.18 and Figure 5.26. Figure 5.31 illustrates that the

fabricated back-to-back elevated E-plane probe transitions present a loss factor lower than the broadband transitions. It is worth noting that the two back-to-back structures were fabricated and assembled using the same procedures and under the same conditions. Finally, accounting for the loss factor of Figure 5.2, due to the two waveguide

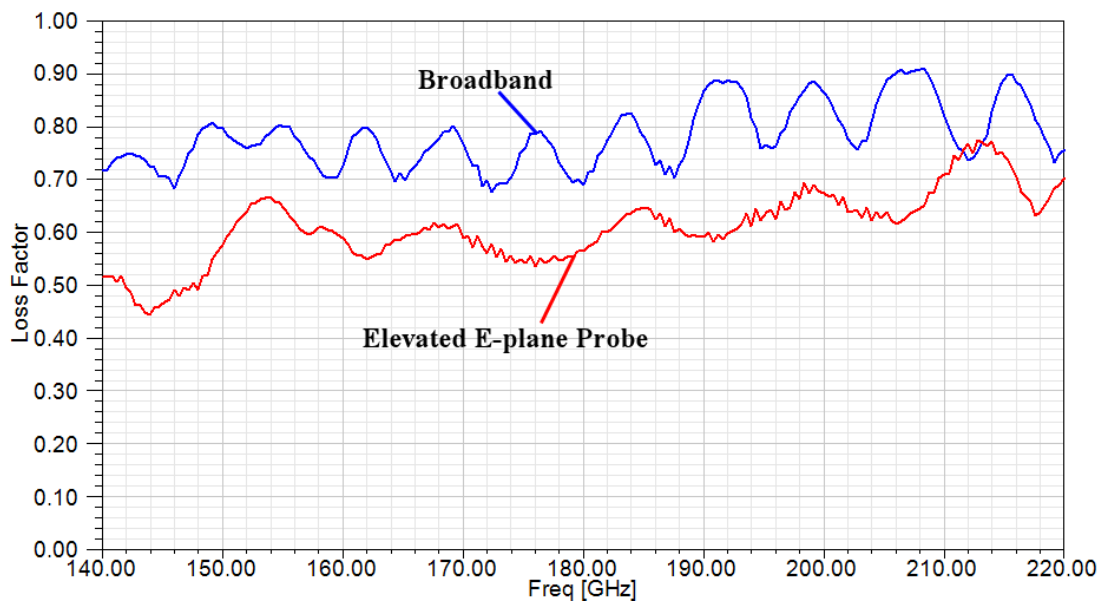


FIGURE 5.31: Loss Factor for back-to-back broadband (blue) and elevated E-plane probe (red) transitions.

bends, in the data of Figure 5.31, it is possible to plot the loss factor for single transition and 1.5mm of microstrip line as shown in Figure 5.32.

It is evident how the single elevated E-plane probe presents a lower loss factor than the single broadband waveguide to microstrip transition.

5.7 Conclusions

In the present chapter, instrumentation and preliminary calibration procedure for G-band waveguide measurements have been described. Fabricated split-block G-band waveguides are tested and measurement results validate the mechanical CNC milling process which allowed excellent transmission and reflection properties for the devices. Split-block housing, fabricated using the same milling process, is measured and the impact of substrate material and its edge, when used for the transition, is investigated through measurements. A broadband waveguide-to-microstrip transition is tested and measurements reveal that when waveguide flange misalignments are considerable with respect to the operating frequency this can be problematic. Their behavior is also evaluated through simulations highlighting the overall detrimental factor.

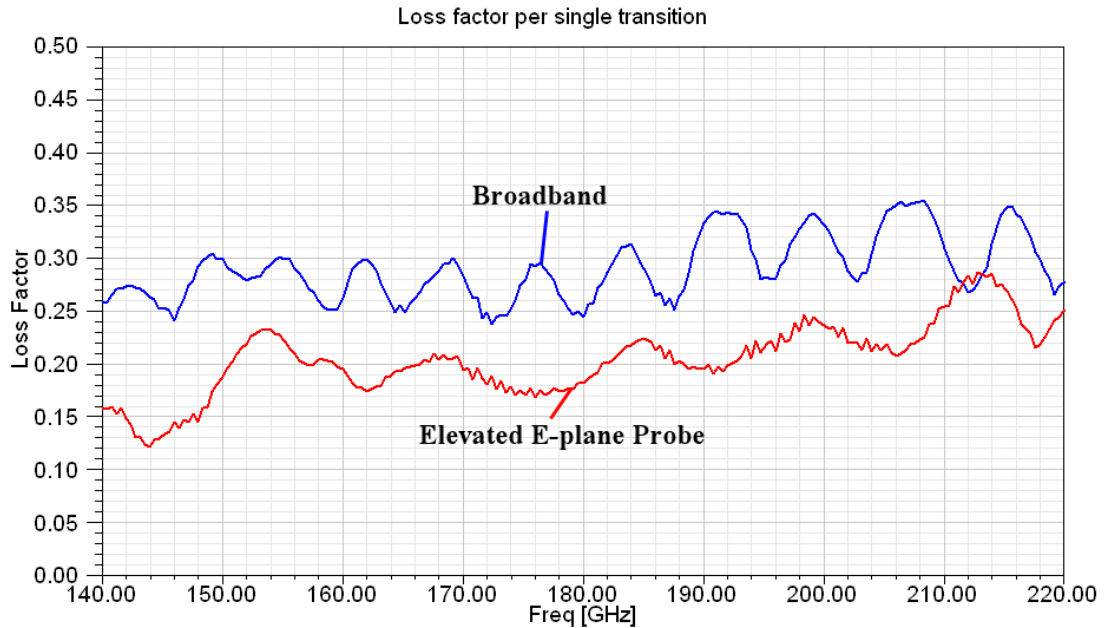


FIGURE 5.32: Loss Factor for single broadband (blue) and single elevated E-plane probe (red) transition.

The fabricated novel Elevated E-plane probe is used to realize a GaAs integrated waveguide-to-microstrip transition. Measurements validate the design and demonstrate its effectiveness when low power reflection levels are desired. A bandwidth of 150-200 GHz with reflection lower than -10dB is achieved, its lowest level at 183GHz measures -22dB. These measurements are relative to two waveguide-to-microstrip transitions in back-to-back configuration. The results make it an ideal candidate when implemented for EM detection in water vapor absorption band where signals power levels are dramatically attenuated.

Possible losses in the waveguide bends, used in the split-block housing, are estimated by measuring the reflection and transmission properties for a single fabricated waveguide bend also accounting for flanges misalignments.

Finally, from the measurements results, the loss factors for single waveguide bend, broadband transition and elevated E-plane probe transition are calculated and compared in order to estimate the loss factor due to a single transition.

Chapter 6

Conclusions and Future Work

6.1 Conclusions

This work presented a novel waveguide to microstrip transition operating in the G-band and featuring an Elevated E-plane probe. The transition has numerous advantages such as being GaAs-integrated and MMICs compatible meaning that its fabrication can be carried out in parallel with the rest of the RF circuits reducing processing and assembly time. The design of the Elevated E-plane probe was carried out with the aid of a full-wave EM solver called HFSS. Its fabrication involved a successful extension of the MMICs air-bridges technique which was optimized after several iterations delivering a stable result. An appropriate metal enclosure, in the form of split-block waveguides, was also designed aiming to house the transitions and to be connected to the measurement instruments. The Measurements agreed and validated the simulation results with very good correlation demonstrating that the Elevated E-plane probe provides lower reflection loss and good performance when compared to transition structures previously realised at the G-band. Moreover, the transition presents robustness to measurement inaccuracies due to critical dimensions and alignment which characterise the waveguides measurement setups for MMW. The potential of having a transition integrated with the MMICs should reduce the overall complexity when implemented as part of a front-end receiver and the Elevated E-plane probe proved to be an excellent option. The transition design and the selection of its architecture arise from pondered considerations and tradeoffs throughout the different chapters of this work.

The first chapter discussed the atmospheric properties at MMW and the phenomenology associated with it. Real-time imagers and their design parameters at system level were introduced, pointing out the benefits of an increased operating frequency on the performance and portability.

Prototypes and initial examples of imagers developed at QinetiQ were then discussed, commenting on the technology implemented. The chapter ended highlighting the importance of the interconnections between different parts of the system such as waveguides and RF circuits and how they affect the sensitivity of the receiver. Hence, the design of a transition between rectangular waveguide and RF circuits should aim to low reflection loss to guarantee decent level of receiver sensitivity.

The second chapter presented an extensive literature review on the various architectures previously used to design waveguide to planar line transitions discussing advantages and disadvantages for the different cases and providing a table listing characteristics such as substrate materials, bandwidth, performance and assembly. The table also included the waveguide to microstrip transition using the Elevated E-plane probe developed in this work.

Chapter 3 provided an insight into design techniques used to model a waveguide to microstrip lines focusing on the use of antipodal fin-lines, printed dipoles and transversal probes. Both antipodal fin-line and dipoles represents good options in realizing a transition. However, they are strongly influenced by substrate resonances and poor impedance matching levels when the design has limiting specifications such as the use of high permittivity materials and when the use of very thin substrates is required, in which case fabrication becomes complex and unreliable.

There is not a defined formula to design waveguide to microstrip transitions and there are several parameters involved in the structure which require the use of EM simulation software such as HFSS, from Ansys. A high level of expertise is required to drive the software and to properly set up the EM problem with relative excitations and boundary conditions. HFSS is a full wave 3D FEM solver and requires computers with large amount of RAM memory and high speed processors. An extensive number of simulations and iterations were carried out to model the transitions and to extract the tuning effects of the different variables involved.

Transversal transitions were also considered and a broadband design was modeled and simulated, highlighting the fundamental design parameters and their influence when impedance matching had to be accomplished over the entire G-band.

From this example, the novel structure of waveguide to microstrip transition using Elevated E-plane Probe was conceived. The peculiarities of the structure is the elevation height of the probe that allows us the decomposition of the interaction of the substrate material with the probe structure. The elevation of the probe represents an additional tuning parameter which allows one to achieve a wider variety of impedance matching levels than the canonical printed probe. The design is optimized for 183GHz, a critical frequency in the G-band, where the EM radiation is strongly attenuated due to water vapor absorption band.

The fourth chapter discussed processes and machines used in the MMICs technology at

the University of Glasgow. E-beam, photolithography, metals evaporation and wet-etch processes are all used in the fabrication of the Elevated E-plane probe and for substrate processing. The fabrication involved several iterations before achieving a defined and reliable procedure to manufacture waveguide transitions.

G-band split-block waveguides were also designed and the manufacture was carried out in-house with the aid of the Mechanical Workshop personnel. Precise milling tools and processes allowed us to realize G-band waveguide lines and split-block carriers proving that the overall device was conceivable without the use of external facilities.

Device separation and assembly represent the final and crucial steps where precise alignment is necessary so that measurements reveal the desired performance of the transition. Chapter 5 describes the instruments and procedures used to carry out waveguide measurements at G-band. PNA, tools and calibration are described in detail.

A series of measurements were performed on rectangular waveguide lines with different lengths to validate the mechanical fabrication and to estimate the expected losses. Measurements were also carried out on the waveguide split-block carrier to confirm the isolation between input and output waveguides and to validate the EM design.

The broadband waveguide to microstrip transition designed in Chapter 3, including matching network, is measured using PNA and results show that this type of transition, although it works over the full G-band delivers return loss worse than the 10dB, minimum value generally required for signals to be processed by RF circuits. The performance is adversely affected by the detrimental waveguide flange misalignment due to unavoidable mechanical tolerances. Simulation of the misalignment effect is also modeled and results confirm the worsening of the return loss by increasing the level of misalignment. As mechanical manufacturing of the components at G-band presents these type of pitfalls, it is necessary to design a waveguide to microstrip transition that provides lower return loss so that the effects of possible flange misalignment do not mask the performance of the transition to a level where the components is no longer effective.

The Elevated E-plane probe designed and fabricated presents a good performance over the G-band having a wide passband $\Delta f = 150 - 200GHz$ with return loss better than 10dB. Measurements show that the lowest level of return loss is achieved at 183GHz as defined by the design process.

To our knowledge, the Elevated E-plane probe is a novel structure and it is presented for the first time in this thesis. Since the transition was tested in back-to-back configuration and the split-block carrier consisted of waveguide bends, a single split-block waveguide bend was also designed, fabricated and measured. Again the effects of flange misalignment were detected. Additional models and simulations of misalignments were made and results were compared with measurements confirming the level of transmitted and reflected power. Loss factor was used to estimate the loss level due to the implemented waveguide bends at G-band.

As a final result, the waveguide to microstrip transition using Elevated E-plane probe on SI-GaAs presents good performance and his high level of integration when used in a receiver module for MMW applications would certainly contribute to improvements in the overall system performance. The consequent reduction of complexity during assembly and the smaller volume occupied by the MMICs represent desirable conditions to avoid possible internal package resonances, which represent additional issues to address in the design of circuits at high frequency.

6.2 Future Developments

Although the research for this thesis has been extensive, there are still some aspects that need to be explored and can be proposed for future work:

- The integration of the Elevated E-plane probe with a G-band amplifier in order to build a full receiver module. MMICs G-band amplifiers on GaAs are still in the experimental phase at the University of Glasgow.
- The design and fabrication of a narrow band filter cascaded with the transition in order to filter out all the spectral components at G-band apart from the range of frequencies covering the water vapor absorption band. This would enable us to selectively amplify only the spectral components most attenuated.
- Recently [13] it was possible to improve detectors' sensitivity by using other substrate such as antimonide-based material rather than GaAs. It would be interesting to investigate the possibility of reducing the total dimension of a receiver module, including the detector stage, by implementing the *flip-chip* technology [84]. So this would enable the metal cavity housing the MMICs to be small and minimize substrate modes.
- The use of a different shape for the waveguide flanges could improve measurements effectiveness and they could also be implemented in multi-stage systems whenever modularity is desired.

Recent developments have been made in this direction and new standards for the flange profile have been adopted for frequencies above 110GHz, trying to better address misalignments issues, some examples are shown in Figure 6.1 [85].

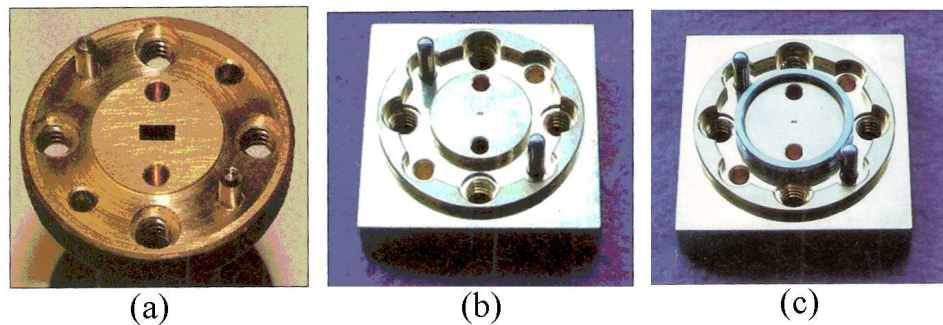


FIGURE 6.1: New waveguide flange standard IEEE P1785 (a)-(c) proposed for next generation waveguide fabrication

Appendix A

Rectangular Waveguide Theory

A.1 Modes and Propagation

A.1.1 From Maxwell's Equations to TE/TM/TEM

The electric and magnetic fields associated with a time harmonic source of radiation need to satisfy the Maxwell's Equations in the phasor form:

$$\nabla \times \underline{E} = -j\omega\mu\underline{H} \quad (\text{A.1})$$

$$\nabla \times \underline{H} = j\omega\varepsilon\underline{E} \quad (\text{A.2})$$

The source free equation can be manipulated into wave equations for the electric and magnetic fields:

$$\nabla^2 \underline{E} + k^2 \underline{E} = 0$$

$$\nabla^2 \underline{H} + k^2 \underline{H} = 0$$

$$k = \omega\sqrt{\mu\varepsilon}$$

where the wavenumber k is real-valued for lossless media and is complex for lossy media. The electric and magnetic fields of a general wave propagating in the $+z$ direction into an arbitrary medium with propagating constant γ are characterized by a z -dependence

$e^{-\gamma z}$. The electric and magnetic fields can be then written in rectangular coordinates:

$$\underline{E}(x, y, z) = \underline{E}(x, y)e^{-\gamma z}$$

$$\underline{H}(x, y, z) = \underline{H}(x, y)e^{-\gamma z}$$

$$\gamma = \alpha + j\beta$$

where α is the wave attenuation constant and β is the phase constant. If the wave travels without attenuation, the propagation constant is purely imaginary. From the expansion of the curl operator of the source-free Maxwell's equations in rectangular coordinates, the derivatives of the transverse field components respect to z can be written as:

$$\frac{\partial \underline{E}_x}{\partial z} = -\gamma \underline{E}_x \quad \frac{\partial \underline{E}_y}{\partial z} = -\gamma \underline{E}_y$$

$$\frac{\partial \underline{H}_x}{\partial z} = -\gamma \underline{H}_x \quad \frac{\partial \underline{H}_y}{\partial z} = -\gamma \underline{H}_y$$

Equating the vector components on each side of the Maxwell curl equations it gives:

$$j\omega\varepsilon \underline{E}_x = \frac{\partial \underline{H}_z}{\partial y} + \gamma \underline{H}_y \quad (\text{A.3a})$$

$$j\omega\varepsilon \underline{E}_y = -\gamma \underline{H}_x - \frac{\partial \underline{H}_z}{\partial x} \quad (\text{A.3b})$$

$$j\omega\varepsilon \underline{E}_z = \frac{\underline{H}_y}{\partial x} - \frac{\partial \underline{H}_x}{\partial y} \quad (\text{A.3c})$$

$$-j\omega\mu \underline{H}_x = \frac{\partial \underline{E}_z}{\partial y} + \gamma \underline{E}_y \quad (\text{A.4a})$$

$$-j\omega\mu \underline{H}_y = -\gamma \underline{E}_x - \frac{\partial \underline{E}_z}{\partial x} \quad (\text{A.4b})$$

$$-j\omega\mu \underline{H}_z = \frac{\partial \underline{E}_y}{\partial x} - \frac{\partial \underline{E}_x}{\partial y} \quad (\text{A.4c})$$

These equations can be manipulated to solve for the longitudinal field components in terms of the transverse field components.

$$\text{solving A.3a and A.4b for } \underline{H}_y \quad \underline{E}_x = \frac{1}{h^2} \left(-\gamma \frac{\partial \underline{E}_z}{\partial x} - j\omega\mu \frac{\partial \underline{H}_z}{\partial y} \right)$$

$$\text{solving A.3b and A.4a for } \underline{H}_x \quad \underline{E}_y = \frac{1}{h^2} \left(-\gamma \frac{\partial \underline{E}_z}{\partial y} + j\omega\mu \frac{\partial \underline{H}_z}{\partial x} \right)$$

TABLE A.1: Propagation modes and relative longitudinal field conditions

Mode	Fields Components	Propagation Type
TEM Transverse Electromagnetic	$\underline{E}_z = 0, \underline{H}_z = 0$	Plane waves, Transmission line
TE Transverse Electric	$\underline{E}_z = 0, \underline{H}_z \neq 0$	Waveguide
TM Transverse Magnetic	$\underline{E}_z \neq 0, \underline{H}_z = 0$	Waveguide
EH/HE Hybrid	$\underline{E}_z \neq 0, \underline{H}_z \neq 0$	Waveguide

solving A.3b and A.4a for \underline{E}_y $\underline{H}_x = \frac{1}{h^2} \left(j\omega\varepsilon \frac{\partial \underline{E}_z}{\partial y} - \gamma \frac{\partial \underline{H}_z}{\partial x} \right)$

solving A.3a and A.4b for \underline{E}_x $\underline{H}_y = \frac{1}{h^2} \left(-j\omega\varepsilon \frac{\partial \underline{E}_z}{\partial x} - \gamma \frac{\partial \underline{H}_z}{\partial y} \right)$

where the constant h is defined by:

$$h^2 = \gamma^2 + \omega^2 \mu \varepsilon = \gamma^2 + k^2 \quad \implies \quad \gamma = \sqrt{h^2 - k^2}$$

The equations for the transverse field components in terms of the longitudinal components describe the different modes for guided/unguided wave propagation as summarised in Table A.1.

Let's consider the case of a guided or unguided waves propagating in an ideal lossless medium and assume the propagations of TEM modes respecting the conditions from Table A.1. The only case in which those conditions can be respected together with non-zero field transverse components is having:

$$\gamma = \sqrt{-k^2} = jk = \alpha + j\beta \implies (\alpha = 0 \text{ lossless medium}) \implies \beta = k$$

Thus for TEM waves travelling along a lossless medium/transmission line we have:

$$\gamma = jk = j\beta$$

Oppositely, considering a TE, TM or EH/HE propagating modes it has to be $h \neq 0$ to have finite transverse field components, hence $\beta \neq k$. The propagation constant for these modes can be written as:

$$\gamma = \sqrt{h^2 - k^2} = \sqrt{-k^2 \left(1 - \frac{h^2}{k^2} \right)} = jk \sqrt{1 - \left(\frac{h}{k} \right)^2}$$

The propagation constant of TE or TM modes has got different characteristics from the

propagation constant for TEM modes. The ratio h/k for TE and TM can be written in terms of *cut-off frequency* f_c as follows:

$$\frac{h}{k} = \frac{h}{\omega\sqrt{\varepsilon\mu}} = \frac{h}{2\pi f\sqrt{\varepsilon\mu}} = \frac{f_c}{f}$$

$$f_c = \frac{h}{2\pi\sqrt{\varepsilon\mu}}$$

The waveguide propagation constant in terms of the cut-off frequency can be written as:

$$\gamma = jk\sqrt{1 - \left(\frac{f_c}{f}\right)^2}$$

The propagation constant reveals if the relative mode propagates or it is attenuated in which case it is called *evanescent* mode.

$$f \leq f_c \implies \gamma = \alpha \quad \text{purely real value} \quad e^{-\gamma z} = e^{-\alpha z} \quad \text{evanescent mode}$$

$$f > f_c \implies \gamma = j\beta \quad \text{purely imaginary value} \quad e^{-\gamma z} = e^{-j\beta z} \quad \text{propagating mode}$$

Hence, to have a propagating mode the operating frequency of the source has to be higher than the cut-off frequency. If the operating frequency is lower than the cut-off frequency then the mode is *evanescent* and is attenuated with an attenuation constant equal to α .

A.1.2 Modes in Rectangular Waveguides

The rectangular waveguide can support TE and TM modes. The rectangular cross-section with $a > b$ allows for single -mode operation, meaning that only one mode propagates in the waveguide over a determined frequency band.

Rectangular Waveguide TM modes

The longitudinal electric field of the TM modes within rectangular waveguide is the solution to the equation:

$$\nabla^2 \underline{E}_z^{TM} + k^2 \underline{E}_z^{TM} = 0$$

the equation can be expanded in rectangular coordinates as:

$$\frac{\partial \underline{E}_z^{TM}}{\partial x^2} + \frac{\partial \underline{E}_z^{TM}}{\partial y^2} + \frac{\partial \underline{E}_z^{TM}}{\partial z^2} + k^2 \underline{E}_z^{TM} = 0 \quad (\text{A.5})$$

The electric field can be determined by using the separation of variables technique and assuming that the solution has the form:

$$\underline{E}_z^{TM} = X(x)Y(y)e^{-j\beta z} \quad (\text{A.6})$$

by substituting this into A.5 we have:

$$Y(y) \frac{d^2 X(x)}{dx^2} e^{-j\beta z} + X(x) \frac{d^2 Y(y)}{dy^2} e^{-j\beta z} + (k^2 - \beta^2) X(x) Y(y) e^{-j\beta z} = 0 \quad (\text{A.7})$$

$$Y(y) \frac{d^2 X(x)}{dx^2} e^{-j\beta z} + X(x) \frac{d^2 Y(y)}{dy^2} e^{-j\beta z} + h^2 X(x) Y(y) e^{-j\beta z} = 0 \quad (\text{A.8})$$

where $h^2 = \gamma^2 + k^2 = k^2 - \beta^2$. By dividing A.8 by A.6 it gives:

$$\frac{1}{X(x)} \frac{d^2 X(x)}{dx^2} + \frac{1}{Y(y)} \frac{d^2 Y(y)}{dy^2} + h^2 = 0 \quad (\text{A.9})$$

This result has the first term as a function of x and the second term as function of y only. In order for A.9 to be satisfied for every x and every y within the waveguide, each of the first two terms in the equation must be constants.

$$\frac{1}{X(x)} \frac{d^2 X(x)}{dx^2} = -k_x^2 \quad \implies \quad \frac{d^2 X(x)}{dx^2} + k_x^2 X(x) = 0 \quad (\text{A.10})$$

$$\frac{1}{Y(y)} \frac{d^2 Y(y)}{dy^2} = -k_y^2 \quad \implies \quad \frac{d^2 Y(y)}{dy^2} + k_y^2 Y(y) = 0 \quad (\text{A.11})$$

$$h^2 = k_x^2 + k_y^2 \quad (\text{separation equation}) \quad (\text{A.12})$$

The original second order partial differential equation A.8 in two variables has been separated into two second order ordinary differential equations in one variable each. The two general solutions are:

$$X(x) = A \sin k_x x + B \cos k_x x \quad (\text{A.13})$$

$$Y(y) = C \sin k_y y + D \cos k_y y \quad (\text{A.14})$$

hence the resulting longitudinal electric field for a rectangular waveguide TM mode is:

$$E_z^{TM}(x, y, z) = (A \sin k_x x + B \cos k_x x)(C \sin k_y y + D \cos k_y y) e^{-j\beta z}$$

The TM boundary conditions for the rectangular waveguide are:

$$E_z^{TM}(0, y, z) = E_z^{TM}(a, y, z) = 0$$

$$E_z^{TM}(x, 0, z) = E_z^{TM}(x, b, z) = 0$$

By applying the boundary conditions it gives:

$$E_z^{TM}(0, y, z) = 0 \quad \Longrightarrow \quad B = 0$$

$$E_z^{TM}(a, y, z) = 0 \quad \Longrightarrow \quad k_x a = m\pi \quad (m = 1, 2, 3, \dots) \quad \Longrightarrow \quad k_x = \frac{m\pi}{a}$$

$$E_z^{TM}(x, 0, z) = 0 \quad \Longrightarrow \quad D = 0$$

$$E_z^{TM}(x, b, z) = 0 \quad \Longrightarrow \quad k_y b = n\pi \quad (n = 1, 2, 3, \dots) \quad \Longrightarrow \quad k_y = \frac{n\pi}{b}$$

The resulting product of the constants A and C can be written as a single constant E_0 . The number of TM modes is infinite, based on the infinite possible values of the indices m and n. A single TM mode is identified as TM_{mn} mode. The longitudinal electric field of the TM_{mn} mode is given by:

$$E_z^{TM_{mn}}(x, y, z) = E_0 \sin \frac{m\pi x}{a} \sin \frac{n\pi y}{b} e^{-j\beta z}$$

$$(m = 1, 2, 3, \dots)$$

$$(n = 1, 2, 3, \dots)$$

The transverse field components of the TM_{mn} mode are found by differentiating the longitudinal electric field as defined in the standard TM equations:

$$E_x^{TM_{mn}}(x, y, z) = -\frac{j\beta}{h^2} \frac{\partial E_z^{TM_{mn}}}{\partial x} = -\frac{j\beta}{h^2} \left(\frac{m\pi}{a} \right) E_0 \cos \frac{m\pi x}{a} \sin \frac{n\pi y}{b} e^{-j\beta z}$$

$$E_y^{TM_{mn}}(x, y, z) = -\frac{j\beta}{h^2} \frac{\partial E_z^{TM_{mn}}}{\partial y} = -\frac{j\beta}{h^2} \left(\frac{n\pi}{b} \right) E_0 \sin \frac{m\pi x}{a} \cos \frac{n\pi y}{b} e^{-j\beta z}$$

$$H_x^{TM_{mn}}(x, y, z) = \frac{j\omega\varepsilon}{h^2} \frac{\partial E_z^{TM_{mn}}}{\partial y} = \frac{j\omega\varepsilon}{h^2} \left(\frac{n\pi}{b} \right) E_0 \sin \frac{m\pi x}{a} \cos \frac{n\pi y}{b} e^{-j\beta z}$$

$$H_y^{TM_{mn}}(x, y, z) = -\frac{j\omega\varepsilon}{h^2} \frac{\partial E_z^{TM_{mn}}}{\partial x} = -\frac{j\omega\varepsilon}{h^2} \left(\frac{m\pi}{a} \right) E_0 \cos \frac{m\pi x}{a} \sin \frac{n\pi y}{b} e^{-j\beta z}$$

Rectangular Waveguide TE modes

The longitudinal magnetic field of the TE mode in the rectangular waveguide needs to satisfy the same wave equation as the longitudinal field of the TM modes as:

$$\nabla^2 \underline{H}_z^{TE} + k^2 \underline{H}_z^{TE} = 0$$

which in rectangular coordinates is:

$$\frac{\partial \underline{H}_z^{TE}}{\partial x^2} + \frac{\partial \underline{H}_z^{TE}}{\partial y^2} + \frac{\partial \underline{H}_z^{TE}}{\partial z^2} + k^2 \underline{H}_z^{TE} = 0 \quad (\text{A.15})$$

Using the same technique of the separation of variables used for the longitudinal TM electric field, but applied to the longitudinal TE magnetic field it gives:

$$H_z^{TE}(x, y, z) = (A \sin k_x x + B \cos k_x x)(C \sin k_y y + D \cos k_y y) e^{-j\beta z}$$

To determine the unknown coefficients, the TE boundary conditions must be enforced. They are:

$$E_y^{TE}(0, y, z) = E_y^{TE}(a, y, z) = 0$$

$$E_x^{TE}(x, 0, z) = E_x^{TE}(x, b, z) = 0$$

The transverse components of the TE electric field are related to longitudinal magnetic field by the standard TE equations:

$$E_x^{TE} = -\frac{j\omega\mu}{h^2} \frac{\partial H_z^{TE}}{\partial y} = -\frac{j\omega\mu}{h^2} k_y (A \sin k_x x + B \cos k_x x) (C \cos k_y y - D \sin k_y y) e^{-j\beta z}$$

$$E_y^{TE} = \frac{j\omega\mu}{h^2} \frac{\partial H_z^{TE}}{\partial x} = \frac{j\omega\mu}{h^2} k_x (A \cos k_x x + B \sin k_x x) (C \sin k_y y - D \cos k_y y) e^{-j\beta z}$$

The application of the TE boundary conditions gives:

$$E_x^{TE}(x, 0, z) = 0 \quad \Longrightarrow \quad C = 0$$

$$E_x^{TE}(x, b, z) = 0 \quad \Longrightarrow \quad k_y b = n\pi \quad (n = 0, 1, 2, 3, \dots) \quad \Longrightarrow \quad k_y = \frac{n\pi}{b}$$

$$E_y^{TE}(0, y, z) = 0 \quad \Longrightarrow \quad A = 0$$

$$E_y^{TE}(a, y, z) = 0 \quad \Longrightarrow \quad k_x a = m\pi \quad (m = 0, 1, 2, 3, \dots) \quad \Longrightarrow \quad k_x = \frac{m\pi}{a}$$

Combining the constant B and D into a single constant H_0 the resulting longitudinal magnetic field of the TE_{mn} mode is:

$$H_z^{TE_{mn}}(x, y, z) = H_0 \cos \frac{m\pi x}{a} \cos \frac{n\pi y}{b} e^{-j\beta z}$$

$$(m = 1, 2, 3, \dots)$$

$$(n = 1, 2, 3, \dots)$$

$$(m = n \neq 0)$$

The indices include $m = 0$ and $n = 0$ in the TE solution since these values still yield a non-zero longitudinal magnetic field. The case $m=n=0$ is not allowed as this gives all of

the transverse field components zero. The transverse fields for the TE modes are:

$$E_x^{TE_{mn}}(x, y, z) = -\frac{j\omega\mu}{h^2} \frac{\partial H_z^{TE_{mn}}}{\partial y} = \frac{j\omega\mu}{h^2} \left(\frac{n\pi}{b}\right) H_0 \cos\frac{m\pi x}{a} \sin\frac{n\pi y}{b} e^{-j\beta z}$$

$$E_y^{TE_{mn}}(x, y, z) = \frac{j\omega\mu}{h^2} \frac{\partial H_z^{TE_{mn}}}{\partial x} = -\frac{j\omega\mu}{h^2} \left(\frac{m\pi}{a}\right) H_0 \sin\frac{m\pi x}{a} \cos\frac{n\pi y}{b} e^{-j\beta z}$$

$$H_x^{TE_{mn}}(x, y, z) = -\frac{j\beta}{k_c^2} \frac{\partial H_z^{TE_{mn}}}{\partial x} = \frac{j\beta m\pi}{k_c^2 a} H_0 \sin\frac{m\pi x}{a} \cos\frac{n\pi y}{b} e^{-j\beta z}$$

$$H_y^{TE_{mn}}(x, y, z) = -\frac{j\beta}{k_c^2} \frac{\partial H_z^{TE_{mn}}}{\partial y} = \frac{j\beta n\pi}{k_c^2 b} H_0 \cos\frac{m\pi x}{a} \sin\frac{n\pi y}{b} e^{-j\beta z}$$

where (m=0,1,2,...) and (n=0,1,2,...) but m=n≠0 for the TE_{mn} mode.

Parameters of TE and TM modes in rectangular waveguide

The propagation constant for TE_{mn} and TM_{mn} is defined as:

$$\begin{aligned}\gamma_{mn} &= \sqrt{h_{mn}^2 - k^2} = \sqrt{(k_x^2 + k_y^2) - k^2} \\ h_{mn} &= \sqrt{k_x^2 + k_y^2} = \sqrt{\left(\frac{m\pi}{a}\right)^2 + \left(\frac{n\pi}{b}\right)^2} \\ \gamma_{mn} &= \sqrt{\left(\frac{m\pi}{a}\right)^2 + \left(\frac{n\pi}{b}\right)^2 - k^2} = \sqrt{\left(\frac{m\pi}{a}\right)^2 + \left(\frac{n\pi}{b}\right)^2 - w^2\mu\varepsilon}\end{aligned}$$

The equation of the propagation constant γ_{mn} can be used to find the cut-off frequency of the waveguide modes. The propagation characteristics are determined by the values of h_{mn} and k .

$$\text{if } h_{mn} = k \implies \gamma_{mn} = 0 \implies \text{cut-off frequency}$$

$$\text{if } h_{mn} > k \implies \gamma_{mn} \in \Re \implies \text{evanescent modes}$$

$$\text{if } h_{mn} < k \implies \gamma_{mn} \in \Im \implies \text{Propagating modes}$$

Therefore the cut-off frequencies for the TE and TM modes in the rectangular waveguide are found solving the equation:

$$\begin{aligned}h_{mn} &= \sqrt{\left(\frac{m\pi}{a}\right)^2 + \left(\frac{n\pi}{b}\right)^2} = k_{c_{mn}} = 2\pi f_{c_{mn}} \sqrt{\mu\varepsilon} \\ f_{c_{mn}} &= \frac{1}{2\sqrt{\mu\varepsilon}} \sqrt{\left(\frac{m}{a}\right)^2 + \left(\frac{n}{b}\right)^2}\end{aligned}$$

It has to be noticed that the cut-off frequency depends on the dimensions of the waveguide (a, b), the material inside the waveguide (ε, μ) and the mode (m, n).

The rectangular waveguide has to operate at frequency above the cut-off frequency for the respective mode to propagate.

Modes TE_{10} and TE_{01} have both cut-off frequency lower than the lowest TM mode (TM_{11}). To achieve single mode operation the rectangular waveguide operates above the cut-off frequency of the dominant TE_{10} mode, but below the cut-off frequency of the next highest mode. A waveguide operating with more than one propagating mode is called *overmoded*.

Appendix B

Fundamental Parameters of Electromagnetic Transitions

B.1 Insertion/Return Loss, S-parameters and relative links

EM transitions can be interpreted as imperfections in electrical links and as such, they can be analyzed in terms of *insertion/return loss* or their equivalent network behaviour represented by the scattering parameters more commonly known as *S-parameters*.

In this analysis, the ratio P_R/P_I represents the power of a wave reflected from an imperfections (P_R) to that of the incident wave (P_I) and it is commonly used to estimate the performance of the communication link. Hence, the *Return Loss* describes the reduction in the amplitude of the reflected power, as compared to the forward power and it is usually expressed in decibels:

$$ReturnLoss = 10 \cdot \log_{10} \left(\frac{P_I}{P_R} \right) [dB] \quad (B.1)$$

A high value of return loss is then desirable in order to maximize the power transfer through a microwave transition. Similarly to the return loss the *Insertion Loss* is defined as:

$$InsertionLoss = 10 \cdot \log_{10} \left(\frac{P_I}{P_T} \right) [dB] \quad (B.2)$$

Where P_T is the power transmitted after the insertion of a device in a transmission line and P_I is the power transmitted before its insertion. Both return loss and insertion loss are conventionally positive numbers.

The EM junction represented by a transition between two propagating media can also

be analyzed in terms of passive network component with its performance described with the aid of S-parameters.

Scattering parameters are the most frequently used network parameters in microwave engineering because they are derived on the base of incident and reflected travelling waves on transmission lines connecting microwave circuits.

In the present case, an EM transition between rectangular waveguide and a generic planar transmission line can be equivalently considered as *two-ports* network component with voltage waves and current waves on its terminals, *representing the reference planes*, as illustrated in Figure B.1. The current and voltage waves will be used to define the S-parameters. It is possible to consider the voltage wave V_1 at one port as the superposition

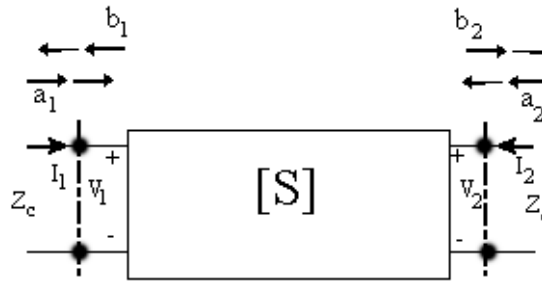


FIGURE B.1: Representation of incident and reflected waves at the terminals of a linear two-port network

of forward, V_1^+ , and backward, V_1^- , waves as follows:

$$V_1 = V_1^+ + V_1^- \quad (\text{B.3})$$

The current wave at the same port can be defined as:

$$I_1 = \frac{1}{Z_c} (V_1^+ - V_1^-) \quad (\text{B.4})$$

Where Z_c is the characteristic impedance of the port transmission line, usually considered 50Ω . Similarly, for the second port it is:

$$V_2 = V_2^+ + V_2^-; \quad I_2 = \frac{1}{Z_c} (V_2^+ - V_2^-) \quad (\text{B.5})$$

The above equations (B.3), (B.4) and (B.5) can be solved to determine the forward and backward voltage waves at the two ports:

$$V_1^+ = \frac{V_1 + Z_c I_1}{2} \quad (\text{B.6})$$

$$V_1^- = \frac{V_1 - Z_c I_1}{2} \quad (\text{B.7})$$

$$V_2^+ = \frac{V_2 + Z_c I_2}{2} \quad (\text{B.8})$$

$$V_2^- = \frac{V_2 - Z_c I_2}{2} \quad (\text{B.9})$$

Incident and reflected voltages are then normalized to the characteristic impedance, Z_c , of the port transmission line:

$$a_{1,2} = \frac{V_{1,2}^+}{\sqrt{Z_c}} \quad (\text{B.10})$$

$$b_{1,2} = \frac{V_{1,2}^-}{\sqrt{Z_c}} \quad (\text{B.11})$$

The normalization allows us to write incident, $P_{1,2}^+$, and reflected, $P_{1,2}^-$, powers as:

$$P_{1,2}^+ = \frac{1}{2} |a_{1,2}|^2 \quad (\text{B.12})$$

$$P_{1,2}^- = \frac{1}{2} |b_{1,2}|^2 \quad (\text{B.13})$$

Following these normalizations, it is possible to define the scattering parameters as:

$$b_1 = S_{11}a_1 + S_{12}a_2 \quad (\text{B.14})$$

$$b_2 = S_{21}a_1 + S_{22}a_2 \quad (\text{B.15})$$

Where S_{nm} accounts the output voltage on port n due to the input on port m . The same equations can be put in the form:

$$\begin{bmatrix} b_1 \\ b_2 \end{bmatrix} = \begin{bmatrix} S_{11} & S_{12} \\ S_{21} & S_{22} \end{bmatrix} \begin{bmatrix} a_1 \\ a_2 \end{bmatrix} \quad (\text{B.16})$$

The S-parameter representation fully characterizes the linear two-port network if the reference planes and the normalizing impedance are specified.

There is a need to distinguish *reciprocal* and *non-reciprocal* networks in the particular

case of a transition between two different transmission lines.

A network is known to be reciprocal if it is passive, hence it adds no energy to the travelling signal, and contains only isotropic materials. Examples of reciprocal networks include cables, attenuators, and all passive power splitters and couplers.

It is worth noting that it is important to have the same characteristic impedance on all ports to have symmetric S-parameters for reciprocal networks. This partly explains why most transitions described in this chapter are designed in back-to-back configuration, although other possible reasons relate to easy assembly and to measurements procedures. In the case where the two-port network is *lossless*, the input S-parameters obey the equation:

$$1 = |S_{11}|^2 + |S_{21}|^2 \quad (\text{B.17})$$

If $a_2 = 0$ then from B.14 and B.15:

$$S_{11} = \frac{b_1}{a_1} = \frac{V_1^-}{V_1^+} \quad (\text{B.18})$$

$$S_{21} = \frac{b_2}{a_1} = \frac{V_2^-}{V_1^+} \quad (\text{B.19})$$

From this case it is easy to link S-parameters with return and insertion loss:

$$\text{ReturnLoss} = \left| 20 \cdot \log_{10} |S_{11}| \right| [dB] \quad (\text{B.20})$$

$$(\text{B.21})$$

$$\text{InsertionLoss} = -20 \cdot \log_{10} |S_{21}| [dB] \quad (\text{B.22})$$

An advantage of the input and output S-parameters is that, being vector quantities, they contain magnitude and phase information. Hence, they can be presented on a polar display on the Smith Chart without any transformation and the corresponding normalized impedances can be readily obtained on the same chart.

In estimating the performance of a network junction as a transition between rectangular waveguide and planar transmission line, the insertion/return loss and S-parameters are then the main indicators of the level of a successful design.

Appendix C

Mechanical CAD Tables

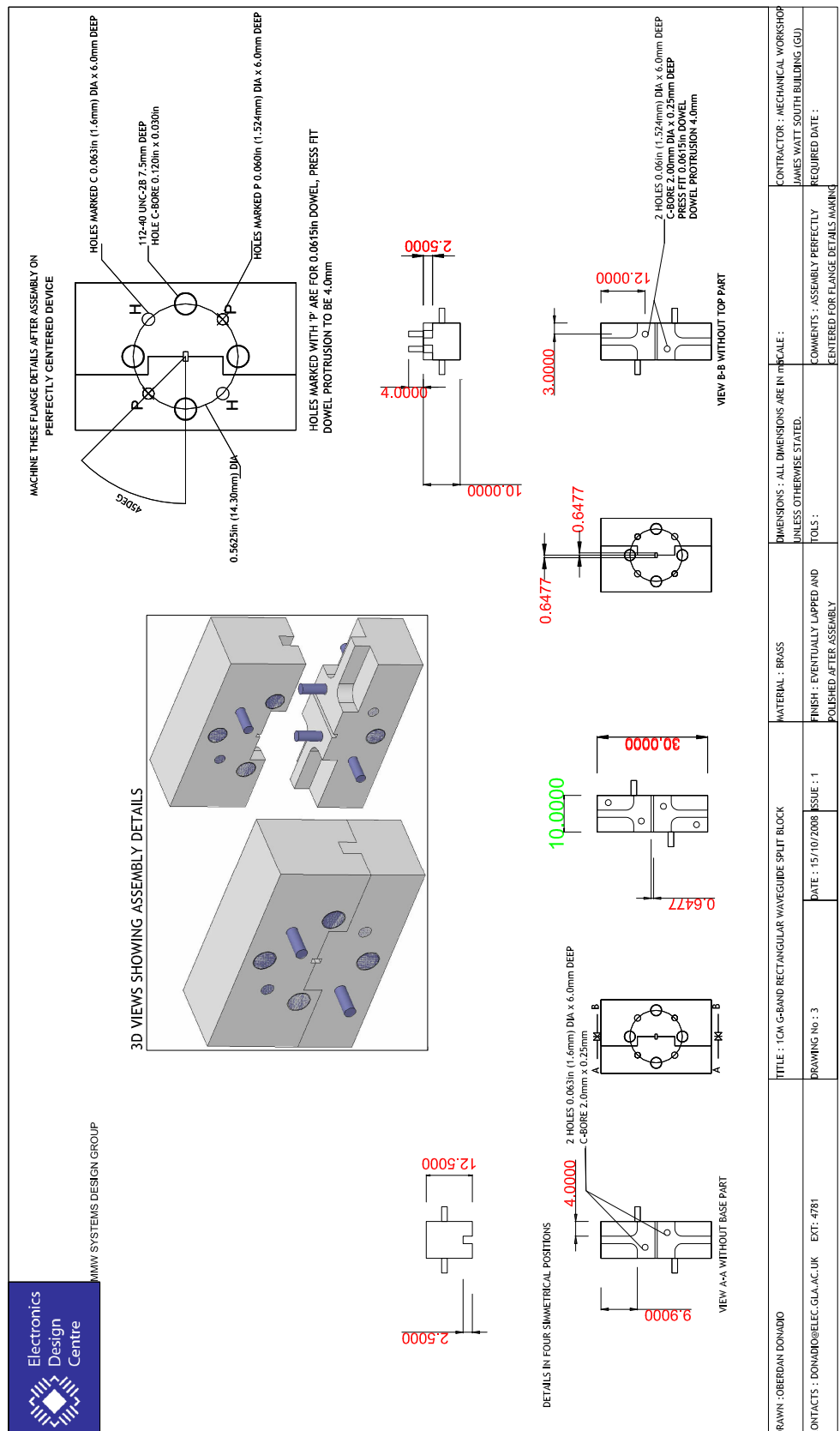


FIGURE C.1: Mechanical Cad table for the fabrication of 1cm waveguide.

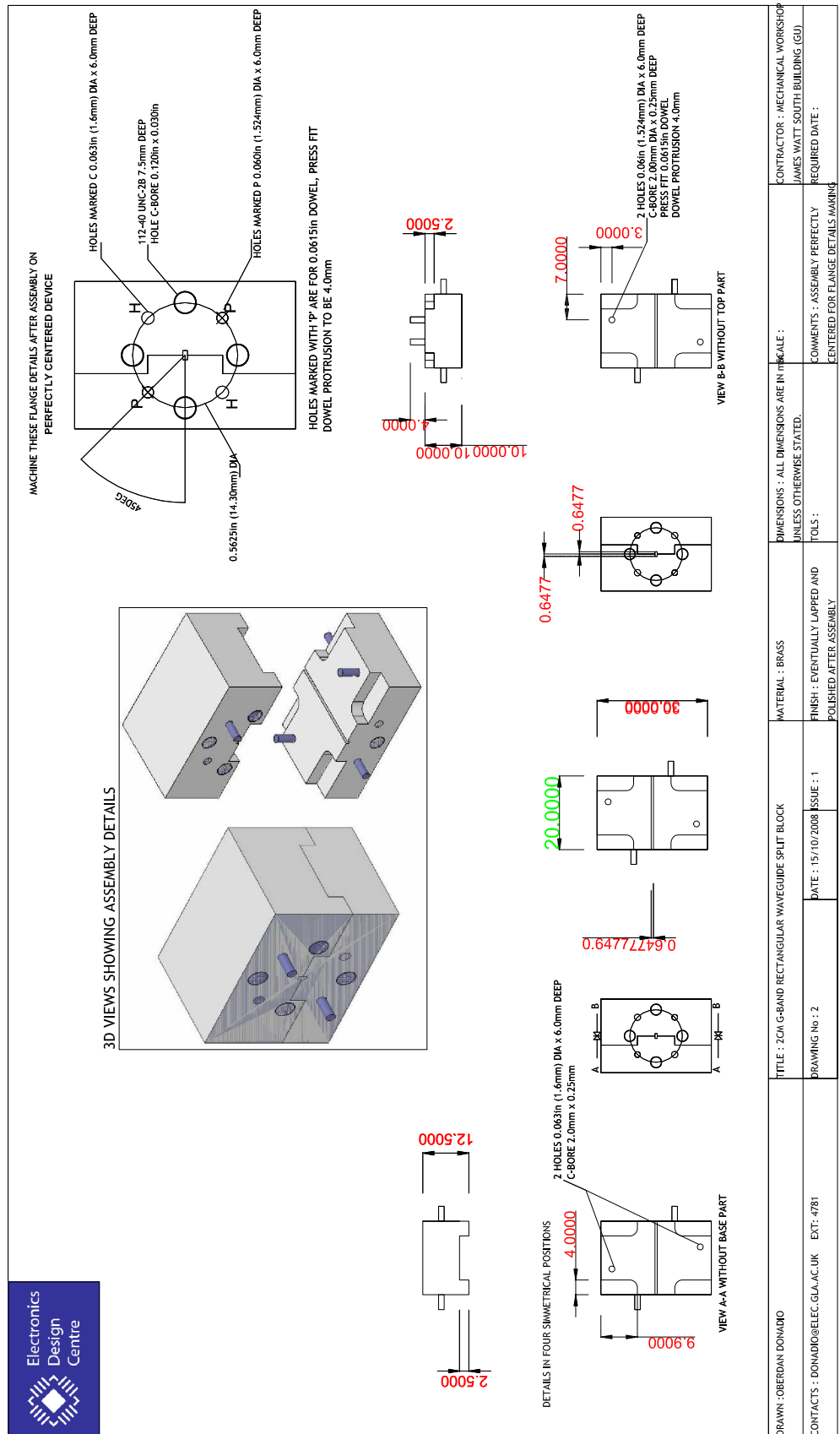


FIGURE C.2: Mechanical Cad table for the fabrication of 2cm waveguide.

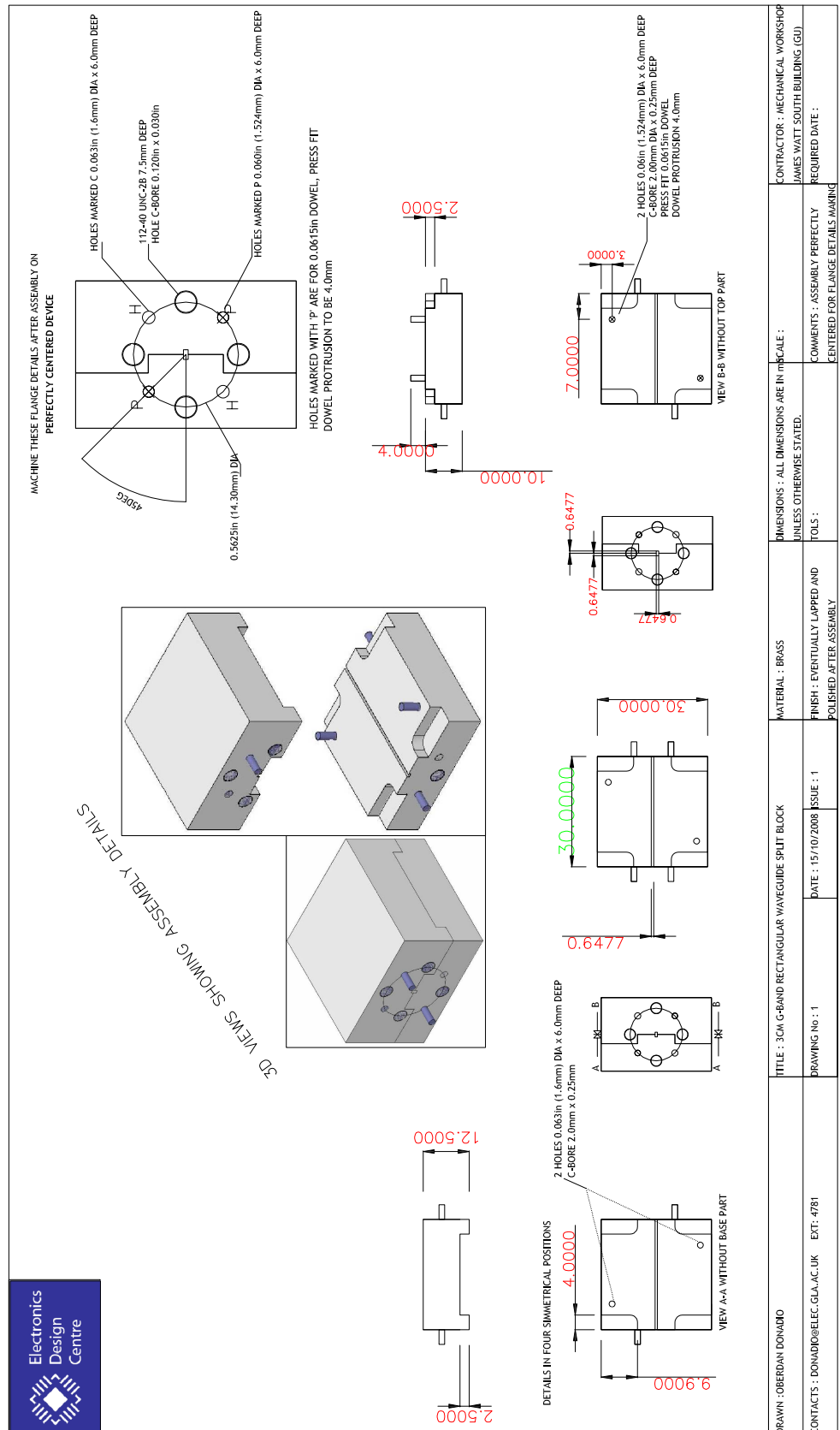


FIGURE C.3: Mechanical Cad table for the fabrication of 3cm waveguide.

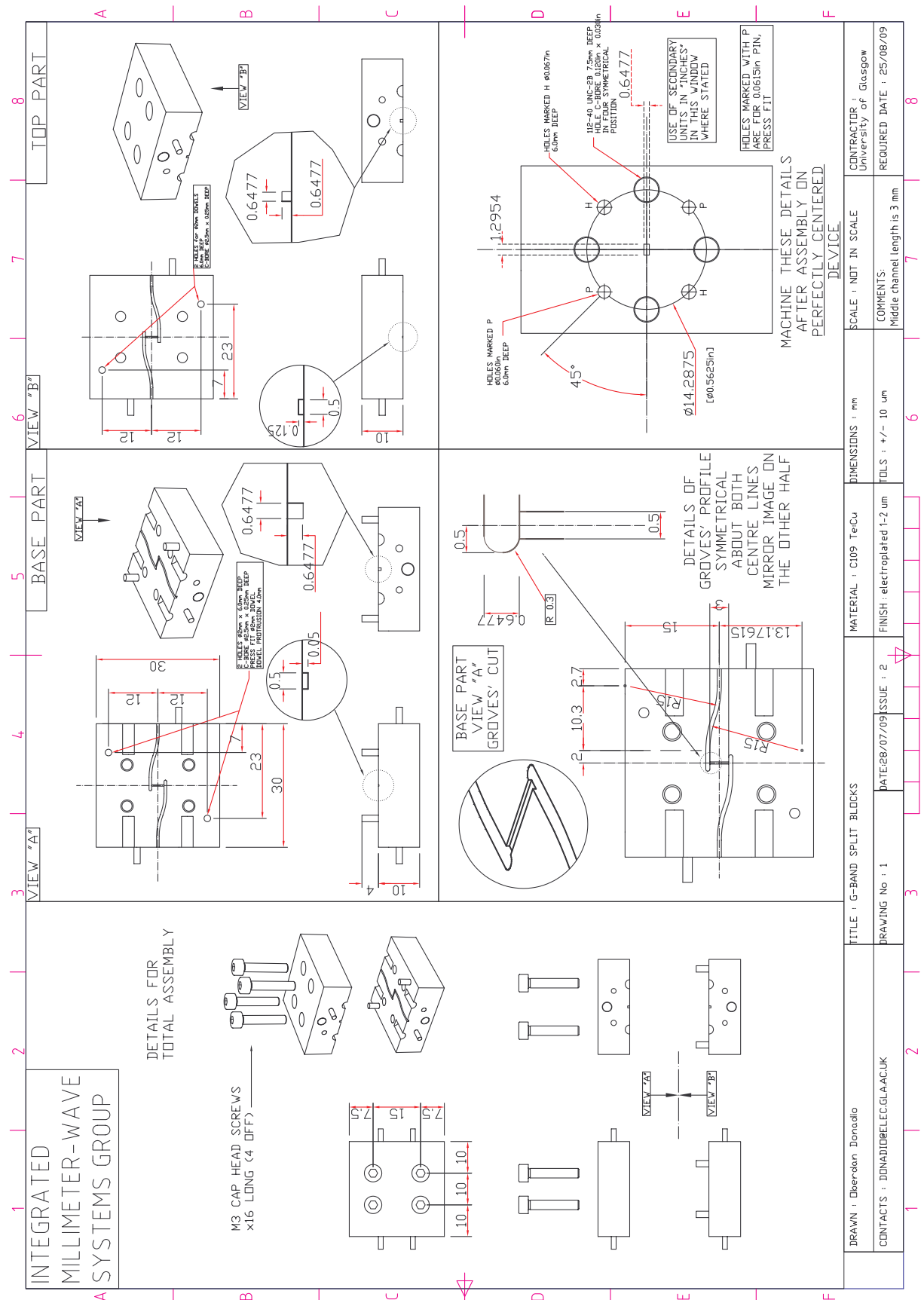
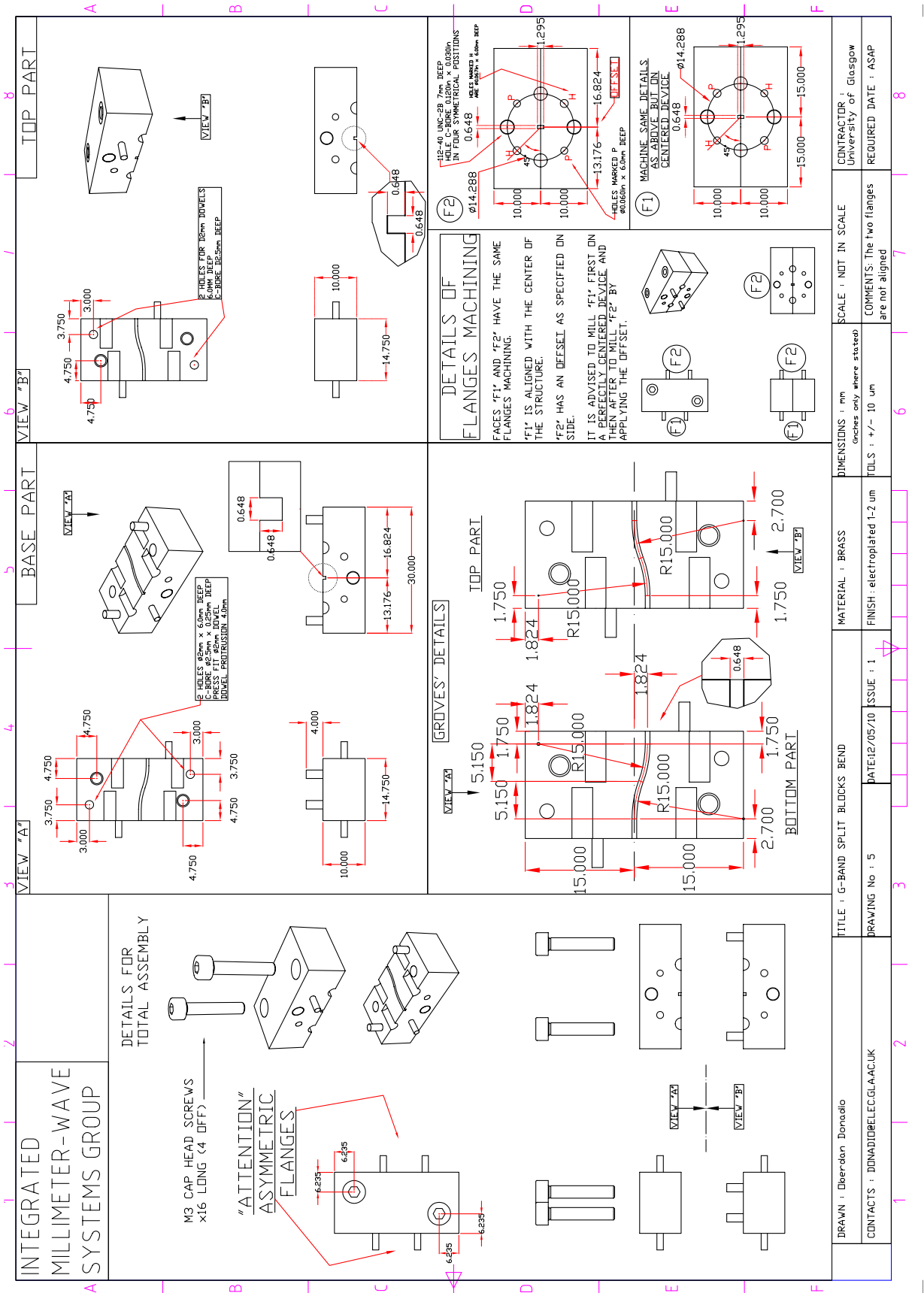


FIGURE C.5: Mechanical Cad table for the fabrication of G-band housing of transitions.



Appendix D

TRL Signal Flow Graphs Equations

With reference to Figure 5.5, for the *thru* connection the signal flow graph gives:

$$T_{11} = \left. \frac{b_1}{a_1} \right|_{a_2=0} = S_{11} + \frac{S_{22}S_{12}^2}{1 - S_{22}^2} \quad (\text{D.1})$$

$$T_{12} = \left. \frac{b_1}{a_2} \right|_{a_1=0} = \frac{S_{12}^2}{1 - S_{22}^2} \quad (\text{D.2})$$

By assumptions of symmetry and reciprocity $T_{22} = T_{11}$ and $T_{21} = T_{12}$. The *Reflect* connection signal flow graph gives the following equation:

$$R_{11} = \left. \frac{b_1}{a_1} \right|_{a_2=0} = S_{11} + \frac{S_{12}^2\Gamma_L}{1 - S_{22}\Gamma_L} \quad (\text{D.3})$$

Also in this case we assume $R_{22} = R_{11}$. For the *Line* connection the corresponding signal flow gives the equations:

$$L_{11} = \left. \frac{b_1}{a_1} \right|_{a_2=0} = S_{11} + \frac{S_{22}S_{12}^2e^{-2\gamma l}}{1 - S_{22}^2e^{-2\gamma l}} \quad (\text{D.4})$$

$$L_{12} = \left. \frac{b_1}{a_2} \right|_{a_1=0} = \frac{S_{12}^2e^{-2\gamma l}}{1 - S_{22}^2e^{-2\gamma l}} \quad (\text{D.5})$$

Also in this last case $L_{11} = L_{22}$ and $L_{21} = L_{12}$.

The eqs. D.2-D.5 form a five equations system with five unknowns: $S_{11}, S_{22}, S_{21}, \Gamma_L$ and $e^{-\gamma l}$, hence the solution is unique.

From eq. D.3 it is possible to solve for Γ_L after found all the other four unknowns. Eq. D.2 can be used to eliminate S_{12} from D.2 and D.5. Consequently, S_{11} can be eliminated from D.2 and D.5, leaving two equations:

$$L_{12}e^{-2\gamma l} - L_{12}S_{22}^2 = T_{12}e^{-\gamma l} - T_{12}S_{22}^2e^{-\gamma l} \quad (\text{D.6})$$

$$e^{-2\gamma l}(T_{11} - S_{22}T_{12}) - T_{11}S_{22}^2 = L_{11}(e^{-2\gamma l} - S_{22}^2) - S_{22}T_{12} \quad (\text{D.7})$$

Eq. D.6 is solved for S_{22} and then substituted into D.7 to give a quadratic equation in $e^{-\gamma l}$, having the solution:

$$e^{-\gamma l} = \frac{L_{12}^2 + T_{12}^2 - (T_{11} - L_{11})^2 \pm \sqrt{[L_{12}^2 + T_{12}^2 - (T_{11} - L_{11})^2]^2 - 4L_{12}^2T_{12}^2}}{2L_{12}T_{12}} \quad (\text{D.8})$$

The choice of the sign is related to the sign of Γ , hence from the type of reflection we consider. In our case it is a short. Now, by multiplying D.2 by S_{22} and subtract the result from D.2 it comes to:

$$T_{11} = S_{11} + S_{22}T_{12} \quad (\text{D.9})$$

Similarly multiplying D.5 by S_{22} and subtracting from D.5 we get:

$$L_{11} = S_{11} + S_{22}L_{12}e^{-\gamma l} \quad (\text{D.10})$$

Eliminating S_{11} from D.9 and D.10 by subtracting from each other, it gets to an equation for S_{22} in terms of $e^{-\gamma l}$:

$$S_{22} = \frac{T_{11} - L_{11}}{T_{12} - L_{12}e^{-\gamma l}} \quad (\text{D.11})$$

Now solving D.9 for S_{11} :

$$S_{11} = T_{11} - S_{22}T_{12} \quad (\text{D.12})$$

and solving D.10 for S_{12} :

$$S_{12}^2 = T_{12}(1 - S_{22}^2) \quad (\text{D.13})$$

Finally D.3 can be solved for Γ_L to give:

$$\Gamma_L = \frac{R_{11} - S_{11}}{S_{12}^2 + S_{22}(R_{11} - S_{11})} \quad (\text{D.14})$$

The eqs. D.8 and D.11-D.14 give the S-parameters for the error boxes, the propagation constant with $e^{-\gamma l}$ and the reflection coefficient Γ_L . The definition of the scattering matrix for the error boxes is then used to de-embed the DUT S-parameters from what effectively the instrumentation is measuring.

If $[A]$ is the error box S-parameters matrix and $[A^m]$ is the S-parameters matrix of the

real measurements, the DUT S-parameters matrix $[A']$ is given by:

$$[A'] = [A]^{-1} \cdot [A^m] \cdot [A] \quad (\text{D.15})$$

Bibliography

- [1] R. Appleby. Passive millimetre-wave imaging and how it differs from terahertz imaging. *Philosophical Transactions of the Royal Society of London. Series A: Mathematical, Physical and Engineering Sciences*, 362(1815):379–393, 2004. doi: 10.1098/rsta.2003.1323. URL <http://rsta.royalsocietypublishing.org/content/362/1815/379.abstract>.
- [2] D. Le Vine N. Skou. *Microwave Radiometer Systems: design and analysis*. Artech House, 2006.
- [3] Mark J. Rosker H. Bruce Wallace. Analytical performance comparison of active and passive smmw imaging for contraband detection. *Millimetre Wave and Terahertz Sensors and Technology II*, 7485, 2009.
- [4] L. Yujiri. Passive millimeter wave imaging. In *Microwave Symposium Digest, 2006. IEEE MTT-S International*, pages 98 –101, 11-16 2006. doi: 10.1109/MWSYM.2006.249938.
- [5] Roger Appleby, Peter Coward, and Gordon Sinclair. Terahertz detection of illegal objects. In Robert Miles, Xi-Cheng Zhang, Heribert Eisele, and Arunas Krotkus, editors, *Terahertz Frequency Detection and Identification of Materials and Objects*, volume 19 of *NATO Security through Science Series*, pages 225–240. Springer Netherlands, 2007.
- [6] R. Appleby and H.B. Wallace. Standoff detection of weapons and contraband in the 100 ghz to 1 thz region. *Antennas and Propagation, IEEE Transactions on*, 55 (11):2944 –2956, 2007. ISSN 0018-926X. doi: 10.1109/TAP.2007.908543.
- [7] G.N. Sinclair, R.N. Anderton, and R. Appleby. Outdoor passive millimetre wave security screening. In *Security Technology, 2001 IEEE 35th International Carnahan Conference on*, pages 172 –179, oct 2001. doi: 10.1109/.2001.962830.
- [8] R. Appleby. Passive millimetre wave imaging and security. In *European Radar Conference 2004, Amsterdam*, 2004.

- [9] Richard G. Humphreys, Stephen M. Taylor, Paul A. Manning, Paul D. Munday, and Jeff Powell. Performance of 94ghz receivers for passive imaging. volume 6548, page 65480H. SPIE, 2007. doi: 10.1117/12.723784. URL <http://link.aip.org/link/?PSI/6548/65480H/1>.
- [10] Jonathan J. Lynch, Perry A. Macdonald, Harris P. Moyer, and Robert G. Nagele. Passive millimeter wave imaging sensors for commercial markets. *Appl. Opt.*, 49(19):E7–E12, 2010. URL <http://ao.osa.org/abstract.cfm?URI=ao-49-19-E7>.
- [11] Sbastien Chartier, Axel Tessmann, Arnulf Leuther, Rainer Weber, Ingmar Kallfass, Michael Schlechtweg, Stephan Stanko, Helmut Essen, and Oliver Ambacher. Advanced mhemt mmics for 220 ghz high-resolution imaging systems. *physica status solidi (c)*, 6(6):1390–1393, 2009. ISSN 1610-1642. doi: 10.1002/pssc.200881536. URL <http://dx.doi.org/10.1002/pssc.200881536>.
- [12] A. Tessmann, A. Leuther, H. Massler, M. Kuri, and R. Loesch. A metamorphic 220-320 ghz hemt amplifier mmic. In *Compound Semiconductor Integrated Circuits Symposium, 2008. CSIC '08. IEEE*, pages 1–4, oct. 2008. doi: 10.1109/CSICS.2008.12.
- [13] P. Fay, J.N. Schulman, III Thomas, S., D.H. Chow, Y.K. Boegeman, and K.S. Holabird. High-performance antimonide-based heterostructure backward diodes for millimeter-wave detection. *Electron Device Letters, IEEE*, 23(10):585 – 587, oct 2002. ISSN 0741-3106. doi: 10.1109/LED.2002.803760.
- [14] G.E. Ponchak and R.N. Simons. A new rectangular waveguide to coplanar waveguide transition. pages 491–492 vol.1, may. 1990. doi: 10.1109/MWSYM.1990.99626.
- [15] E.M. Godshalk. A v-band wafer probe using ridge-trough waveguide. In *Microwave Symposium Digest, 1991., IEEE MTT-S International*, pages 1129–1132 vol.3, July 1991. doi: 10.1109/MWSYM.1991.147215.
- [16] R. Shireen, S. Shi, P. Yao, C.A. Schuetz, J. Macario, and D.W. Prather. A w-band transition from coplanar waveguide to rectangular waveguide. pages 1–4, jul. 2008. doi: 10.1109/APS.2008.4619920.
- [17] R. Shireen, Shouyuan Shi, Peng Yao, C.A. Schuetz, J. Macario, and D.W. Prather. Cpw to rectangular waveguide transition on an substrate. *Microwave Theory and Techniques, IEEE Transactions on*, 57(6):1494–1499, jun. 2009. ISSN 0018-9480. doi: 10.1109/TMTT.2009.2020673.
- [18] Wilfried Grabherr and Wolfgang Menzel. A new transition from microstrip line to rectangular waveguide. volume 2, pages 1170–1175, sep. 1992. doi: 10.1109/EUMA.1992.335862.

- [19] D.Pozar. *Microwave Engineering*. John Wiley & Sons; 2nd Edition edition, 1998.
- [20] W. Grabherr, W.G.B. Huder, and W. Menzel. Microstrip to waveguide transition compatible with mm-wave integrated circuits. *Microwave Theory and Techniques, IEEE Transactions on*, 42(9):1842 –1843, sep. 1994. ISSN 0018-9480. doi: 10.1109/22.310597.
- [21] L. Hyvonen and A. Hujanen. A compact mmic-compatible microstrip to waveguide transition. volume 2, pages 875 –878 vol.2, jun. 1996. doi: 10.1109/MWSYM.1996.511077.
- [22] W. Simon, M. Werthen, and I. Wolff. A novel coplanar transmission line to rectangular waveguide transition. volume 1, pages 257 –260 vol.1, jun. 1998. doi: 10.1109/MWSYM.1998.689369.
- [23] H IIZUKA, T WATANABE, K SATO, and K NISHIKAWA. Millimeter-wave microstrip line to waveguide transition fabricated on a single layer dielectric substrate. *IEICE Trans Commun (Inst Electron Inf Commun Eng)*, E85-B(6):0916-8516, 2002.
- [24] Constantine A. Balanis. *Antenna Theory: Analysis and Design*. Wiley-Interscience, 2005.
- [25] H. Iizuka, K. Sakakibara, and N. Kikuma. Millimeter-wave transition from waveguide to two microstrip lines using rectangular patch element. *Microwave Theory and Techniques, IEEE Transactions on*, 55(5):899 –905, may. 2007. ISSN 0018-9480. doi: 10.1109/TMTT.2007.895139.
- [26] T. Cavanna, L. Vanni, L. Di Cecca, A. Salome, and M. Ruggieri. W band technologies for data collection experiment of the david mission. volume 1, pages 1 – 269 vol.1, mar. 2003. doi: 10.1109/AERO.2003.1235058.
- [27] D. Deslandes and Ke Wu. Integrated transition of coplanar to rectangular waveguides. volume 2, pages 619 –622 vol.2, 2001. doi: 10.1109/MWSYM.2001.966971.
- [28] T. Cavanna, E. Franzese, E. Limiti, G. Pelosi, S. Selleri, and A. Suriani. Fem-based evaluation of manufacturing tolerances on a millimeter-waves rectangular to coplanar waveguide transition. volume 1, pages 190 – 193 Vol.1, may. 2004.
- [29] F. Poprawa, A. Ziroff, and F. Ellinger. A novel approach for a periodic structure shielded microstrip line to rectangular waveguide transition. pages 1559 –1562, jun. 2007. doi: 10.1109/MWSYM.2007.380572.
- [30] P.Wade. Rectangular waveguide to coax transition design, Nov/Dec 2006. URL http://www.wighz.org/QEX/Rectangular_Waveguide_to_Coax_Transition_Design.pdf.

- [31] Y.-C. Shih, T.-N. Ton, and L.Q. Bui. Waveguide-to-microstrip transitions for millimeter-wave applications. pages 473 –475 vol.1, may. 1988. doi: 10.1109/MWSYM.1988.22077.
- [32] Yoke-Choy Leong and S. Weinreb. Full band waveguide-to-microstrip probe transitions. volume 4, pages 1435 –1438 vol.4, 1999. doi: 10.1109/MWSYM.1999.780219.
- [33] S. Llorente-Romano, B.P. Dorta-Naranjo, F. Perez-Martinez, and M. Salazar-Palma. Ka-band waveguide-to-microstrip transition design and implementation. volume 3, page 404, 2002.
- [34] Kang Wook Kim, Chae-Ho Na, and Dong-Sik Woo. New dielectric-covered waveguide-to-microstrip transitions for ka-band transceivers. volume 2, pages 1115 – 1118 vol.2, jun. 2003.
- [35] Y. Deguchi, K. Sakakibara, N. Kikuma, and H. Hirayama. Millimeter-wave microstrip-to-waveguide transition operating over broad frequency bandwidth. page 4 pp., jun. 2005. doi: 10.1109/MWSYM.2005.1517163.
- [36] A. Tessmann, A. Leuther, M. Kuri, H. Massler, M. Riessle, H. Essen, S. Stanko, R. Sommer, M. Zink, R. Stibal, W. Reinert, and M. Schlechtweg. 220 ghz low-noise amplifier modules for radiometric imaging applications. pages 137 –140, sep. 2006. doi: 10.1109/EMICC.2006.282770.
- [37] J. W. Kooi, G. Chattopadhyay, S. Withington, F. Rice, J. Zmuidzinas, C. Walker, and G. Yassin. A full-height waveguide to thin-film microstrip transition with exceptional rf bandwidth and coupling efficiency. *International Journal of Infrared and Millimeter Waves*, 24:261–284, 2003. ISSN 0195-9271. URL <http://dx.doi.org/10.1023/A:1021903132609>. 10.1023/A:1021903132609.
- [38] A. Navarrini, T. Pisanu, S. Mariotti, and T. Idda. A simple k-band waveguide-to-microstrip probe transition. *Microw. Opt. Technol. Lett.*, 49(7):1098-2760, 2007. URL <http://dx.doi.org/10.1002/mop.22558>.
- [39] L. Samoska, W.R. Deal, G. Chattopadhyay, D. Pukala, A. Fung, T. Gaier, M. Soria, V. Radisic, X. Mei, and R. Lai. A submillimeter-wave hemt amplifier module with integrated waveguide transitions operating above 300 ghz. *Microwave Theory and Techniques, IEEE Transactions on*, 56(6):1380 –1388, jun. 2008. ISSN 0018-9480. doi: 10.1109/TMTT.2008.923353.
- [40] J.H.C. van Heuven. A new integrated waveguide-microstrip transition (short papers). *Microwave Theory and Techniques, IEEE Transactions on*, 24(3):144 – 147, March 1976. ISSN 0018-9480. doi: 10.1109/TMTT.1976.1128796.

- [41] E. Daniel, V. Sokolov, S. Sommerfeldt, J. Bublitz, K. Olson, B. Gilbert, L. Samoska, and D. Chow. Packaging of microwave integrated circuits operating beyond 100 ghz. pages 374 – 383, aug. 2002. doi: 10.1109/LECHPD.2002.1146777.
- [42] G. Ponchak and N. Simons. A new model for broadband waveguide to microstrip transition design. Tech. Memorandum 88905, NASA, Dec 1986.
- [43] V.S. Mottonen. Wideband coplanar waveguide-to-rectangular waveguide transition using fin-line taper. *Microwave and Wireless Components Letters, IEEE*, 15(2):119 – 121, feb. 2005. ISSN 1531-1309. doi: 10.1109/LMWC.2004.842855.
- [44] A. Ramdane, E. Richalot, O. Picon, J. Puech, and L. Lapierre. Rectangular waveguide-to-cpw transition without air-bridge in the ka-band. *Microw. Opt. Technol. Lett.*, 49(3):1098-2760, 2007. URL <http://dx.doi.org/10.1002/mop.22182>.
- [45] Ting-Huei Lin and Ruey-Beei Wu. Cpw to waveguide transition with tapered slot-line probe. *Microwave and Wireless Components Letters, IEEE*, 11(7):314 – 316, jul. 2001. ISSN 1531-1309. doi: 10.1109/7260.933782.
- [46] Ting-Huei Lin and Ruey-Beei Wu. A broadband microstrip-to-waveguide transition with tapered cps probe. pages 1 – 4, sep. 2002. doi: 10.1109/EUMA.2002.339360.
- [47] Cheng-Fu Hung, An-Shyi Liu, Chih-Hung Chien, C.-L. Wang, and Ruey-Beei Wu. Bandwidth enhancement on waveguide transition to conductor backed cpw with high dielectric constant substrate. *Microwave and Wireless Components Letters, IEEE*, 15(2):128 – 130, feb. 2005. ISSN 1531-1309. doi: 10.1109/LMWC.2004.842862.
- [48] Rodney B. Waterhouse. *Printed antennas for wireless communications*. John Wiley and Sons, 2007.
- [49] N. Kaneda, Yongxi Qian, and T. Itoh. A broadband microstrip-to-waveguide transition using quasi-yagi antenna. volume 4, pages 1431 – 1434 vol.4, 1999. doi: 10.1109/MWSYM.1999.780218.
- [50] N. Kaneda, Y. Qian, and T. Itoh. A broadband cpw-to-waveguide transition using quasi-yagi antenna. volume 2, pages 617 – 620 vol.2, 2000. doi: 10.1109/MWSYM.2000.863260.
- [51] Ruei-Ying Fang and Chun-Long Wang. Wideband slotline-to-rectangular waveguide transition using truncated bow-tie antenna. pages 1395 – 1398, dec. 2006. doi: 10.1109/APMC.2006.4429668.

- [52] Kook Joo Lee, Dong Ho Lee, Jae-Sung Rieh, and Moonil Kim. A v-band waveguide transition design appropriate for monolithic integration. pages 1–4, dec. 2007. doi: 10.1109/APMC.2007.4554756.
- [53] K. Leong, W.R. Deal, V. Radisic, Xiao Bing Mei, J. Uyeda, L. Samoska, A. Fung, T. Gaier, and R. Lai. A 340-380 ghz integrated cb-cpw-to-waveguide transition for sub millimeter-wave mmic packaging. *Microwave and Wireless Components Letters, IEEE*, 19(6):413–415, jun. 2009. ISSN 1531-1309. doi: 10.1109/LMWC.2009.2020043.
- [54] V.S. Mottonen and A.V. Raisanen. Novel wide-band coplanar waveguide-to-rectangular waveguide transition. *Microwave Theory and Techniques, IEEE Transactions on*, 52(8):1836–1842, aug. 2004. ISSN 0018-9480. doi: 10.1109/TMTT.2004.831580.
- [55] Yu Lou, Chi Hou Chan, and Quan Xue. An in-line waveguide-to-microstrip transition using radial-shaped probe. pages 3117–3120, jun. 2007. doi: 10.1109/APS.2007.4396196.
- [56] B. M. Reljic. Lowloss mic/mmic compatible microstrip to waveguide transition without a balun. *Microw. Opt. Technol. Lett.*, 50(1):1098-2760, 2008. URL <http://dx.doi.org/10.1002/mop.23012>.
- [57] Y. Tikhov, Jeong-Woo Moon, Yuon-Jin Kim, and Yu. Sinelnikov. Refined characterization of e-plane waveguide to microstrip transition for millimeter-wave applications. pages 1187–1190, 2000. doi: 10.1109/APMC.2000.926043.
- [Ansoft] Ansoft. *HFSS guide*. Ansoft.
- [58] J.-F. Lee, D.-K. Sun, and Z.J. Cendes. Full-wave analysis of dielectric waveguides using tangential vector finite elements. *Microwave Theory and Techniques, IEEE Transactions on*, 39(8):1262–1271, aug 1991. ISSN 0018-9480. doi: 10.1109/22.85399.
- [59] Inder Bahl A. Ittipiboon R. Garg, P. Bhartia. *Microstrip Antenna Design Handbook*. Artech House, 2000.
- [60] R. Collin. *Field Theory of Guided Waves*. McGraw Hill, 1960.
- [61] Peter Delmotte. Waveguide-coaxial line transitions. In *Belgian Microwave Roundtable*, 2001.
- [62] I.A. Eshrah, A.A. Kishk, A.B. Yakovlev, and A.W. Glisson. Equivalent circuit model for a waveguide probe with application to dra excitation. *Antennas and Propagation, IEEE Transactions on*, 54(5):1433–1441, may 2006.

- [63] R. Collin. *Field Theory of Guided Waves*. McGraw Hill, 1960.
- [64] G.H. Robinson. Resonant frequency calculations for microstrip cavities (correspondence). *Microwave Theory and Techniques, IEEE Transactions on*, 19(7):665 – 666, jul 1971. ISSN 0018-9480. doi: 10.1109/TMTT.1971.1127602.
- [65] R. Raja, M. Nishimoto, B. Osgood, M. Barsky, M. Sholley, R. Quon, G. Barber, P. Liu, R. Lai, F. Hinte, G. Haviland, and B. Vacek. A 183 ghz low noise amplifier module with 5.5 db noise figure for the conical-scanning microwave imager sounder (cmis) program. In *Microwave Symposium Digest, 2001 IEEE MTT-S International*, volume 3, pages 1955 –1958 vol.3, 2001. doi: 10.1109/MWSYM.2001.967292.
- [66] A. Zirotti, M. Nalezinski, and W. Menzel. A novel approach for ltcc packaging using a pbg structure for shielding and package mode suppression. In *Microwave Conference, 2003. 33rd European*, volume 1, pages 419 – 422 Vol.1, oct. 2003. doi: 10.1109/EUMC.2003.1262311.
- [67] Thoms S. and Macintyre D. Electron beam lithography course. 2008, University of Glasgow.
- [68] MicroChem. Nanopmma and copolymer. Technical report, MicroChem Corp., 2001.
- [69] Haltermann. Methyl isobutyl ketone (mibk). Technical report, Johann Haltermann Ltd., 2000.
- [70] Clariant. Az 4500 series, thick film photoresists. Technical report, Clariant, 2000.
- [71] Clariant. Az 400k, developer for az 4500 series. Technical report, Clariant, 2000.
- [72] Shipley. Microposit, s1800 series photo resists. Technical report, Shipley, 2000.
- [73] Shipley. Microposit, mf-319 developer. Technical report, Shipley, 2000.
- [74] Elgaid K. *A Ka-band GaAs MESFET Monolithic Downconverter*. PhD thesis, Department of Electronics and Electrical Engineering, University of Glasgow, 1998.
- [75] Chang-Hwang Hua Hiep Pham. Strength improvement for the gaas thin wafer. In *Intern. Conf. on Compound Semiconductor Mfg.*, 2003.
- [76] Charles Oleson and Anthony Denning. Millimeter wave vector analysis calibration and measurement problems caused by common waveguide irregularities. In *ARFTG Conference Digest-Fall, 56th*, volume 38, pages 1 –9, nov. 2000. doi: 10.1109/ARFTG.2000.327428.
- [77] Dynamics Incorporated Datron. Datron, tool catalog 2007. Technical report, 2007.

- [Aremco] Aremco. Aremco bond silver epoxy 556a-b. Technical report, Aremco.
- [78] M.I. Aksun N. Kinayman. *Modern Microwave Circuits*. Artech House, 2005.
- [79] E. N. Horner N. Kerr, A.R. Wollack. Waveguide flanges for alma instrumentation. Memo 278, Alma project, November 1999.
- [80] O. Donadio, K. Elgaid, and R. Appleby. Waveguide-to-microstrip transition at g-band using elevated e-plane probe. *Electronics Letters*, 47(2):115–116, january 2011. ISSN 0013-5194. doi: 10.1049/el.2010.2926.
- [81] J. Carroll, M. Li, and K. Chang. New technique to measure transmission line attenuation. *Microwave Theory and Techniques, IEEE Transactions on*, 43(1):219–222, jan 1995. ISSN 0018-9480. doi: 10.1109/22.362986.
- [82] Jet propulsion Laboratory Ponchak, G. Die attachment. *GaAs MMIC Reliability Assurance Guideline for Space Applications*, pages 181–184, 1996.
- [83] D. Markell J. Capwell, T. Weller and L. Dunleavy. Automation and real-time verification of passive component s-parameter measurements using loss factor calculations. *Microwave Journal*, Vol.47, 2004.
- [84] P.; Beyne E.; Tpper M.; Dietrich L.; Becks K.H.; Wermes N.; Ehrmann O.; Reichl H. Wolf, J.; Gerlach. High density pixel detector module using flip chip and thin film technology. In *International Conference on High-Density Interconnect and Systems Packaging ;2000, Denver/Colo.¿*, 2000.
- [85] Ginley R A Ridler, N M. Ieee p1785 - a new standard for waveguide above 110 ghz. *Microwave Journal*, 54 (supplement):20, 2011.